

FUNDAMENTAL PROPERTIES OF A MICROWAVE INDUCED
ARGON PLASMA

E SURREY

POLYTECHNIC OF NORTH LONDON

MARCH 1987

A dissertation submitted in partial fulfilment of the
regulations for the degree of Ph.D. of the CNA.

FUNDAMENTAL PHYSICAL PROPERTIES OF A MICROWAVE INDUCED ARGON PLASMA

E SURREY

Abstract

The behaviour of a microwave excited electrodeless argon discharge is investigated at pressures between 0.02 and 6.00 mbar. Spectroscopic measurements of twenty one emission lines of the argon I spectrum and seven lines of the argon II spectrum are combined with microwave impedance and Langmuir probe measurements. The population densities of some seventeen levels of the argon atom are evaluated and the results analysed in terms of a collisional-radiative recombination model due to Fujimoto. The atomic system is shown to be in the saturation phase above the 5p level and the population coefficients for seven levels of the argon atom are determined.

Values of ion density and electron temperature are derived from probe measurements. The former are compared with values of electron density derived from impedance measurements and it is shown that the condition of electrical neutrality is not valid in this plasma. Ion loss to the walls of the discharge tube is demonstrated to be a major contributor to the non-neutrality of the plasma.

The effect of a double Maxwellian distribution of electrons upon the double floating probe characteristics is investigated. A pair of equations is derived to describe the characteristic under this condition and the results are shown to fit an observed, but previously undescribed, form of characteristic. The behaviour of the characteristic for different ratios of electron temperature and electron density of the two distributions is examined and it is shown that careful consideration must be given to the interpretation of double floating probe characteristics to avoid ambiguous results.

The effect of microwave power on the population densities of the argon atom and ion, the electron temperature and the electron and ion densities is examined. It is shown that power and pressure are not independent variables and the consequences of this for the analysis of the data is discussed.

The author attended the 16th EGAS conference, London, 1984 and in 1986 presented a paper containing some of the work described here at the SAC/BNASS conference at Bristol. The conference proceedings were not published.

ACKNOWLEDGEMENTS

I should like to thank my supervisor Dr. M. Outred for his guidance, Dr. F.L. Whittaker of Thorn Lighting, Leicester for his help and suggestions and Mr. D. Cross, the glass blower, for so skillfully forming the probe tube.

I am also indebted to my parents for their material support and encouragement and to P.D.A. for his contribution to my spiritual welfare.

CONTENTS

Abstract	
List of Figures	v
List of Tables	xi
CHAPTER 1 REVIEW OF PREVIOUS WORK	1
Introduction	2
1.1 Plasma Models	2
1.2 Earlier Studies of Microwave Excited Discharges	4
1.2.1 Spectroscopic Studies	4
1.2.2 Probe Studies	6
1.2.3 Microwave Measurements	8
1.3 Scope of this Work	15
CHAPTER 2 DESCRIPTION OF EXPERIMENTAL ARRANGEMENT	16
2.1 Introduction	17
2.2 The Vacuum System	17
2.2.1 Low Vacuum Arm	19
2.2.2 High Vacuum Arm	19
2.2.3 Problems of Design	23
2.3 The Discharge Tubes	23
2.3.1 The Plain Tube	23
2.3.2 The Probe Tube	23
2.3.3 Construction of the Probes	24
(a) Choice of Probe Material	24
(b) Preparation of Probes	26
2.4 Resistance to Contamination	27
2.5 The Spectral Recording System	28

2.5.1	Entrance Optics	31
2.5.2	The Monochromator	32
2.5.3	The Detector System	32
2.6	The Microwave Excitation System	33
2.6.1	The Cavity	36
2.6.2	The Variable Attenuator	36
2.7	Probe Characteristic Measuring System	38
2.7.1	The Voltage Ramp Generator	38
2.7.2	Probe Characteristic Circuit	38
CHAPTER 3 MICROWAVE MEASUREMENTS		45
3.1	Theory	46
3.1.1	t-paramter representation	48
3.2	Preliminary Measurements	50
3.2.1	Determination of Reference Plane of Cavity	51
3.2.2	Response of the Diode Rectifier	54
3.3	Measurement of the VSWR	57
CHAPTER 4 SPECTROSCOPIC MEASUREMENTS		59
4.1	Theory	60
4.2	Consideration of the Argon I Lines	60
4.3	Calibration of Optical System	61
4.4	Comparison of Continuum and Discrete Spectra	66
4.5	Measurement of the Argon Spectra	70
4.5.1	The Argon I Spectrum	70
4.5.2	The Argon II Spectrum	71

CHAPTER 5	PROBE MEASUREMENTS	73
5.1	Theory	74
5.1.1	Introduction	74
5.1.2	Formulation of Probe Equations	76
5.2	Interpretation of Probe Characteristics	80
5.2.1	Determination of Electron Temperature, T_e	80
5.2.2	Determination of the Carrier Density	85
5.3	Acquisition of Probe Data	86
CHAPTER 6	SPECTROSCOPIC RESULT	89
6.1	Calculation of Population Density	90
6.2	Boltzmann Plots for the Argon I System	91
6.3	Comparison of Plain and Probe Tubes	94
6.4	Variation of Population Density with Distance from the Cavity	98
6.5	Variation of Population Density with Power	98
6.6	The Second Spectrum of Argon	111
6.7	Variation of Intensity with Pressure	117
6.8	Stark Broadening	126
CHAPTER 7	RESULTS OF LANGMUIR PROBE MEASUREMENTS	128
7.1	Appearance of Probe Characteristics	129
7.2	Evaluation of Plasma Parameters	129
7.2.1	Calculation of Electron Temperature, T_e	129
7.2.2	Variation of T_e with Power and Pressure	140
7.2.3	Calculation of Carrier Density, n_+	145
7.2.4	Variation of n_+ with Power and Pressure	147
7.3	Variation of T_e and n_+ with Distance from the Cavity	158

CHAPTER 8	MICROWAVE RESULTS	160
8.1	Calculation of the Microwave Impedance	164
8.2	Variation of Impedance with Power	168
8.3.1	Calculation of Electron Density	168
8.3.2	Variation of Electron Density with Pressure and Power	173
8.4	Comparison of Real and Imaginary Components of Z	183
CHAPTER 9	CHARACTERISATION OF THE PLASMA AND CONCLUSIONS	192
9.1	Preamble	193
9.2	Comparison of the Carrier Density Measurements	193
9.2.1	Relationship between the Ion and Electron Density	193
9.2.2	Comparison of the Ion and Electron Densities	196
9.3	Determination of Plasma Phase	204
9.3.1	The Plasma Regimes	204
9.3.2	The Plasma Phase	207
9.4	Determination of the Population Coefficient $r_m^{(1)}$	215
9.5.1	Determination of Plasma Type	216
9.5.2	Results from Cavity Centre	221
9.5.3	Results from Outside the Cavity	221
9.6	Relationship between Population Density and Energy of Level	221
9.7	Excitation Mechanism	222
9.8	Evaluation of Spectral Excitation Temperature	224
9.9	Probe Characteristics of the Third Type	227
9.9.1	Double Floating Probe Equations for a Double Maxwellian Electron Distribution	227

9.9.2	Behaviour of the Equations	233
9.9.3	Electron Temperature and Ion Density Results	242
9.9.3	(i) Ion Density Measurements	242
9.9.3	(ii) Electron Temperature Measurements	243
9.10	Conclusions	246
9.10.1	Spectroscopic Features	246
9.10.2	Measurement of Electron Density	247
9.10.3	Power Dependence of Plasma Parameters	247
9.10.4	Probe Measurements	248
9.10.4	(i) Ion Density	248
9.10.4	(ii) Effect of Electron Distribution Function	248
	REFERENCES	250
	APPENDIX I	A1
	APPENDIX II	A5
	APPENDIX III	A9

LIST OF FIGURES

Figure	Title	Page
1.1	Variation of electron temperature with pressure (Avni & Winefordner, 1975)	9
1.2	Electron temperature as a function of pressure at 50W & 25W (Brassem & Maessen, 1976 & Busch & Vickers, 1973)	10
1.3	Electron temperature as a function of microwave power (Brassem & Maessen, 1976)	11
1.4	Electron temperature as a function of microwave power (Avni & Winefordner, 1975)	12
1.5	Electron concentration as a function of pressure (Brassem & Maessen, 1976 & Busch & Vickers, 1973)	13
1.6	Electron concentration as a function of pressure (Avni & Winefordner, 1975)	14
2.1	Schematic diagram of vacuum system	18
2.2	Pressure vs time curve for the two sorption pumps	20
2.3	Variation of indicated pressure with true pressure for pirani gauge operating in argon	22
2.4	Positioning of probes in discharge tube	25
2.5	Method of setting molybdenum wire in perspex matrix	25
2.6	Rate of out-gassing for plain and probe discharge tubes	29
2.7	The spectral recording system	30
2.8	Reference signal amplifier circuit	34
2.9	The microwave excitation system	35
2.10	The cavity and positioning of discharge tube: sketch and plan view	37
2.11	The voltage ramp generator	39
2.12	The probe characteristic recording system	34

Figure	Title	Page
3.1	Simple schematic diagram of a cavity and feed line	47
3.2	Division of slab-line cavity to calculate t-parameters	47
3.3	Experimental arrangement to measure distance to reference plain of cavity	52
3.4	Variation of distance to reference plane of cavity with wavelength	53
3.5	Experimental arrangement to measure diode rectifier behaviour	55
3.6	Diode behaviour at high and low powers	56
4.1	Atomic energy level diagram for argon	63
4.2	Variation of intensity of calibration lamp with time	65
4.3	Wavelength response of optical filters	67
4.4	Typical calibration curve for the spectral response of the system	68
5.1	Potential distribution of a double floating probe system	75
5.2	Ideal probe characteristic	75
5.3	Practical probe characteristic	77
5.4	Comparison of electron temperatures calculated by "equivalent resistance" and "logarithmic plot" methods	84
5.5	Comparison of ion densities calculated from equations 5.9 and 5.21	87
6.1	Population densities of argon atom (a) calculated from peak areas (b) calculated from peak heights	92 93
6.2	Typical Boltzmann plot for the argon I system	95
6.3	Boltzmann plot showing flattening of curve for higher atomic levels	96

Figure	Title	Page
6.4	Variation of population density with distance from cavity centre	99
6.5(a)	Population density of 4p level as a function of input power	
	(i) Pressures 6.00, 3.00, 2.00 mbar	101
	(ii) Pressures 1.00, 0.70, 0.50 mbar	102
	(iii) Pressures 0.20, 0.10, 0.07 mbar	103
6.5(b)	Population density of 6s' level as a function of input power	
	(i) Pressures 6.00, 3.00, 2.00 mbar	104
	(ii) Pressures 1.00, 0.70, 0.50 mbar	105
	(iii) Pressures 0.20, 0.10, 0.07 mbar	106
6.5(c)	Population density of 8s level as a function of input power	
	(i) Pressures 6.00, 3.00, 2.00 mbar	107
	(ii) Pressures 1.00, 0.70, 0.50 mbar	108
	(iii) Pressures 0.20, 0.10, 0.07 mbar	109
6.6	Variation with input power of the population density of 4p ⁴ p ⁰ multiplet of the argon ion	112
6.7	Variation with input power of the population density of 4p ² F ⁰ multiplet of the argon ion	113
6.8	Typical extended Boltzmann plot for atomic and ionic levels	114
6.9	Extended Boltzmann plot (a) 0.10 mbar, 50mA	115
	(b) 0.05 mbar, 50mA	116
6.10	Variation of relative population densities of the atomic and ionic levels with pressure	118
6.11	Variation with pressure of relative population densities of atomic levels	
	(a) 4p	120
	(b) 6s	121
	(c) 6d	122
6.12	Comparison of observed and calculated intensities in helium (Llewellyn Jones)	
	(a) 2 ³ P - 3 ³ D	124
	(b) 2 ³ P - 4 ³ D	124
	(c) 2 ¹ S - 3 ¹ P	125
	(d) 2 ³ S - 4 ³ P	125
7.1	Typical plot of probe data	130
7.2	The third type of probe characteristic	131
7.3	(a) Determination of maximum and minimum values of i ₊ for types I and III characteristics	133
	(b) Determination of maximum and minimum values of i ₊ for type II characteristics	134

Figure	Title	Page
7.4	Variation of electron temperature with pressure	
	(a) 40mA magnetron current	136
	(b) 50mA magnetron current	137
	(c) 100mA magnetron current	138
	(d) 150mA magnetron current	139
7.5	Electron temperature as a function of input power	
	(a) Pressures 2.00, 1.00, 0.70, 0.50 mbar	141
	(b) Pressures 0.20, 0.10, 0.07 mbar	142
7.6	Variation of electron temperature with pressure	
	(a) 50W, 30W normalised power	143
	(b) 40W, 25W normalised power	144
7.7	Ion density as a function of pressure	
	(a) 40mA magnetron current	148
	(b) 50mA magnetron current	149
	(c) 100mA magnetron current	150
	(d) 150mA magnetron current	151
7.8	Variation of ion density with input power	
	(a) Pressures 2.00, 1.00, 0.70 mbar	153
	(b) Pressures 0.50, 0.20, 0.10 mbar	154
	(c) Pressures 0.70, 0.05, 0.02 mbar	155
7.9	Ion density as a function of pressure	
	(a) 50W, 30W normalised input power	156
	(b) 60W, 40W, 25W normalised input power	157
8.1	Variation of microwave impedance with pressure for probe discharge tube	
	(a) 40mA magnetron current	163
	(b) 50mA magnetron current	164
	(c) 100mA magnetron current	165
	(d) 150mA magnetron current	166
8.1(e)	Variation of microwave impedance with pressure for plain discharge tube, 100mA magnetron current	167
8.2	Microwave impedance as a function of input power	
	(a) Pressures 6.00, 3.00, 2.00 mbar	169
	(b) Pressures 1.00, 0.70, 0.50 mbar	170
	(c) Pressures 0.20, 0.10, 0.07 mbar	171
8.3	Variation of electron density with pressure	
	(a) 40mA magnetron current	174
	(b) 50mA magnetron current	175
	(c) 100mA magnetron current	176
	(d) 150mA magnetron current	177

Figure	Title	Page
8.4	Electron density as a function of input power (a) Pressures 6.00, 3.00, 2.00 mbar (b) Pressures 1.00, 0.70, 0.50 mbar (c) Pressures 0.20, 0.10, 0.07, 0.05 mbar	178 179 180
8.5	Variation of electron density with pressure (a) 50W, 30W normalised power (b) 40W, 25W normalised power	181 182
8.6	Ratio of imaginary to real parts of microwave impedance as a function of input power (a) Pressures 6.00, 3.00, 2.00 mbar (b) Pressures 1.00, 0.70, 0.50 mbar (c) Pressures 0.20, 0.10, 0.07 mbar	184 185 186
8.7	Ratio of imaginary to real parts of microwave impedance as a function of pressure (a) 50W, 30W normalised power (b) 40W, 25W normalised power	187 188
8.8	Variation of microwave impedance with pressure (a) 50W, 30W normalised power (b) 40W, 25W normalised power	190 191
9.1	Ratio of electron to ion density as a function of pressure (a) 50W, 30W normalised power (b) 40W, 25W normalised power	197 198
9.2(a)	Comparison of measured ion loss to tube walls and loss calculated from ambipolar diffusion theory	202
9.2(b)	Comparison of measured ion loss to tube walls and loss calculated from free-fall diffusion theory	203
9.3	Variation of population coefficient with electron density (Fujimoto 1979)	206
9.4	Variation of population density with electron density for 4p', 5p, 6d, 8s, 9s atomic levels (a) 25W normalised input power (b) 30W normalised input power (c) 40W normalised input power (d) 50W normalised input power	208 209 210 211
9.4(e)	Variation of population density with electron density for 4p, 6s', 7s, 6d atomic levels, 50W normalised input power	212
9.5	Population density vs electron density for pressures ≥ 2.00 mbar	214

Figure	Title	Page
9.6	Variation of population coefficient with energy of atomic level	218
9.7	Comparison of Boltzmann & Saha equations with measured population density	220
9.8	Variation of spectral excitation temperature with energy of atomic level	226
9.9	Result of plotting the sum of equations 9.14 and 9.15	231
9.10	Example of a type III characteristic	232
9.11	Variation of type III characteristic with T_e	
	(a) $T_e = 2 \times 10^4 K$	234
	(b) $T_e = 5 \times 10^4 K$	234
	(c) $T_e = 8 \times 10^4 K$	235
9.12	Variation of type III characteristic with T_e'/T_e	
	(a) $T_e'/T_e = 50$	235
	(b) $T_e'/T_e = 5$	237
	(c) $T_e'/T_e = 2$	238
9.13	Variation of type III characteristic with i'/i	
	(a) $i'/i = 0.01$	239
	(b) $i'/i = 0.05$	240
	(c) $i'/i = 0.5$	241
	(d) $i'/i = 1.0$	241
9.14	Example of a double distribution function	245

LIST OF TABLES

Table	Title	Page
2.1	Vacuum System Equipment	41
2.2	Instrumentation - Optics	42
2.3	Instrumentation - Microwave	43
2.4	Instrumentation - Probes	44
4.1	Selected Lines of the Argon I Spectrum	62
4.2	Selected Lines of the Argon II Spectrum	72
6.1	Ratio of Population Densities at Different Pressures	110
6.2	Ratio of Atomic to Ionic Population Densities	110
7.1	Calculated Values of Electron Temperature	135
7.2	Calculated Values of ion Density	135
7.3	Variation of T_e and n_+ with Distance from Cavity Centre	159
8.1	Measured Impedance Values (Z/Ω)	162
8.2	Calculated Values of Electron Density ($n_e \times 10^{-18}/m^{-3}$)	162
9.1	Comparison of Measured and Calculated Values of Ion Loss to the Discharge Tube Walls	200
9.2	Calculated Values of the Population Coefficient $r_m^{(1)}$	217
9.3	Gradients of $\log(n_m/g_m)$ vs $\log(E_m^{ion})$	217

CHAPTER 1
REVIEW OF PREVIOUS WORK

Introduction

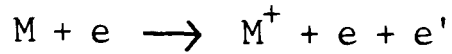
A full characterisation of a discharge is of prime importance if the processes contributing to excitation within the discharge are to be understood and some model devised which predicts the values of the observed parameters. Interest has already been shown in the characterisation of the microwave excited electrodeless discharge (Busch & Vickers 1973, Avni & Winefordner 1975, Brassem, Maessen, et al 1974-78). None of this work resulted in a satisfactory model for low pressure discharges.

1.1 Plasma Models

It has been established by previous workers (Busch & Vickers 1973, Avni & Winefordner 1975, Brassem & Maessen 1974) that low pressure microwave discharges deviate from local thermodynamic equilibrium by varying degrees as the free electron density changes. It would be expected that, at low pressures, the low particle density would cause a relative increase in radiative decay with respect to collisional de-excitation. Several attempts have been made to produce models which reproduce this effect. The most successful of these is the radiative-recombination model first proposed by Schlüter (1963) and applied to these discharges by Busch & Vickers (1973). This model was later extended by Fujimoto (1972) in the form of the collisional-radiative model.

The radiative recombination model assumes two groups of electrons: one, the more numerous, with low energy and a second, less numerous

group but with higher energy. This second group, it is believed, controls ionisation through the reaction:



The low energy electrons induce excitation and are captured by the reaction:



where M^* denotes an excited atom. The population distribution over the higher atomic energy levels is determined by the low energy group down to some level called the thermal limit and corresponds to a Boltzmann distribution. Levels below the thermal limit are not in Boltzmann equilibrium because for these levels the probability of radiative decay exceeds that of collisional de-excitation. Thus the population of levels below the thermal limit is determined by the high energy group.

This model was extended by Fujimoto et al (1972, 1979) to include an intermediary phase between that of a radiative dominated plasma (coronal phase) and a collision dominated plasma (partial local thermodynamic equilibrium). This intermediary phase is termed the (quasi-) saturation phase and is considered to be a phase in which electronic excitation is balanced by electronic de-excitation. The "collisional-radiative" model of Fujimoto gives an expression for the population density n_m of the m^{th} level of the form

where $r_m^{(0)}$, $r_m^{(1)}$ are the population coefficients, n_m^S , n_m^B are the populations expected from the Saha and Boltzmann equations. The

population coefficients are particular to the given level and atomic species. Values have been calculated for hydrogen by Fujimoto (1979) but values for argon, either calculated or measured, are few.

This model provides a method of determining the phase of the plasma by plotting n_m as a function of electron density. Several papers (Tachibana et al 1979, Raaijmakers et al 1983, van der Mullen et al 1980) have produced evidence of the existence of the (quasi-) saturation phase in the plasma column of a hollow cathode arc, a d.c. argon discharge and in an argon ICP but not, to date, in the microwave discharge.

1.2 Earlier Studies of Microwave Excited Discharges

The studies which have been performed on the microwave discharge use two methods of analysis: the intensities of spectral emission lines and the voltage-current characteristics of Langmuir probes. Both of these methods yield an "excitation temperature" which, if the plasma is in equilibrium, should have the same value for each method.

1.2.1 Spectroscopic Studies

The work of Busch & Vickers (1973) uses relative intensity measurements of lines in the argon I emission spectrum to deduce a "spectral temperature". However, all the lines originate from the 5p and 5p' levels, giving a spread in energy of only 1747 cm^{-1} . A temperature is then deduced from a Boltzmann plot using a weighted least squares fit. It is perhaps not surprising that over such a small energy range it is possible to fit the curve to a straight line. In view of later work (Tachibana et al 1973, van der Mullen et al 1980) it would be surprising

if a straight line would have resulted from a Boltzmann plot over a wider range of energy levels. In addition, using the Boltzmann plot technique presupposed the plasma to be in equilibrium, something which has been shown to be highly unlikely, even at the highest pressure used of 33 mbar. Avni & Winefordner (1975) criticise the work of Busch & Vickers on the grounds that the 5p and 5p' levels could be populated by recombination of argon ions. They propose that transitions originating and terminating close the ground state should be selected. However, Fujimoto (1979), Tachibana et al (1973) and van der Mullen (1980) show that the atomic levels fall consecutively into equilibrium with the ion ground state with increasing electron density, starting with the highest levels. That is, there is an increase in the population densities of the lower levels (below the thermal limit) with respect to values calculated from the Boltzmann-Saha equilibrium equations. This implies that unless the transition selected originates from a level above the thermal limit the parameter 'temperature' is at worst meaningless and, at best, can only be applied to each particular level individually.

Avni & Winefordner themselves measure the reversal temperature of a spectral line of thallium which is introduced as an impurity. Whilst recognising that the reversal temperature probably does not represent the excitation temperature of the argon (their results show it to be on order of magnitude less), Avni & Winefordner assume that it does represent the gas temperature.¹ However, the perturbing effect of impurities (in concentrations as low as 1%) has been noted by Brassem et al (1976) and is self-evident from the curves of excitation

¹ That is to say that the population of the metastable level ($6^2P_{3/2}$) of thallium is mainly determined as a result of the gas temperature in the plasma i.e., by a Boltzmannian distribution as opposed to by inelastic collisions with electrons.

temperature against pressure produced by Avni & Winefordner (fig 1.1). In respect of the importance of gas purity the latter two workers have only a "buffer" of 1.3×10^3 mbar between their empty system and the maximum gas pressure used.

Brassem et al (1974-78) take a much more cautious approach to intensity measurements, preferring to rely on probe measurements to derive plasma parameters. In the 1978 paper a comparison is made of the radiative-recombination model due to Schlüter and experimental results of intensity measurements of ten helium emission lines from which excitation temperature is derived. Again, the arguments raised above as to the applicability of the term "temperature" are relevant. Their conclusion is that the radiative-recombination and local thermodynamic equilibrium models apply equally well.

1.2.2 Probe Studies

Most of the results to date have in fact been derived from Langmuir probe work. All the authors have used tungsten probes although the size of the probe penetrating the plasma varies. Ideally the surface area in contact with the plasma should be as small as possible to avoid perturbation of the plasma. Brassem & Maessen (1976) have examined the perturbing effect by measuring spectral intensities in the presence and absence of the probes and found no influence of the probes on the plasma. (This is despite taking the unusual step of positioning the probes in that part of the discharge which is inside the microwave cavity).

There is some argument as to the exact form of the probe equations.

Avni & Winefordner argue that due to the longer mean free path and greater drift velocity of the electrons with respect to the ions, the electrons recombine at the tube walls giving a relationship between the two densities n_e and n_+ of

$$n_e (v_e)_{\text{drift}} \approx 2 n_+ (v_+)_{\text{drift}}$$

Other workers assume the electrical neutrality of the plasma ie.

$n_+ = n_e$. In addition to the question of electrical neutrality, the probe equations themselves are only applicable if the electron mean free path is greater than the probe radius. Busch & Vickers (1973) calculate that this restricts their use to pressures below 1.3 mbar and acknowledge the inherent inaccuracies in the estimation of electron density at pressures between 4 and 33 mbar.

It is difficult to draw any conclusions from the results of the probe work and even more difficult to compare the results of different groups of workers. The main problem is inconsistencies between individual groups. For example, in measuring the variation of excitation temperature and electron density with pressure, Busch & Vickers operated at a microwave power of 25W whereas Brassem & Maessen operated at 50W power, and Avni & Winefordner give no value of operating power. Similarly for variation of excitation temperature and electron density with power the groups have made measurements at different pressures.

Generally speaking, the same orders of magnitude for excitation temperature and electron density are found by all groups despite the different ranges of pressure used. The trends, however, do differ:

Busch & Vickers find a linear relationship between pressure and excitation temperature in the range 6 to 33 mbar (fig 1.2). This result is verified by Avni & Winefordner (fig 1.1) who obtained similar results to Brassem & Maessen (1974) at pressures between 1 and 8 mbar. For electron density the results are somewhat less in agreement; the relationship between electron density and pressure found by Avni & Winefordner (fig 1.6) is different to that found by the other two groups (fig 1.5). This may not be surprising in respect of their abandonment of electrical neutrality but clearly shows the need for a careful appraisal of diagnostic techniques where Langmuir probes are involved.

1.2.3 Microwave Measurements

Whilst some workers have attempted to examine the influence of microwave power on plasma parameters, this has not been given detailed attention. Avni & Winefordner, Busch & Vickers, Brassem & Maessen all use the incident microwave power as the relevant power variable. No attempt has been made to measure the reflected power nor has there been any measurement of microwave parameters. One parameter of the plasma which is of interest is its microwave impedance. It would be expected that the impedance would be dependent in some way upon the electron density and may provide a method of verifying (or otherwise) the probe measurements.

Avni & Winefordner find a different relationship between excitation and incident power (fig 1.4) to that reported by Brassem & Maessen and Busch & Vickers (fig 1.3). Avni & Winefordner show that the form of

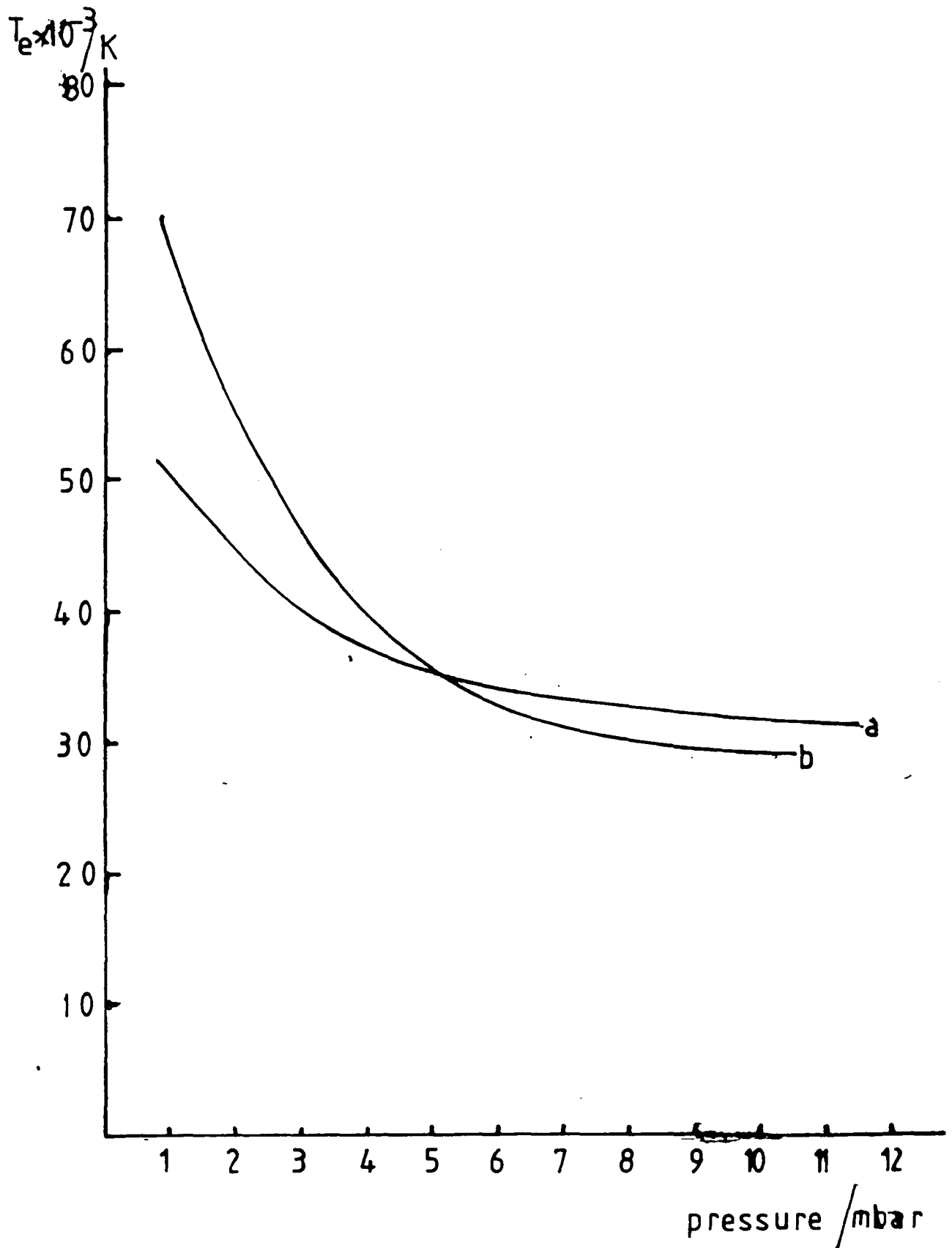


Figure 1.1 Variation of electron temperature with pressure (Avni & Winefordner, 1975) a Ar + 10 gTl
b Ar

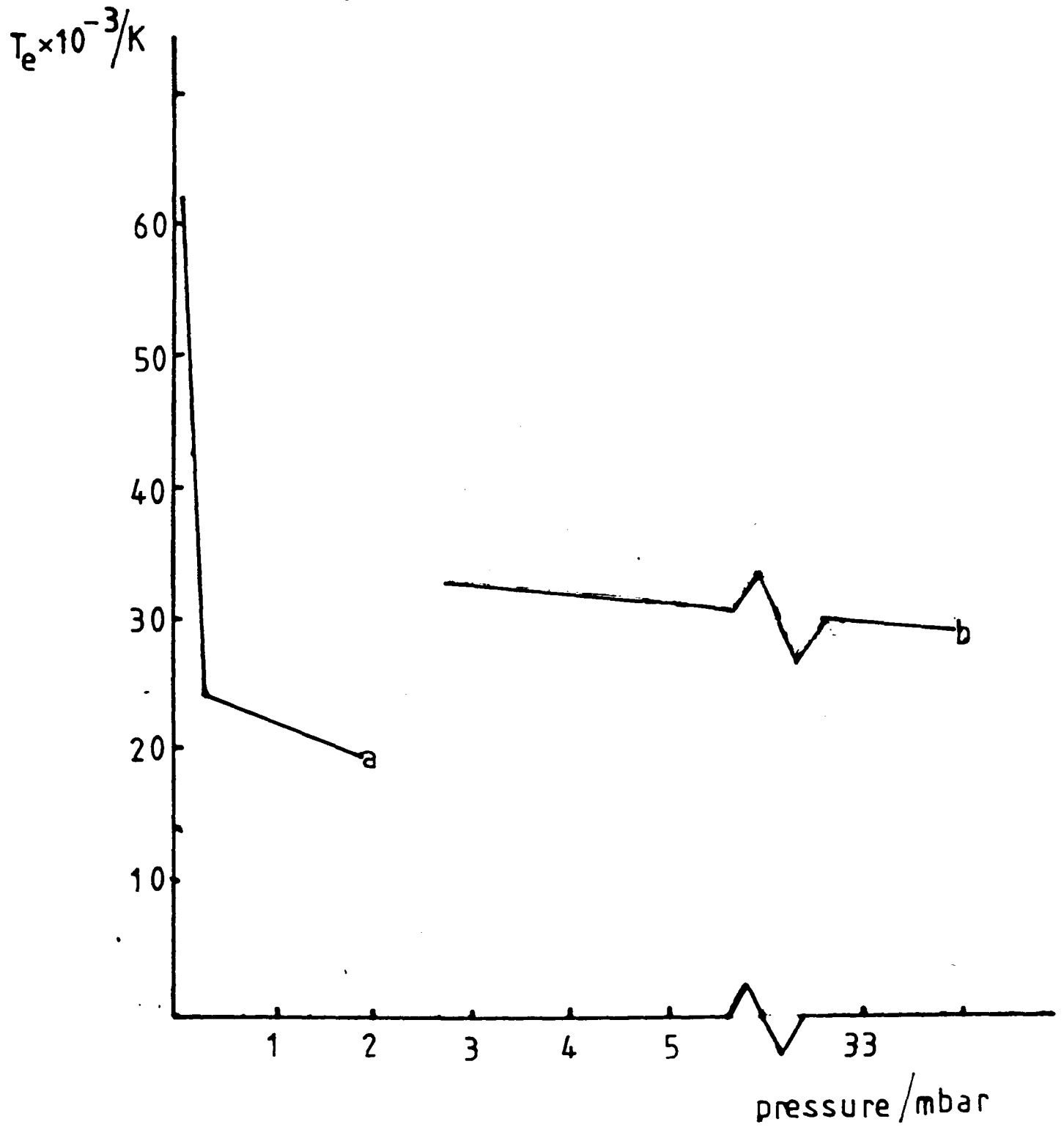


Figure 1.2 a Electron temperature as a function of pressure at 50W (Brassem & Maessen, 1976); b idem. as found by Busch & Vickers , 1973 at 25W

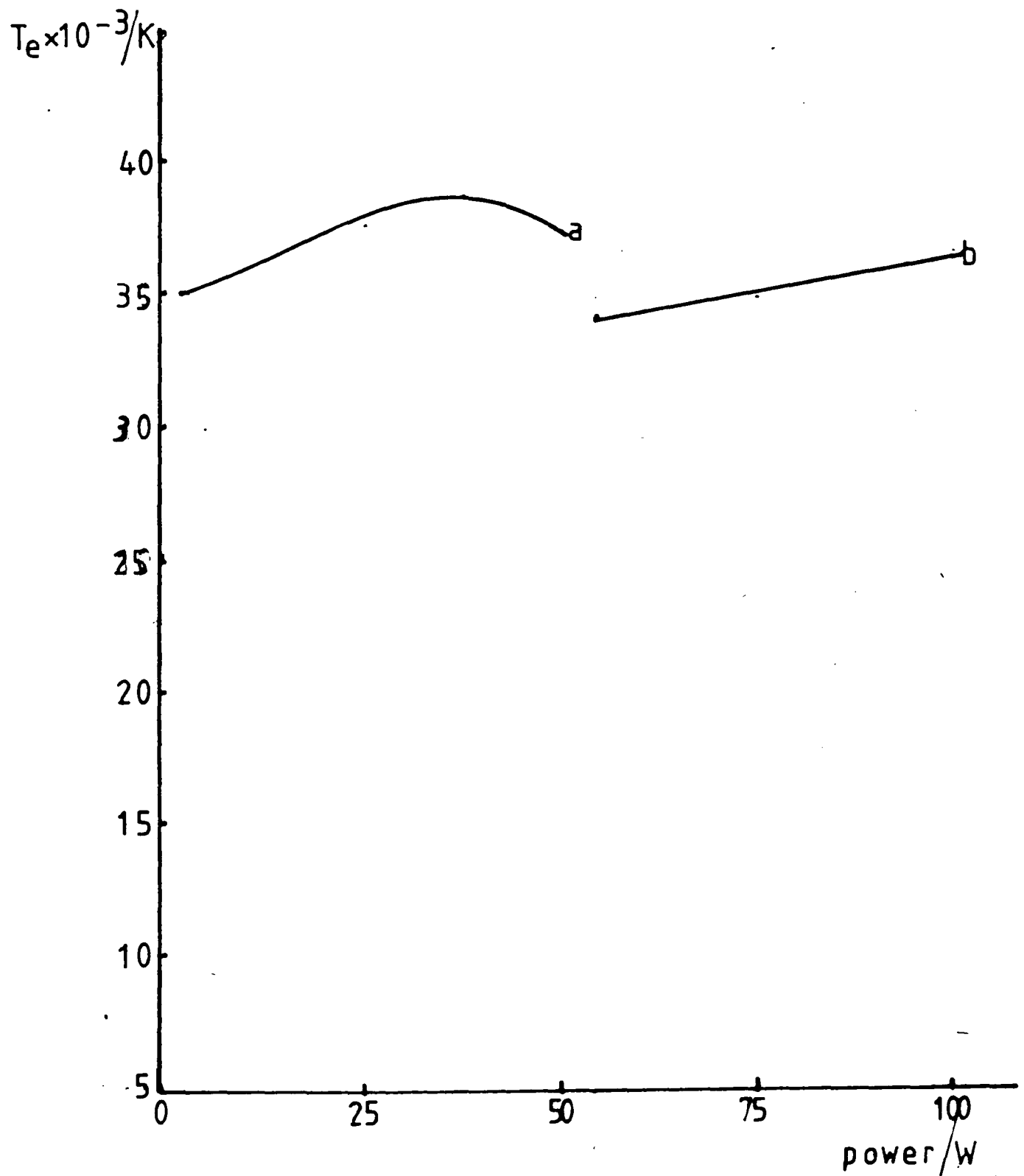


Figure 1.3 a-Electron temperature as a function of microwave power ; b idem.as found by Busch & Vickers, 1973 (Brassem & Maessen, 1976)

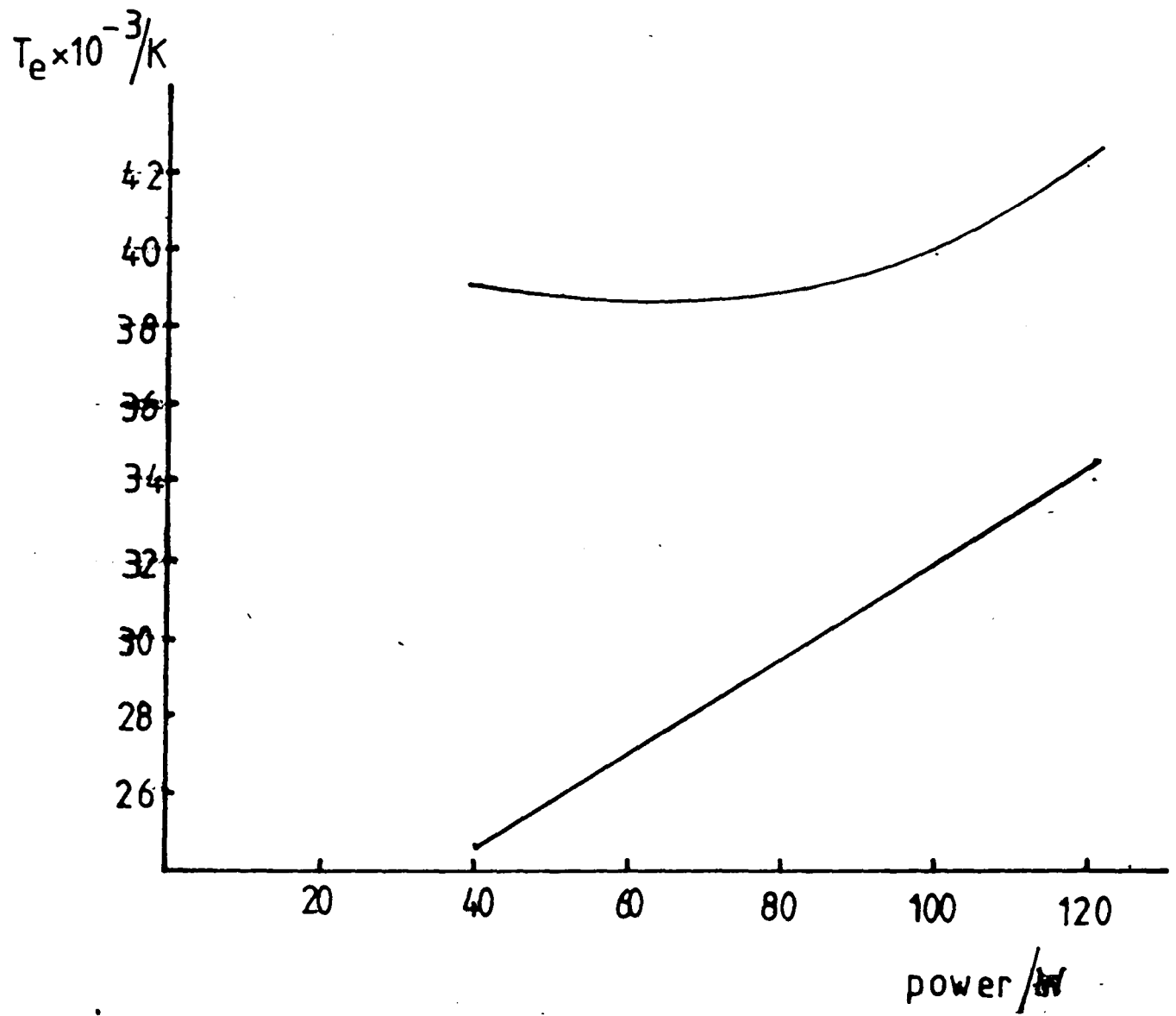


Figure 1.4 Electron temperature as a function of microwave power for pressures .2.6mbar (a) and 13mbar (b) (Avni & Winefordner, 1975)

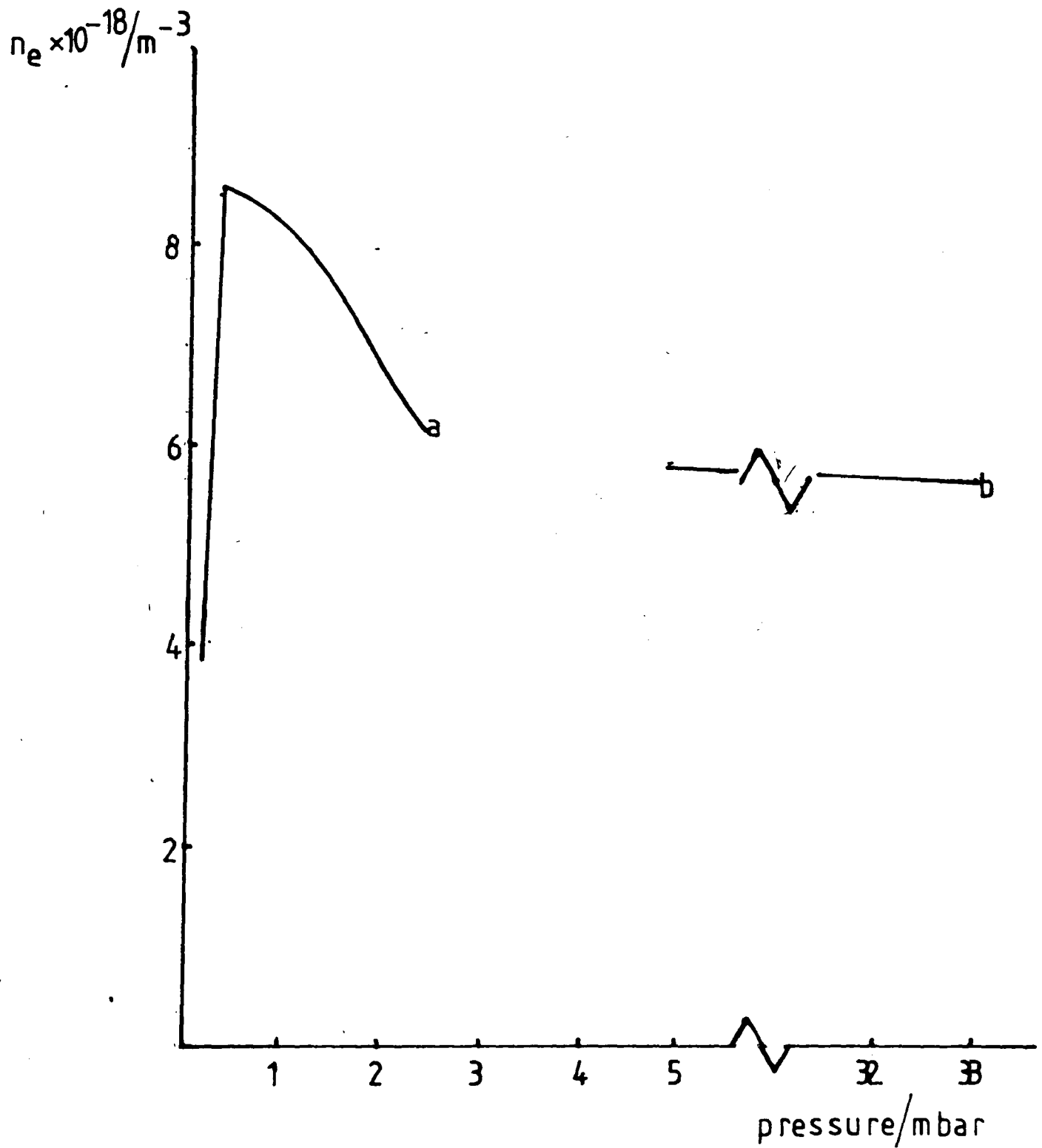


Figure 1.5 Electron concentration as a function of pressure (a-Brassen & Maessen, 1976 ; b Busch & Vickers, 1973)

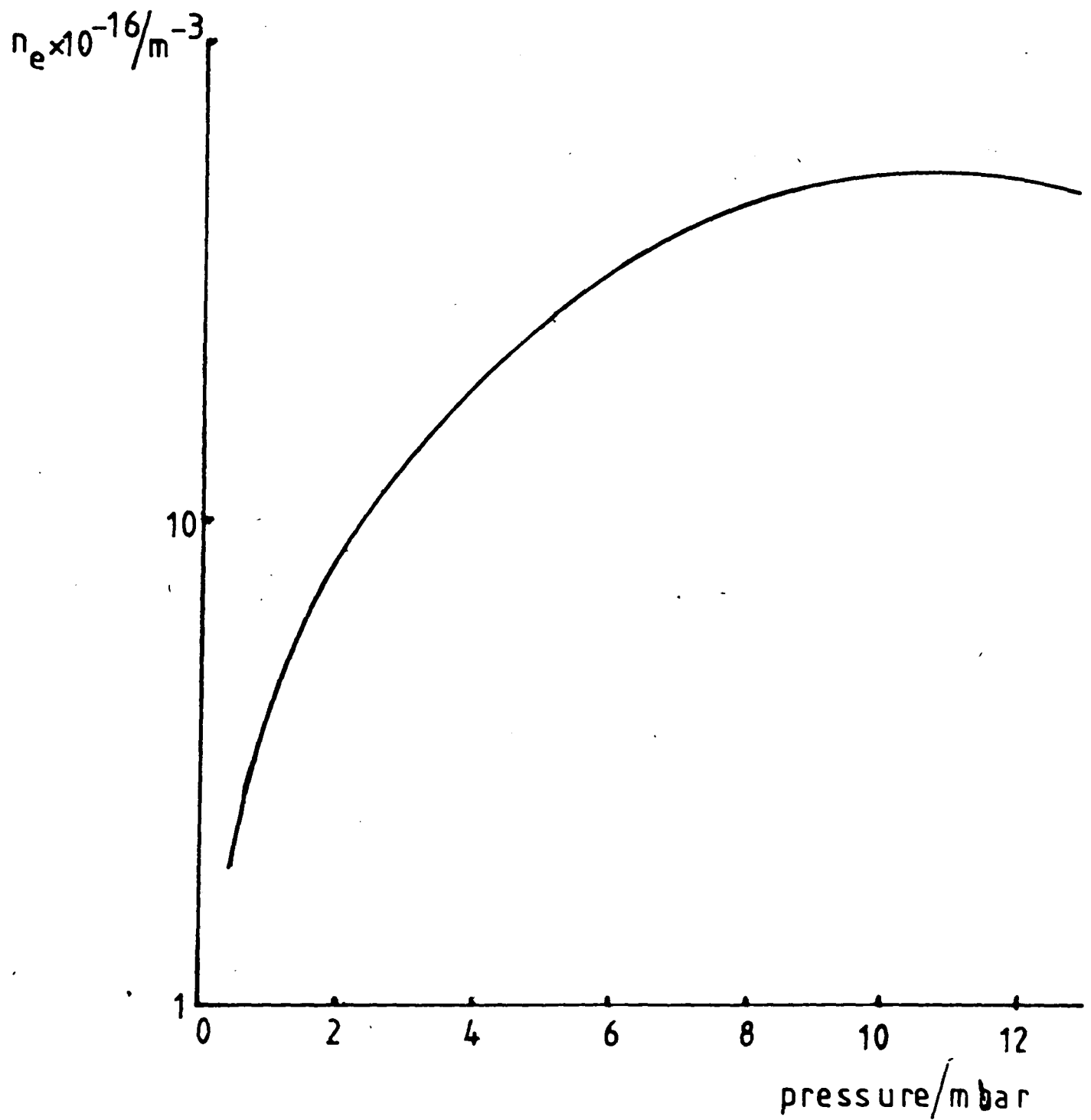


Figure 1.6 Electron concentration as a function of pressure (Avni & Winefordner, 1979)

variation of temperature with power depends upon the gas pressure. Busch & Vickers and Brassem & Maessen present results only for one pressure viz 4 mbar and 0.3 mbar respectively. As no knowledge of the amount of power absorbed by the plasma is available, the results are difficult to compare.

1.3 Scope of This Work

Clearly from the preceding sections, a comprehensive study of the behaviour of microwave excited discharges would be desirable. Of particular interest would be measurements of the microwave properties of these discharges. In addition, the existence of the saturation phase has yet to be demonstrated in these plasmas.

The use of Langmuir probes for the measurement of carrier densities and excitation temperatures also needs consideration, particularly with reference to the applicability of the probe equations.

It is to these objectives that this work is intended to apply together with an extension of the pressure range over which the electrodeless microwave discharge has been investigated.

CHAPTER 2
DESCRIPTION OF EXPERIMENTAL ARRANGEMENT

2.1 Introduction

The experimental arrangement described in this section was developed over a period of two years specifically for the measurements described in Chapters 3, 4 & 5. In particular, the vacuum system was designed and assembled for this work. This system is a semi-UHV system enabling an ultimate pressure of 2×10^{-8} mbar to be obtained. Since gas purity has been shown to be of paramount importance (Brassem & Maessen 1976), the major criterion of the vacuum system's performance is resistance to contamination.

The vacuum system was originally connected to a plain quartz tube and certain spectral and microwave measurements, described in Chapters 4 and 3 respectively, made in order to assess the behaviour of the system. The plain tube was later replaced by a discharge tube containing Langmuir probes (section 2.3) and the measurements described in Chapters 3, 4 & 5 made in order to obtain a fuller description of the behaviour of the plasma and to assess the effect of introducing Langmuir probes into the plasma.

2.2 The Vacuum System

With the exception of the discharge tube and liquid nitrogen cold trap (fig. 2.1), the vacuum system was composed of stainless steel modules (Table 2.1). The system can essentially be divided into two parts: the low vacuum side, which contains all lines from the two sorption pumps up to (but excluding) the triode ion pump; and the high vacuum side, in part of which the discharge itself was contained.

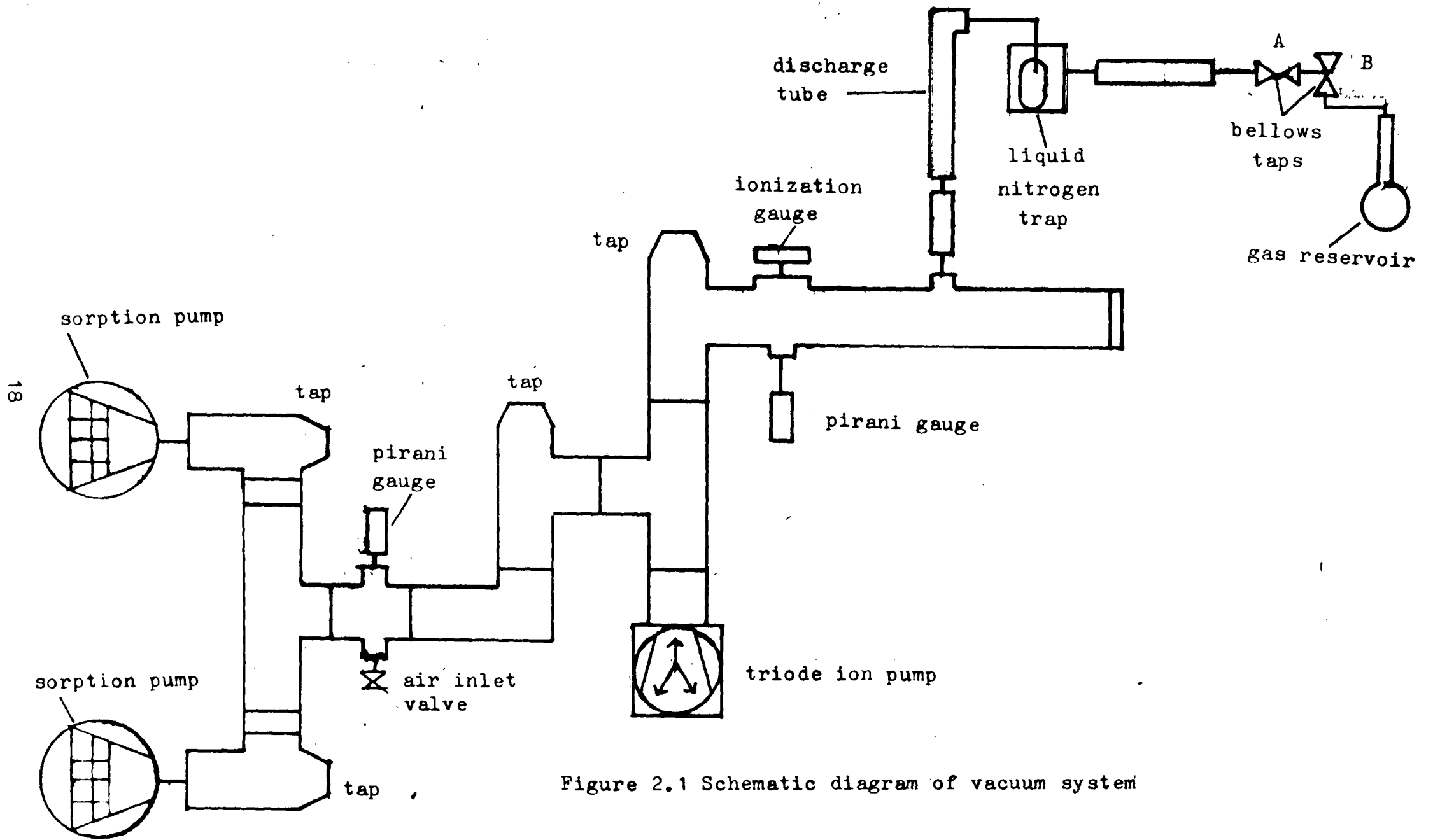


Figure 2.1 Schematic diagram of vacuum system

2.2.1 Low Vacuum Arm

The low vacuum side was constructed from 40mm and 32mm diameter tubing joined by 'quick release' clamps and sealed by vitalan (viton) O-rings. The pressure in this section (and when the system was in use, the argon pressure) was controlled by the two sorption pumps connected in parallel. The Vacuum Generators pump contains 0.6 kg of molecular sieve filling and the AEI sorption pump contains 1.2 kg; the molecular sieve was Zeolite 5A.

Figure 2.2 shows pressure vs time curves for each individual pump evacuating the system volume of 1 litre of air. The sorption pumps are provided not only to regulate the argon pressure in the discharge but also to reduce the pressure in the entire system to a value suitable for the activation of the triode ion pump (2.6×10^{-2} to 2.2×10^{-2} mbar). As can be seen from fig. 2.2, either pump was capable of evacuating the system to a suitable pressure in less than 5 minutes. The provision of two sorption pumps, however, provided the option of using only one pump at time, thus reducing the frequency of reactivation of the zeolite or, where heavy pumping loads are encountered, eg. air with a high water vapour content, using both pumps sequentially and reducing the pump down time.

Pressure in the low vacuum side is monitored by a pirani gauge and this branch is provided with an air admittance valve, should it be required that the system return to atmospheric pressure.

2.2.2 High Vacuum Arm

The triode ion pump contained ~ 1 litre volume and gave a pumping speed

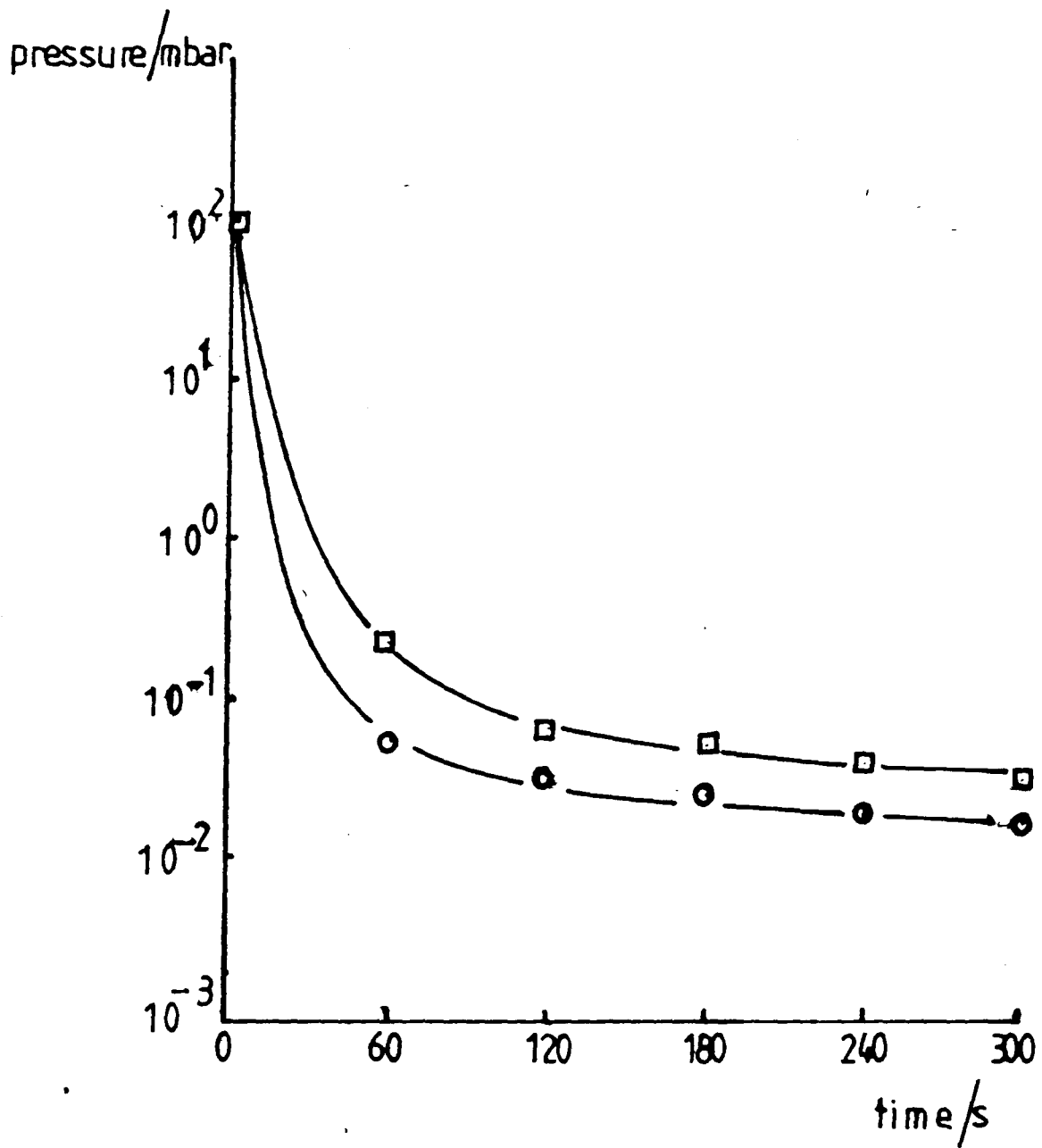


Figure 2.2 Pressure vs time curves for the two sorption pumps: \square AEI, \circ VG

of 60 l s^{-1} for dry air between 10^{-6} and 10^{-9} mbar. This speed drops by between 10% and 30% for argon; the effective pumping speed at the pump after conductances have been accounted for being 1.6 l s^{-1} . The pump could be isolated from the remainder of the high vacuum side by a bellows sealed tap (fig. 2.1). Two pressure gauges were provided to cover the complete range of pressures encountered in using the system. Pressures in the range 10^3 mbar to 10^{-3} mbar (dry air) were monitored by a Pirani gauge, whilst pressures from 10^{-3} mbar to 10^{-9} mbar were measured by an ionisation gauge. The pirani gauge was calibrated for dry nitrogen and an adjustment to the pressure reading had to be made when the gauge was used in argon. Fig. 2.3 shows the conversion curve for the gauge from nitrogen to argon. As can be seen, the curve is linear from 10^{-3} mbar to 6 mbar above which the pressure change indicated on the gauge becomes small for a relatively large change in the true argon pressure. Thus 6 mbar was the upper pressure limit in argon at which the pirani could be used with any certainty.

The high vacuum arm seals were made by aluminium rings clamped by collar clamps. This gave a high vacuum system with a theoretical leak rate of 10^{-9} mbar l s^{-1} and a maximum baking temperature of 200°C . Connection to the discharge tube was made via 100 mm klein flange bellows to allow flexibility. The discharge tube rested at the two extremes of its length on simple wooden supports. Connection to the gas source was made via a liquid nitrogen cold trap and a second set of bellows. The trap was included to condense contaminant gases such as water vapour and carbon dioxide. Access to the gas reservoir was made via two bellows sealed taps placed so that the bellows opened

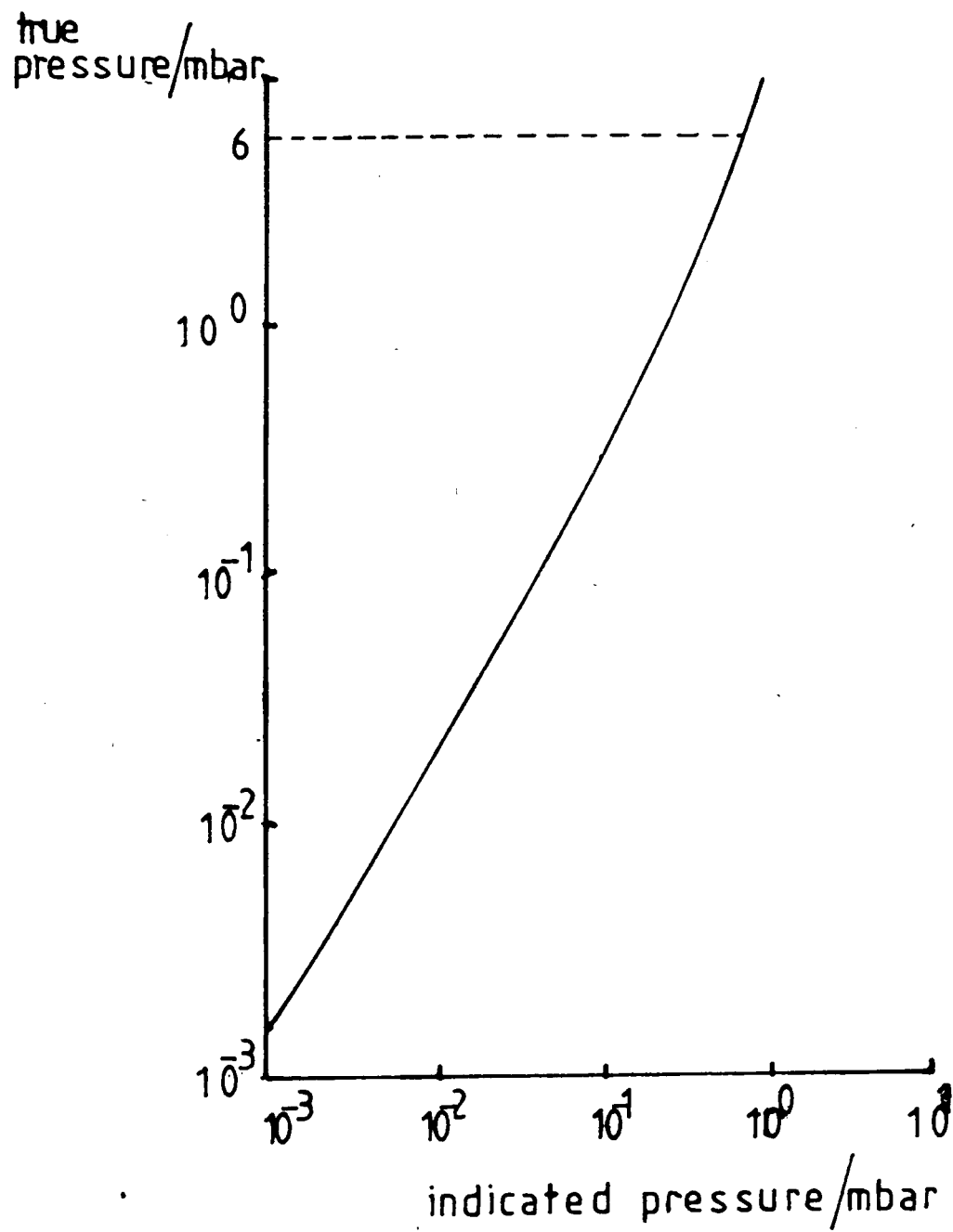


Figure 2.3 Variation of indicated pressure with true pressure for pirani gauge operating in argon

mutually at right angles. Originally, a needle valve was included at this point. However, during testing the performance of the system it became clear that air was admitted to the system on opening the valve. Consequently the valve was removed and the two bellows sealed taps substituted.

2.2.3 Problems of Design

Severe problems with the 10 KF seals at the reservoir end of the discharge tube were encountered, especially during baking of the system. Despite the flexible bellows, the seal between these and the discharge tube seemed susceptible to cooling after baking and only by replacing the seal and fine control of the rate of cooling could an adequate seal be achieved at this point.

2.3 The Discharge Tubes

2.3.1 The Plain Tube

The original discharge tube was a simple quartz glass tube of internal diameter 1 cm and length approximately 50 cm. With this tube in position measurements of the argon I spectrum were made as described in Chapter 4 and microwave measurements made as described in Chapter 3.

2.3.2 The Probe Tube

The second discharge tube was identical to the plain tube except for containing six pairs of probes situated symmetrically around the microwave cavity at distances of 3 cm, 6 cm and 9 cm from the centre of the cavity. The probes were sealed with "Torrseal" low vapour pressure resin into 0.5 mm capillary tube of outer dimension 5 mm. The capillary tube was then, in turn, sealed into 7 mm tube. This larger tube then

formed a side arm onto the discharge tube itself.

The probe penetrated the plasma, perpendicular to the axis of the main discharge tube, to a depth of 1 mm (fig. 2.4), the distance between the two probes of each pair being 1.5 cm. The combined diameter and depth of penetration of the probes gave a probe surface area of 1.77 mm^2 compared to areas of 9.71 mm^2 (Avni & Winefordner 1975) to 1.29 mm^2 (Brassem & Maessen 1974) used by previous workers. The problem was one of compromise to achieve maximum collecting area (and hence current) but minimum perturbation in the plasma.

The probes enter the discharge tube from below so as to avoid interference with the spectral measurements from either the connecting wires or the probes themselves.

2.3.3 Construction of the Probes

(a) Choice of probe material.

The commonly used materials for probes are tungsten (Busch & Vickers 1973, Brassem, et al, 1974-78), molybdenum (Polman 1966) and platinum (Avni & Winefordner 1975). The main requirements are that the material should have a melting point much higher than the thermal temperature encountered in the plasma, a low rate of thermionic emission and that it should be chemically inert in the plasma gas.

Although the most widely used material is tungsten, molybdenum was chosen for this programme of work mainly because of the possibility of sealing directly into quartz, although this later proved not to be possible with molybdenum wire. The molybdenum wire obtained for this

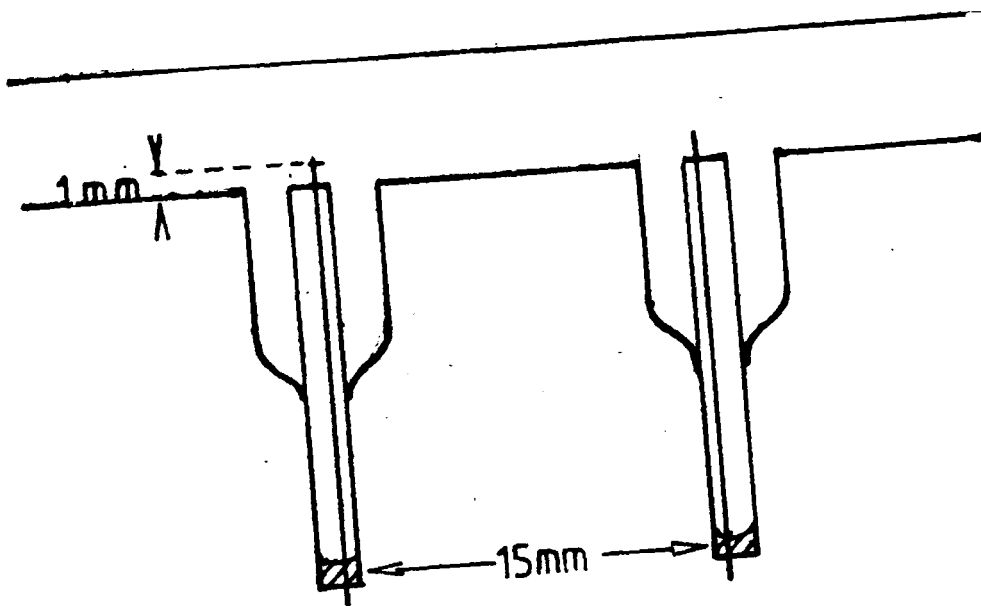


Figure 2.4 Positioning of probes in discharge tube

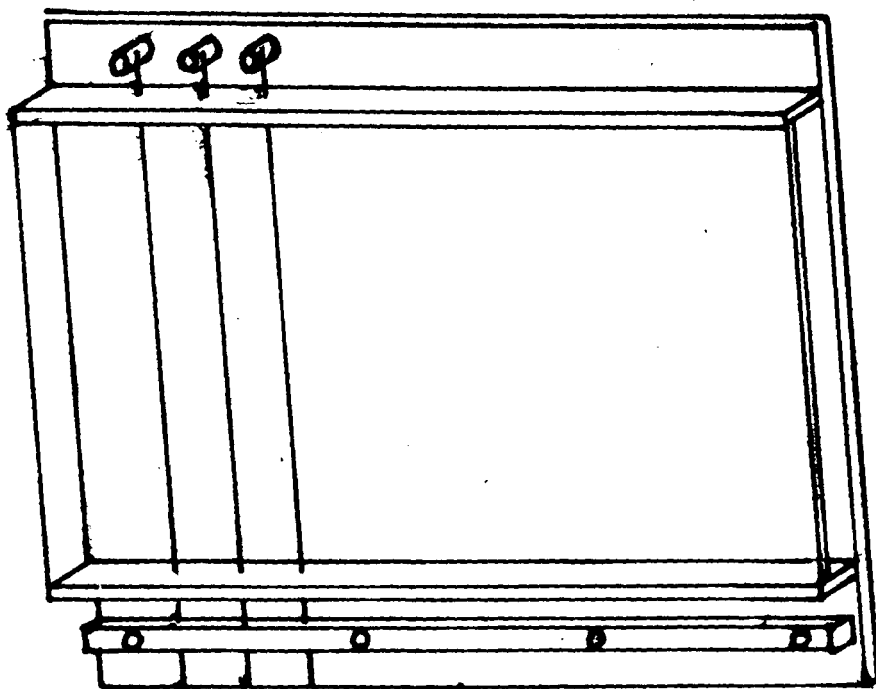


Figure 2.5 Method of setting molybdenum wire in perspex matrix

purpose was of 0.5 mm diameter and of 99.95% purity.

(b) Preparation of probes.

The equations used to analyse the probe characteristics are dependent, not only upon the probe surface area, but also upon the geometry of the probes themselves. Therefore it is important to obtain probes of known geometry with as little deviation as possible.

To produce a cylindrical probe from the molybdenum wire, the probe tips were milled and in order to prevent splitting of the wire, it was first moulded into a supporting block. Polymethylmethacrylate ("Perspex") was chosen as the moulding matrix since it can easily be milled and offers the advantage of being transparent.

The wires were set, under tension (achieved by suspending 2kg masses from their ends), in the moulding frame (fig. 2.5) and the 'perspex' side plates were sealed into position with silicone rubber compound. The 1mm gap left between the side plates, through which the wires passed, was then filled with tensol cement No. 7. This cement is partially polymerised methyl methacrylate to which an initiator is added prior to use. The mould was then placed vertically to allow air bubbles to rise to the surface during solidification. Thus a continuous block free from air bubbles was formed suitable for milling. (Originally, glass side plates were used and a methylmethacrylate monomer with initiator was used to fill the mould. The polymerisation is so highly exothermic, however, that the monomer boiled before polymerisation was complete, giving a block full of air bubbles and unsuitable for working on a milling tool).

When solid, straight sections of the wire of suitable length (3 to 5 cm) were identified, and the block cut so as to expose the face of the wire at these points. The exposed faces were then milled and ground using wet and dry emery of grades 400 and 600 successively.

The final probe surface was obtained by hand polishing with British American Optical Co. centriforce abrasive BM303 on a glass plate. The probe surface was periodically examined under a microscope of magnification x 7 until it showed an even reflection of white light.

The completed probes were then removed from the perspex by dissolving the matrix in trichloromethane (CHCl_3) and were positioned within the capillary tube, to an accuracy of ± 0.01 mm, by means of the calibrated eyepiece graticule of a microscope.

2.4 Resistance to Contamination

The high vacuum side, although so-called, is not under high vacuum during operation of the discharge. This section, because it contains the discharge, must be capable of resisting contamination from either real leaks (from the atmosphere) or virtual leaks (degassing from the vacuum system itself). It has been noted (Brassem et al 1976) that the contamination of a microwave discharge at a level of only 1% vol/vol can significantly change the discharge characterisation. So, for the lowest argon pressure used ($\approx 10^{-2}$ mbar), the system must be able to contain a contaminant pressure to below 10^{-4} mbar for a considerable period of time (or at least the time taken to complete a set of measurements).

To remove possible sources of contamination, the system underwent extensive baking and pumping at a temperature of 120°C , this being the temperature limit of the viton rings in the taps. During this

time the system was periodically cooled, tested for leaks with helium and a plot of pressure rise against time made. When clean and leak proof (to the limit of detection) ultimate pressures of 2×10^{-8} mbar and 9×10^{-8} mbar were regularly obtainable in the cases of the plain discharge tube and the probe tube respectively.

Fig. 2.6(a) shows that for the plain tube the high vacuum arm can maintain a pressure below 10^{-5} mbar for over 24 hours. Whilst fig. 2.6(b) shows the equivalent curve for the probe tube. Although the outgassing from the probe tube results in a pressure some one hundred times higher than in the plain tube, it was still possible to maintain a pressure below 5×10^{-5} mbar for over 24 hours.

Consequently it can be inferred that contamination of the plasma gas from the vacuum system will not be significant.

During the operation of the probe tube, considerable sputtering occurred from the two pairs of tubes closest to the cavity. Spectral scans failed to reveal the presence of any spectral emission lines from molybdenum and so contamination by molybdenum vapour was not considered to be a major problem.

2.5 The Spectral Recording System

Figure 2.7 shows a schematic diagram of the spectral recording system and equipment used is tabulated in Table 2.2. So that changes in the excitation conditions with distance from the cavity could be investigated, it was necessary to be able to record spectra from several points along the discharge tube. This consideration and ease of focussing, were the main criteria for design of the entrance optics.

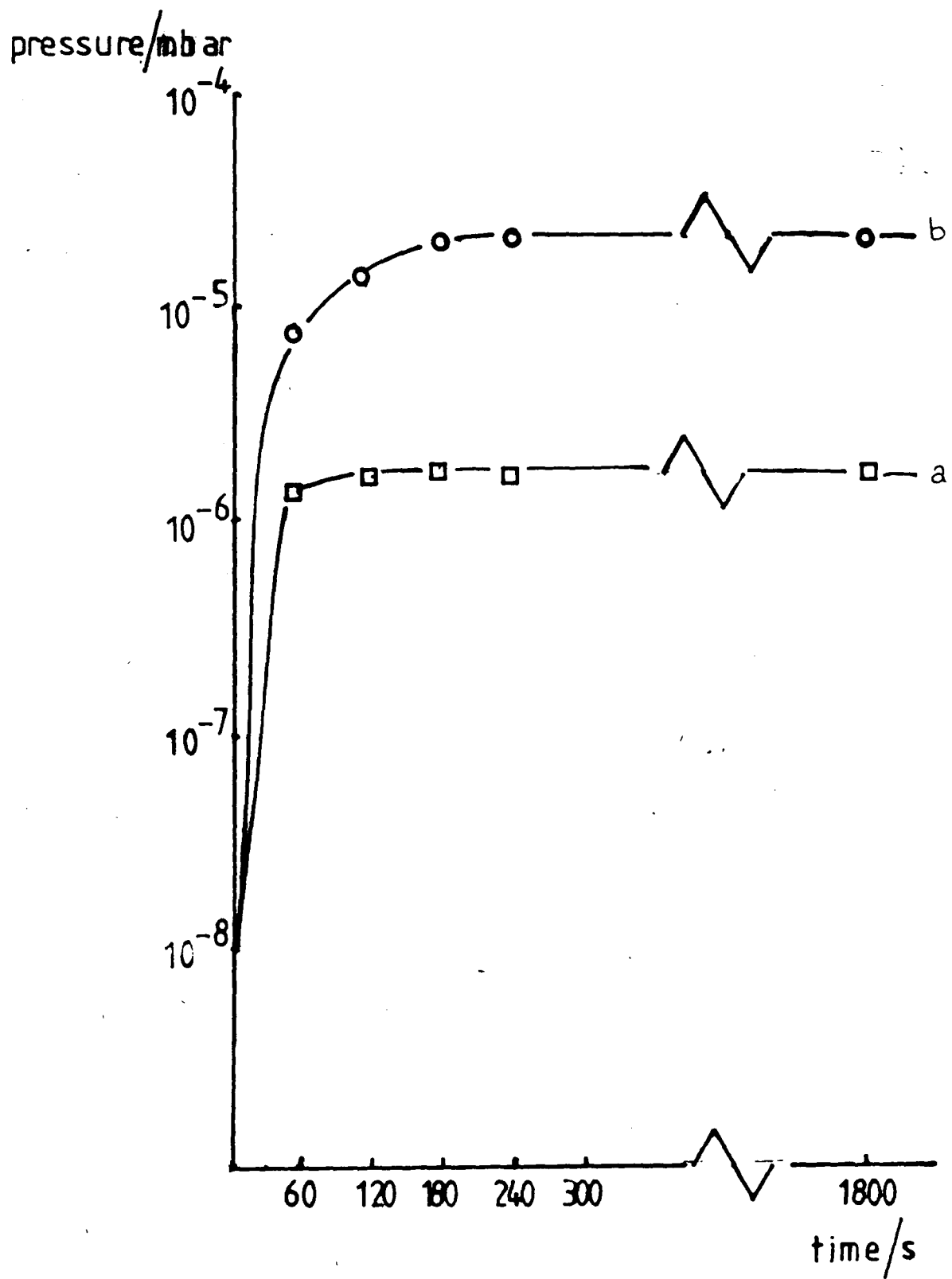


Figure 2.6 Rate of out-gassing for plain discharge tube (□) and probe tube (○)

Key

- A attenuator
- L-AMP lock-in amplifier
- VD voltage divider
- CR chart recorder

STANDARD TUNGSTEN
FILAMENT LAMP

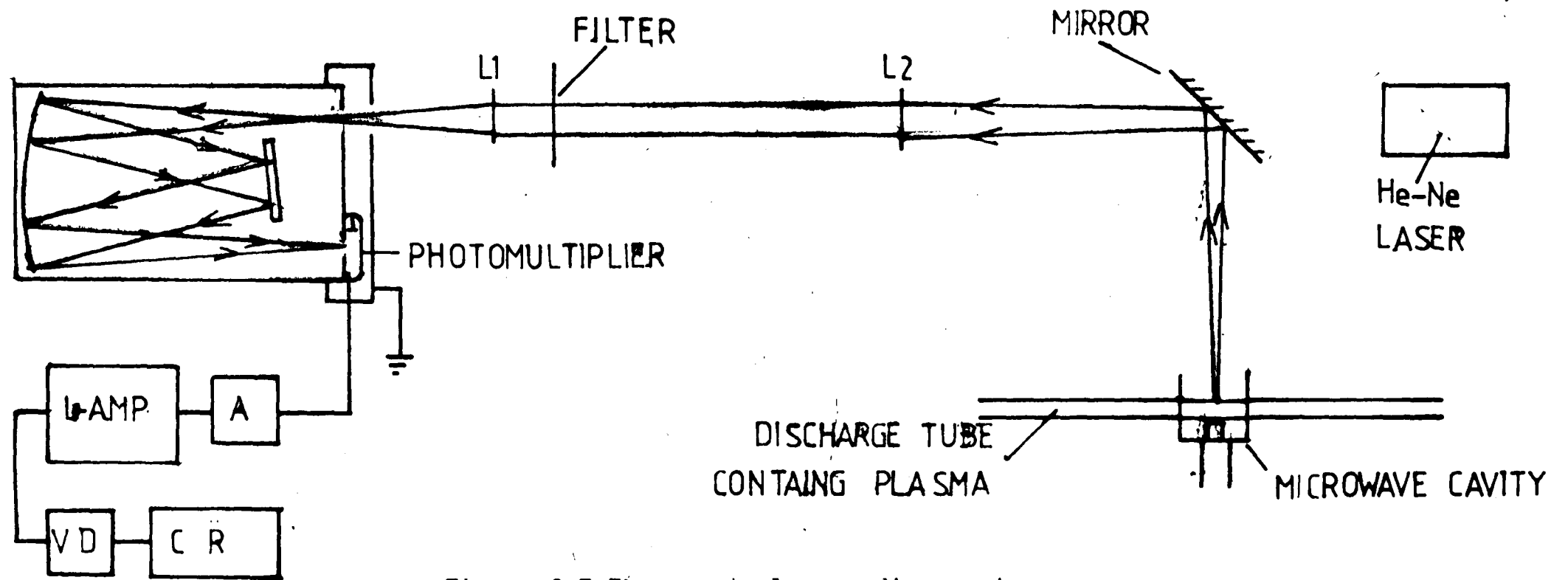


Figure 2.7 The spectral recording system

2.5.1 Entrance Optics

For the reasons stated above, the entrance optics were designed to give flexibility of sampling point, together with a simple method of focussing.

The quartz lens of 30 cm focal length, L1, is positioned at a distance from the entrance slit of the monochromator equal to its focal length. Thus a parallel beam will be focussed upon the entrance slit, regardless of the distance between the mirror and L1. The parallel beam was produced, quite simply, by maintaining the path length between the source and the quartz lens L2 (via the surface mirror) equal to the focal length of L2 (40 cm). In this way the discharge could be focussed on the entrance slit at any point along its length essentially by maintaining a constant distance between L2 and the mirror, providing that the discharge tube was parallel to the optical axis. The optical system provided a magnification of 0.8 with an acceptance angle of 5×10^{-3} steradians.

The He-Ne laser provided a reference for the optical axis. The discharge tube was aligned by attaching identical optical pins to each end of the tube and adjusting the height and orientation of the entire vacuum system until the tips of the pins impinged upon the laser beam. In this manner the aparallelism of the discharge tube to the optical axis was reduced to less than 3 mm.

Opposite the discharge tube and at an equal distance from the optical axis was the movable standard tungsten ribbon filament lamp, provided to obtain the optical response of the system. The lamp could be

positioned at the same distance from the monochromator slit as the point of measurement of the discharge. By rotating the mirror through 90° , the tungsten lamp could be focussed on the monochromator entrance slit.

2.5.2 The Monochromator

The Ebert-type monochromator has a grating of $1200 \text{ lines mm}^{-1}$. The height of the entrance and exit slits can be varied from zero to 30 mm and the slit width from $4 \mu\text{m}$ to $500 \mu\text{m}$. The calibration of the slit width micrometer was checked by examining the diffraction pattern of the 632.8 nm line, produced by the He-Ne laser, at the first mirror of the monochromator. It was found that the calibration was $1 \mu\text{m}$ per division, but with a zero error of 20 divisions. The entrance and exit slit widths were set to $20 \mu\text{m}$ and their heights to 8 mm. The focussing of the monochromator was also adjusted to give a maximum signal in the photomultiplier and symmetrical line shape.

2.5.3 The Detector System

The photomultiplier provided the ability to record spectra in the wavelength region 175-850 nm. The photomultiplier was operated at 900V and the dark current was typically of the order 3 nA when measured as a voltage across the load resistor. The load resistor itself was a $1 \text{ M}\Omega$, high stability ($\pm 1\%$) type.

The signal from the photomultiplier was input, via an optional attenuator, to the lock-in amplifier. The optional attenuator provided attenuations of 0, 26.7, 51.7 and 75.1 percentages of total signal, these values being specifically chosen to prevent overload by the most

intense lines of the argon I spectrum and the calibration lamp. The reference signal to the lock-in amplifier was provided by a small filament lamp incorporated into the monochromator at the entrance slit. The output of this lamp was chopped by the same blade as the spectral input. The modulated light falls on a light sensitive diode and the signal produced passes through a waveform amplifying circuit (fig. 2.8) to provide a 1 V rms square wave signal of frequency 200 Hz.

2.6 The Microwave Excitation System

A schematic diagram of the microwave excitation system is shown in fig. 2.9 and equipment used tabulated in Table 2.3. The magnetron produces a nominal frequency of 2.45 GHz at powers from 20 to 200 W, although both these parameters are dependent upon the magnitude and phase of the reflected wave.

The double stub tuner enables the power delivered to the cavity to be maximised. This results in a minimum of reflected power at the microtron, as measured by the reflected power meter A between the tuning stubs and the magnetron generator.

Although the microtron output is calibrated in watts, the measured variable is the anode current in milliamperes. The relationship between the two is only approximately linear and so an alternative method of measuring incident and reflected power was preferred. This was provided by the TFT power heads connected to the two directional couplers. Two couplers are used as opposed to one four-port coupler, since this reduces reflections onto the main-line, giving a more accurate measurement of power. (Outred ,1980)

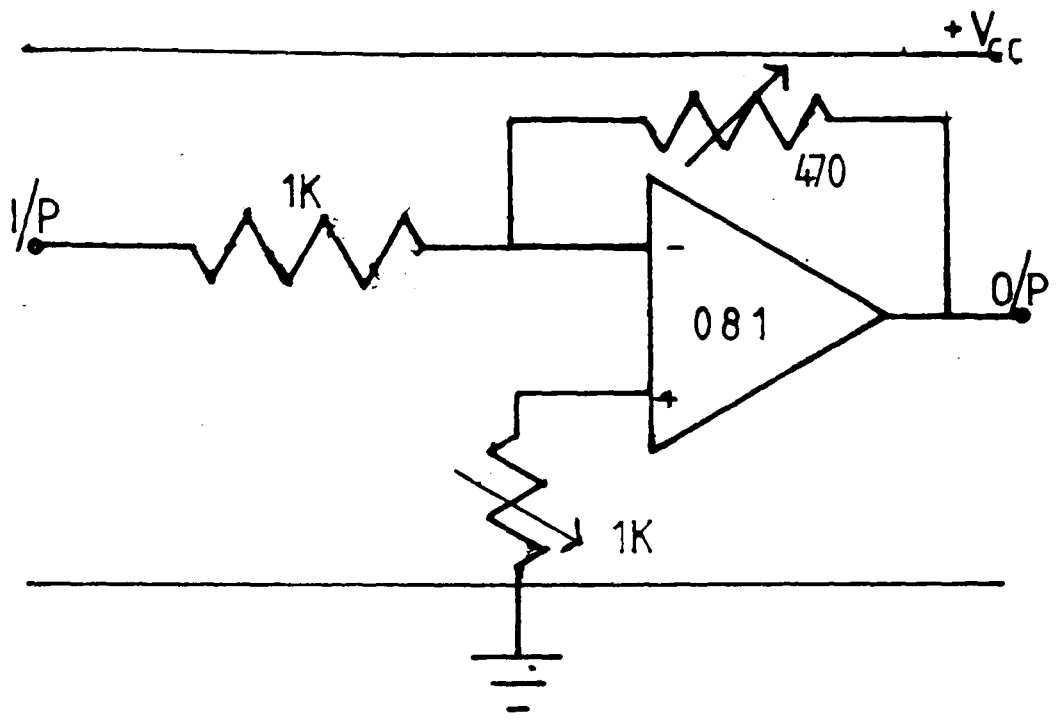


Figure 2.8 Reference signal amplifier circuit

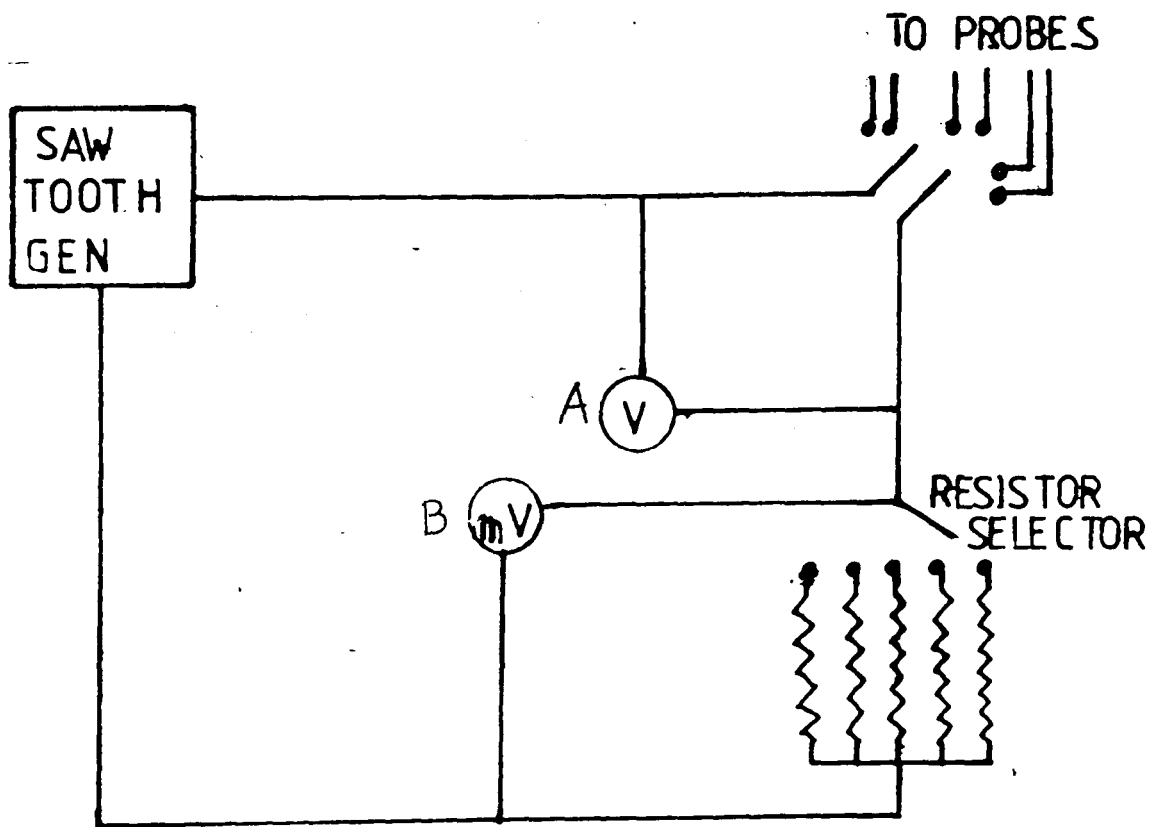


Figure 2.12 Probe characteristic recording system

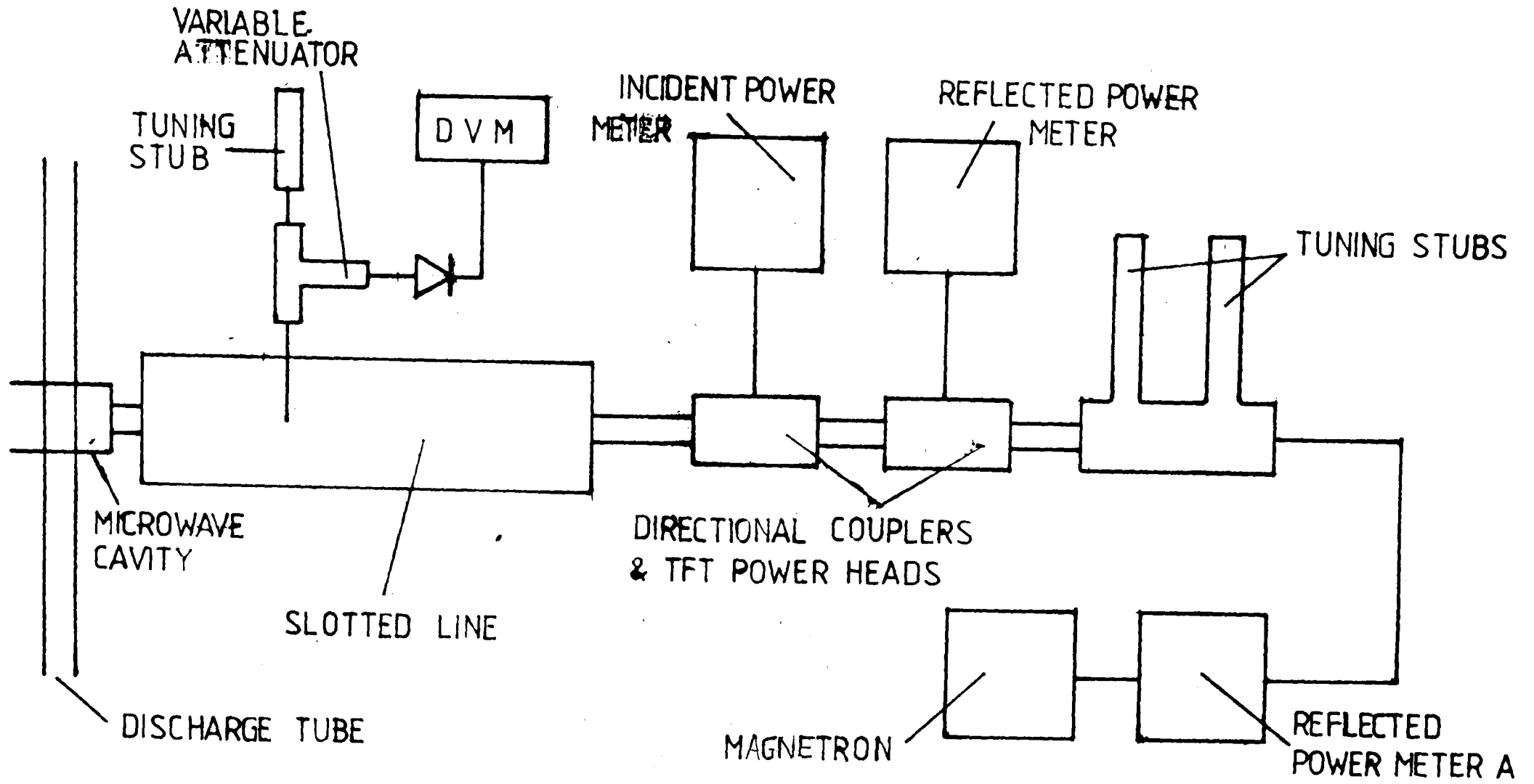


Figure 2.9 The microwave excitation system

The relative positions of the slotted line section, the directional couplers and the double stub tuner are important. The slotted line section must immediately precede the cavity if measurements are to be related to the properties of the cavity. With the directional couplers placed immediately before the slotted line, true measurements of incident and reflected power can be made (losses in the slotted line are very small, less than 0.004 dB cm^{-1}) without their presence affecting measurements made at the slotted line. Finally, the position of the double stub tuner prevents it influencing the value of cavity reflection coefficient calculated from the slotted line measurements.

2.6.1 The Cavity

The slab line cavity being used has been developed at the Polytechnic specifically for the microwave excitation of gaseous discharges (Hammond, 1978, Outred and Hammond, 1976,1980) Fig. 2.10 shows the cavity and the positioning of the discharge tube within it. The cavity consists of two sections each nominally a quarter wavelength in length. The externally visible inner is of diameter 6.32 mm, whilst the concealed inner of the low impedance section is of diameter 7.90 mm. The separation of the side plates is 25.50 mm. The discharge tube was placed at a given distance from the end of the cavity inner so that the axis of the tube intersected the axis through the cavity inner.

2.6.2 The Variable Attenuator

The signal from the sampling probe of the slotted line section was fed to a variable attenuator (fig. 2.9). The attenuator was included in

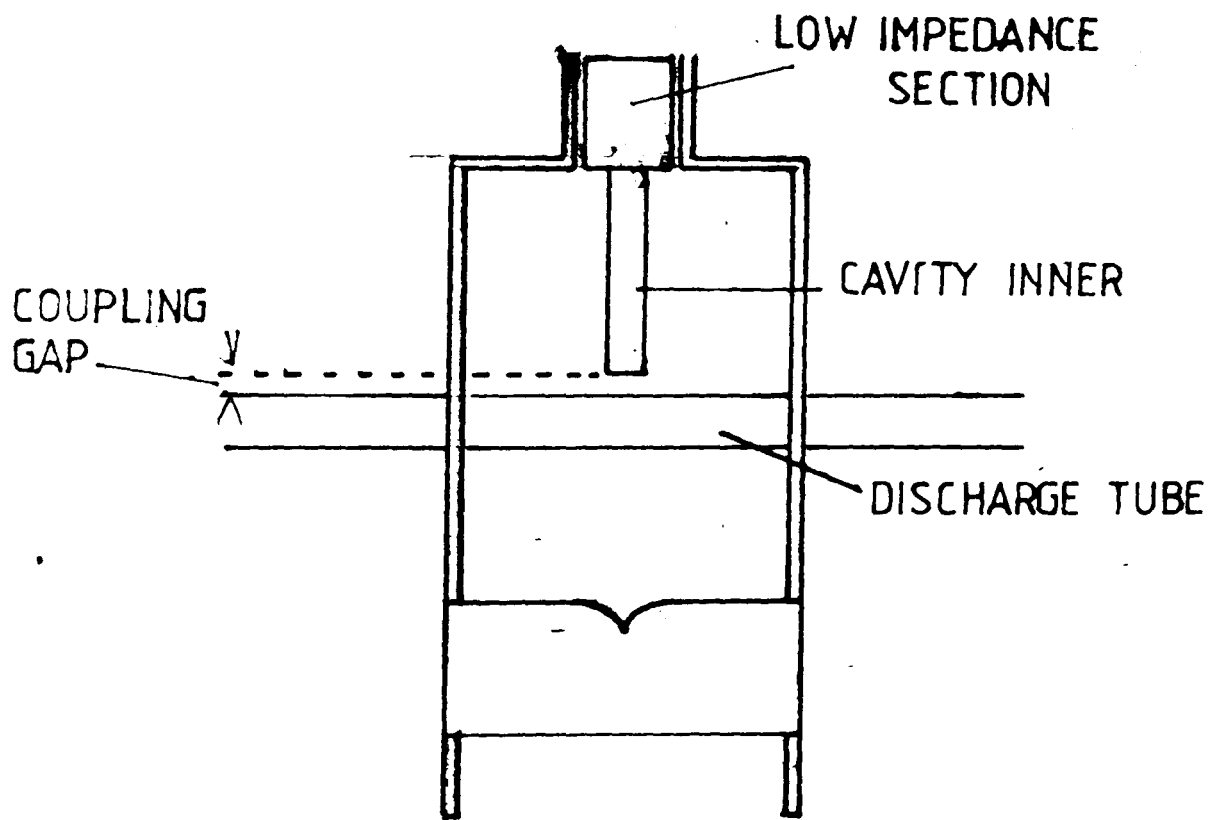
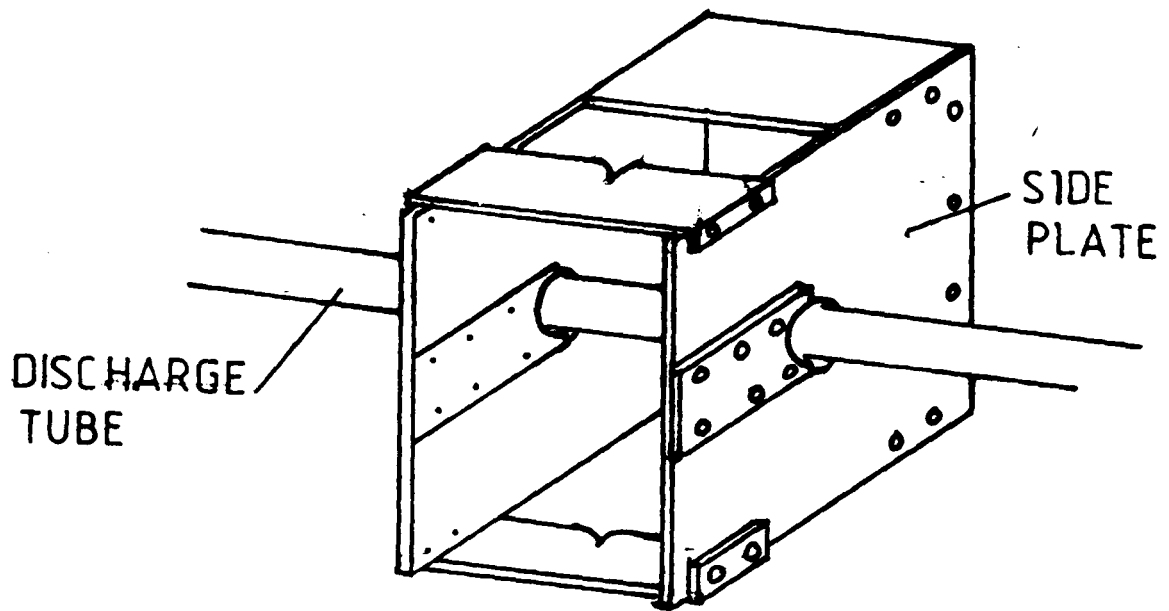


Figure 2.10 The cavity & positioning of the discharge tube: sketch & plan view

order to measure the voltage standing wave ratio (VSWR) in the slotted line (Chapter 3). The purpose of the single tuning stub connected to the attenuator was to eliminate the need for a correction of the attenuation figure read on the scale, as described by the manufacturer. The attenuator also ensured that, at the typical high powers encountered, the crystal rectifier was not overloaded. After passing through the rectifier (IN21B), the signal was recorded as a voltage on the digital voltmeter.

2.7 Probe Characteristic Measuring System

The probes are used in the "double floating probe" configuration. The voltage between the probes was provided by a sawtooth generator and amplifier (section 2.7.1) and the current in the probe circuit was measured as the drop in potential across a resistor of suitable value. Control of the programmable equipment and acquisition of data was achieved by a PDP-11 microcomputer via IEEE-488 interfaces. Table 2.4 provides a list of equipment.

2.7.1 The Voltage Ramp Generator

The circuit for the voltage ramp generator, constructed specifically for the work described, is shown in fig. 2.11. The 8321 integrated circuit provides a linear voltage ramp between $\pm 1.5V$ with a period of 25 seconds and a duty cycle of approximately 90%. This output is amplified by a 3582J integrated circuit amplifier to provide a linear voltage ramp between $\pm 40V$ or $\pm 60V$, dependent upon the amplifier gain.

2.7.2 Probe Characteristic Circuit

Fig. 2.12 shows the probe measurement circuit. The output of the

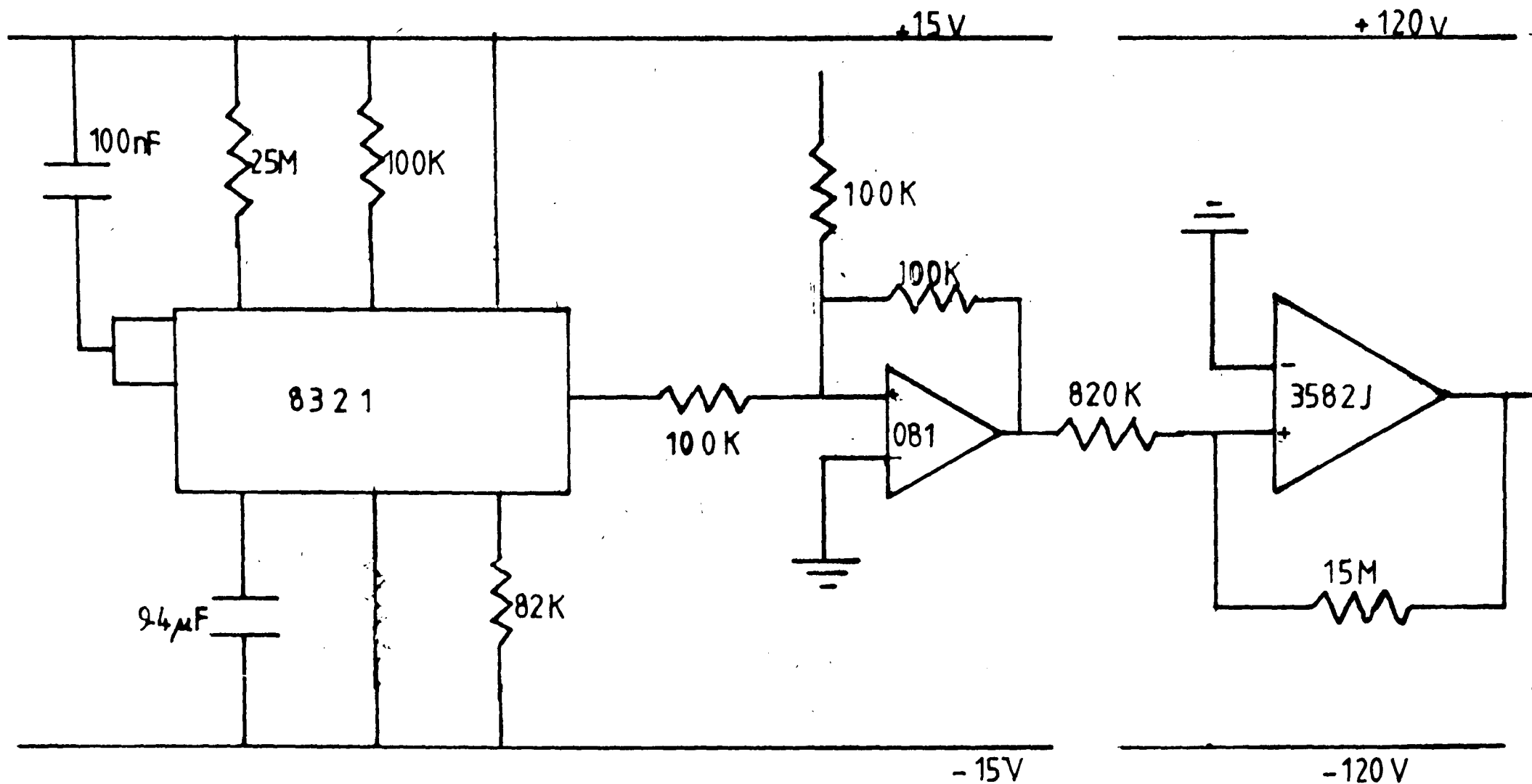


Figure 2.11 The voltage ramp generator

voltage ramp generator was passed, after amplification, to a programmable switch selector. This could be programmed from the microcomputer terminal to select certain pairs of probes for connection to the voltage ramp. The probe pairs were then sequentially connected to the voltage ramp. The voltage across each pair of probes was recorded by digital panel voltmeter A (fig. 2.12) whilst the current was measured as a function of the voltage dropped across a resistor and was measured by voltmeter B. The value of the resistance could be chosen from the computer terminal via the programmable switch unit. Values of resistance used were 84Ω , 169Ω , 269Ω , 558Ω and 748Ω and were chosen so as to prevent overloading of the 200mV meter (B) whilst providing the maximum possible drop in voltage across the resistor.

The data from the two voltmeters were acquired automatically and were stored initially on flexible disc before being transferred to magnetic tape for more permanent storage.

TABLE 2.1 Vacuum System Equipment

Low Vacuum Arm	Axial Quick Release Coupling Vitilan O ring gaskets	Leybold Heraeus GmbH
High Vacuum Arm	Axial Quick Release Coupling Aluminium UHV disc	Leybold Heraeus GmbH
10 KF Bellows seal	Type 28230	Leybold Heraeus
32 KF Taps	Type VRD38	GmbH
Sorption Pump	Type MS100	Vacuum Generators
	Type SP3	AEI Ltd
Triode Ion Pump	Type P60	AEI Ltd
Ion Pump Control	Type P25	AEI Ltd
Pirani Gauge	Type PVG3	Vacuum Gen.
	Type PVG4	
Gauge Control	Type PIR2	Vacuum Gen.
Ionization Gauge	Type VIG8	Vacuum Gen.
Gauge Control	Type IGCl0	Vacuum Gen.

TABLE 2.2 Instrumentation - Optics

Scanning Monochromator	Ebert Mounting 0.8 m focal length ₃ Resolution 8×10^{-3} nm	Philips Scientific Ltd.
PMT	Type 9558Q	Thorn EMI Electron Tube Division
Lens	Fused silica 30 cm, 40 cm focal lengths, 5 cm diam.	Optical Works Ltd.
Mirror	Flat, surface aluminised	
PMT power supply	Type PM28B	Thorn EMI Electron Tube Division
Lock-in amplifier	Type 5205	EG & G Brookdeal Electronics, Princeton Applied Research
Calibration lamp	Tungsten Ribbon 6V, 8A	Philips Research Laboratory
Chart Recorder	0.25 second response time	Honeywell Brown Ltd.

TABLE 2.3 Instrumentation - Microwave

Microwave Generator Reflected Power Meter	Microtron 200 Mk 3	Electromedical Supplies
Tuning Stubs Calibrated Attenuator	874 D20 L 874 GAL	General Radio Corp. USA
Diode Rectifier Assembly	432B IN21B	Hewlett Packard Hewlett Packard
Slotted line	805C/D	Hewlett Packard
Directional Couplers	3003-20	Narda Microwave Corp. USA
TFT Power Heads Power Meters	6423 6460	Marconi Sanders Ltd.
DVM	LM 1420.2	Solartron Electronics
Double Quarter Wave Slab line cavity Double Stub Tuner base		Polytechnic of North London

TABLE 2.4 Instrumentation - Probes

Probes	Tungsten wire 0.5 mm diam. 99.95% purity	Goodfellow Metals Ltd.
Voltage ramp generator	8321 IC	R S Components Ltd
3582J Power Supply	3582J op amp Type 2217	Burr Brown Teledyne Philbrick
Programmable Switch Unit	9812	Time Electronics
DPM 200V	Model 87	Amplicon
DPM 200mV	Model 87	Amplicon
Microcomputer	PDP-11 VT103	Digital Equipment Corp.

CHAPTER 3
MICROWAVE MEASUREMENTS

3.1 Theory

A detailed analysis of the slab line cavity is provided by Hammond (1978) from which details are included here. First a general description of the use of scattering parameters for the analysis of cavity behaviour is given, followed by the specific equations used in the calculation of plasma parameters.

Figure 3.1 shows a feed line of characteristic impedance Z_f carrying an incident wave V_{i1} and a reflected wave V_{r1} , where these represent un-normalised voltage-like variables. The cavity section has a characteristic impedance Z_c and carries the waves V_{r2} and V_{i2} . By definition:

$$\begin{bmatrix} V_{r1} \\ V_{r2} \end{bmatrix} = \begin{bmatrix} S_{11} & S_{12} \\ S_{21} & S_{22} \end{bmatrix} \begin{bmatrix} V_{i1} \\ V_{i2} \end{bmatrix} \quad 3.1$$

and, assuming an attenuation coefficient of travelling waves within the cavity of α and a loss-less short circuit at B:

$$V_{i2} = -e^{-2\alpha L} V_{r2} \quad 3.2$$

The equations give the overall reflection coefficient for the cavity as seen by the feed as:

$$\mathcal{A}_1 = \frac{V_{r1}}{V_{i1}} = S_{11} - \frac{S_{12} S_{21} e^{-2\alpha L}}{1 + S_{22} e^{-2\alpha L}} \quad 3.3$$

where S_{22} is approximately (-1), a short circuit.

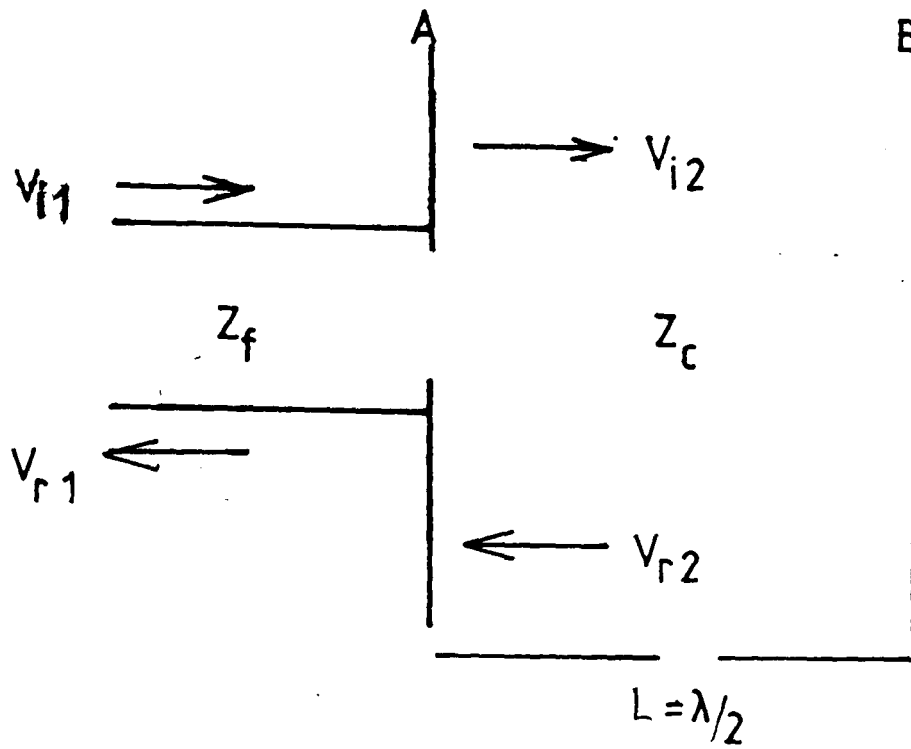


Figure 3.1 Simple schematic diagram of a cavity and feed line

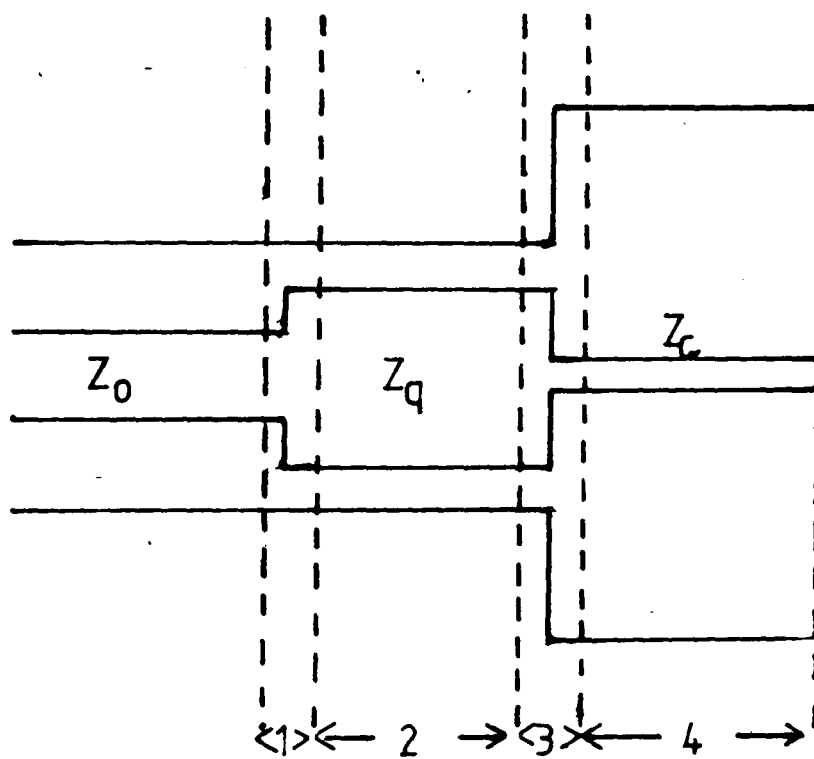


Figure 3.2 Division of slab-line cavity to calculate t-parameters

This simple transmission line analysis may be extended to include the loading effect of an electrodeless discharge tube for the case where this is symmetrically mounted within the cavity and does not perturb the resonant section between A and B in fig. 3.1. If this is the case, the electrodeless discharge tube will give rise to a reflection coefficient.

$$\rho_T = \frac{Z_T - Z_0}{Z_T + Z_0} \quad 3.4$$

where Z_T is the characteristic impedance of the tube. For this case

$$V_{i2} = V_{r2} e^{-2\alpha L} \rho_T \quad 3.5$$

and

$$\rho_1 = \frac{V_{r1}}{V_{i1}} = S_{11} - \frac{S_{12} S_{21} e^{-2\alpha L} \rho_T}{1 + S_{22} e^{-2\alpha L} \rho_T} \quad 3.6$$

Thus, if ρ_1 is measured and the S-parameters are known, ρ_T can be determined.

3.1.1 t - parameter representation

For practical calculations the model of the cavity is somewhat more sophisticated and includes an estimate of the cavity losses, the variation in wavelength from the source as excitation conditions in the discharge change and any slight inexactitude in the lengths of the quarter-wavelength sections. These effects may be conveniently included by working in terms of transmission or t- parameters. In normalised form they are defined by the equations:

$$a_2 = t_{11}^N b_1 + t_{12}^N a_1 \quad 3.7a$$

$$b_2 = t_{21}^N b_1 + t_{22}^N a_1 \quad 3.7b$$

$$\text{where } a_1 = \frac{V_{i1}}{2Z_f} \quad b_1 = \frac{V_{r1}}{2Z_f} \quad a_2 = -b_2 e^{-2\alpha L}$$

To calculate the t-parameters, the cavity may be divided into four sections, as shown in fig. 3.2. The overall t-matrix, in un-normalised form, is then given by:

$$\begin{bmatrix} e^{\gamma_c L_c} & 0 \\ 0 & e^{-\gamma_c L_c} \end{bmatrix} \begin{bmatrix} \frac{Z_q + Z_c}{2Z_q} & \frac{Z_q - Z_c}{2Z_q} \\ \frac{Z_q - Z_c}{2Z_q} & \frac{Z_q + Z_c}{2Z_q} \end{bmatrix} \begin{bmatrix} e^{\gamma_q L_q} & 0 \\ 0 & e^{-\gamma_q L_q} \end{bmatrix} \begin{bmatrix} \frac{Z_o + Z_q}{2Z_o} & \frac{Z_o - Z_q}{2Z_o} \\ \frac{Z_o - Z_q}{2Z_o} & \frac{Z_o + Z_q}{2Z_o} \end{bmatrix} \quad 3.8$$

$$\text{where } \gamma_c = \alpha_c + j\beta_c \quad 3.9a$$

$$\gamma_q = \alpha_q + j\beta_q \quad 3.9b$$

are the propagation coefficients in the different sections.

The values α_c and α_q are derived from a relationship given by Waldron (1970) for α in a coaxial line:

$$\alpha = 9.95 \times 10^{-6} \sqrt{\frac{\epsilon_r f}{\sigma}} \left(\frac{1}{r} + \frac{1}{R} \right) \log_{10} \left(\frac{R}{r} \right) \text{dBm}^{-1} \quad 3.10$$

where f = frequency

σ = conductivity of the surface of the inner and outer conductors

r = radius of the inner conductor

R = radius of the outer conductor

This equation was used directly to calculate α_q and a value of α_c was derived by putting $2R = 4a/\pi$ where a is the separation of the side plates of the slab line cavity.

As for the S-parameter representation:

$$V_{i2} = t_{11}V_{r1} + t_{12}V_{i1} \quad 3.11a$$

$$V_{r2} = t_{21}V_{r1} + t_{22}V_{i1} \quad 3.11b$$

with

$$\frac{V_{r1}}{V_{i1}} = \rho_c \quad 3.12$$

and

$$\rho_T = \frac{t_{11}\rho_c + t_{12}}{t_{21}\rho_c + t_{22}} \quad 3.13$$

From ρ_T , the plasma impedance Z_T can be obtained via the equation

$$Z_T = \frac{1 + \rho_T}{1 - \rho_T} \quad 3.14$$

3.2 Preliminary measurements

Before measuring the microwave impedance of the plasma, it was necessary to determine two factors: the position of the reference plane at the entrance to the cavity and the behaviour of the crystal rectifier diode at the high microwave powers encountered.

3.2.1 Determination of reference plane of cavity

The reference plane of the cavity is defined as that plane at the entrance to the cavity where the phase of the unloaded cavity reflection coefficient is zero when the cavity is exactly tuned. It is the position to which all phase angles are referenced. Clearly, this plane will not coincide with the zero on the scale of the slotted line section whose position is arbitrary. For this reason the distance from the reference plane to the scale zero must be ascertained and included when calculating the microwave parameters.

Measurements were made using the circuit of fig. 3.3. It became apparent from the results that a capacitative effect in the adaptor between the slotted line and the short circuit (the adaptor would be present in the operational microwave circuit) caused the distance to the reference plane to be dependent on the frequency of the incident signal. For this reason, the distance to the reference plane was measured for frequencies from 2.20 to 2.70 GHz at a nominal interval of 0.05 GHz.

The distance to the reference plane was calculated from each of the VSWR minima, which were located by the "method of bracketing".

Measurements were made four times for each frequency, ensuring that the frequency meter, which is itself a resonant cavity, was far from resonance.

The results in fig. 3.4 show the average distance to the reference plane, l , as a function of frequency. The curve is a linear least squares fit to the data, the standard deviation of the l values about

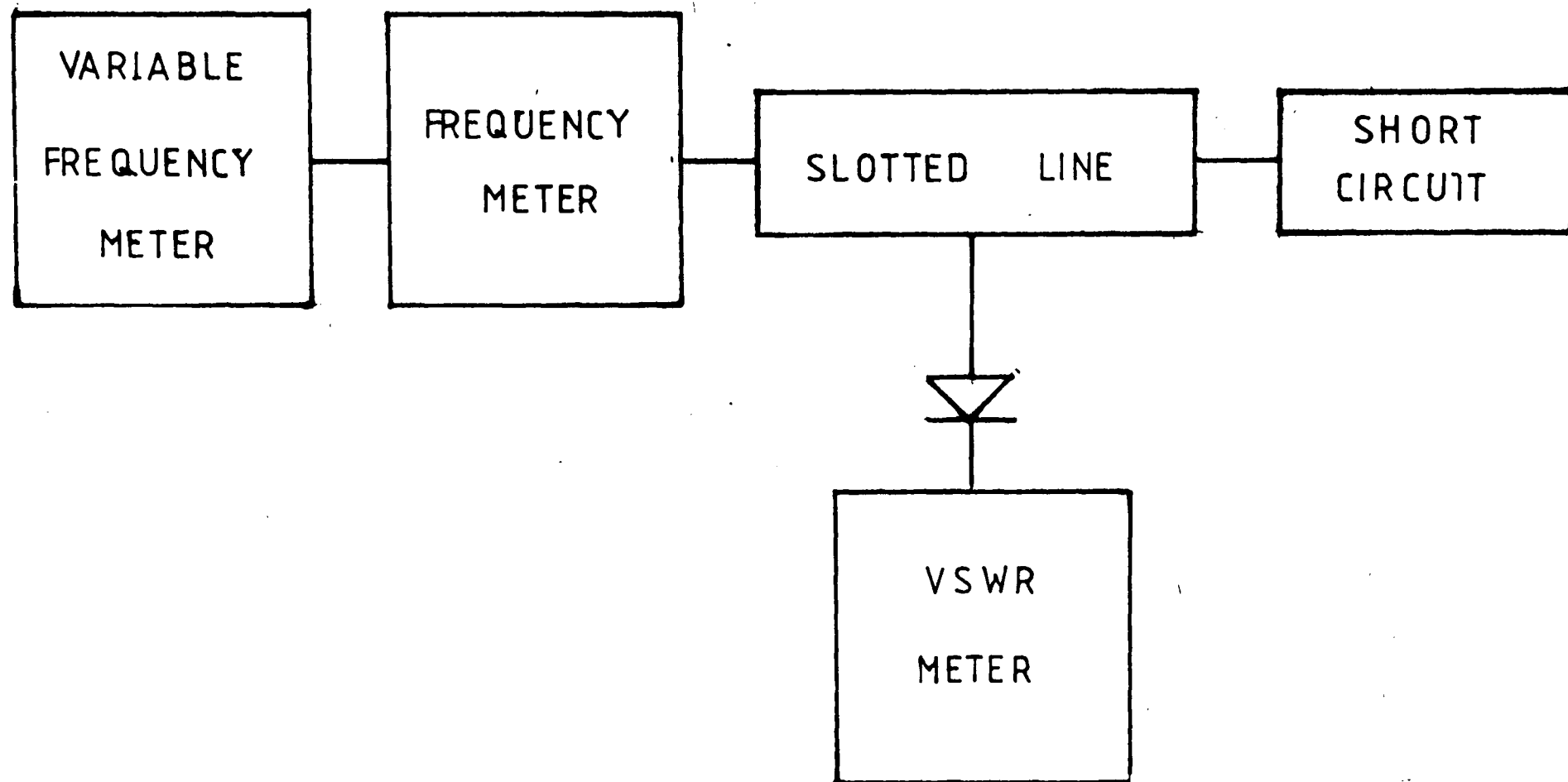


Figure 3.3 Experimental arrangement to measure distance to reference plane of cavity

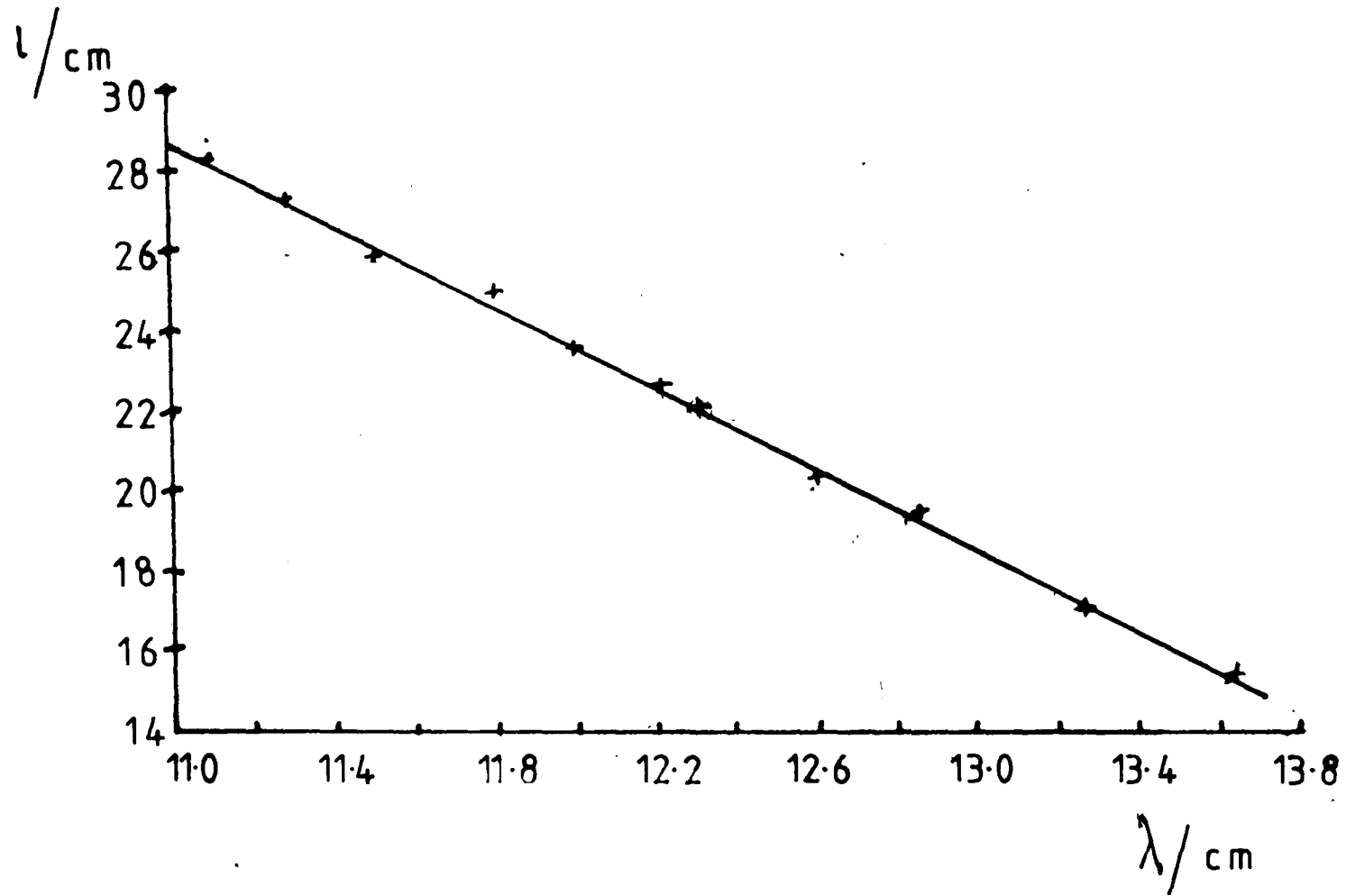


Figure 3.4 Variation of distance to reference plane of cavity, l , with wavelength, λ

the fitted curve being 9.1×10^{-2} . The data points were later used to form part of a computer programme to interpolate for any wavelength within the limits of the data and provide the appropriate value of l .

3.2.2 Response of the diode rectifier

It was necessary to decide between the two methods of measuring the VSWR in the slotted line which presented themselves, viz. the "added attenuation" method and the "width of minimum" method. The latter depends upon the square law relationship between the incident microwave power and the voltage developed at the diode (type IN21B). Generally speaking, this relationship is only achieved at low powers. It was therefore decided to check, at high and low powers, the diode behaviour. The circuit used is shown in fig. 3.5, where for low powers the source is a Sanders 6056 generator and for high powers, the magnetron.

Positions along the slotted line which gave convenient deflections D on the standing wave meter were noted. In order to determine the response of the diode a curve was plotted of

$$\log_{10} D \text{ vs } \log_{10} \sin\left(\frac{2\pi l'}{\lambda_g}\right)$$

where l' is the distance from the reference plane to the position of the probe on the slotted line. For square law behaviour, the gradient of this curve should have a single value of 2.0. The results for the low and high power behaviour of the diode are shown in fig. 3.6, where the curves are least square linear fits. The gradient of each curve is:

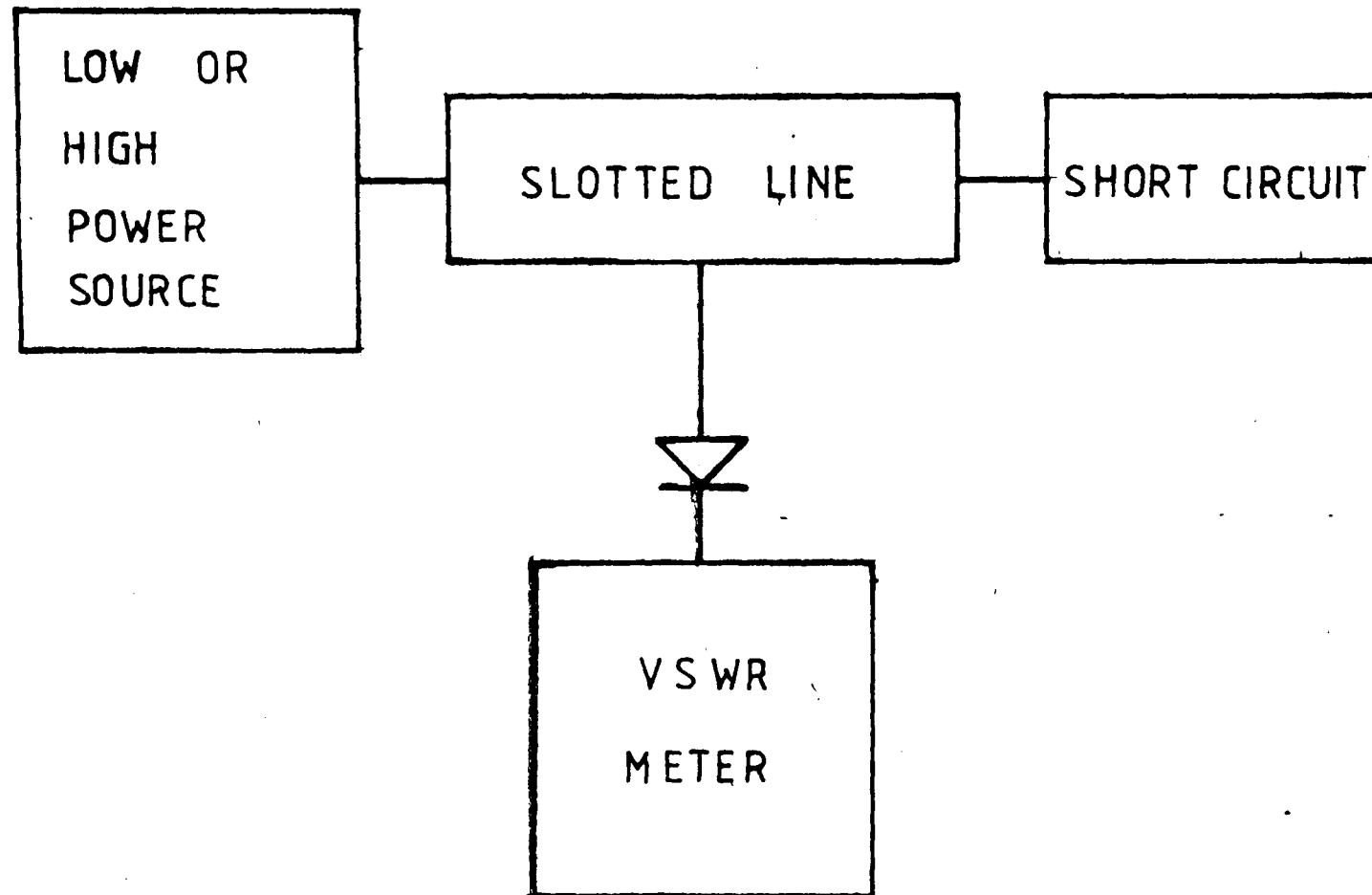


Figure 3.5 Experimental arrangement to measure diode rectifier behaviour

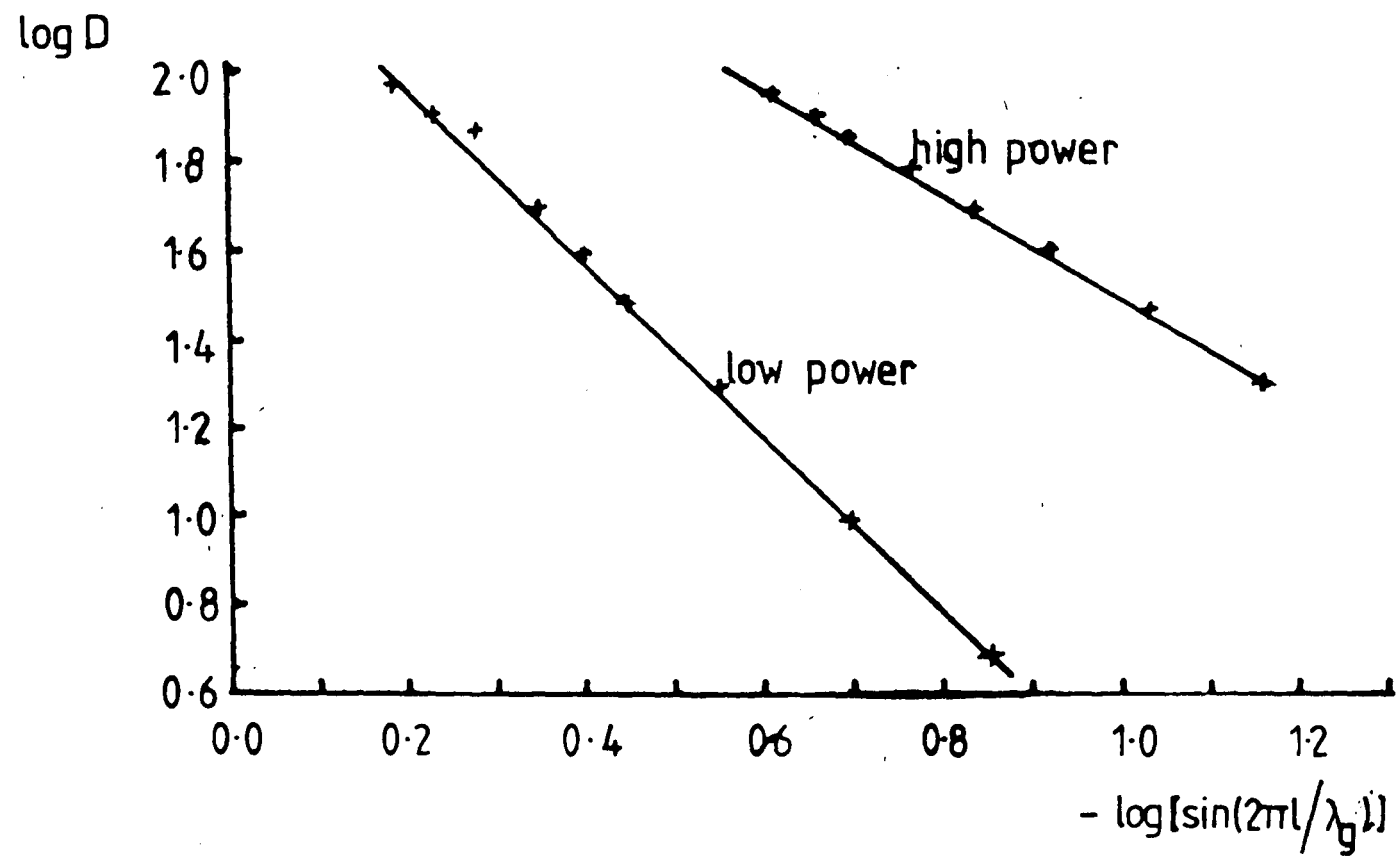


Figure 3.6 Diode behaviour at high and low powers

low power 1.97 ± 0.07

high power 0.93 ± 0.07

Clearly, then, at the high microwave power ($\sim 100\text{W}$) encountered in the work, the diode does not operate in the manner of a square-law detector. This result automatically invalidates the "width of minimum" method for measuring the VSWR, leaving only the "added attenuation" method.

3.3 Measurement of the VSWR

As described in section 3.2.2., the method employed to measure the VSWR is that of "added attenuation".

The positions of the VSWR minima were determined by the "method of bracketing" and allowed the microwave guide wavelength to be determined. The location of the minima was performed with 5dB attenuation. This ensured that the attenuation achieved was as shown on the attenuator barrel, as described by the manufacturer. In addition, it reduced the noise on the digital voltmeter (DVM) reading.

At the positions of VSWR maxima, the attenuation was increased to a maximum and slowly reduced until the same DVM reading as at the VSWR minima was obtained. Thus all measurements of the VSWR minima were approached from the direction of highest attenuation. This eliminated backlash on the attenuator.

The VSWR was calculated from the added attenuation, A dB, using the equation:

$$\text{VSWR} = \text{antilog} \left(\frac{A}{20} \right) \quad 3.15$$

The reflection coefficient ρ_c was calculated from the VSWR from the equation:

$$\rho_c = \frac{\text{VSWR} - 1}{\text{VSWR} + 1}$$

which after substitution into equation 3.13 yielded ρ_T and hence Z_T was obtained from equation 3.14.

CHAPTER 4
SPECTROSCOPIC MEASUREMENTS

4.1 Theory

The investigation of the behaviour of a plasma with reference to the plasma "phase" or "regime" requires the measurement of the population densities of the levels of the atomic (and ionic) system.

The intensity, I_{ji} , of a given spectral emission line of frequency ν_{ji} from an optically thin source of thickness l is

$$I_{ji} = \frac{1}{4\pi} N_j A_{ji} h \nu_{ji} l \quad (\text{Jm}^{-2}\text{srad}^{-1}\text{s}^{-1}) \quad 4.1$$

where A_{ji} is the transition probability for a transition from level j to level i and N_j is the population density of the level j . Thus the population density of a given level j can be calculated from the measured intensity of a spectral emission line which is the result of a transition from level j to some lower level. In practice, the response of the measuring system must be accounted for when using intensity measurements to deduce N_j .

It should be stressed that such information as may be deduced from the intensities of spectral emission lines concerns only radiative decay. That is to say that no information about collisional decay processes can be obtained from spectral intensity measurements.

4.2 Consideration of the argon I lines

From the results of previous workers (Fujimoto 1972, Tachibana 1973, van der Mullen et al 1980, Raaijmakers et al 1983) it seems clear that a complete understanding of the plasma requires an investigation of the differences in behaviour of the different levels within the atomic

system of the plasma gas atoms. That is to say that the various (de-) excitation processes available to the atomic levels become more, or less, important to different levels under different conditions. For this reason it was decided that the intensities of spectral emission lines from as many groups of levels as possible should be measured. In particular, the work of Tachibana et al (1973) has shown that the higher lying levels may be expected to reach equilibrium with the ion ground state at a lower free electron density than the lower atomic levels. It was therefore considered important to obtain measurements from atomic levels of principal quantum number $n=7$ and above. The major source of uncertainties in such measurements lies in the large errors in the transition probabilities, typically greater than 50% (Wiese, 1969), leading to large uncertainties in the final population densities.

The selected argon I spectral lines are tabulated in Table 4.1, together with the upper and lower energy levels pertaining to the transition (Wiese, 1969), whilst fig. 4.1 shows an energy level diagram of the argon atom.

4.3 Calibration of Optical System

As indicated in section 2.5.1, the optical response of the system was calibrated by means of a standard tungsten ribbon filament lamp. The intensity of the lamp measured by the optical system is related to the intensity obtained when the known filament temperature is substituted into the equation of Planck's law.

The lamp itself was calibrated, by an optical pyrometer, at a wavelength

TABLE 4.1 SELECTED LINES OF THE ARGON I SPECTRUM

Wavelength (nm)	Transition	
415.86	5p $[3/2]_1$	4s $[3/2]_2^0$
420.07	5p $[5/2]_3$	4s $[3/2]_2^0$
433.36	5p' $[3/2]_2$	4s' $[1/2]_1^0$
488.63	10d $[7/2]_4^0$	4p $[5/2]_3$
492.10	10d $[7/2]_3^0$	4p $[5/2]_2$
495.68	9d $[7/2]_4^0$	4p $[5/2]_3$
504.88	8s $[3/2]_1^0$	4p $[1/2]_1$
506.01	8d $[7/2]_4^0$	4p $[5/2]_2$
515.14	6d $[1/2]_0^0$	4p $[1/2]_1$
517.75	9s $[3/2]_2^0$	4p $[5/2]_3$
542.14	8s $[3/2]_2^0$	4p $[5/2]_3$
545.17	7s $[3/2]_2^0$	4p $[1/2]_1$
563.91	9s $[3/2]_1^0$	4p $[1/2]_0$
588.26	6s' $[1/2]_1^0$	4p $[1/2]_1$
603.21	5d $[7/2]_4^0$	4p $[5/2]_3$
641.63	6s $[3/2]_2^0$	4p $[1/2]_1$
666.07	6s' $[1/2]_1^0$	4p $[3/2]_2$
675.28	4d $[3/2]_2^0$	4p $[1/2]_1$
696.54	4p' $[1/2]_1$	4s $[3/2]_2^0$
727.29	4p' $[1/2]_1$	4s $[3/2]_1^0$
751.47	4p $[1/2]_0$	4s $[3/2]_1^0$

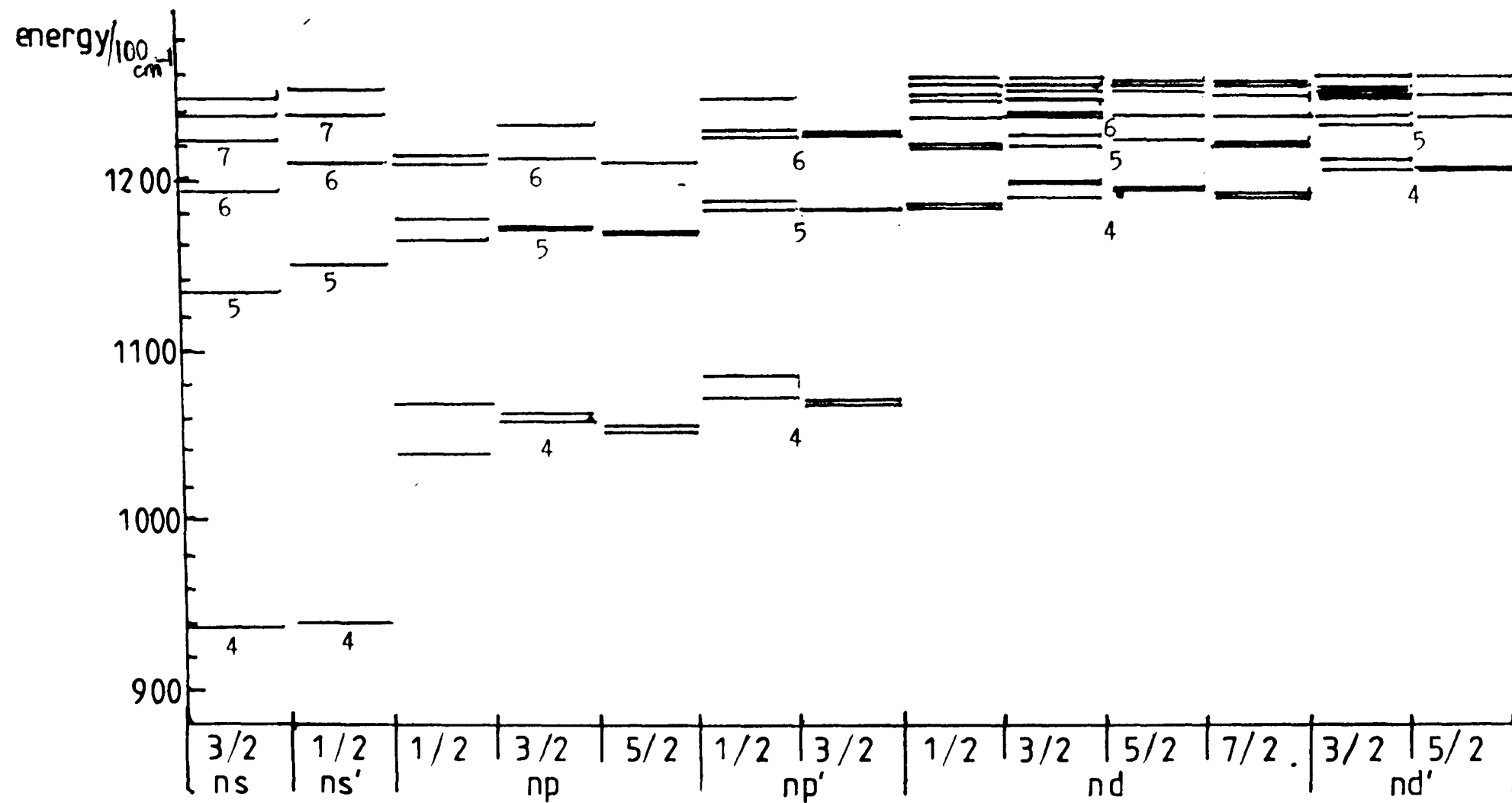


Figure 4.1 Atomic energy level diagram for argon

of 665.0 nm before being used to calibrate the optical system and its brightness temperature, T' , at this wavelength was found to be 2293K.

The true temperature, T , at some wavelength λ is given by (Griem 1964):-

$$T = \left[\frac{1}{T'} - \frac{\lambda_1}{C_2} \ln(\tau(\lambda_1) \epsilon(\lambda_1))^{-1} \right]^{-1} \quad 4.2$$

where λ_1 is the calibration wavelength

T' is the brightness temperature at λ_1

$\tau(\lambda_1)$ is the transmission of quartz at λ_1

$\epsilon(\lambda_1)$ is the emissivity of tungsten at λ_1

C_2 is the second radiation constant

The true temperature at a wavelength λ is then substituted into the Planck equation which, after multiplication by $\epsilon(\lambda)$ and $\tau(\lambda)$ ¹ yields the intensity I at the desired wavelength, ie:-

$$I(\lambda) = \frac{2hc^2}{\lambda^5} \left[\exp\left(\frac{hc}{\lambda kT}\right) - 1 \right]^{-1} \epsilon(\lambda) \tau(\lambda) \quad 4.3$$

The lamp was provided with a constant current of 6A from a stabilised constant current supply. After switching on, the lamp was allowed to stabilise for approximately 15 minutes before being used. After this time the intensity at a given wavelength was found to be constant (fig. 4.2).

Measurements of the continuum of the tungsten ribbon lamp were made over an interval of 1.5 Å about the centre of each argon spectral line. Calibration of the optical system was repeated at intervals of approximately 48 hours using a scanning speed of 0.5 Å min⁻¹ (as used for the argon spectrum). In order to remove second and third

¹ Values of $\tau(\lambda)$ and $\epsilon(\lambda)$ were taken from tables supplied by the manufacturer of the lamp.

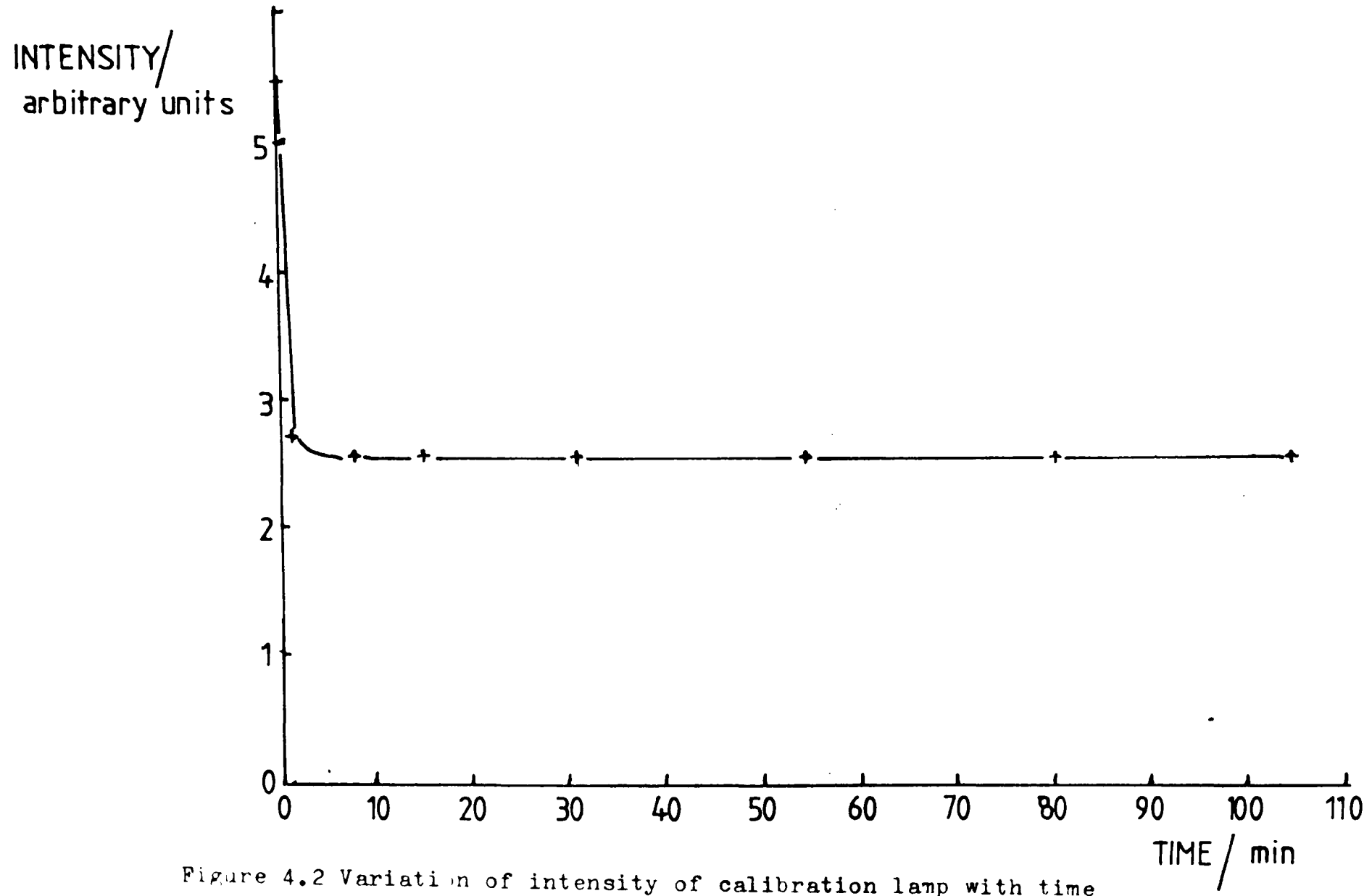


Figure 4.2 Variation of intensity of calibration lamp with time

order contributions from other wavelengths, the following filters were used in the wavelength regions shown:-

400 to 500 nm	Filter OB8
500 to 750 nm	Filter OY4

The transmission properties of the two filters are shown in fig. 4.3(a) and (b) and a typical calibration curve is shown in fig. 4.4.

4.4 Comparison of Continuum and Discrete Spectra

The different distribution of intensity between a spectral emission line and a continuum requires some compensation for the contribution from the latter caused by finite widths of the entrance and exit slits of the monochromator. The response R of an optical system to either a discrete source or a continuum source is given by Lincke (1968) as:-

$$R_{\text{line}} = d_1 \eta_{\lambda}^* \eta_{\lambda_0} I_{\text{line}} \quad 4.4$$

and

$$R_{\text{cont}} = d_1 \frac{d_2}{D} \eta_{\lambda}^* \eta_{\lambda_0} I(\lambda) \quad 4.5$$

where d_1 is the entrance slit width

d_2 is the exit slit width

D is the linear dispersion $dl/d\lambda$

I_{line} is the total line intensity

$I(\lambda)$ is the continuum intensity at wavelength λ per unit wavelength

η_{λ}^* is the relative detector sensitivity at λ

η_{λ_0} is the detector sensitivity at some reference wavelength, λ_0

Thus a factor d_2/D must be taken into account when using a tungsten

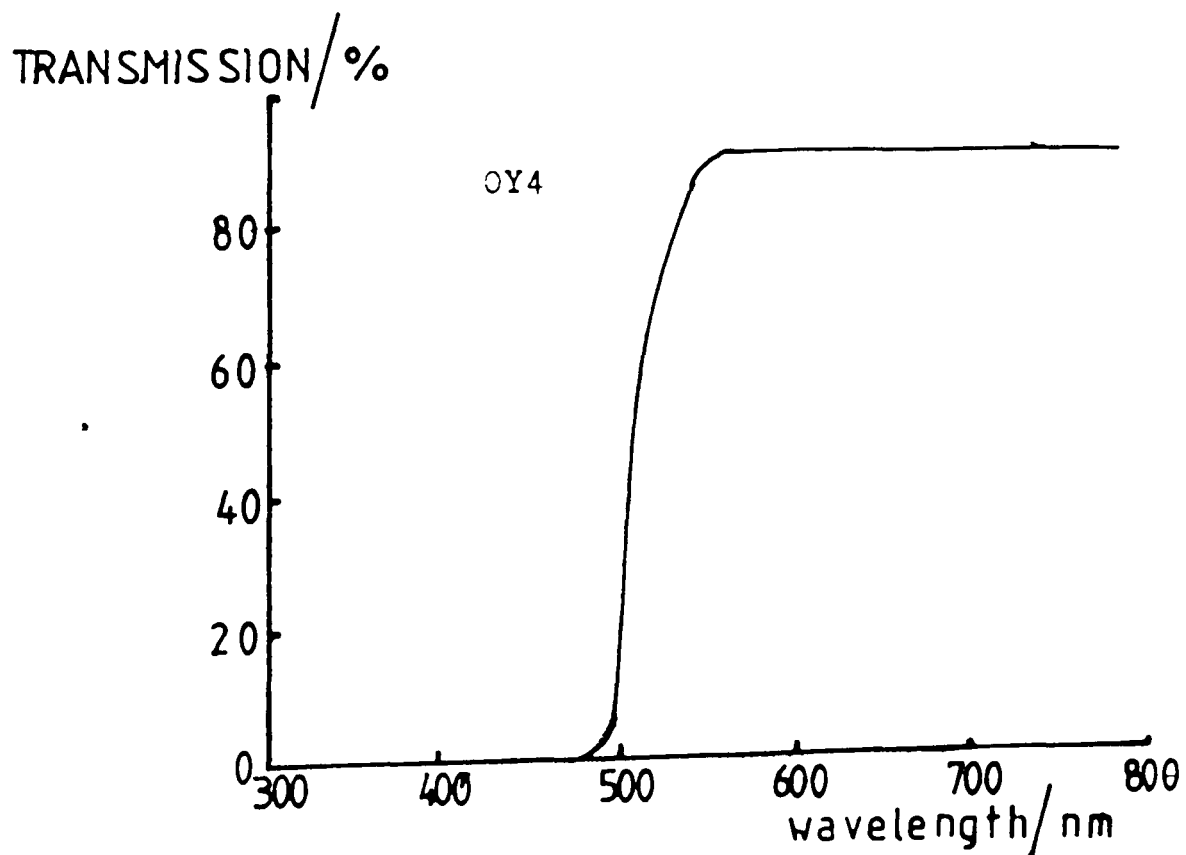
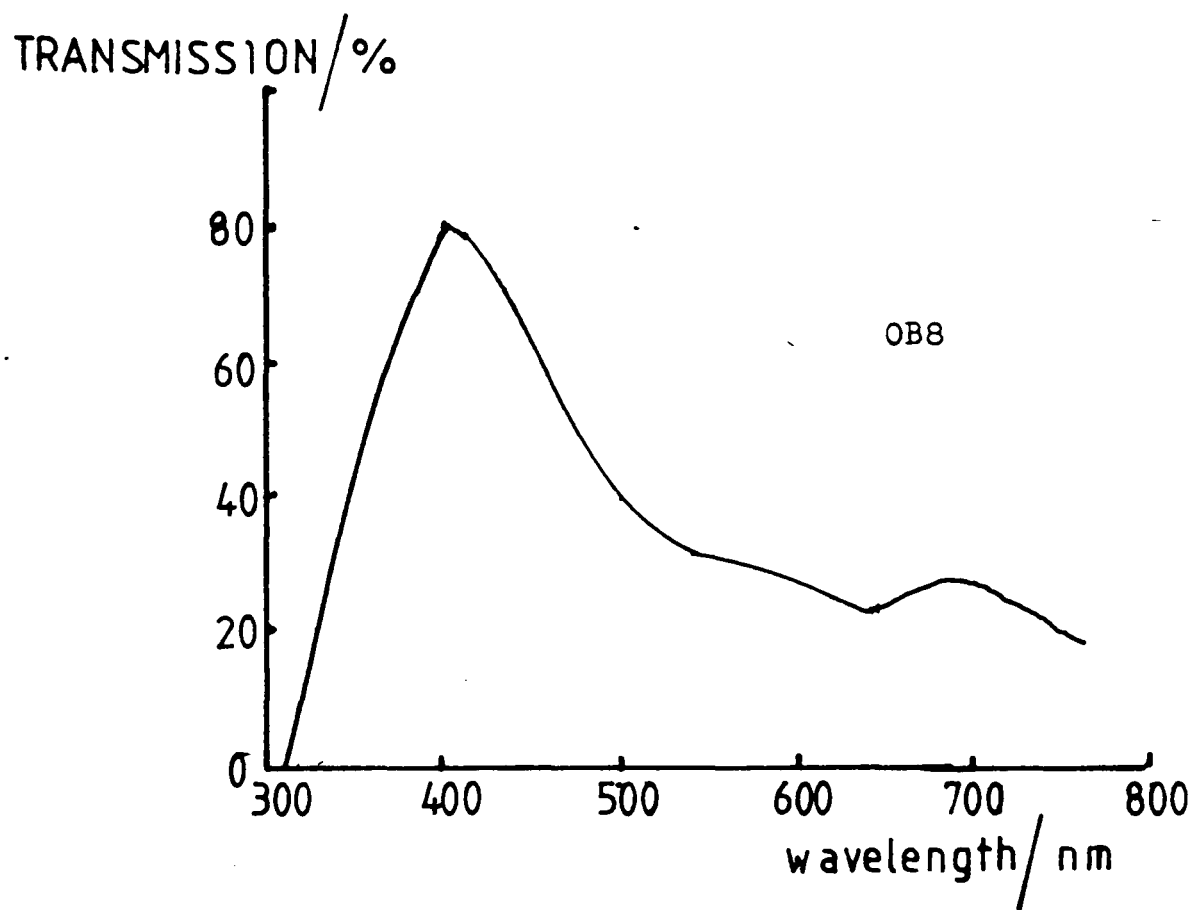


Figure 4.3 Wavelength response of optical filters

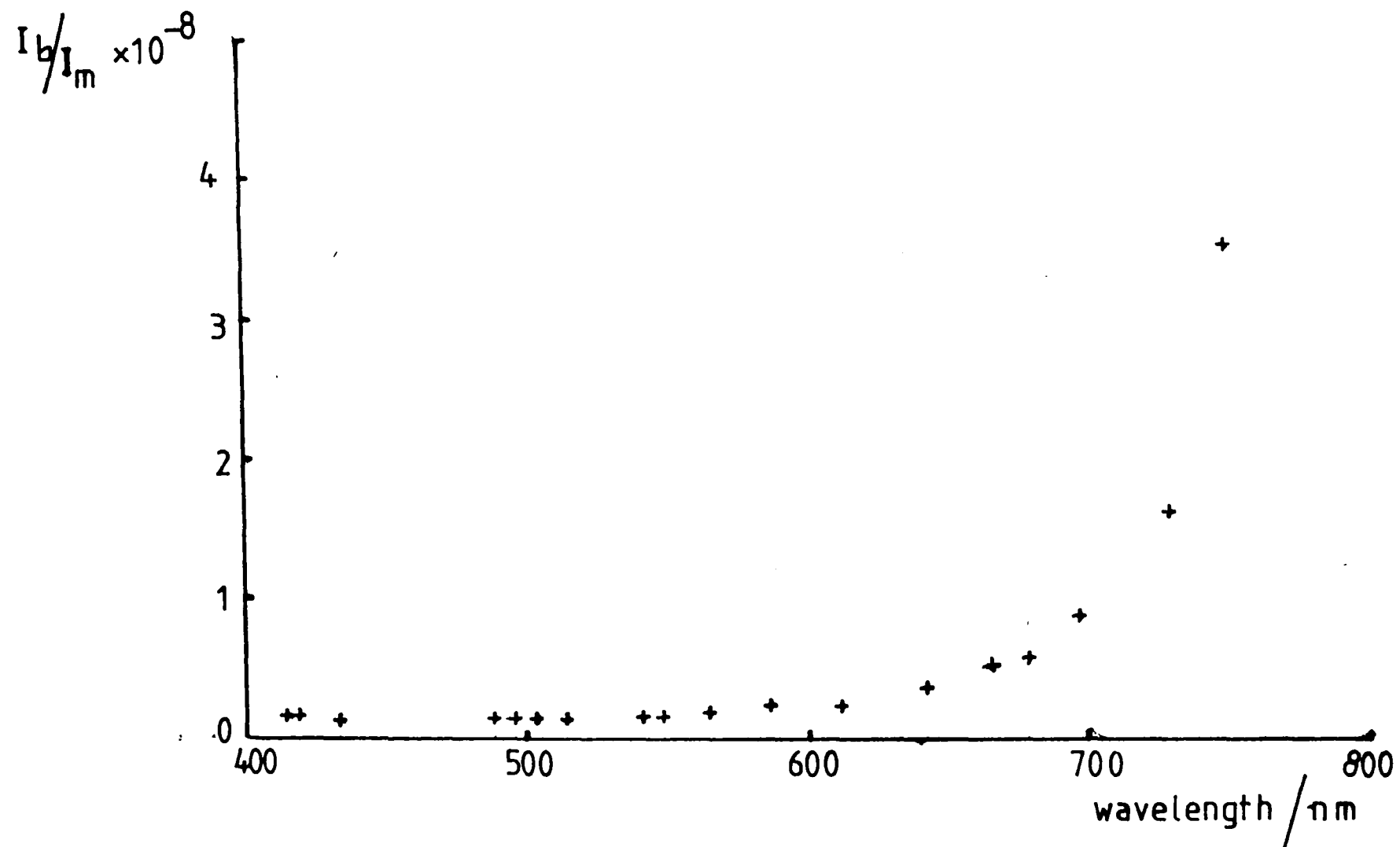


Figure 4.4 A typical calibration curve for the spectral response of the system
 I_b = black body intensity, I_{planck} I_m = measured intensity (arbitrary units)

filament lamp to calibrate an optical system for intensity measurements of a discrete spectrum. As the intensity of either the continuum or a spectral line was to be calculated from either the area under the line or the peak or continuum height as recorded on the chart recorder, it was necessary to measure the dispersion as represented on the chart recorder.

In the first order, the linear dispersion, D , has been shown to vary by 10% over the wavelength region 300 nm to 800 nm (Burke, 1986). Two lines of the first spectrum of mercury with wavelengths 313.155 nm and 313.183 nm were selected as suitable candidates for measuring the value of D as its representation on the chart recorder. These two lines are conveniently close to each other and can be easily obtained from a mercury vapour lamp.

A Philips low pressure mercury lamp was at first employed but it was found that after a period of 30 minutes operation the two spectral lines were so broadened as to be unresolved. A single isotope mercury lamp was substituted, but the intensity of the two spectral lines from this was so low as to degrade the signal-to-noise ratio to an unacceptable level. Eventually, the measurement was made using three low pressure mercury lamps in rotation so that measurements were always made on a lamp which started 'cold'. Ten measurements of the dispersion λ as represented on the chart at a mean wavelength of 313.169 nm were made, giving an average of

$$D = 0.909 \text{ m nm}^{-1}$$

and a standard deviation of $\sigma = 1 \times 10^{-3}$

From equation 4.4, the true spectral intensity is given by

$$I_{\text{line}} = R_{\text{line}} \frac{1}{d_1 \eta_{\lambda}^* \eta_{\lambda_0}} \quad 4.6$$

and the factor $(d_1 \eta_{\lambda}^* \eta_{\lambda_0})$ can be determined from the calibration continuum measurement, viz:

$$d_1 \eta_{\lambda}^* \eta_{\lambda_0} = \frac{R_{\text{cont}}}{I(\lambda)} \frac{d_2}{D} \quad 4.7$$

So that the true intensity of the spectral line is given by

$$I_{\text{line}} = R_{\text{line}} \frac{I(\lambda)}{R_{\text{cont}}} \frac{d_2}{D} \quad 4.8$$

4.5 Measurement of the Argon Spectra

4.5.1 The Argon I Spectrum

The spectral intensities of the argon emission lines listed in table 4.1 were each examined at a variety of pressures and positions along the discharge tube. All the measurements, including calibration were made with entrance and exit slit widths of 20 μm and a slit height of 8 mm. The slit height was limited by the size of the image of the discharge tube on the monochromator entrance slit. The slit width was the result of a compromise between the minimum value at which the weakest lines were detectable and the maximum value possible to maintain a symmetrical line shape within the limits of focussing of the monochromator.

The complete set of spectral line intensities was recorded at positions along the two discharge tubes corresponding to the positions of the probe pairs and at the cavity centre. Thus for both the probe discharge

tube and the plain discharge tube, measurements were made at distances of 0, 3 cm, 6 cm and 9 cm from the cavity centre. Each set of measurements was made at pressures of 1.0, 0.2, 0.5 and 0.7 in each decade from 1.0 mbar to 10^{-3} mbar and at pressures of 2.0, 3.0 and 6.0 mbar. As described in section 2.2.2, the upper pressure limit was a result of the behaviour of the pirani pressure gauge. For the probe discharge tube the above measurements were made for magnetron anode currents of 40mA, 50mA, 100mA, 150mA. For the plain tube, the full set of measurements was made at all pressures for a magnetron anode current of 100mA and at pressures of 6.0, 3.0, 0.2 and 0.02 mbar for currents of 40, 50, 150 and 200mA. A scanning speed of 0.5\AA min^{-1} was used throughout.

4.5.2 The Argon II Spectrum

Measurement of the lines of the argon II spectrum given in Table 4.2 were made at the cavity centre for pressures from 0.5 mbar to 0.02 mbar and all four values of magnetron current used for the probe tube measurements (see section 4.5.1). At pressures greater than 0.5 mbar, the low degree of ionisation prevented useful measurement of the argon II spectrum.

TABLE 4.2 Selected lines of the Argon II Spectrum

Wavelength (nm)	Upper array and multiplet	Lower array and multiplet
434.81	$3p^4(3P)4p^4D^0$	$3p^44s^4P$
437.97	$3p^4(3P)4p^4D^0$	$3p^44s^4P$
460.96	$3p^4(1D)4p^2F^0$	$3p^44s^2D$
472.69	$3p^4(3P)4p^2D^0$	$3p^44s^2P$
473.59	$3p^4(3P)4p^4P^0$	$3p^44s^4P$
480.60	$3p^4(3P)4p^4P^0$	$3p^44s^4P$
487.99	$3p^4(3P)4p^2D^0$	$3p^44s^2P$

CHAPTER 5

PROBE MEASUREMENTS

5.1 Theory

5.1.1 Introduction

It is not intended to provide here a detailed analysis of the theoretical treatment of double floating probe systems as this aspect is described by Schwar (1966) and Swift and Schwar (1970). A brief description of the principle of the floating probe system will, however, be useful.

The principle of double floating probe measurements consists of applying a d.c. voltage, V_d , between the two probes and measuring the current in the associated circuit as a function of that voltage. With the two probes biased with respect to each other but isolated from ground, the whole system 'floats' with the plasma and follows any change in plasma potential.

The potential distribution is shown in fig. 5.1. Since the electron velocities are much higher than the ion velocities and the ratio of the surface areas of the two probes is close to unity, both the probes must be slightly negative with respect to the plasma, for all values of V_d , to prevent a net electron current from flowing in the whole system.

The probe to plasma potential is varied by changing V_d , the probe to which the positive potential is applied moving closer to plasma potential. This results in an increase in electron current to this probe and a decrease in electron current to the second (more negative) probe. As V_d is increased a point is reached where the second probe has become so negative with respect to the plasma that no electrons can reach it.

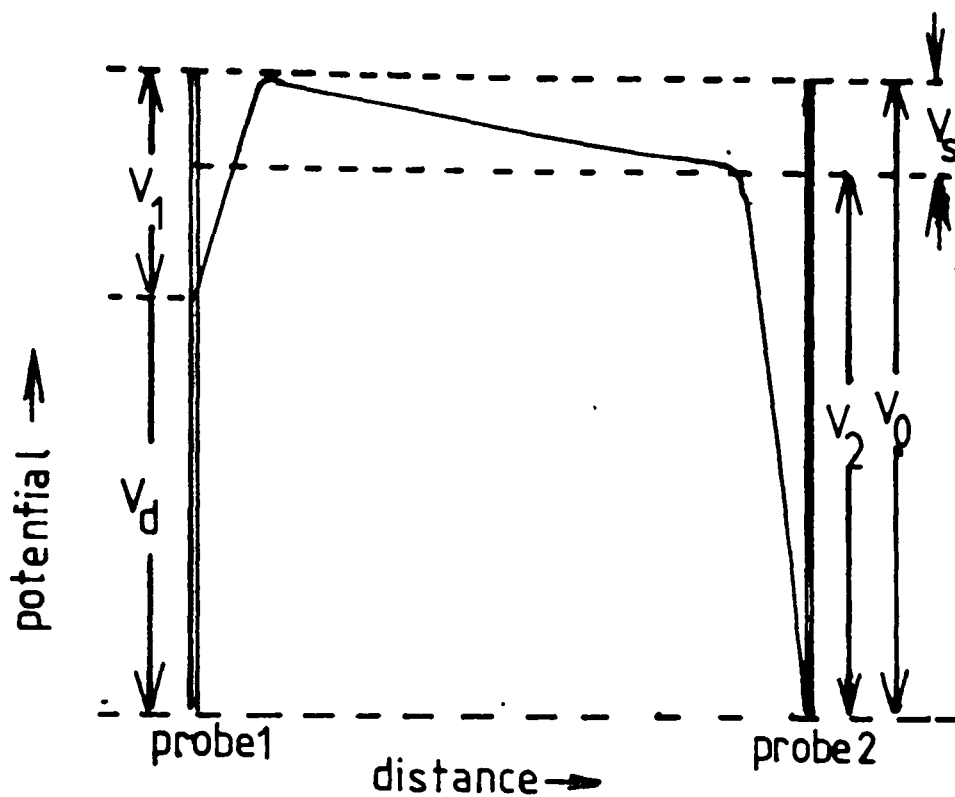


Figure 5.1 Potential distribution of a double floating probe system

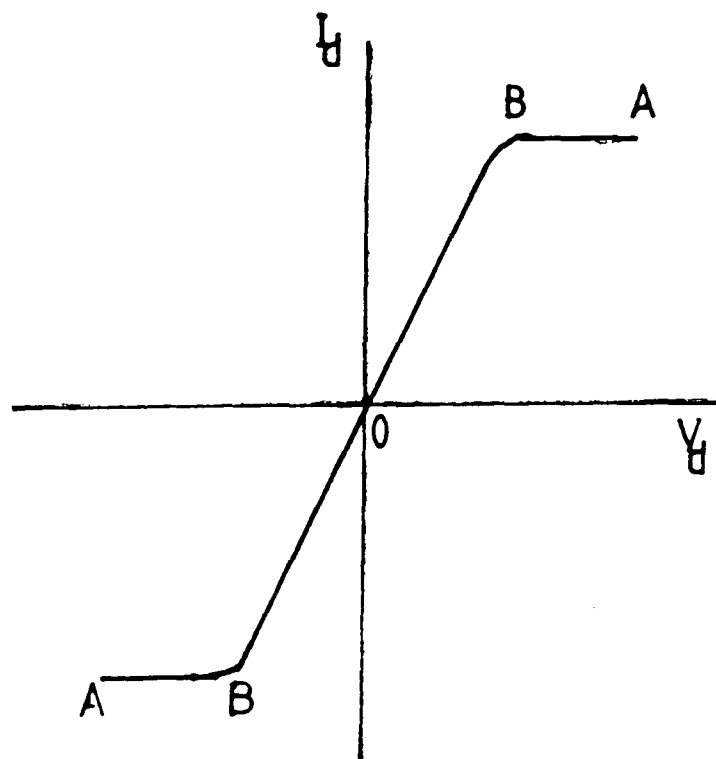


Figure 5.2 Ideal probe characteristic showing 'saturation' regions AB

In order to satisfy the floating conditions (no overall carrier drain from the plasma) in this case, it is necessary that the electron current i_{e1} to the first probe is equal to the sum of the ion currents i_{+1} , i_{+2} flowing to the first and second probes respectively, ie.

$$i_{e1} = i_{+1} + i_{+2} \quad 5.1$$

All the electrons are now repelled by the second probe and so, making V_d more positive cannot result in a further decrease of electron current to probe 2. Consequently, there can be no increase in electron current to probe 1 without violating the floating condition. Thus i_{e1} remains constant for all more positive values of V_d . This part of the double probe characteristic is known as the saturation region. Figure 5.2 shows an ideal characteristic in which the circuit current I_d reaches a constant value.

In practice, however, the positive ion sheath surrounding the more negative probe may increase in area with increasing negative probe potential. This results in an increase in i_{+2} and hence, from equation 5.1, a corresponding increase in i_{e1} , giving the characteristic a slope in the 'saturation' region (Fig. 5.3).

5.1.2 Formulation of Probe Equations

The analysis of the double floating probe system was first given by Johnson and Malter (1949, 1950). Let V_{p1} and V_{p2} be the probe to plasma potentials to the probes 1 and 2 respectively and let V_s be the difference in plasma potential in the neighbourhood of the two probes.

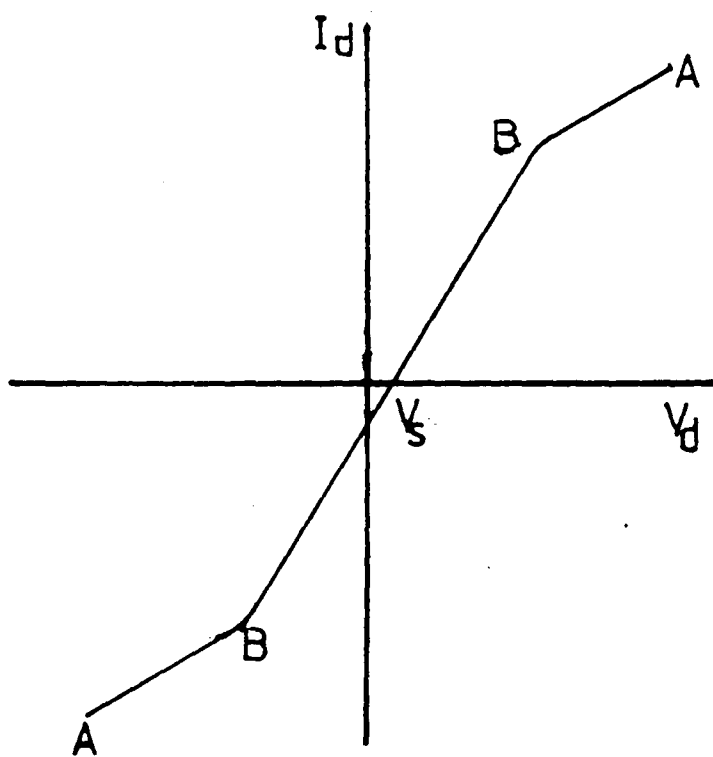


Figure 5.3 Practical probe characteristic showing slope in 'saturation' regions AB

The positive ion currents i_{+1} and i_{+2} are taken to be only slightly dependent on V_{p1} and V_{p2} . The electron current however varies exponentially with probe to plasma potential. The electron currents i_{e1} and i_{e2} being given by:-

$$i_{e1} = i_{e01} \exp\left(\frac{eV_{p1}}{kT_e}\right) \quad 5.2$$

$$i_{e2} = i_{e02} \exp\left(\frac{eV_{p2}}{kT_e}\right) \quad 5.3$$

where $V_{p1}, V_{p2} < 0$ and i_{e0} is the random electron current and T_e the electron temperature.

The floating conditions require that the equality

$$i_{+1} + i_{+2} = i_{e1} + i_{e2} \quad 5.4$$

holds, where the ion currents are taken to be independent of V_p .

Substituting equations 5.2 and 5.3 into equation 5.4 gives

$$\sum i_+ = i_{e01} \exp\left(\frac{eV_{p1}}{kT_e}\right) + i_{e02} \exp\left(\frac{eV_{p2}}{kT_e}\right) \quad 5.5$$

From fig. 5.1 it can be seen that

$$V_{p2} = V_{p1} + V_d - V_s \quad 5.6$$

Hence, substituting equation 5.6 into equation 5.5 and dividing by i_{e1} gives

$$\frac{\sum i_+}{i_{e1}} - 1 = \frac{i_{e02}}{i_{e01}} \exp\left[\frac{e}{kT_e} (V_d - V_s)\right] \quad 5.7$$

or writing $i_{eo} = Aj_{eo}$ where A is the surface area of the probe

$$\frac{\sum i_{+}}{i_{e1}} - 1 = \frac{j_{eo2}A_2}{j_{eo1}A_1} \exp\left[\frac{e}{kT_e} (V_d - V_s)\right] \quad 5.8$$

For practical cases, the assumption that the positive ion currents are independent of the probe to plasma potentials is not valid. For characteristics such as those shown in fig. 5.3, where the saturation region has a slope, it is found that in these saturation regions i_{+1} and i_{+2} vary approximately linearly with V_d . Outside the saturation regions Schwar (1966) gives a relationship between V_p and V_d of

$$\frac{V_p}{V_d} = 0.85$$

(providing that the characteristic is symmetrical) and assumes a linear relationship of V_p with i_+ . Thus, outside the saturation regions the dependence of i_+ on V_d can be assumed to be linear but the rate of change of i_+ with V_d will not be equal to the slope of the saturation region.

In all cases, the ion current to a probe is given by

$$i_+ = C n_+ A \left(\frac{kT_e}{M_+} \right)^{\frac{1}{2}} \quad 5.9$$

where C is some constant, n_+ the ion number density and M_+ the ionic mass. Equation 5.9 is strictly applicable to a spherical probe but by varying the value of C successive authors have used equation 5.9 to approximate the ion current in the case of cylindrical probes.

The considerations and approximations associated with the use of the

equations presented in this section will be given in section 5.2, together with a comparison of the methods available for interpretation of the probe characteristic.

5.2 Interpretation of Probe Characteristics

5.2.1 Determination of Electron Temperature, T_e

Measurement of the electron temperature, that is the value of temperature T_e which describes the electron energy distribution function, is the purpose for which double floating probes are most commonly used. A variety of equations are available, some applying only under certain physical conditions whilst others apply, with some degree of approximation to all plasma conditions.

The equations or methods for determining T_e from the probe characteristics can be divided into two basic types: "logarithmic plot" and "equivalent resistance" methods.

Consider equation 5.8; taking the natural logarithm of both sides gives

$$\ln\left(\frac{\sum i_+}{i_{e1}} - 1\right) = \frac{e V_d}{kT_e} + \ln\left(\frac{j_{e02} A_2}{j_{e01} A_1}\right) - \frac{eV_s}{kT_e} \quad 5.10$$

Thus, provided that V_s remains constant, the electron temperature can be deduced from a plot of the left hand side of equation 5.10 against V_d . This is known as the 'logarithmic plot' method. Although laborious, it has the advantage of giving better protection against gross error than the 'equivalent resistance' methods (Brassem & Maessen, 1974). The major problem is that of extrapolating the saturation regions

(where these have a slope greater than zero) into the areas where appreciable electron currents exist. According to Polman (1966), this problem can be overcome by using equation 5.4 and dividing by i_{e1} , from which

$$\frac{\sum i_+}{i_{e1}} - 1 = \frac{i_{e2}}{i_{e1}}$$

since $i_{+1} + i_{+2} = (i_{e1} + i_{e2})$. Thus the left hand side of equation 5.10 is written in terms of (i_{e2}/i_{e1}) . Polman claims that this arrangement is less sensitive to the method of extrapolation as both i_{e1} and i_{e2} change in the same direction and at the same rate regardless of the method of extrapolation.

The "equivalent resistance" method equations are of two varieties: those applicable to ideal probe characteristics (fig. 5.2) and those applicable to characteristics represented by fig. 5.3. Equation 5.8 may be written as

$$\frac{\sum i_+}{i_{e1}} - 1 = \sigma \exp\left(\frac{eV_d}{kT_e}\right) \quad 5.11$$

where

$$\sigma = \frac{j_{oe2}A_2}{j_{eol}A_1} \exp\left(-\frac{eV_s}{kT_e}\right) \quad 5.12$$

Solving equation 5.11 for i_{e1} gives

$$i_{e1} = \sum i_+ \left[\sigma \exp\left(\frac{eV_d}{kT_e}\right) + 1 \right]^{-1} \quad 5.13$$

The current I_d flowing in the external probe circuit is given by

$$I_d = i_{e1} - i_{+1} = i_{+2} - i_{e2} \quad 5.14$$

so differentiating equation 5.14 with respect to V_d gives

$$\frac{d}{dV_d} I_d = \frac{di_{e1}}{dV_d} \quad 5.15$$

(assuming that i_+ is independent of V_d). Differentiating equation 5.13 with respect to V_d and substituting into equation 5.15 at $V_d = 0$ gives

$$\left. \frac{dI_d}{dV_d} \right|_{V_d=0} = \sum i_+ \frac{e}{kT_e} \cdot \frac{\sigma}{(\sigma+1)^2} \quad 5.16$$

From equation 5.13 it is seen that when $V_d = 0$, σ is given by

$$\sigma = \left(\frac{\sum i_+}{i_{e1}} - 1 \right)_{V_d=0} = \frac{1}{G} - 1 \quad 5.17$$

where $G = (i_{e1} / \sum i_+)_{V_d=0}$ and may be measured directly from the characteristic.

Thus from equation 5.16, the electron temperature is given by (Johnson & Malter 1950) :-

$$T_e = (G - G^2) \frac{e}{k} R_0 \sum i_+ \quad 5.18$$

where $R_0 = (dI_d/dV_d)^{-1}$ at $V_d=0$ has the dimensions of resistance and is called the "equivalent resistance".

Again, the derivation assumes that i_+ is independent of V_d and the problem of extrapolation of i_+ beyond the saturation region applies, unless $V_d = 0$ occurs in the saturation region in which case equation 5.18 is invalid anyway.

In the case of characteristics typified by fig. 5.3, the following

equations have been derived for electron temperature:-

$$(a) \quad T_e = \frac{e}{4k} \left(\sum i_+ - 0.85S\Delta V_d \right) \frac{1}{(1/R_1 - S/2)} \quad 5.19$$

(Burrows 1962) where S is the mean slope of the saturation regions and $R_1 = (dI_d/dV_d)^{-1}$ at $V_d=V_1$ where V_1 is the value of V_d at the point of inflection of the characteristic and ΔV_d is the potential difference between the two points on the characteristic where deviation from the linear saturation region begins.

$$(b) \quad T_e = \frac{e}{k} \left[\frac{\sum i_+ - 0.85 (S_1\Delta V_{d1} + S_2\Delta V_{d2})}{4/R_1 - (S_1 + S_2)} \right] \quad 5.20$$

(Polman 1966) where S_1, S_2 have similar meanings as in (a) but refer to probes 1 and 2 specifically and similarly for ΔV_{d1} and ΔV_{d2} .

As can be seen equations 5.19 and 5.20 are very similar except that the latter does not include the mean value of S_1 and S_2 and differs slightly in the form of the denominator.

Again, the problem of extrapolating the slope of the saturation region to the inflection point of the characteristic is present, as are errors due to difficulties in determining the point of inflection in the characteristic.

Before deciding which of equations 5.10, 5.18, 5.19 and 5.20 would be used, a comparative study was performed between equation 5.10 ("logarithmic plot") and the remaining "equivalent resistance" methods. Fig. 5.4 shows a comparison of T_e values calculated from equation 5.10 and either equation 5.18 or 5.19. (The differences in values of T_e yielded by equation 5.19 or equation 5.20 were not significant, falling well within the error of the calculation). The graph shows that values of the electron temperature calculated from the two methods are

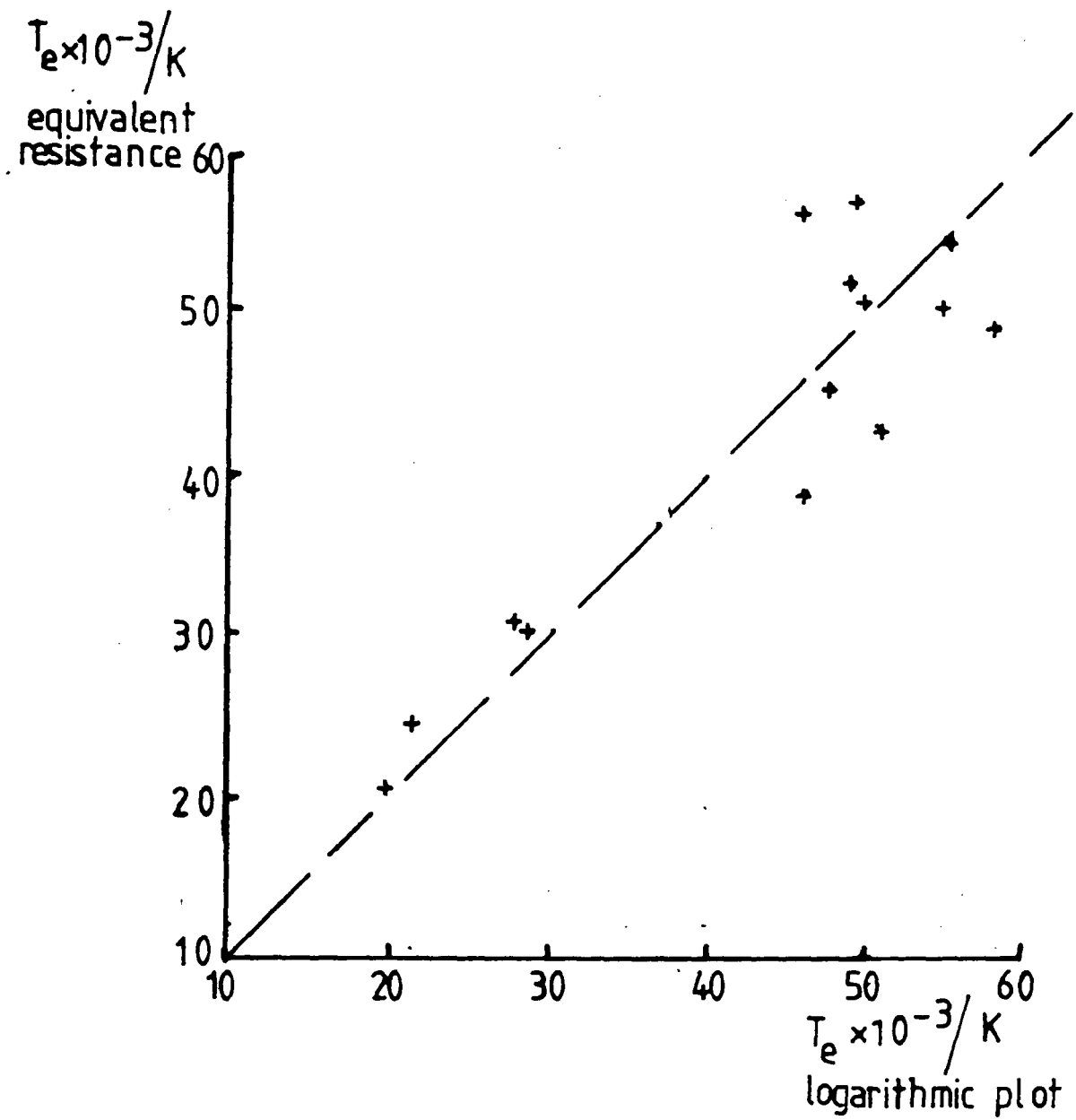


Figure 5.4 Comparison of electron temperature calculated by "equivalent resistance" and "logarithmic plot" methods.

reasonably evenly scattered about a ratio of unity, although the values calculated from equation 5.18 (lower T_e values) are all higher than their counterparts calculated from equation 5.10. In addition the values calculated from 5.18 did not merge smoothly with those T_e values calculated from equation 5.19 when the former ceased to be applicable. Consequently it was decided to adopt the logarithmic plot method, viz. equation 5.10, as this provided continuity in the analysis of the characteristics for all gas pressures.

5.2.2 Determination of the Carrier Density

The most commonly used method for determining carrier density uses equation 5.9 with some variations in the value of C. Values of C range from 0.6 (Busch & Vickers 1973), 0.5 (Brassem & Maessen 1974) to 0.29 (Kagan & Perel 1964). Equation 5.9, in fact, yields the ion density n_+ whereas the parameter of interest is usually the electron density, n_e . Consequently some assumption concerning the relative values of these two quantities must be made.

Most authors assume electrical neutrality of the plasma, although Avni & Winefordner (1975) argue that due to the longer mean free path length of electrons and their greater drift velocity than ions, more collisions between the wall of the discharge vessel and electrons will occur than between the wall and ions. They assume a relationship

$$n_e (v_e)_{\text{drift}} \approx 2n_+ (v_+)_{\text{drift}}$$

Polman (1966) adopts a method due to Hall & Freis (1965). The solution to the Poisson equation yields an asymptotic behaviour of the ion current density at the probe surface as a function of the potential

difference between the probe and the unperturbed plasma, which is described by:-

$$j^2 = j_o^2 + S_H V_1 \quad 5.21$$

where
$$S_H = \frac{0.2e^3 n_+^2}{M_+}$$

It is possible under certain conditions to make the approximation $V_1 = V_d$ and hence the ion density can be calculated from the gradient of a plot of the square of the current density against V_d . However, the problem of electrical neutrality, or otherwise, of the plasma remains.

A comparison of carrier density calculated from equations 5.9 and 5.20 and 5.21 is shown in fig. 5.5. Values from equation 5.21 are generally a factor of 10 lower than those from equation 5.9. This is probably due to approximations made in equating V_1 with V_d . Consequently equation 5.9 was used, with a value of $C = 0.3$, to calculate n_+ from the probe characteristics.

5.3 Acquisition of Probe Data

The voltage and current data for the probe characteristics were acquired automatically under the control of a PDP-11 microcomputer and the program PROBE in appendix 3.

The programme requests data from the two digital panel meters twice per second and allows five cycles of the voltage ramp (25s in duration) for each probe pair. Thus, the characteristic from each pair of probes is comprised of some 250 individual data points.

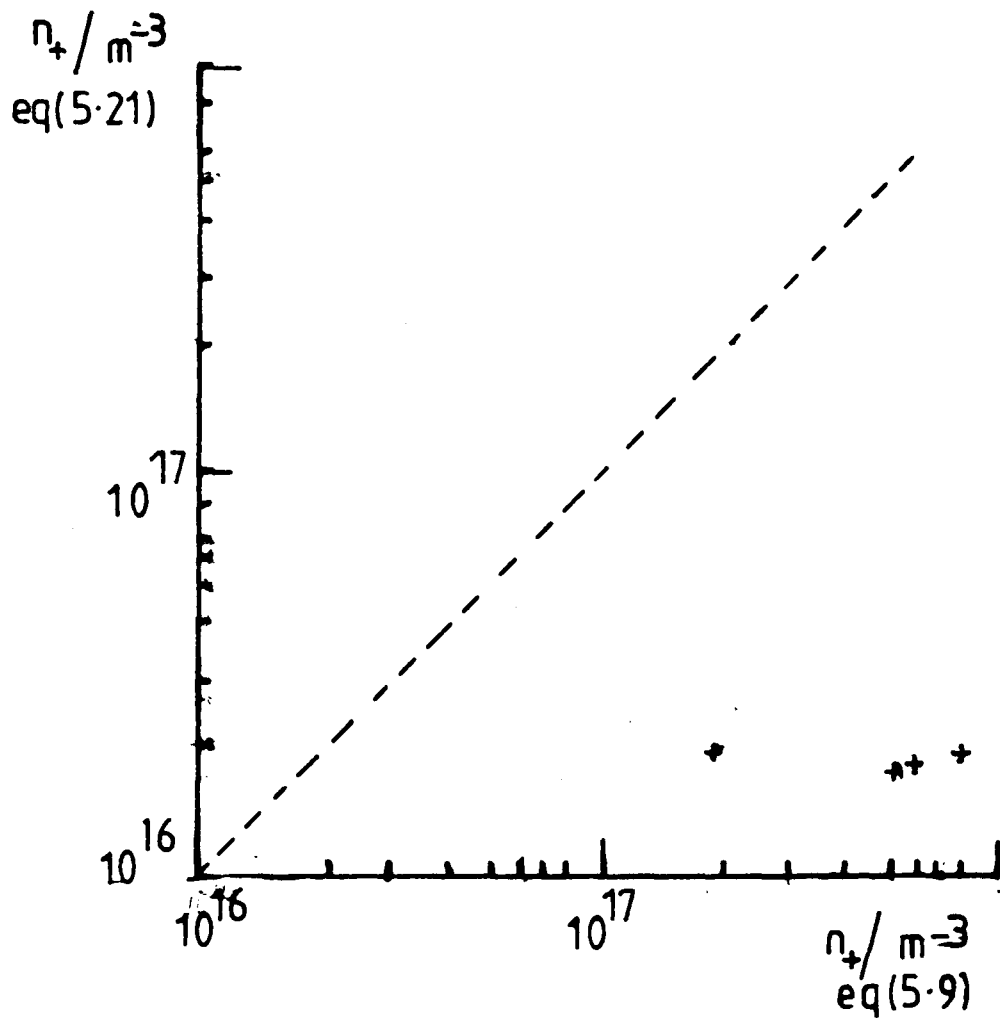


Figure 5.5 Comparison of ion densities calculated from equations 5.9 and 5.21

The data is permanently stored on magnetic tape, but can be transferred to flexible disc for further processing. The characteristics are plotted automatically from disc on a Hewlett Packard HP plotter under control of a PDP-11 processor.

CHAPTER 6
SPECTROSCOPIC RESULT

6.1 Calculation of Population Density

The population densities of the levels of the argon atom were calculated from the measured intensities using the computer programme SDATA3 in Appendix I. The programme effectively converts the measured intensity into a voltage, using the sensitivity of the lock-in amplifier as the converting factor. Calibration curves for the optical system were determined from the programme CAL also in Appendix I, the temperature conversion of equation 4.2 being included in the calculation. A typical calibration curve of the ratio of the calculated Planck intensity to the measured intensity against the wavelength is shown in fig. 4.4. For each set of calibration data the calibration curve was plotted prior to using the data with the argon I spectral intensities, to ensure that any anomalous points were eliminated before the argon population densities were calculated.

The intensity of a given spectral emission line may be measured in two ways, either the peak height of the line may be taken to indicate the intensity or the area under the line may be measured. Clearly, for extremely broadened lines, the latter should be chosen. Although the measured lines of the argon I spectrum were not considerably broadened, it was noted that lines originating from the higher levels (ie. those of greater energy than the 7s level) were considerably broader than those lines originating from the lower levels. For this reason it was decided to use the area under the spectral line as a measure of the intensity. The effects on the calculation of the population densities of using each of the two alternatives as indicative

of the intensity was investigated for the plain tube and the results are shown in fig. 6.1 (a) and (b). The population densities calculated from the line areas were, on average greater by a factor of three, the increase being more pronounced for the higher lying levels as expected.

6.2 Boltzmann Plots for the Argon I System

The Boltzmann equation for the population number density N_j of a given atomic level j , having energy E_j above the ground state is

$$N_j = \frac{Ng_j}{Z(T)} \exp\left(\frac{-E_j}{kT}\right) \quad 6.1$$

where $Z(T)$ is the partition function. From equation 4.1 which relates N_j to the measured intensity of a spectral line originating from level j , it is clear that

$$\ln\left(\frac{I\lambda}{g_j A}\right) = \text{constant} - \frac{E_j}{kT} \quad 6.2$$

For sources in local thermodynamic equilibrium (LTE), where the population densities of the levels are determined by the Boltzmann-Saha equations, a graphical plot of $\ln(I\lambda/gA)$ against E_j is linear with a gradient of $(-kT)^{-1}$ where T in this case is equivalent to the electron temperature and the ion temperature ie. for LTE

$$T_e = T_{\text{ion}} = T \quad 6.3$$

For sources which are not in LTE, the plot of $\ln(I\lambda/gA)$ against E_j is not linear and has no single value of gradient; in this case

$$T_e \neq T_{\text{ion}} \quad 6.4$$

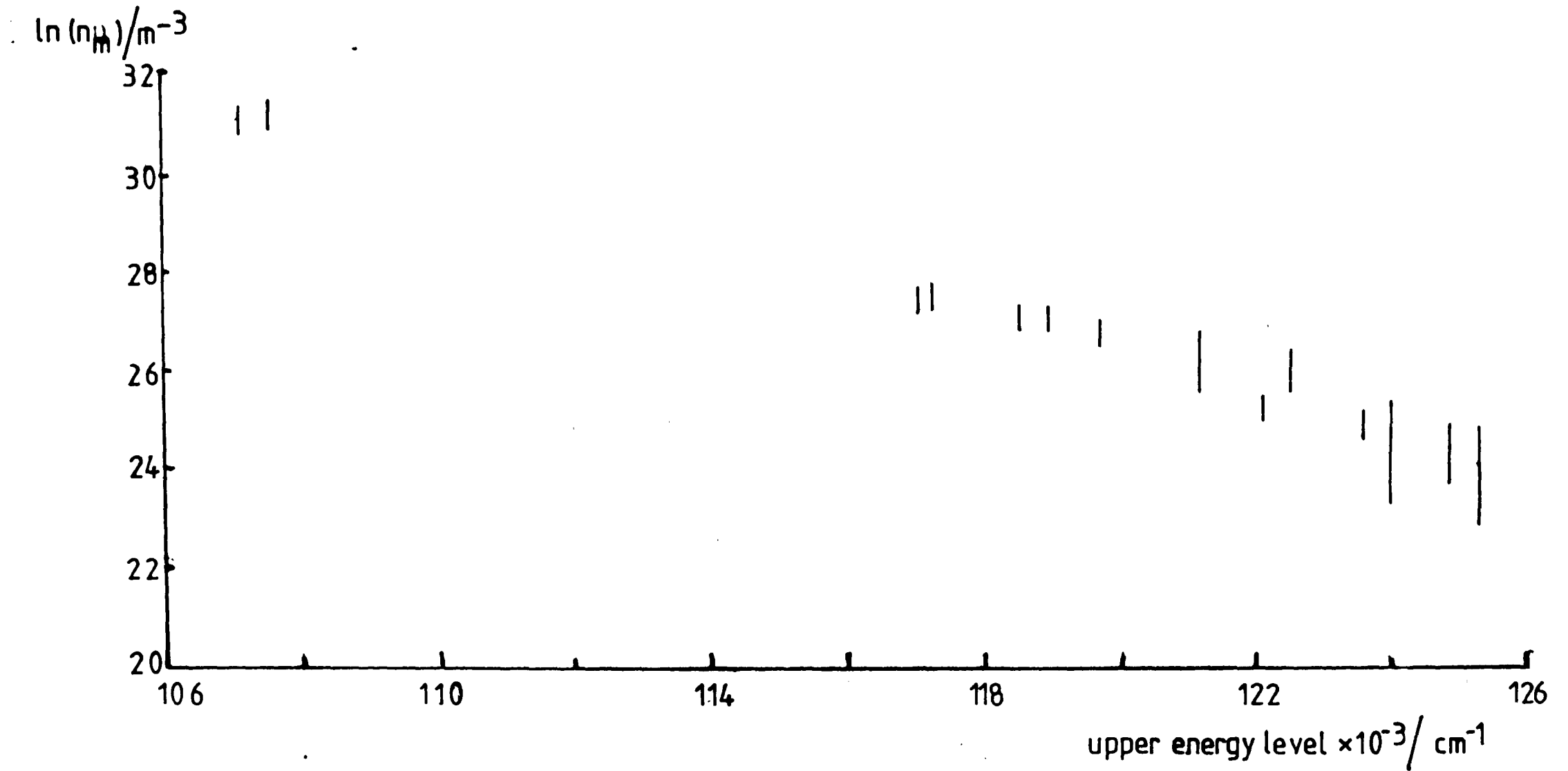


Figure 6.1a Population densities calculated from peak areas. $n_m = \frac{I\lambda}{g_m A}$

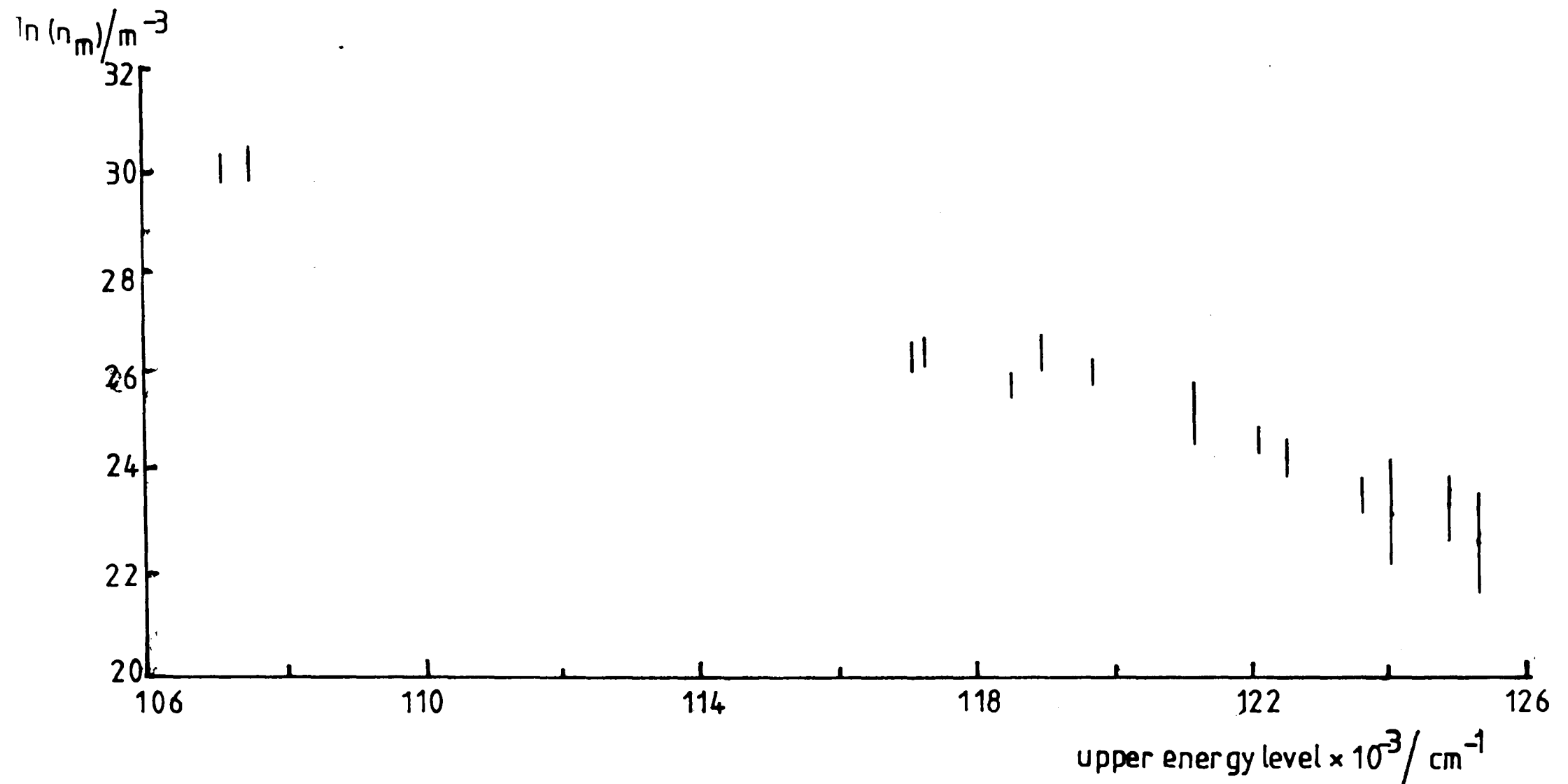


Figure 6.1b Population densities calculated from peak heights. $n_m = \frac{I\lambda}{g_m A}$

Boltzmann plots were made for the argon I system for all examined values of pressure and magnetron current as described in section 4.5.1. The argon I system was found to deviate from both LTE and partial local thermodynamic equilibrium at all combinations of pressure and magnetron current. A typical Boltzmann plot for the argon I system is shown in fig. 6.2.

A more detailed examination of the Boltzmann plots revealed that, for all magnetron currents, at pressures of 3 mbar and 6 mbar the curve was ~~straightened~~ at the highest levels of the argon system, indicating that these levels were falling into some form of equilibrium (fig. 6.3), presumably with the argon ion levels. Unfortunately, the argon II spectrum was too weak to be measured at these pressures. In addition, there is a general lowering of the population densities of all levels of the argon atom at these pressures indicating an increase in the importance of collisional de-excitation at these pressures.

6.3 Comparison of Plain and Probe Tubes

As described in section 4.5.1 in order to evaluate the effect of the probes on the spectroscopic features of the plasma, spectroscopic measurements were made using a plain tube for pressures of 6.0, 3.0, 0.2 and 0.02 mbar with magnetron currents of 50, 100, 150 and 200 mA. together with a set of results for all pressures at a magnetron current of 100 mA.

The most obvious difference in behaviour of the plasma in the two tubes was the length of the discharge in the tube. Earlier work, using the

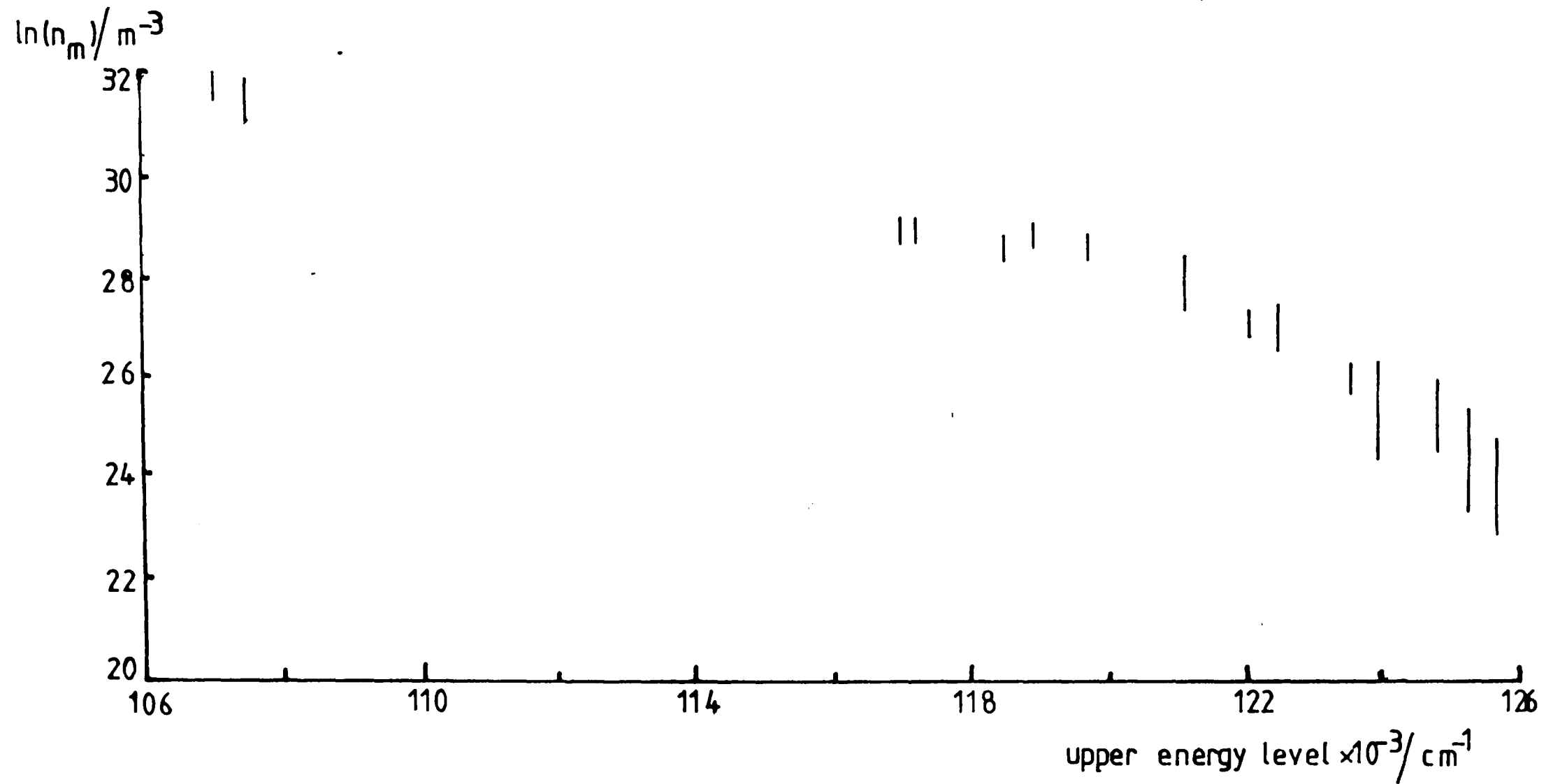


Figure 6.2 Typical Boltzmann plot for the argon I system. Pressure 0.20mbar, magnetron current 50mA. $n_m = \frac{I\lambda}{g_m A}$

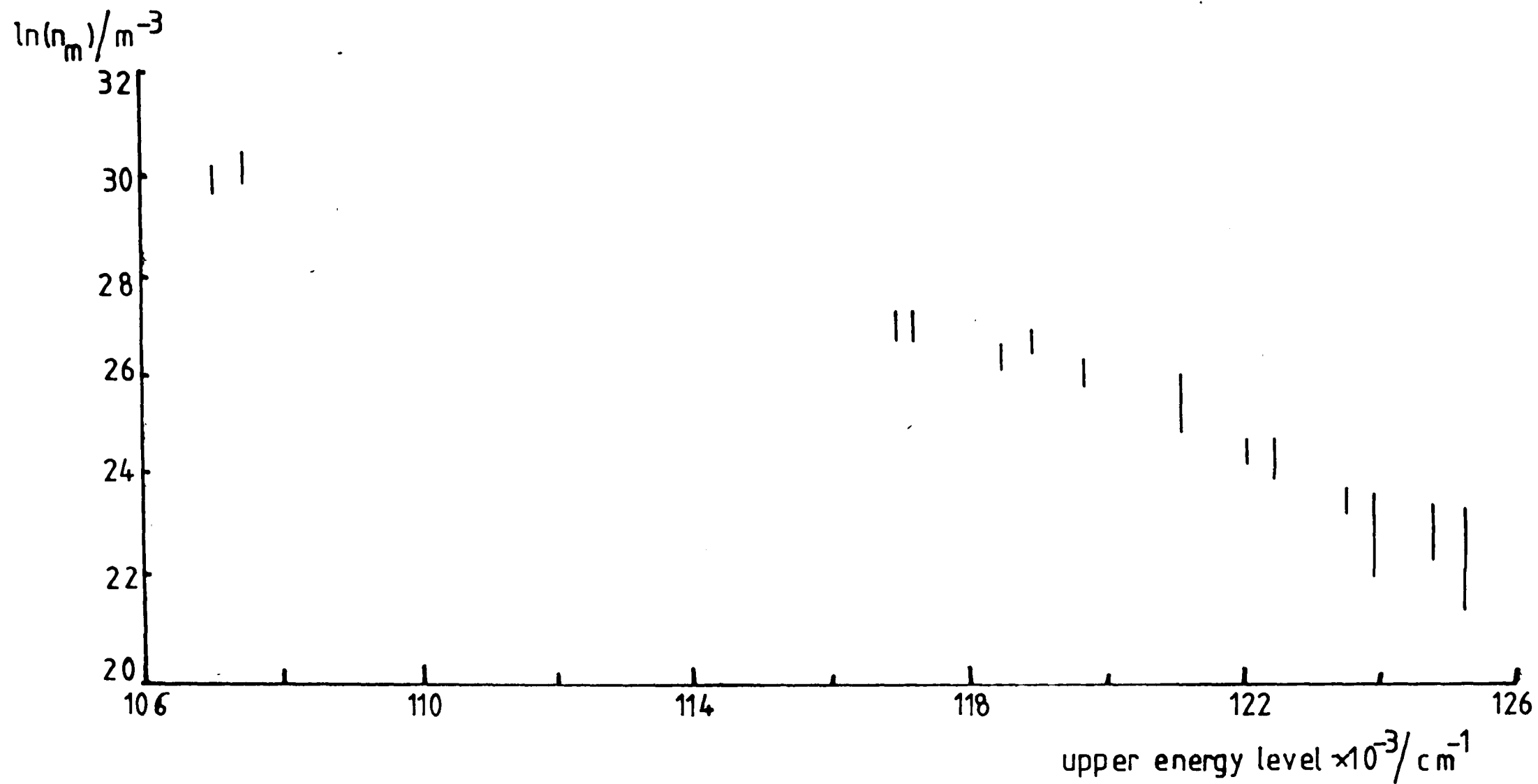


Figure 6.3 Boltzmann plot showing flattening of curve for the higher atomic levels.

Pressure 6.00mbar, magnetron current 50mA. $n_m = \frac{I\lambda}{g_m A}$

plain tube, had indicated that at pressures of 0.2 mbar at the higher magnetron currents, the discharge might be expected to fill the entire length of the tube (approximately 50 cm). For lower magnetron currents and/or greater or lower pressures, the length of the discharge was reduced. When the probe tube was substituted this behaviour was not repeated. Indeed, the positioning of the probe pairs had been determined on the basis of the behaviour in the plain tube. It was found that only for the combination of 2 mbar pressure and 150 mA magnetron current could the probes furthest from the cavity be reached by the plasma. The length of the discharge in the probe tube was severely constricted, never extending to more than approximately 20 cm in length. Furthermore, the greatest length was reached for the higher pressures (3.0 and 2.0 mbar).

A second problem, which restricted the assimilation of data from outside the cavity, was the sputtering of the probes. After some time of operating the discharge at lower pressures (below 0.7 mbar) and at the higher magnetron currents the surface of the discharge tube around the two pairs of probes closest to the cavity eventually became covered with a sputtered layer of molybdenum, thus obscuring the plasma from the optical system. For this reason no spectral measurements could be made at this position and eventually the probes at these positions had to be disconnected from the circuit. Spectral emission lines from either the first or second molybdenum spectrum were not observed, thereby indicating that the sputtering process was not contributing to contamination of the discharge.

Data from measurements taken at the cavity centre showed that the population densities of the argon atomic levels were greater by a factor of approximately two in the probe tube as compared with the plain tube.

6.4 Variation of Population Density with Distance from the Cavity

As a consequence of the problems discussed in section 6.3 which occurred in the probe tube, a full comparison of plasma conditions along the length of the discharge can only be made for the plain tube. The variation of population density for the 4p, 6s and 7s levels with distance from the cavity centre is shown in fig. 6.4. The data is taken from the results of measurements made with 3.0 mbar pressure and 100 mA magnetron current, although the results are similar for all combinations of pressure and magnetron current.

As would be expected, the population densities are greatest within the cavity being reduced by a factor of approximately three immediately outside the cavity. The values of population density remain constant from 3 cm to 8 cm outside the cavity and show only a slight drop at greater distances.

6.5 Variation of Population Density with Power

The complex behaviour of the intensity of a given spectral line with microwave power was noted by Hammond (1978). The major problem in interpretation of the measured plasma parameters is the non-independence of the variables pressure and net microwave input power. It became obvious, when the microwave input power results were considered, that an increased magnetron current did not necessarily result in an

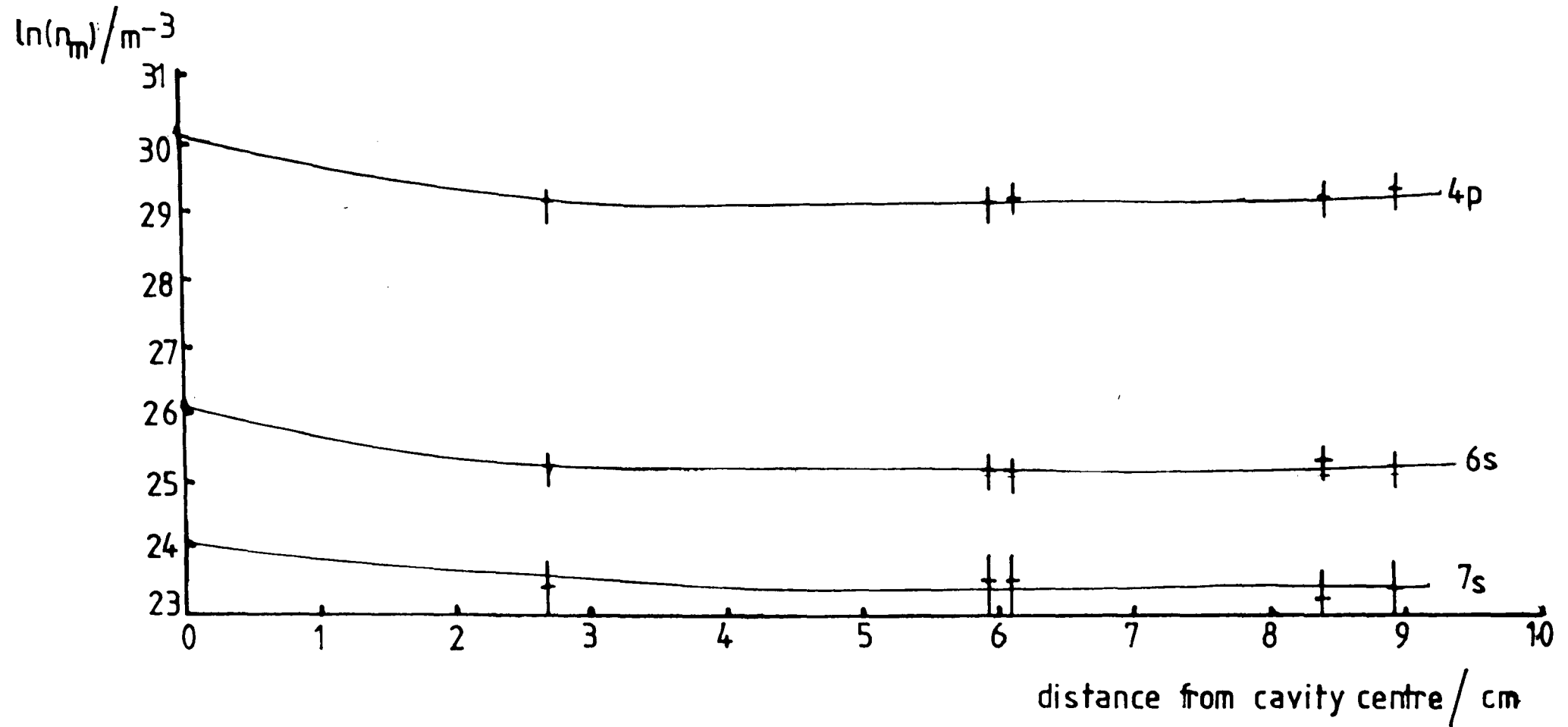


Figure 6.4 Variation of population density with distance from cavity centre $n_m = \frac{I\lambda}{g_m A}$

increase in the microwave power input to the plasma.

To eliminate this inter-dependence of pressure and net input power, values of the population densities of the argon levels were plotted as a function of the input power for each pressure. This generated a set of curves from which the population density could be obtained for a given net input power. Figure 6.5 (a) shows such a diagram for the 4p level. (The data was taken from measurements on the probe tube at the cavity centre). It can be seen that there is a considerable difference between the measured population densities at pressures of 3.0 and 6.0 mbar and those measured at other pressures.

Examination of similar diagrams for all the levels show that as the energy of the level above ground state increases, the difference between the densities measured at pressures 6.0 and 3.0 mbar and other pressures at first increases (see fig. 6.5 (b) for 6s') but for levels above the 7s level this difference becomes approximately constant (fig. 6.5 (c) for 8s).

The ratio of the population densities at different pressures for several levels are presented in table 6.1. The population densities are normalised for a net input power of 25W. Here the ratio with respect to 2.0 mbar pressure is included as figures 6.5 (b) and (c) reveal that for levels above the 4p and 4p' groups, the population densities are lowered for pressures of 2.0 mbar. From the diagrams it can be seen that as the energy of the level increases, the individual pressure curves separate further. That is to say that the spectroscopically measured population densities are more sensitive to

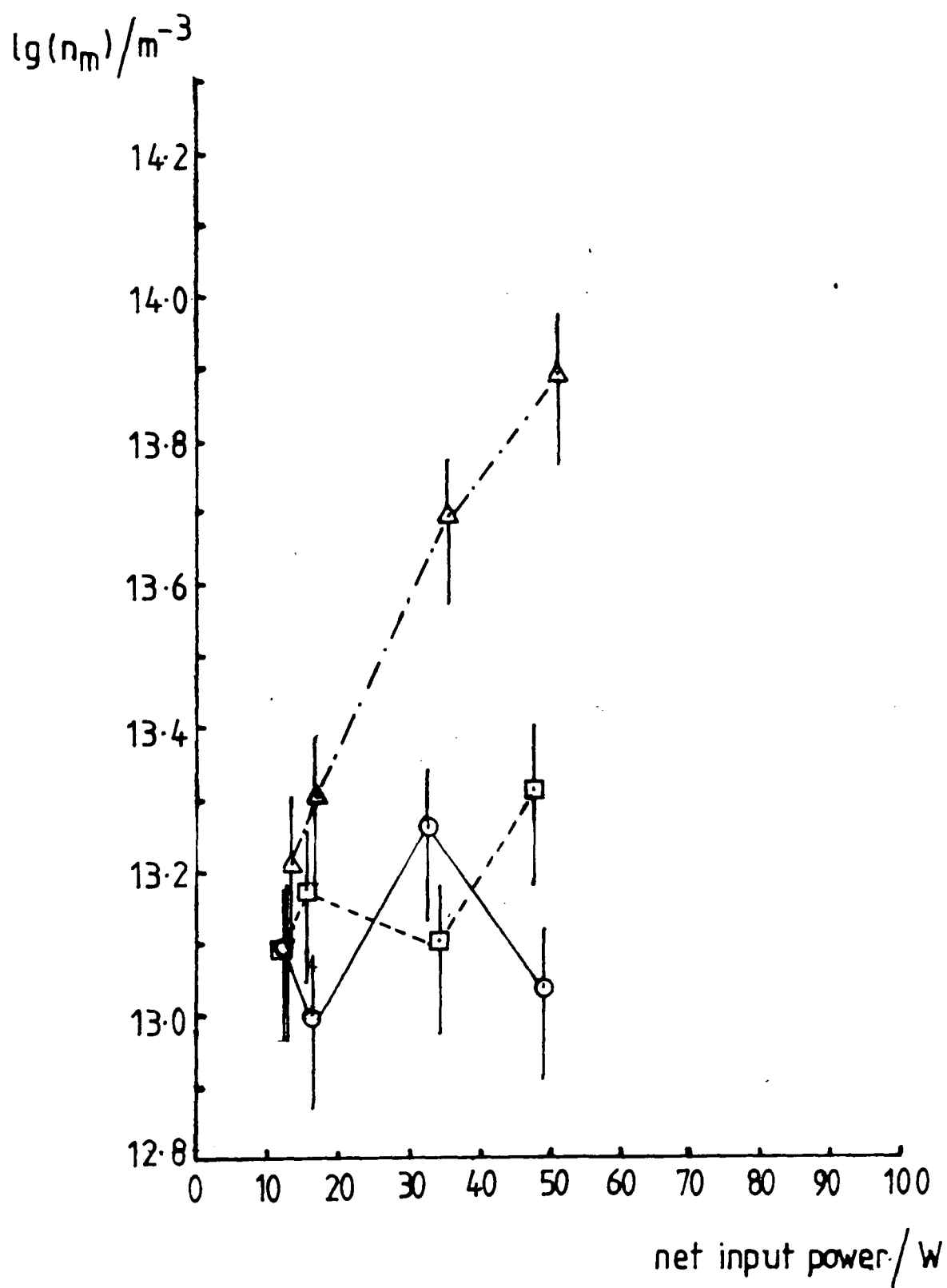


Figure 6.5a(i) Population density of 4p level as a function of input power. Pressures in mbar: O 6.00, □ 3.00, Δ 2.00. $n_m = \frac{I\lambda}{8\pi A}$

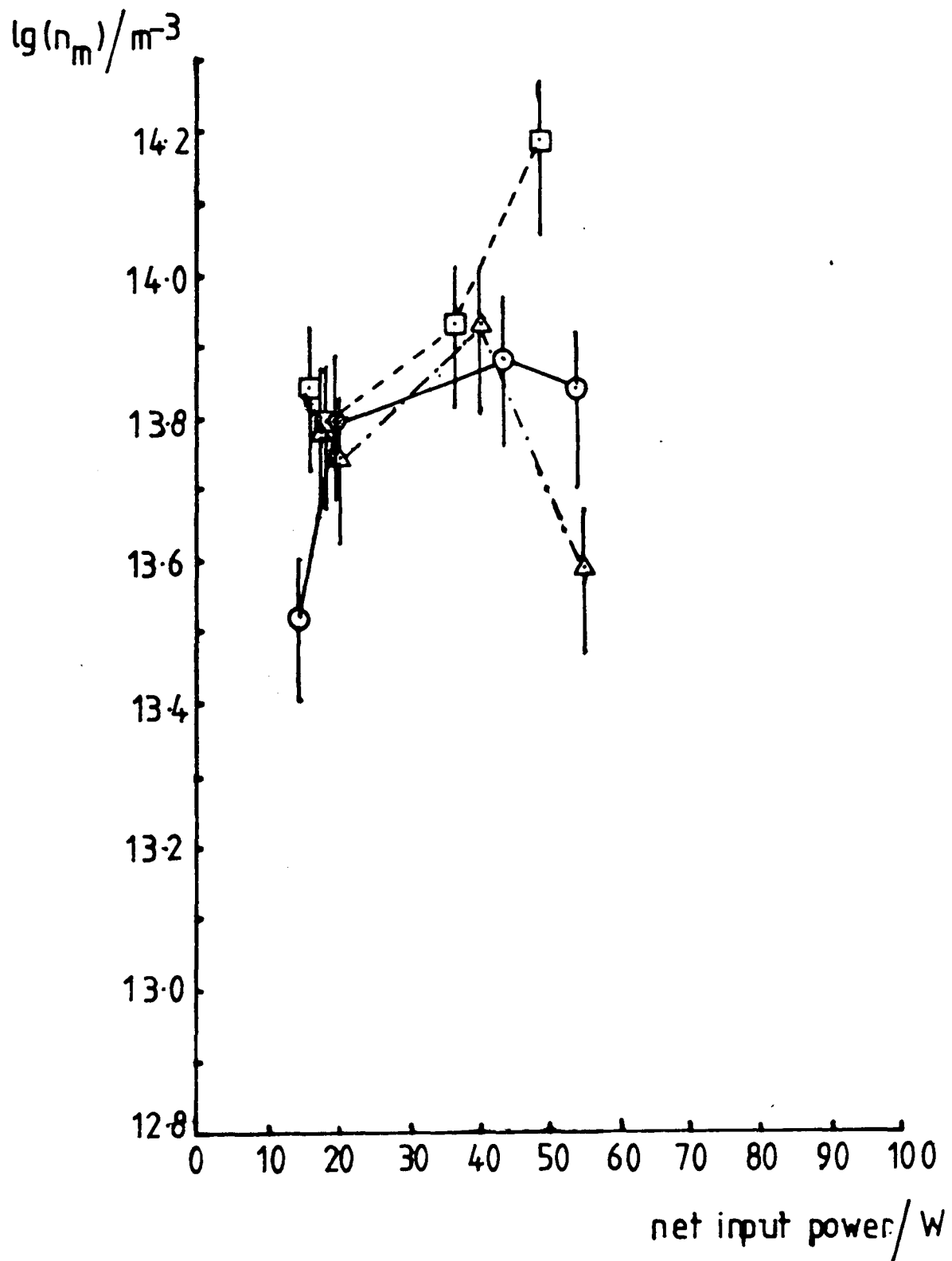


Figure 6.5a(ii) Population density of 4p level as a function of input power. Pressures in mbar: \circ 1.00, \square 0.70, \triangle 0.50. $n_m = \frac{I\lambda}{g_m A}$

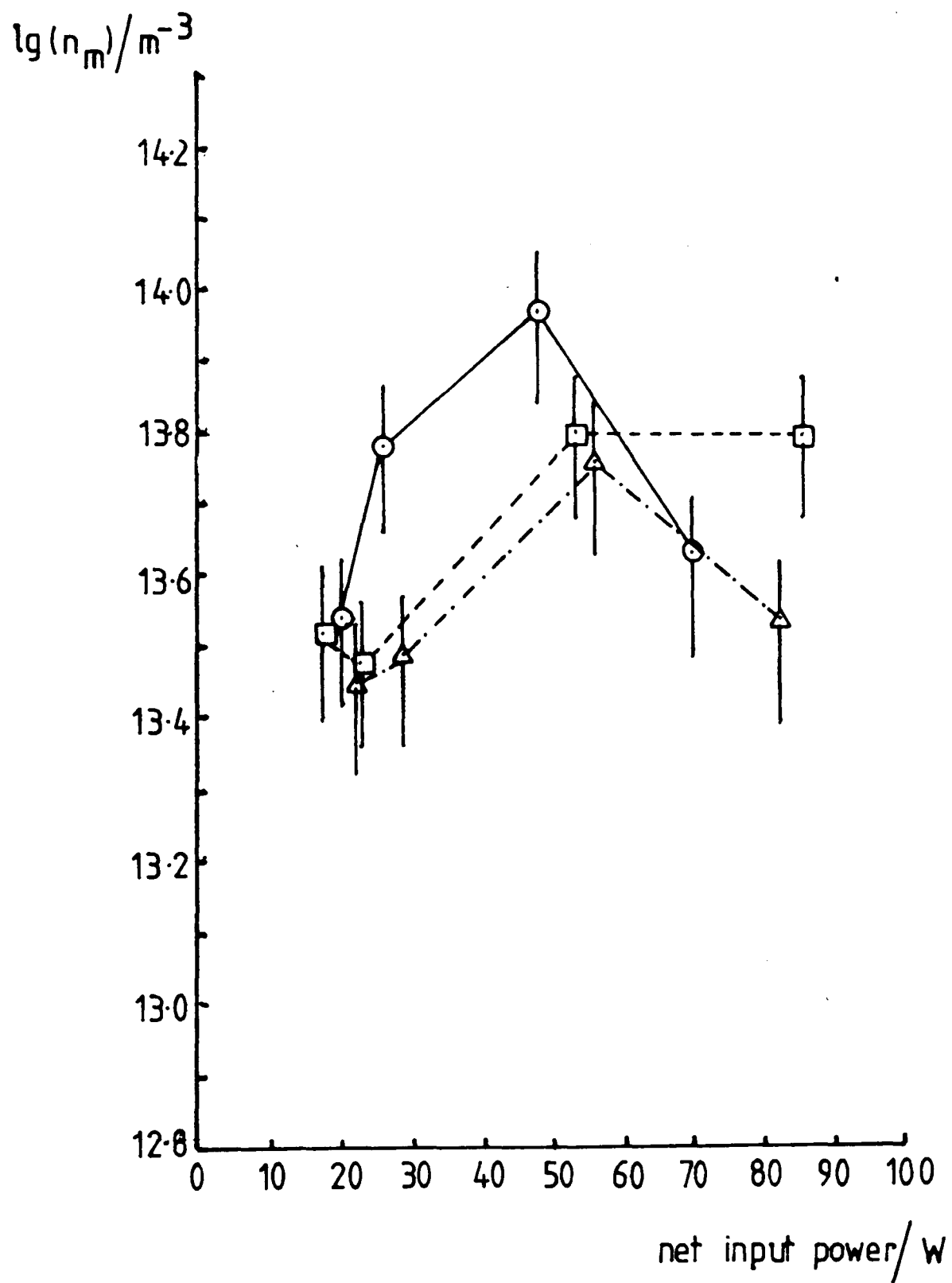


Figure 6.5a(iii) Population density of 4p level as a function of input power. Pressure in mbar: ○ 0.20, □ 0.10, △ 0.07. $n_m = \frac{I\lambda}{g_m A}$

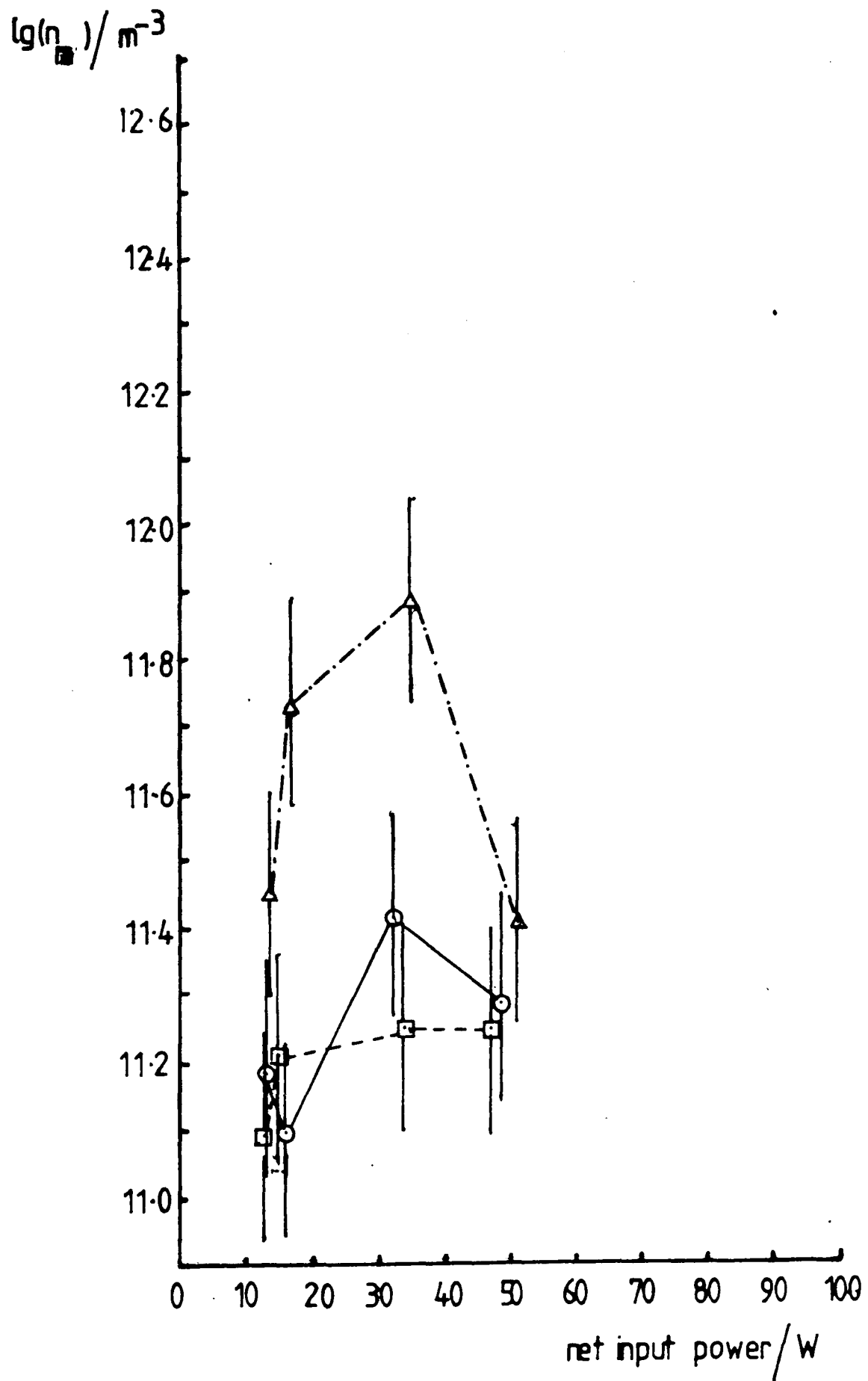


Figure 6.5b(i) Population density of 6s' level as a function of input power. Pressures in mbar: O 6.00, □ 3.00, Δ 2.00. $n_m = \frac{I\lambda}{g_m A}$

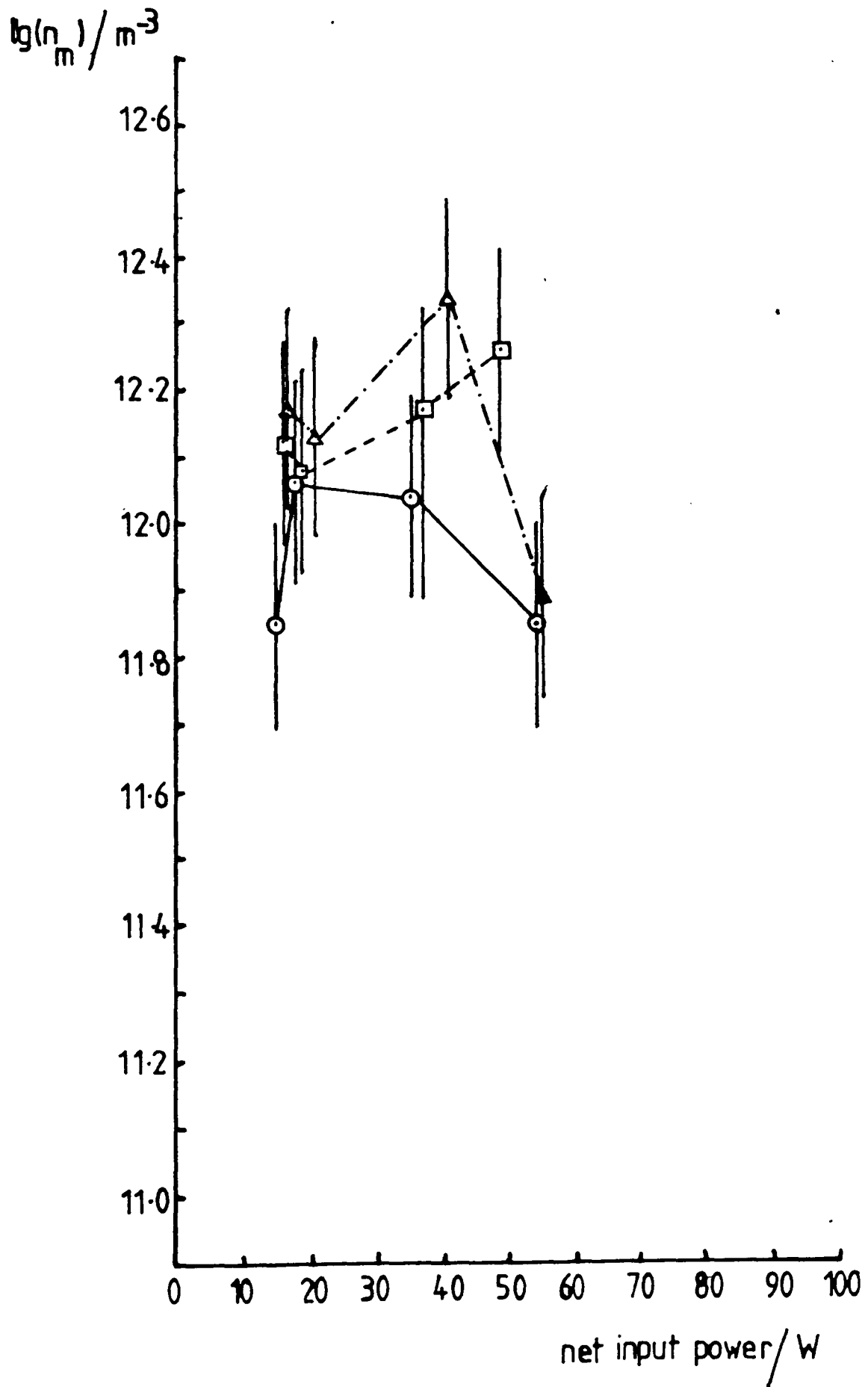


Figure 6.5b(ii) Population density of 6s' level as a function of input power. Pressures in mbar: O 1.00, □ 0.70, Δ 0.50. $n_m = \frac{I\lambda}{g_m A}$

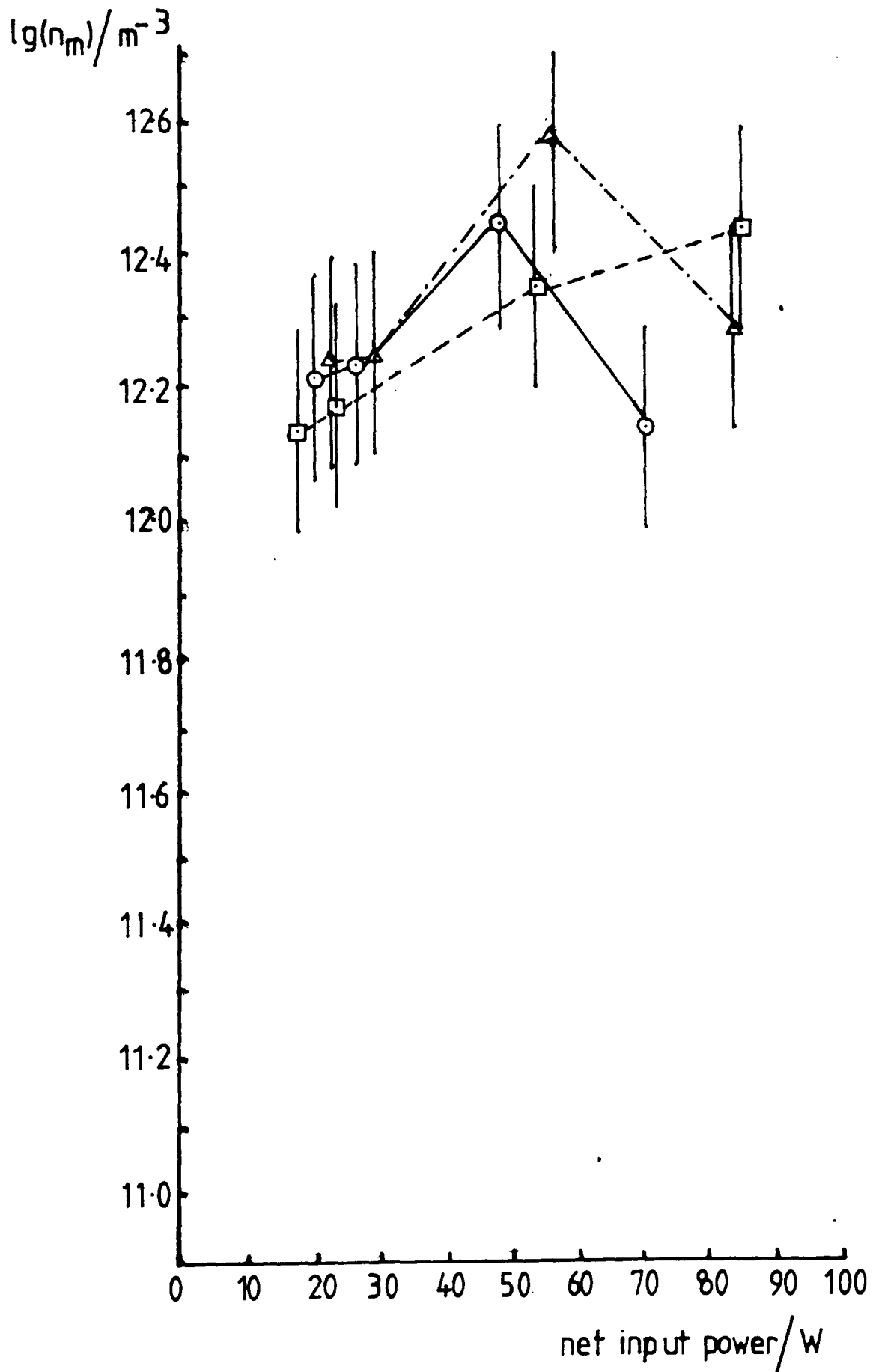


Figure 6.5b(iii) Population density of 6s' level as a function of input power. Pressures in mbar: ○ 0.20, □ 0.10, △ 0.07. $n_m = \frac{I \lambda}{g_m A}$

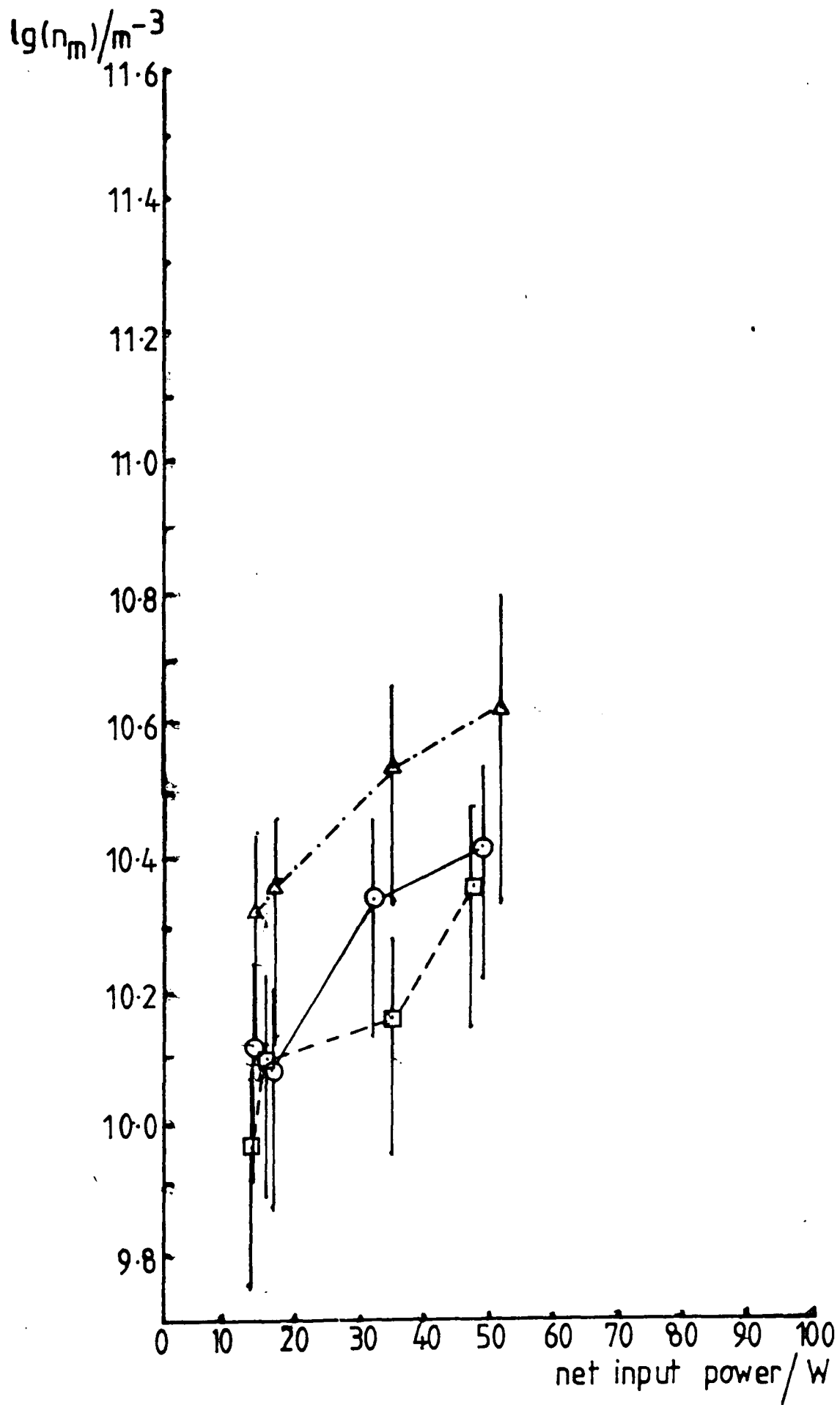


Figure 6.5c(i) Population density of 8s level as a function of input power. Pressures in mbar: \circ 6.00, \square 3.00, \triangle 2.00. $n_m = \frac{I\lambda}{g_m A}$

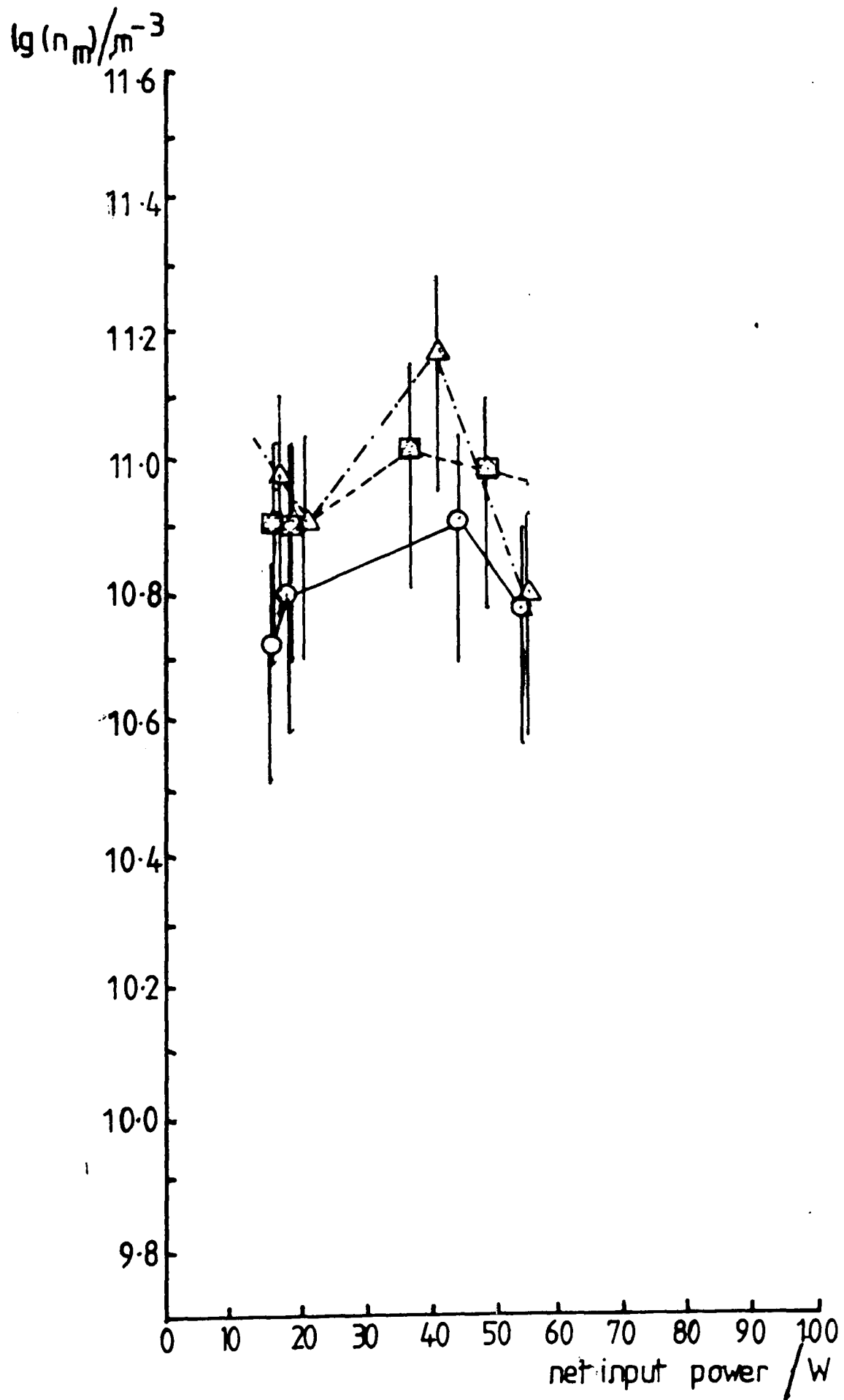


Figure 6.5c(ii) Population density of 8s level as a function of input power. Pressures in mbar: ○ 1.00, □ 0.70, △ 0.50. $n_m = \frac{I\lambda}{8\pi A}$

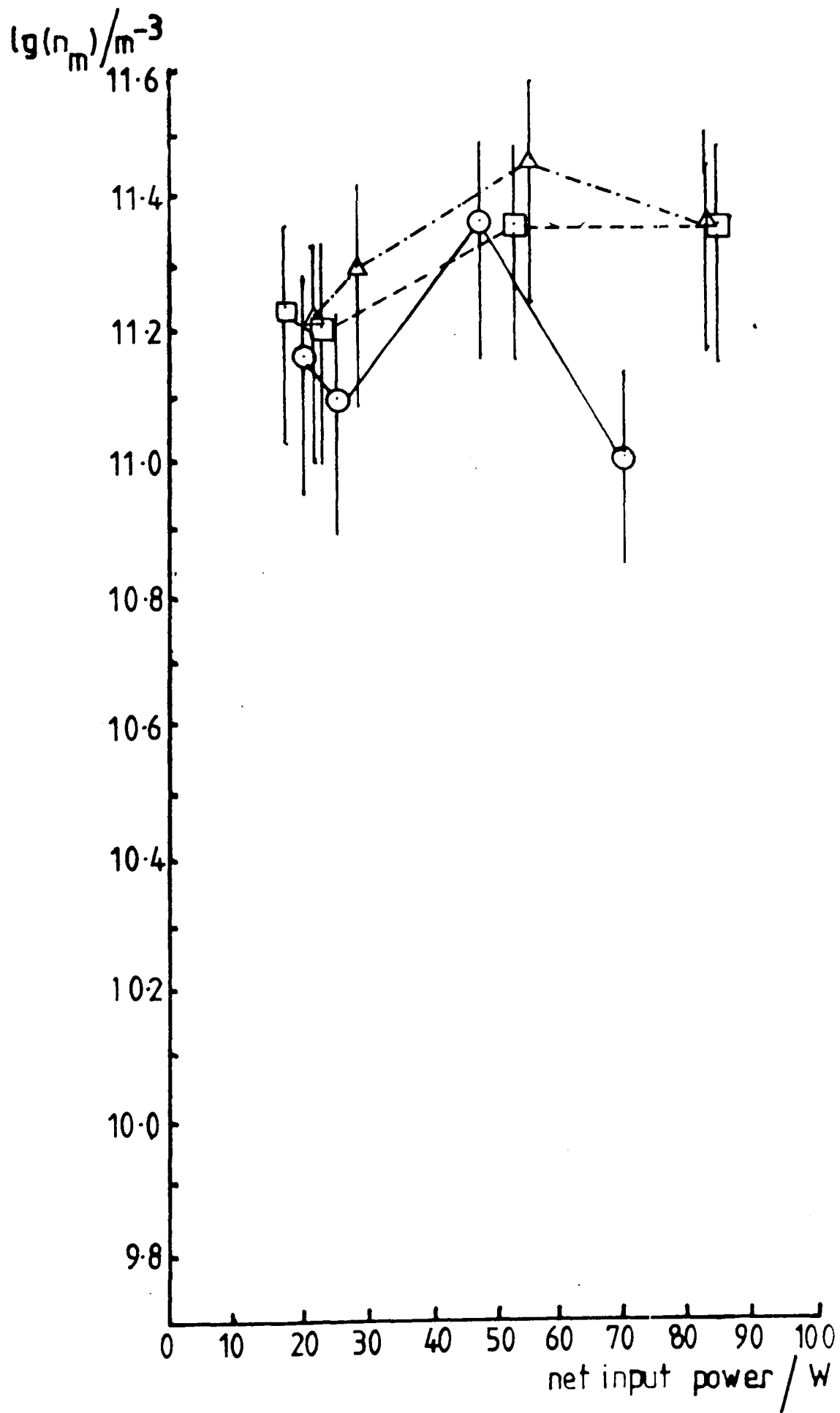


Figure 6.5c(iii) Population density of 8s level as a function of input power. Pressures in mbar: ○ 0.20,

□ 0.10, △ 0.07. $n_m = \frac{I\lambda}{\epsilon_m A}$

Table 6.1 Ratio of Population Densities at Different Pressures

Normalised input power: 25W

Pressure Ratio	4p	5p	6s'	7s	8s
2.00/6.00	2.0 [±] 0.7	2.3 [±] 0.8	3.2 [±] 1.1	1.6 [±] 0.6	1.6 [±] 0.6
0.70/6.00	4.5 [±] 1.6	5.6 [±] 1.9	6.6 [±] 2.3	5.5 [±] 1.9	5.3 [±] 1.9
0.20/6.00	3.8 [±] 1.3	5.4 [±] 1.9	8.7 [±] 3.0	8.1 [±] 2.8	7.2 [±] 2.5
2.00/3.00	2.2 [±] 0.8	2.3 [±] 0.8	3.7 [±] 1.3	2.0 [±] 0.7	2.0 [±] 0.7
0.70/3.00	5.1 [±] 1.8	5.8 [±] 2.0	7.6 [±] 2.7	6.8 [±] 2.4	6.6 [±] 2.3
0.20/3.00	4.1 [±] 1.4	5.5 [±] 1.9	10.0 [±] 3.5	10.0 [±] 3.5	9.1 [±] 3.2
0.70/2.00	2.3 [±] 0.8	2.5 [±] 0.9	2.0 [±] 0.7	3.4 [±] 1.2	3.3 [±] 1.2
0.20/2.00	1.9 [±] 0.7	2.3 [±] 0.8	2.7 [±] 0.9	5.0 [±] 1.8	4.6 [±] 1.6

Table 6.2 Ratio of Atomic to Ionic Population Densities

Input Power/W	Pressure/mbar		
	0.2	0.1	0.07
25	372	631	17.8
30	389	422	8.2
40	343	191	22.9
50	295	85	66

Atomic level 9s $\left[\begin{smallmatrix} 3/2 \\ 1 \end{smallmatrix} \right]_1^0$ Ionic level 4p⁴p⁰

pressure for the higher lying levels than for the lower atomic levels. This implies an increasing contribution for de-excitation by collisions with increasing pressure, such de-excitations being more important for the higher lying levels.

6.6 The Second Spectrum of Argon

The population densities of those levels of the argon ion, tabulated in table 4.2 were calculated in a similar manner to the argon atomic levels. The effect of net input power on the ionic level population densities is shown in fig. 6.6 which shows the variation of the $4p^4P^0$ multiplet. All the selected argon ionic levels lie reasonably close to each other in energy terms and no great diversity of dependence upon power would be expected. Only the upper level pertaining to the transition of wavelength 460.956 nm is separated by any reasonable distance but, as fig. 6.7 shows, there is no significant variation in behaviour between this level and that of fig. 6.6.

A Boltzmann plot of extended energy scale so as to include the levels of the argon ion is shown in fig. 6.8. This demonstrates the relationship between the atomic levels and the ionic levels of argon. Figure 6.8 clearly shows the deviation from equilibrium of even the highest lying levels of the atomic system with the lower levels of the ion, as predicted by the earlier Boltzmann plots described in section 6.2. Subsequent Boltzmann plots for a given magnetron current at pressures between 0.05 and 0.5 mbar show that as the pressure is decreased, the upper atomic levels and the lower ionic levels move closer towards mutual equilibrium as shown by figures 6.9 (a) and (b)

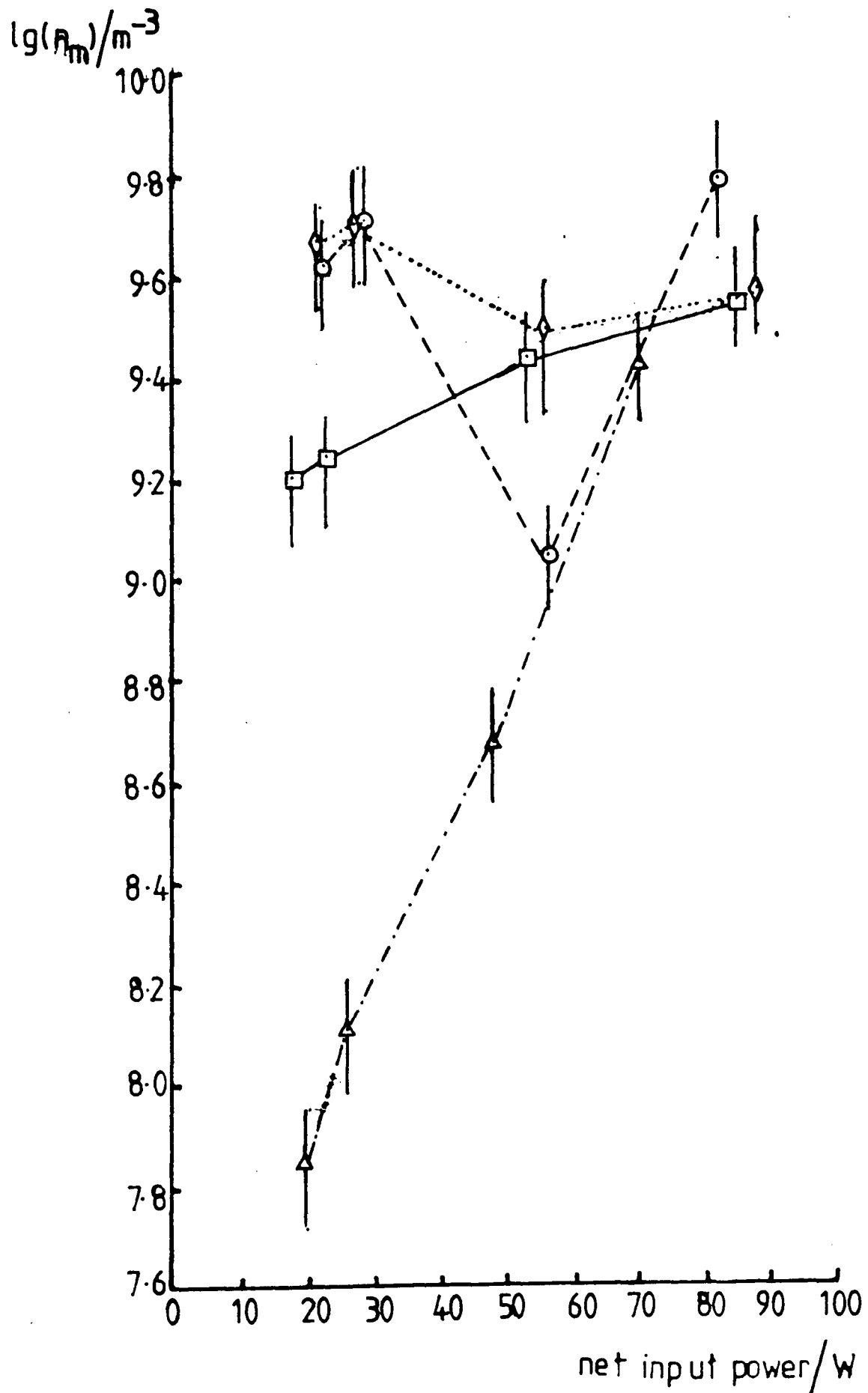


Figure 6.6 Variation with input power of the population density of the $4p^4P^0$ multiplet of the argon ion. Pressures in mbar: Δ 0.20, \square 0.10, \circ 0.07, \diamond 0.05. $n_m = \frac{I\lambda}{g_m A}$

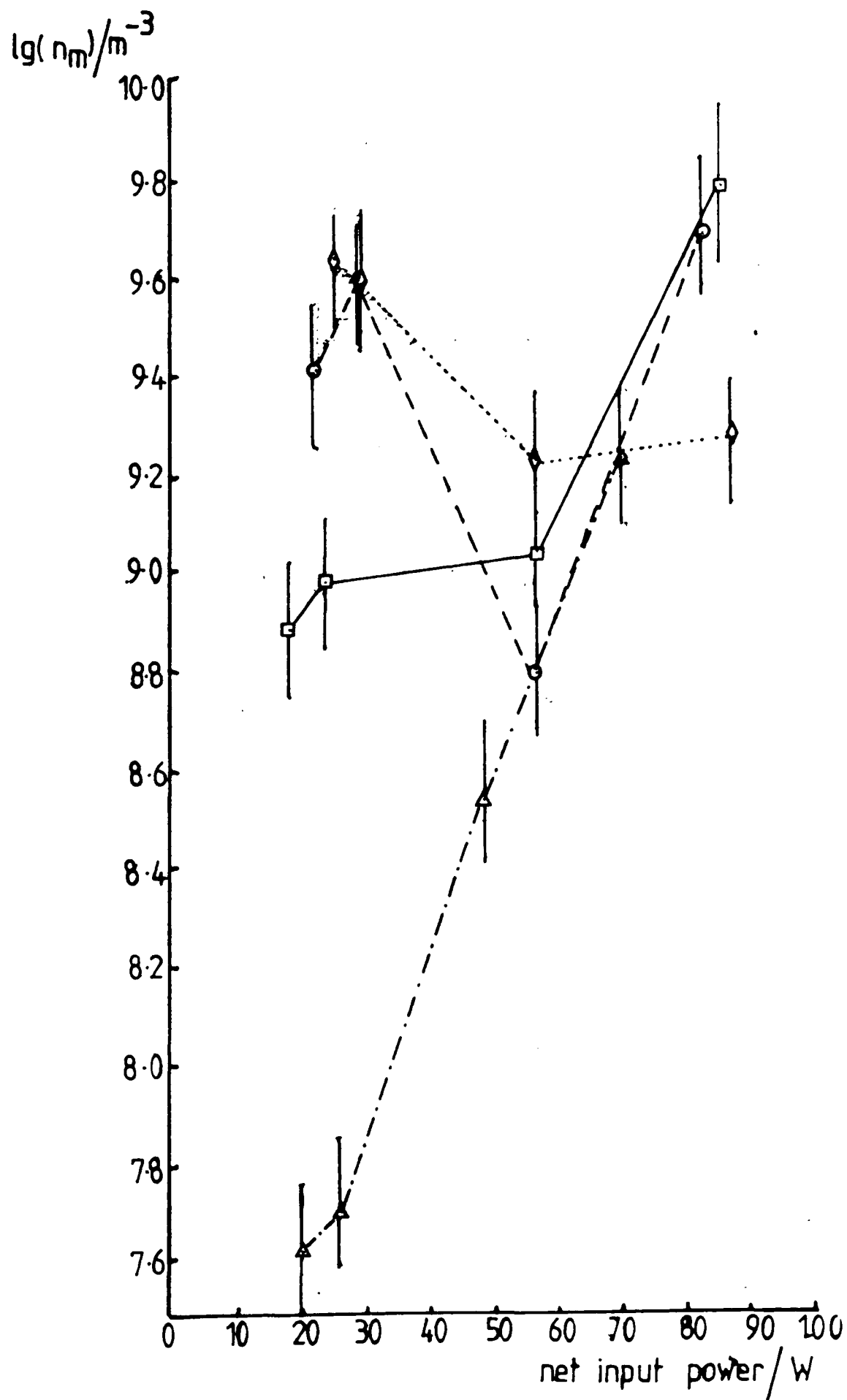


Figure 6.7 Variation with input power of the population density of the $4p'2P_0$ level of the argon ion. Pressures in mbar: Δ 0.20, \square 0.10, \circ 0.07, \diamond 0.05. $n_m = \frac{I\lambda}{8\pi A}$

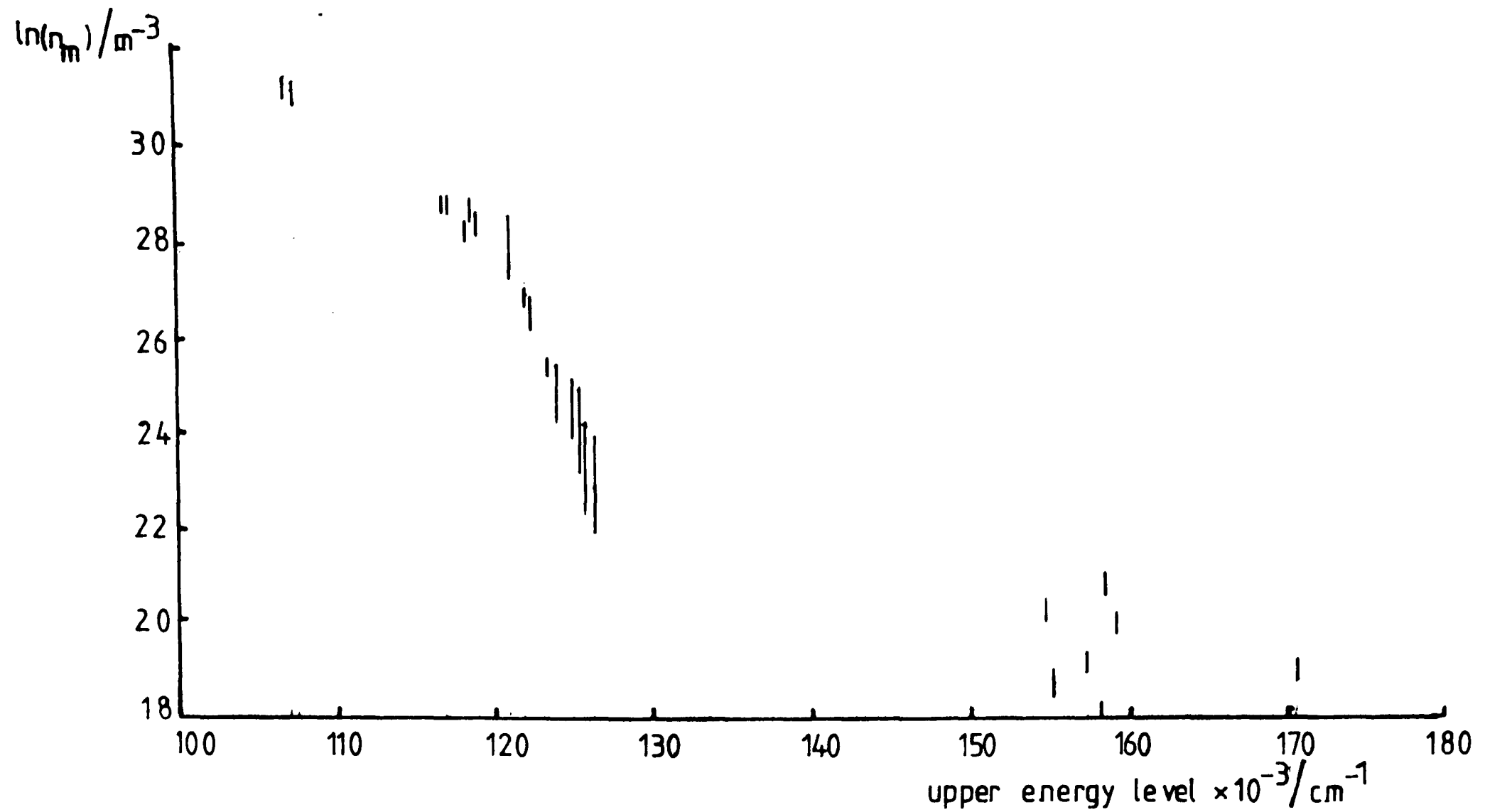


Figure 6.8 Typical extended Boltzmann plot for atomic and ionic levels. Pressure 0.50mbar magnetron current 50mA.

$$n_m = \frac{I \lambda}{2 - \lambda}$$

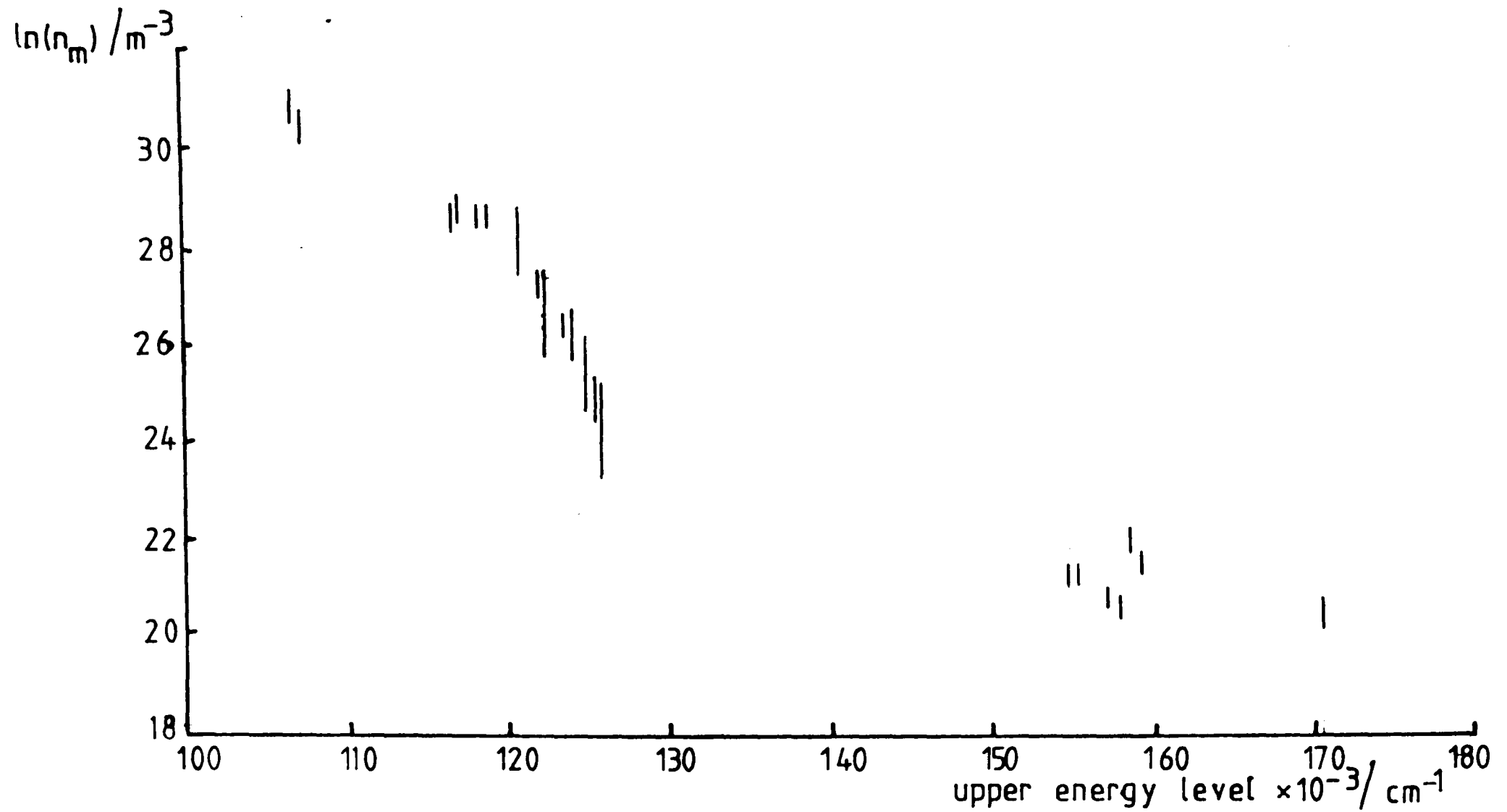


Figure 6.9a Extended Boltzmann plot for atomic and ionic levels. Pressure 0.10mbar, magnetron current 50mA.

$$n_m = \frac{I\lambda}{\pi m A}$$

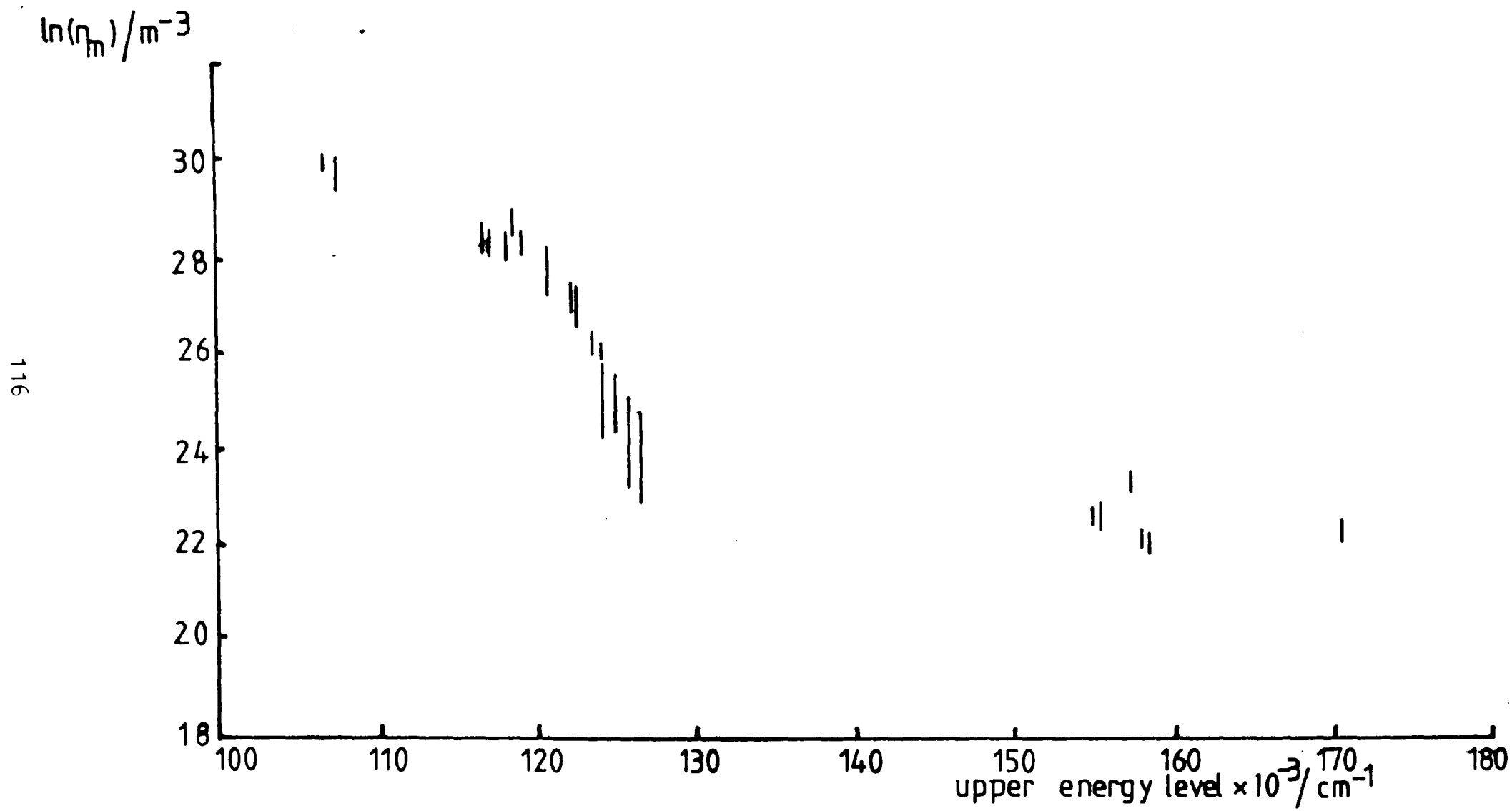


Figure 6.9b Extended Boltzmann plot for atomic and ionic levels. Pressure 0.05mbar, magnetron current 50mA.

$$n_m = \frac{I \lambda}{g \pi A}$$

in conjunction with fig. 6.8. These figures show Boltzmann plots for a magnetron current of 50 mA at pressures of 0.5, 0.1 and 0.05 mbar and clearly exhibit the movement towards Saha equilibrium; with decreasing pressure, of the upper levels of the argon atom.

Calculating the ratio of the population densities of the argon atomic 9s level to the ionic $4p^4P^0$ level shows this effect. The values of this ratio at three pressures and normalised for four net input powers are given in table 6.2.

Plotting the ratio of the atomic population density at a given pressure to the density at 0.05 mbar as a function of the pressure ratio and comparing the curve produced with that for the ion gives fig. 6.10. Clearly, the ionic levels increase more rapidly with decreasing pressure than the atomic levels. This can also be seen from figs. 6.8 and 6.9. Thus the move away from equilibrium at higher pressures can be attributed to a greater rate of decrease of excitation of the ion levels. Conversely, the move towards equilibrium with decreasing pressure is due to the greater rate of increase of excitation of ionic levels over that of atomic levels.

6.7 Variation of Intensity with Pressure

According to Llewellyn Jones (1936), the form of the electron distribution function can be inferred from plots of intensity against the mean energy of the electrons. Unfortunately, no measurement of the mean electron energy has been made in this work but, by plotting the intensity of a given spectral line against pressure, it is possible to compare the form of this curve with those given by Llewellyn Jones. Although the Llewellyn Jones study was conducted upon a helium

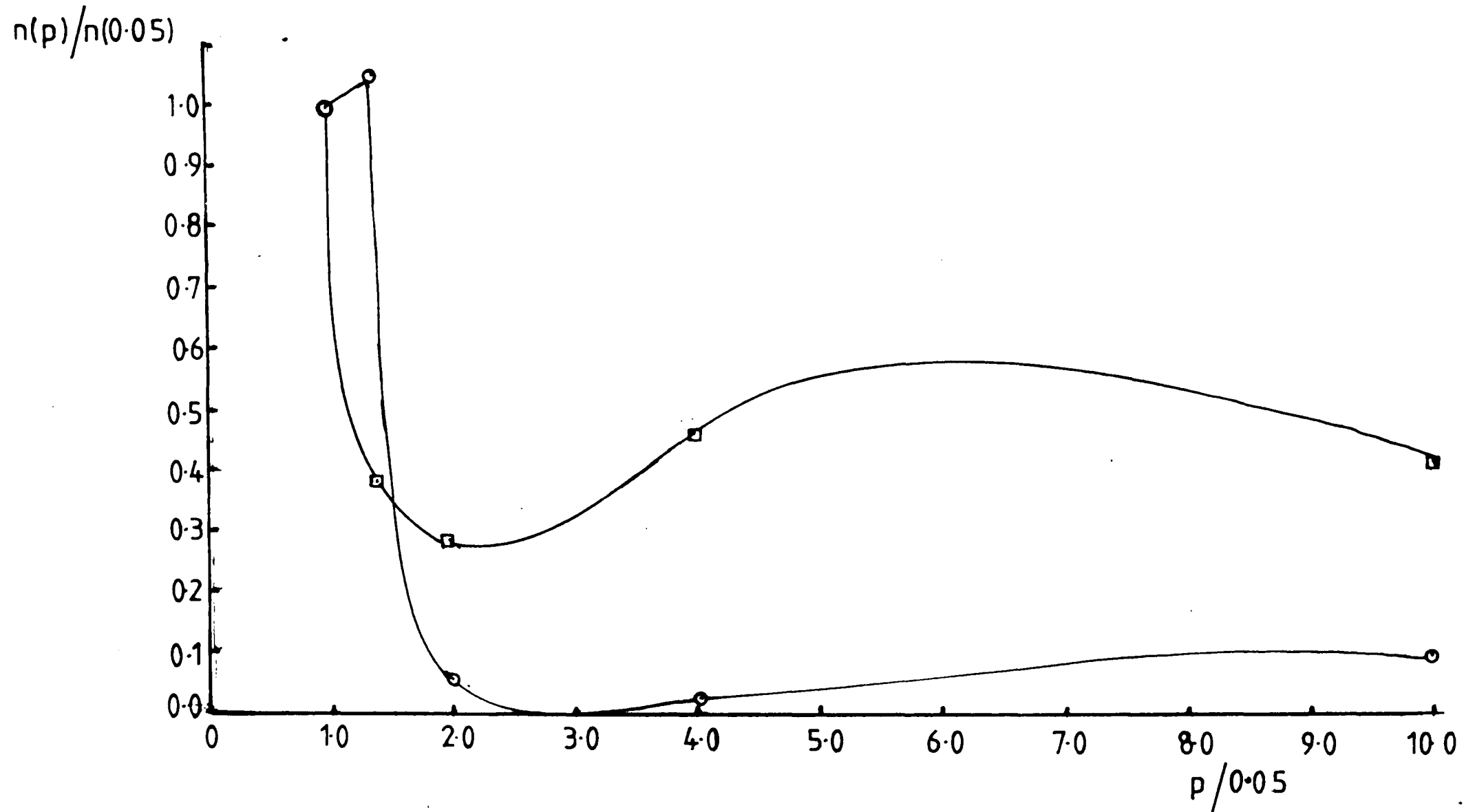


Figure 6.10 Variation of relative population densities of the atomic and ionic levels with pressure.

□ atomic ○ ionic

positive column and makes the assumption that excitation of the atoms is due principally to single collisions of the atoms with electrons of high energy, a comparison with the argon microwave discharge would be of interest. In addition, Keyston (1933) suggests that the applicability of a Maxwellian distribution function for the electrons is doubtful below pressures of approximately 5 mbar. Thus it would be useful for other areas of this work to examine the similarities, or otherwise, between the results of this work and that of Llewellyn Jones.

The results reported by Llewellyn Jones were calculated assuming a constant current in the positive column discharge. For the microwave discharge, which is electrodeless, the concept of 'current' is meaningless. By considering the plasma as a resistive load, it can be seen that the equivalent parameter would be the net microwave input power which, like current, is a function of the plasma impedance. To make the comparison between this work and that of Llewellyn Jones, the relative population density of a given level was plotted as a function of pressure for a normalised input power. This is equivalent to plotting relative intensity as the intensity of a line originating from a given level is proportional to the population of that level.

Figures 6.11 (a), (b) and (c) show relative population density vs pressure for the 4p, 6s and 6d groups of the argon atom. Comparison with those given by Llewellyn Jones, figs. 6.12(a) and (b), show a close similarity in form. Such a similarity implies an electron distribution function of the form (Llewellyn Jones 1936)

$$dn_1 = n_1 (2.07fe^{-3y/2} + 0.7 (1-f)e^{-0.4y^2})y^{\frac{1}{2}}dy \quad 6.5$$

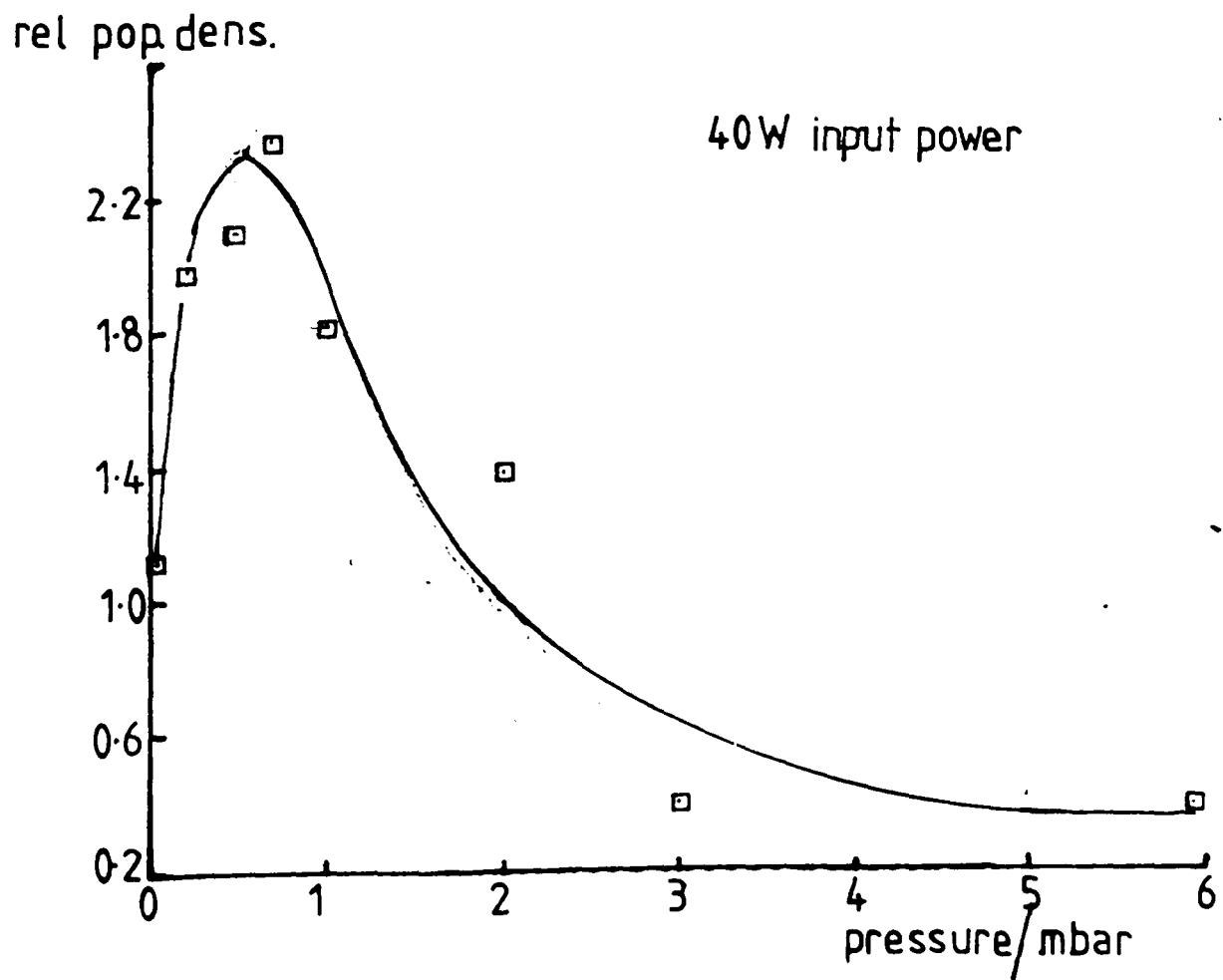
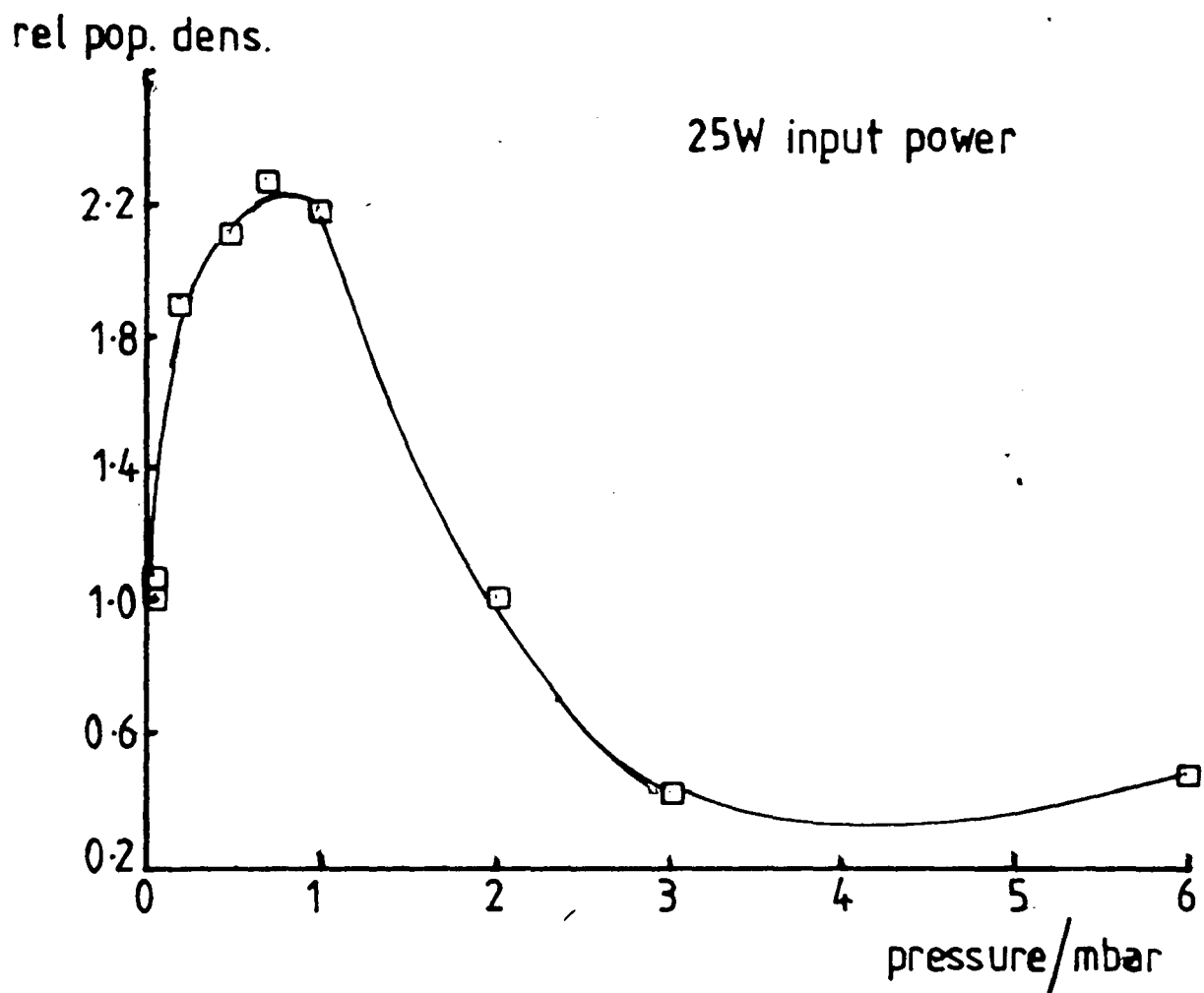
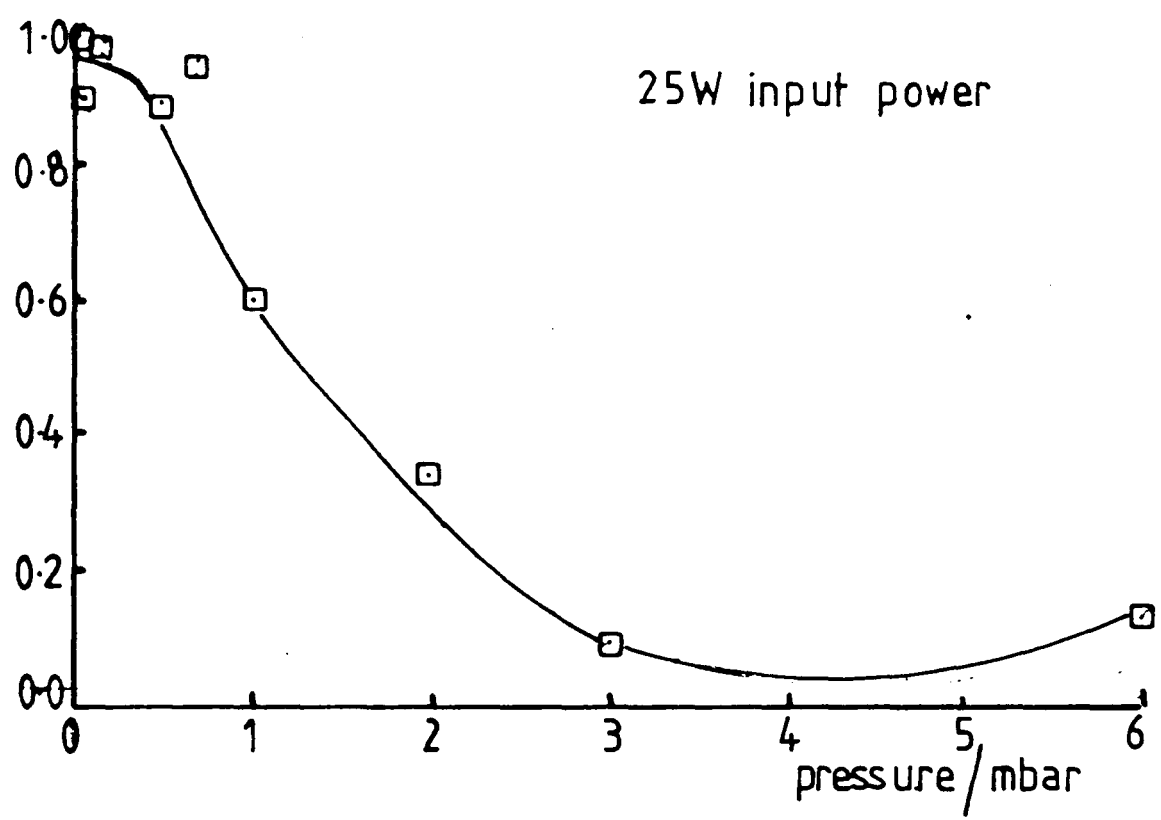


Figure 6.11a Variation of relative population density of 4p level with pressure

rel pop. dens.



rel pop. dens.

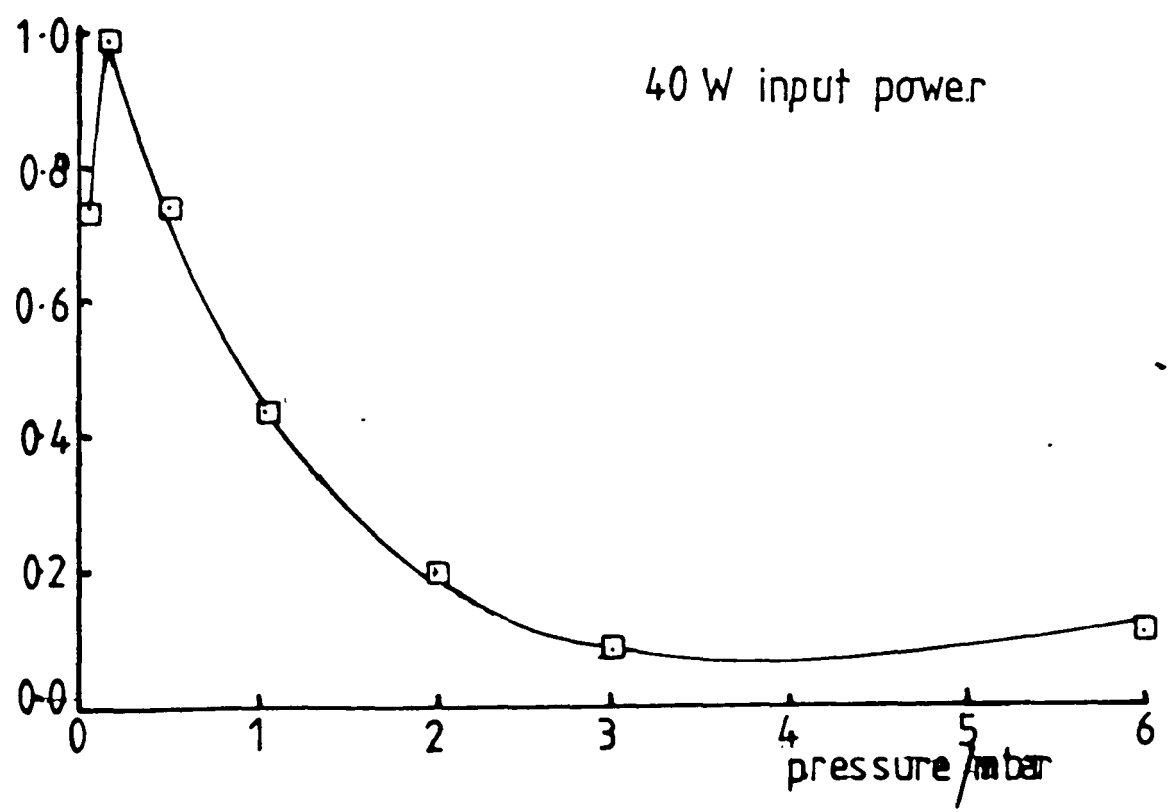


Figure 6.11b Variation of relative population density of 6s level with pressure

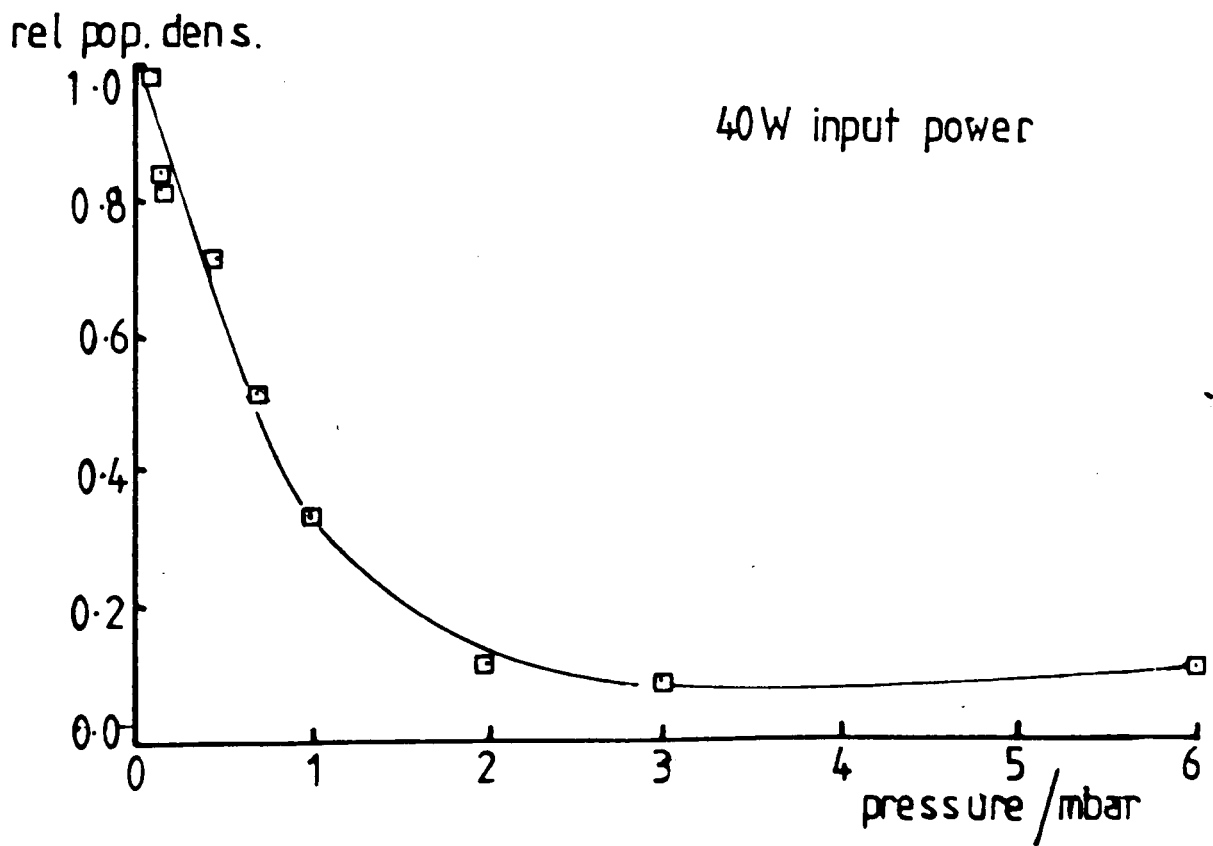
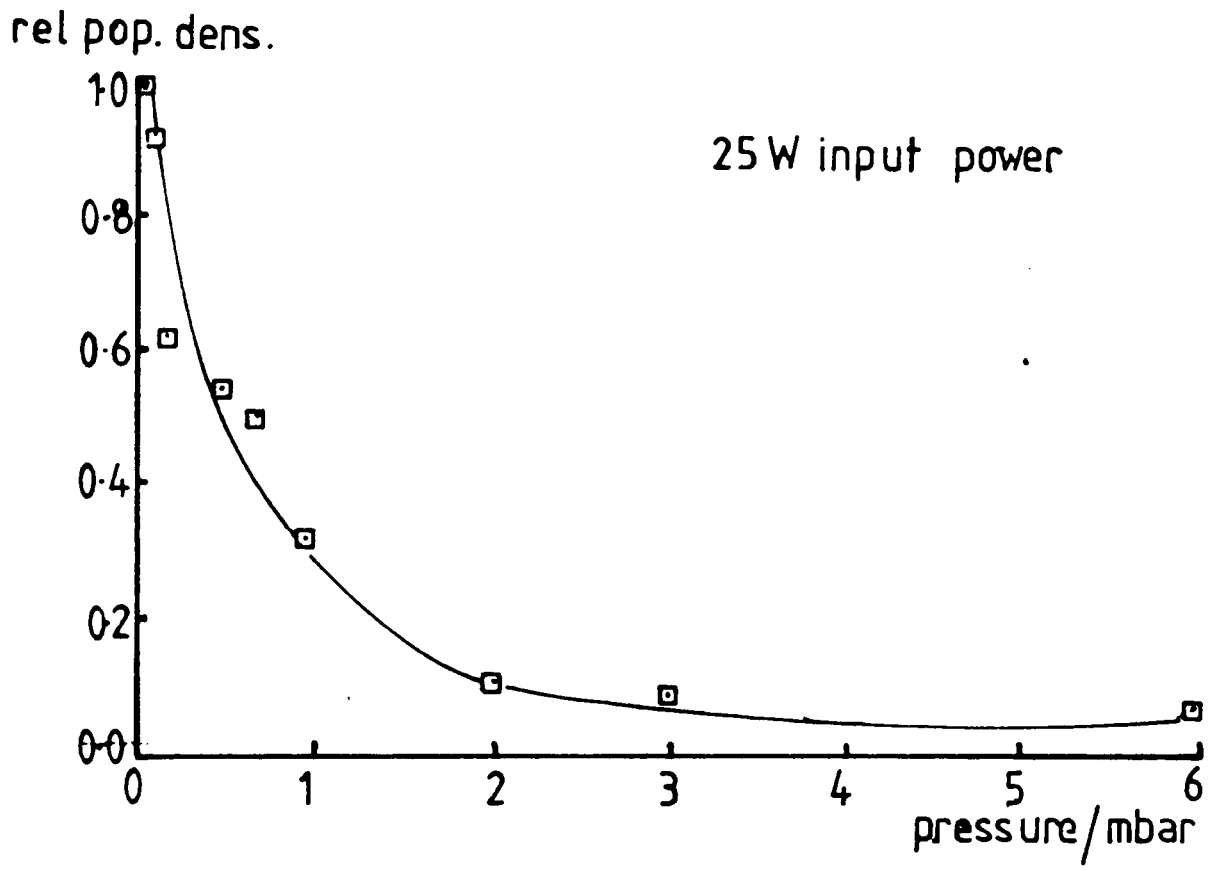


Figure 6.11c Variation of relative population density of 6d level with pressure

where f is a constant of value 1.882×10^{-3} and $y = E_x/E_1$ where E_x is the energy of a given electron and E_1 is mean electron energy. This similarity also provides us with a form for the "probability of excitation" function, that is the probability that collision with an electron of energy E_x will result in the excitation of a given particular atomic level. The two forms given by Llewellyn Jones are:

(i) $P = k$ for $E_j < E_x < \infty$

where k is a constant and E_j the energy of the atomic level. This probability function is applicable to the curves of form fig. 6.12 (b).

(ii) $P = k (E_x - E_j)/E_x$ $E_j < E_x < E_m$
 $P = 0$ $E_x > E_m$

where E_m is the energy at which the excitation curve shows a maximum. This excitation function is applicable to curves of the form fig. 6.12 (a).

Llewellyn Jones gives the number dn of electrons with energies between E_x and $E_x + dE_x$ as

$$(Be^{-3y/2} + e^{-0.4y^2})y^{\frac{1}{2}}dy \quad 6.6$$

with $B = 5.38 \times 10^{-3}$

By considering the number of atoms at a gas pressure p_1 and including the excitation cross sections, an expression for the intensity of a given spectral line may be obtained, the form of the expression being dependent upon the expression used for P . The two intensity expressions are:

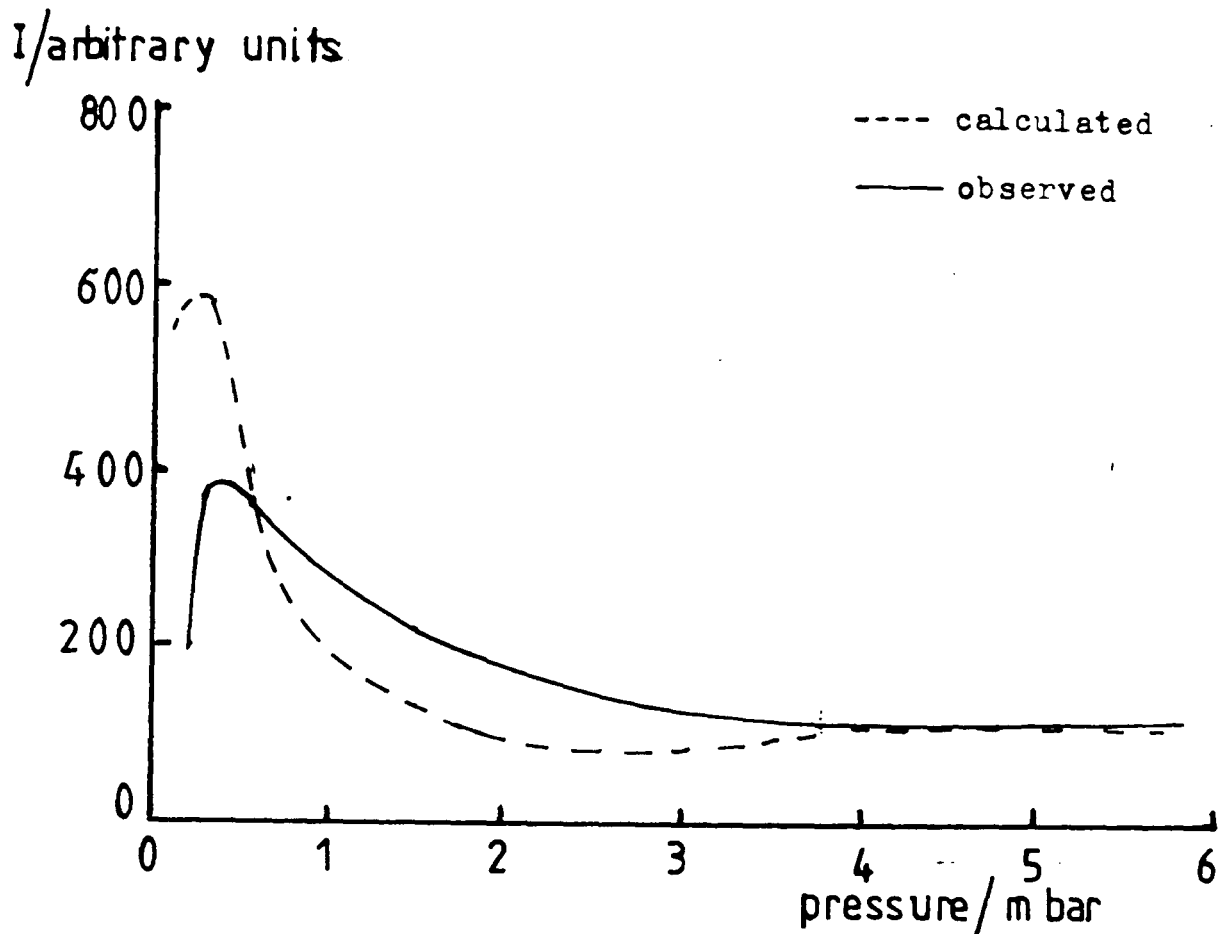


Figure 6.12a Comparison of observed and calculated intensities for the 2^3P-3^3D transition in helium. Taken from Llewellyn Jones.

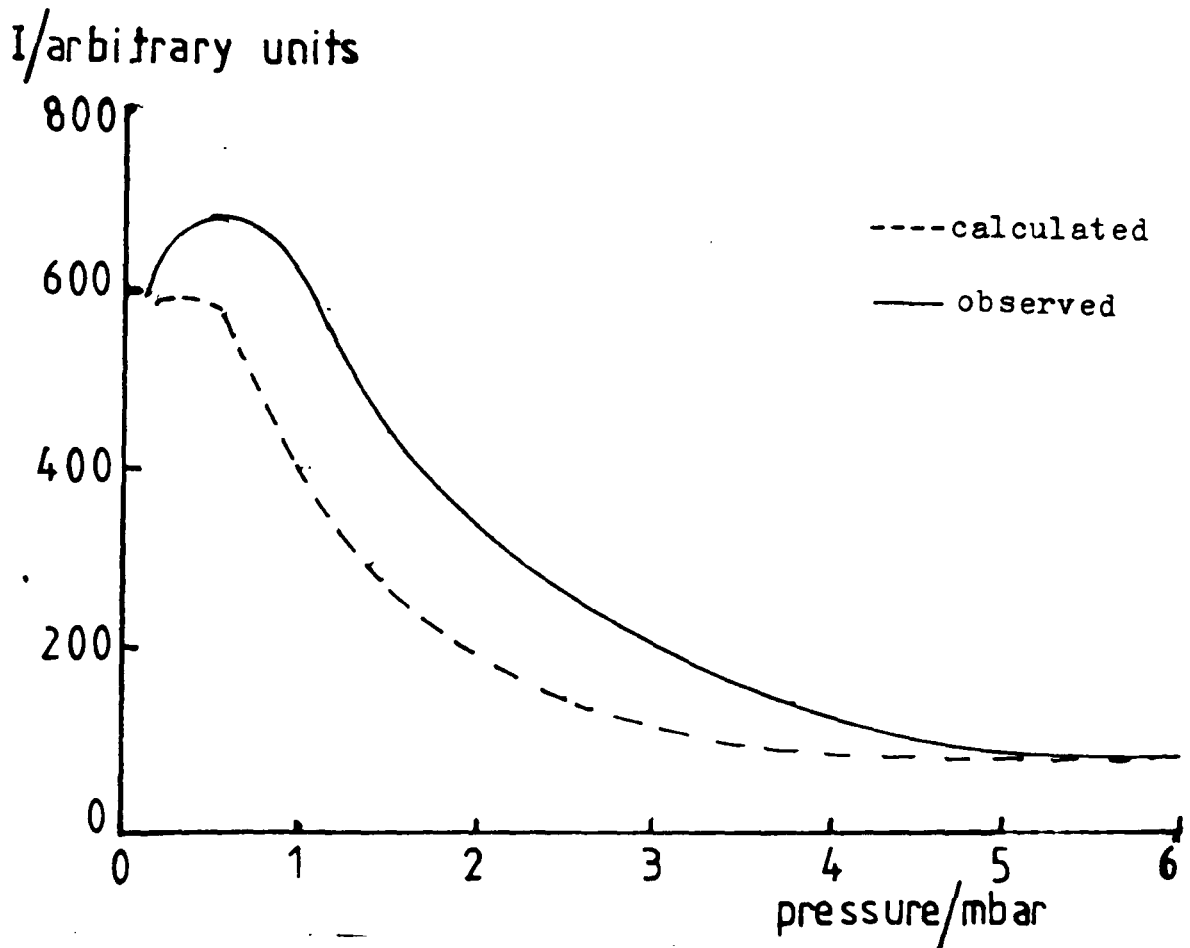


Figure 6.12b Comparison of observed and calculated intensities for the 2^3P-4^3D transition in helium (Llewellyn Jones)

I/arbitrary units

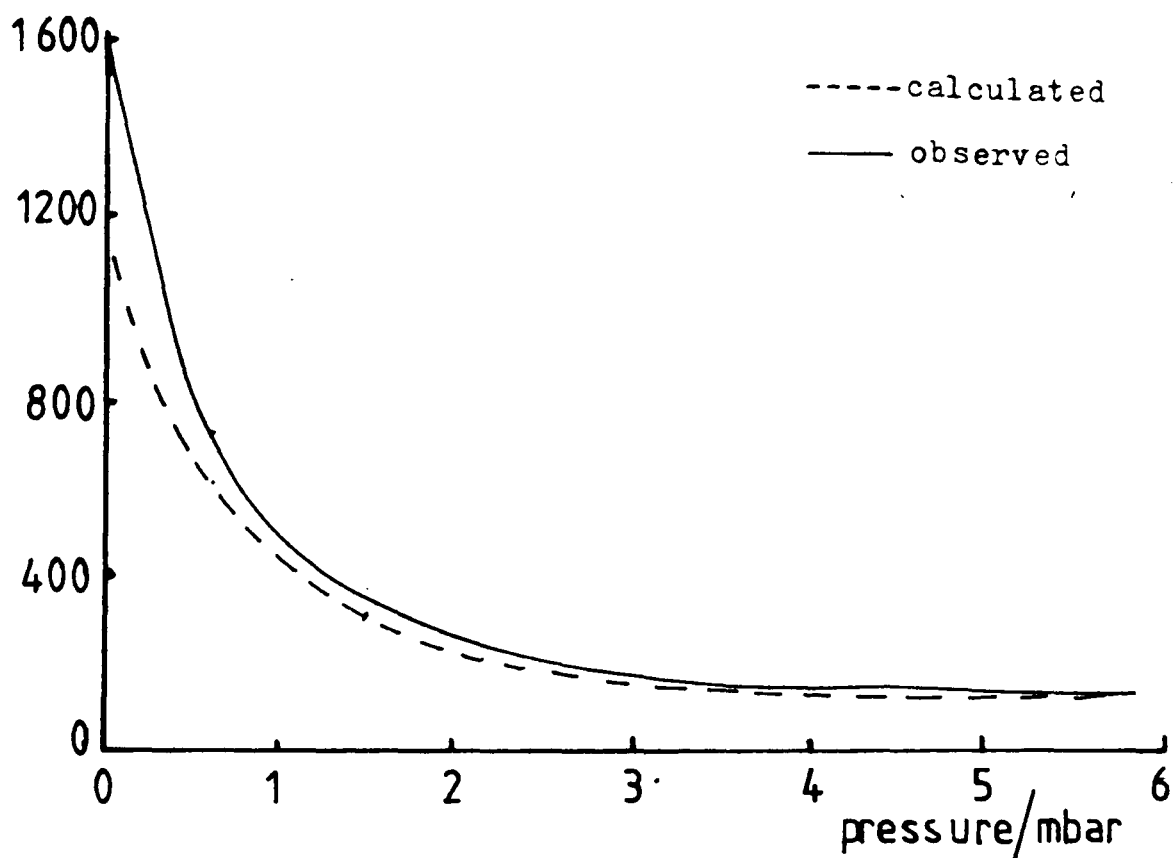


Figure 6.12c Comparison of observed and calculated intensities for the 2^1S-3^1P transition in helium (Llewellyn Jones)

I/arbitrary units

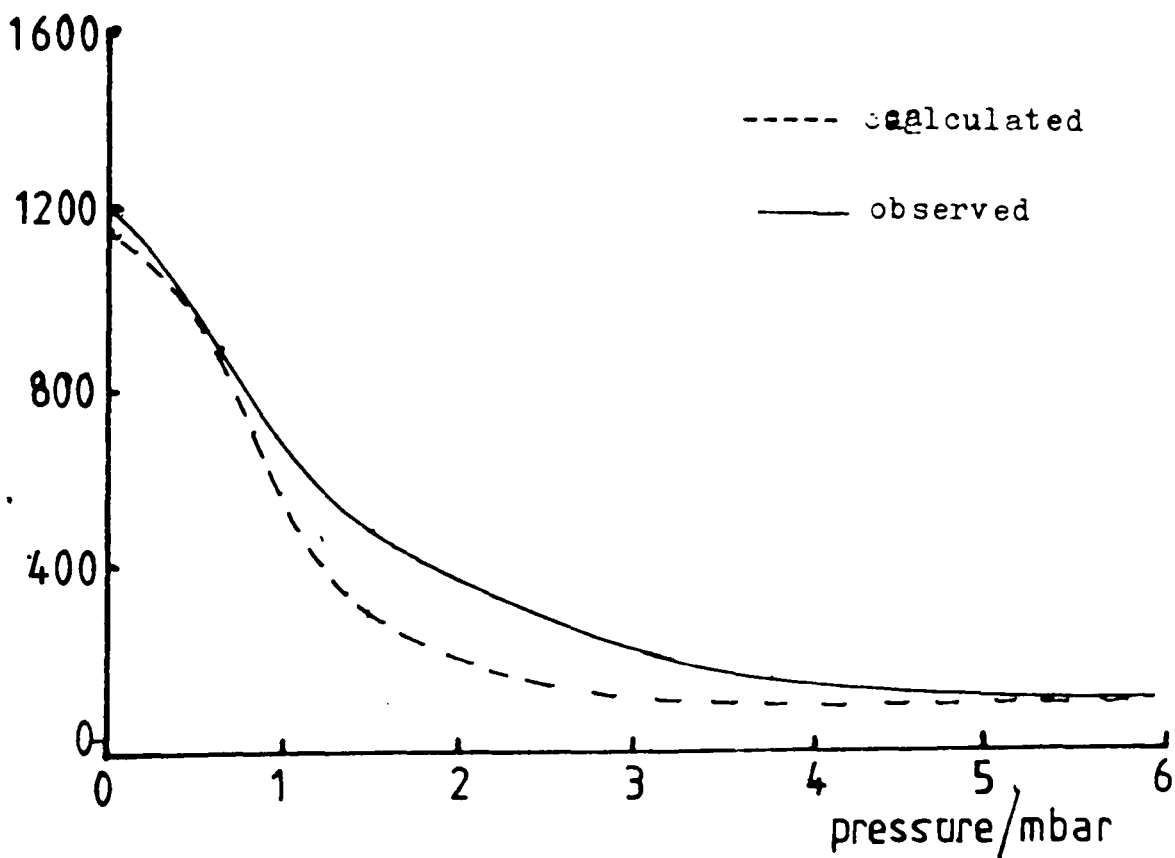


Figure 6.12d Comparison of observed and calculated intensities for the 2^3S-4^3P transition in helium (Llewellyn Jones)

$$(i) \quad P = k$$

The intensity is proportional to

$$n_1 P_1 \left[B(E_j + \frac{2E_1}{3}) \frac{2E_1}{3} e^{-\frac{1}{2} \cdot 3E_j/2E_1} + 1.25E_1^{\frac{1}{2}} e^{-0.4(E_j/E_1)^2} \right] \quad 6.7$$

$$(ii) \quad P = k(E_x - E_j)/E_x$$

The intensity is proportional to

$$n_1 P_1 \left[\frac{4B}{9} E_1^{\frac{1}{2}} e^{-3E_j/2E_1} + 1.25E_1^{\frac{1}{2}} e^{-0.4(E_j/E_1)^2} - 0.79 \sqrt{\pi} E_j E_1^{-\frac{1}{2}} \int_0^{\infty} e^{-\zeta^2} d\zeta \right]$$

$$\text{where } \zeta = 0.64E_j/E_1 \quad 6.8$$

The distribution function of equation 6.5, which is an empirical formula, expresses the distribution of electrons as consisting of a small group with energies distributed according to Maxwell's formula while the distribution of the energies of the majority of the electrons is represented by the Druyvesteyn formula, viz:-

$$dn_1 = n_1 y^{\frac{1}{2}} e^{-0.55y^2} dy \quad 6.9$$

This combination of distribution formulae among the free electrons has been previously recorded in other discharges, for example Thomas (1965).

6.8 Stark Broadening

The broadening of the atomic emission lines by Stark broadening provides a method of determining the electron density. The element most susceptible to Stark broadening of its emission lines is hydrogen and this is commonly realised by introducing trace amounts of this gas into the main plasma. However, owing to the susceptibility of the argon microwave discharge to contamination (section 2.4) this

possibility was eliminated.

In order to establish the feasibility of using the lines of the first argon spectrum, the expected broadening was calculated using the equation of Griem (1964):

$$W_{th} = 2 \left[1 + 1.75 \times 10^{-4} N_e^{1/4} \alpha (1 - 0.068 N_e^{1/6} T_e^{-1/2}) \right] 10^{-16} N_e W$$

where W_{th} is the theoretical half width due to Stark broadening

α is the ion broadening parameter at $N_e = 10^{16} \text{ cm}^{-3}$

W is the electron impact broadening parameter at $N_e = 10^{16} \text{ cm}^{-3}$

N_e is the electron density.

Values of α and W are tabulated by Griem at an electron density of 10^{16} cm^{-3} . This value of electron density is some orders of magnitude greater than would be expected in the microwave plasma at the pressures encountered here. Values of the half width for varying N_e and T_e values have also been tabulated by Konjevic and Roberts (1976). A combination of these two sets of data indicated that values of W_{th} less than approximately 1 Å would be expected. This would be considerably less than broadening due to the monochromator and would also be problematic to deconvolute from the Doppler broadening since the plasma is of the low density, high temperature type. Consequently, the possibility of determining the electron density from the Stark broadening of the argon atomic emission lines was dismissed.

CHAPTER 7
RESULTS OF LANGMUIR PROBE MEASUREMENTS

7.1 Appearance of Probe Characteristics

It was stated in section 6.3 that the discharge was restricted in length in the probe tube when compared with the plain tube. As a consequence, it was not possible to obtain as many probe characteristics as was originally intended, particularly at the greatest distances from the cavity. Those characteristics which were obtained were first plotted automatically (see section 5.3) to check for irregularities in the data. A typical characteristic plot is shown in fig. 7.1, demonstrating the reproducibility of the data points.

As described in section 5.1, two forms of probe characteristic are accounted for by the theory and these are typified by figs. 5.2 and 5.3. When the probe data was plotted however, a third type, not as yet accounted for in theory, was identified. This took the form of fig. 7.2 where the saturation region of the characteristic shows a negative variable gradient. It had originally been intended to analyse the characteristics by computer but it was decided that the analysis would be better performed manually rather than creating three separate computer programmes to analyse the three forms of characteristic.

7.2 Evaluation of Plasma Parameters

7.2.1 Calculation of Electron Temperature, T_e

For the probe characteristic types I and II (figs. 5.2 and 5.3 respectively) the evaluation of the quantity $(\Sigma i_+ / i_{e1})$ was simple and followed the theory presented in section 5.2. For those

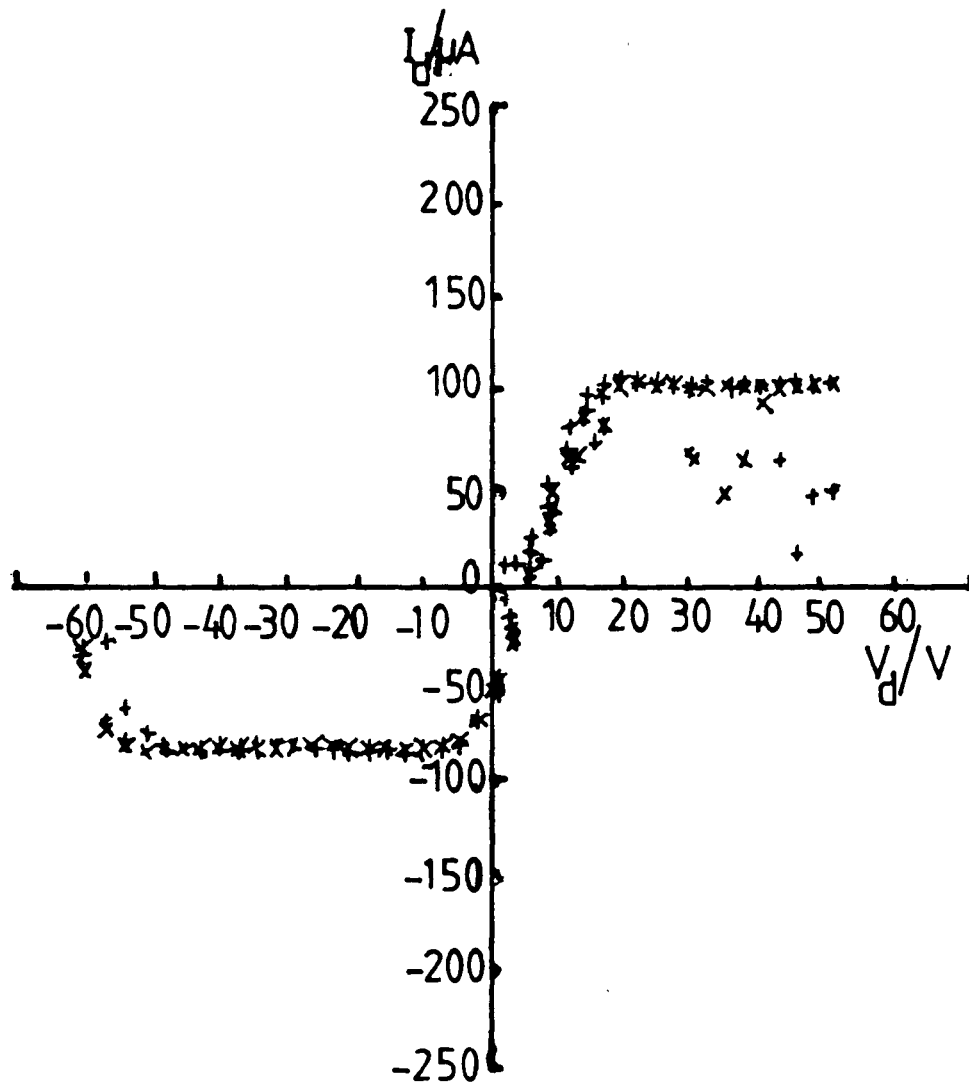


Figure 7.1 Typical plot of probe data.

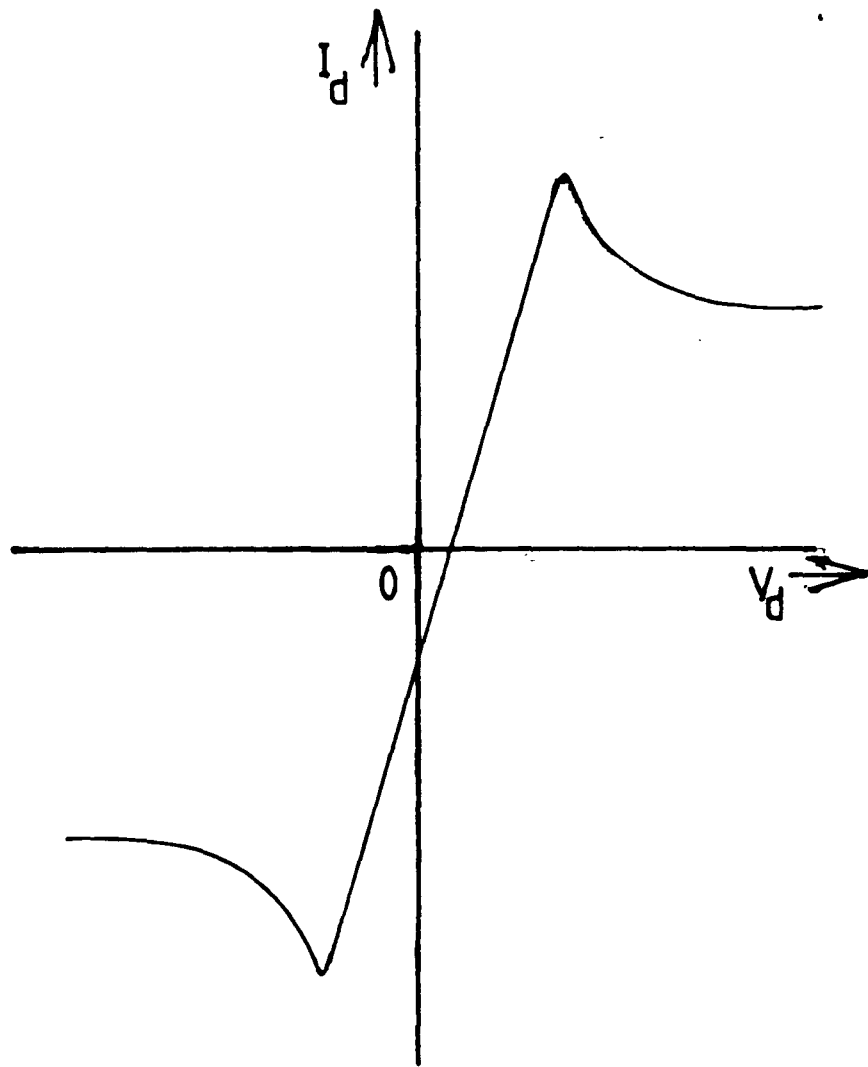


Figure 7.2 The third type of probe characteristic

characteristics of type III (ie. those corresponding to fig. 7.2) it was decided that the sum of the ion currents, $\sum i_+$, should be taken to be the current between the two turning points of the characteristic. Values of $\ln (\sum i_+/i_{e1} - 1)$ were then plotted as functions of the applied voltage V_d and a least squares linear fit performed upon the data to provide the gradient. The electron temperature was then given by equation 5.10.

To obtain the error in the electron temperature the following methods were applied:

- (i) for types I and III the maximum and minimum values of i_{+1} and i_{+2} were taken to be the extreme data points in the saturation regions (fig. 7.3(a)).
- (ii) for type II, the maximum and minimum gradients were drawn through each saturation region (fig. 7.3(b)).

Separate logarithmic plots were then taken using these maximum and minimum values, giving the range of values for T_e .

As stated in section 5.3, a set of five characteristics was taken for each appropriate pair of probes both before and after a set of spectral measurements were made. Consequently there were at least two values of T_e for each pressure and magnetron current and these were averaged using a weighted means method to obtain the final values tabulated in table 7.1.

The values of electron temperature given in table 7.1 are presented as a function of pressure for a given magnetron current in figs. 7.4(a) to (d). The figures show a peak in electron temperature in the

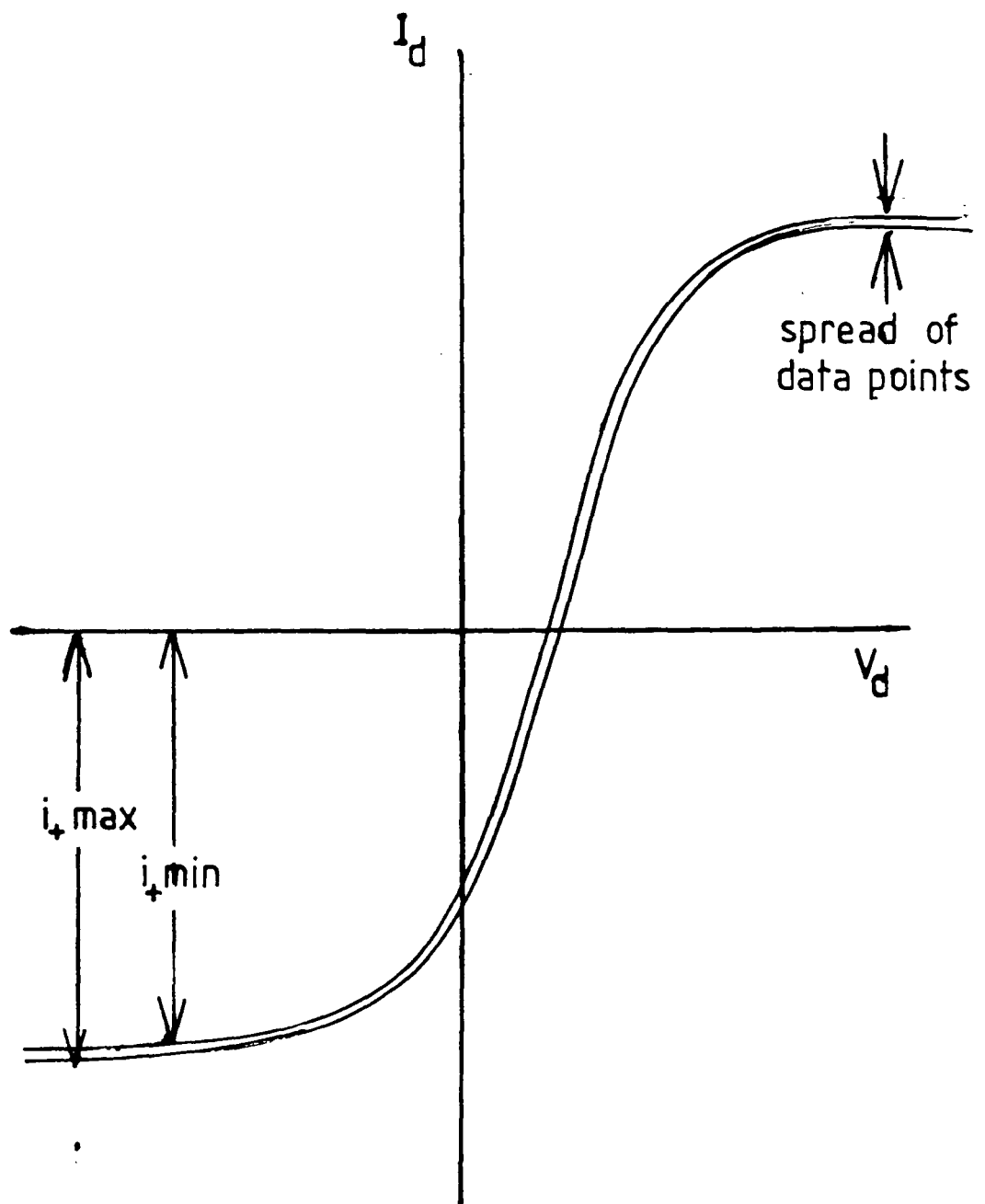


Figure 7.3a Determination of maximum & minimum values of i_d for types I & III characteristics.

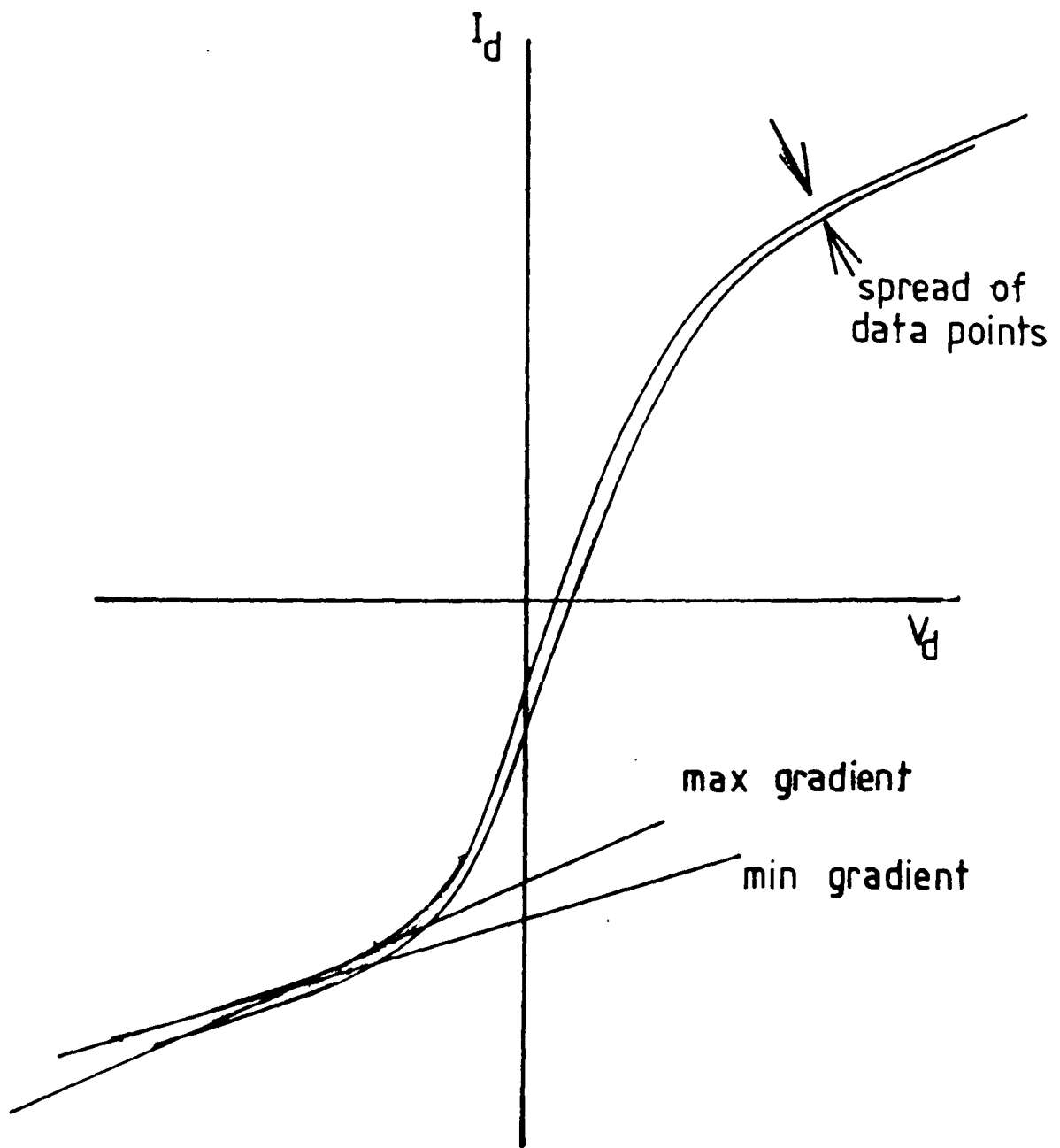


Figure 7.3b Determination of maximum & minimum gradients for type II characteristics.

Table 7.1 Calculated Values of Electron Temperature (T_e/K)

Magnetron current/mA	40	50	100	150
Pressure/mbar				
3.00	21438 ⁺¹²⁸⁶	22465 ⁺⁶⁷⁴	-	-
2.00	28611 ⁺²⁸⁶	30130 ⁺³⁰¹	32137 ⁺²²⁵⁰	38886 ⁺¹⁹⁴⁴
1.00	49234 ⁺⁸³⁶⁹	47929 ⁺¹⁹¹⁷	43820 ⁺¹⁷⁵³	-
0.70	49554 ⁺¹⁴⁸⁷	62890 ⁺¹⁸⁸⁷	57499 ⁺¹¹⁵⁰	63654 ⁺¹²⁷³
0.50	59876 ⁺¹⁷⁹⁶	66568 ⁺³³²⁸	76307 ⁺³⁸¹⁵	67624 ⁺²⁰²⁹
0.20	77107 ⁺¹⁵⁴²	63953 ⁺¹⁹¹⁹	90512 ⁺¹⁸¹⁰²	79985 ⁺¹⁵⁹⁹
0.10	47865 ⁺⁴⁷⁸⁷	50002 ⁺⁵⁵⁰⁰	57386 ⁺¹²⁶²⁵	-
0.07	57297 ⁺⁵¹⁵⁷	50791 ⁺⁵⁵⁸⁷	45065 ⁺⁶³⁰⁹	72993 ⁺⁵⁸³⁹
0.05	58820 ⁺⁸⁸²³	58968 ⁺⁵⁸⁹⁷	64298 ⁺⁹⁶⁴⁵	59467 ⁺⁸⁹²⁰
0.02	-	-	67072 ⁺⁸⁰⁴⁹	63391 ⁺⁸²⁴¹

Distance from cavity = 3 cm

Magnetron current/mA	40	50	100	150
Pressure/mbar				
3.00	8.1 ^{+0.5}	5.7 ^{+0.2}	-	-
2.00	8.4 ^{+0.2}	5.1 ^{+0.2}	15.4 ^{+1.1}	7.8 ^{+0.6}
1.00	6.6 ^{+0.7}	6.6 ^{+0.3}	12.3 ^{+0.5}	-
0.70	5.5 ^{+0.3}	6.3 ^{+0.3}	10.6 ^{+0.4}	9.5 ^{+0.3}
0.50	6.1 ^{+0.3}	6.2 ^{+1.0}	7.6 ^{+0.4}	9.1 ^{+0.5}
0.20	6.1 ^{+0.3}	6.5 ^{+0.3}	5.0 ^{+1.0}	5.8 ^{+0.2}
0.10	1.9 ^{+0.3}	1.9 ^{+0.3}	0.80 ^{+0.24}	-
0.07	1.8 ^{+0.3}	1.7 ^{+0.3}	0.53 ^{+0.14}	3.2 ^{+0.4}
0.05	2.4 ^{+0.5}	1.8 ^{+0.3}	0.96 ^{+0.16}	2.4 ^{+0.5}
0.02	-	-	1.90 ^{+0.4}	5.6 ^{+1.3}

Distance from cavity = 3 cm

Table 7.2 Calculated Values of Ion Density ($n_+/10^{17} m^{-3}$)

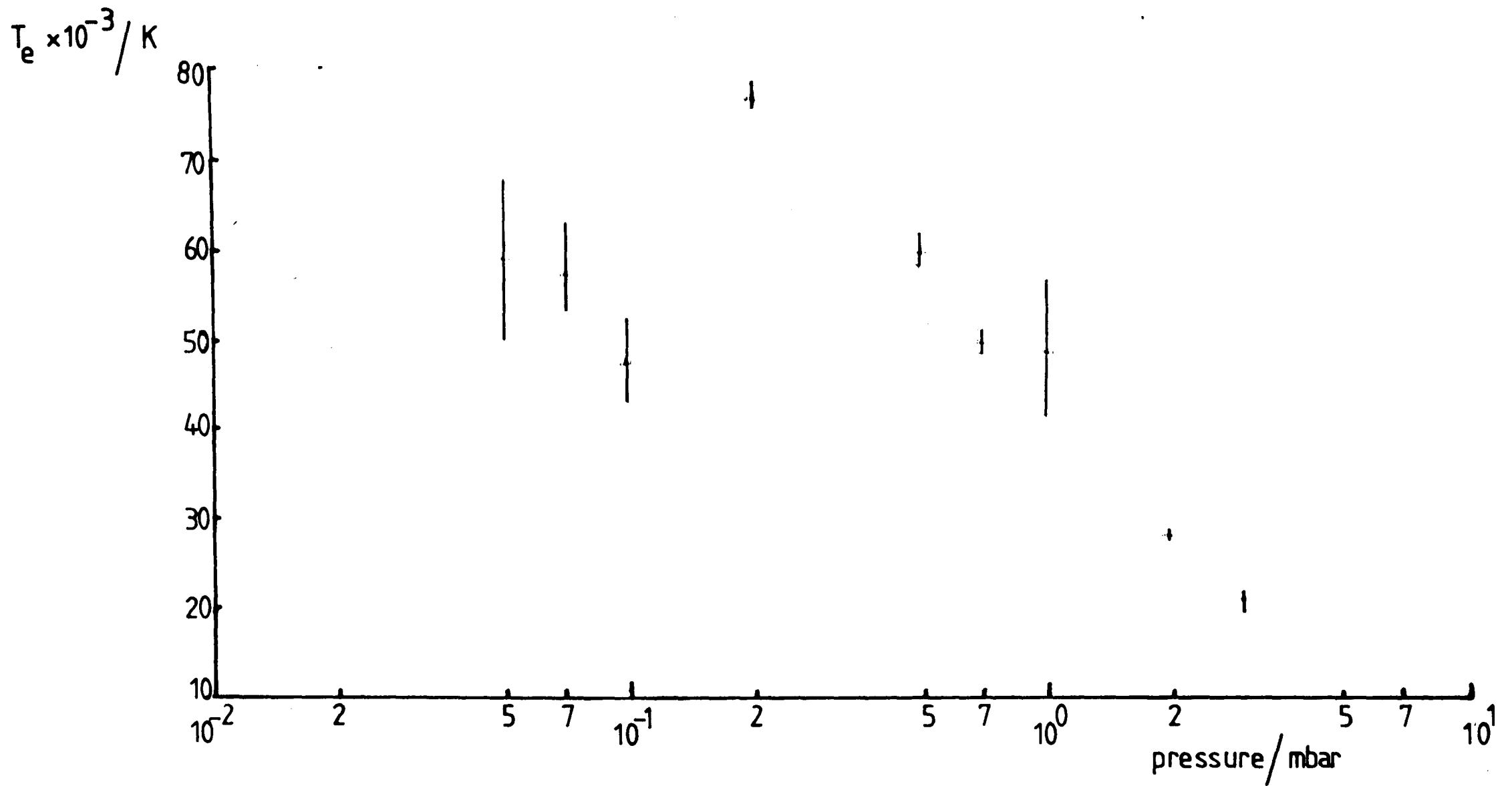


Figure 7.4a Variation of electron temperature with pressure. Magnetron current 40mA.

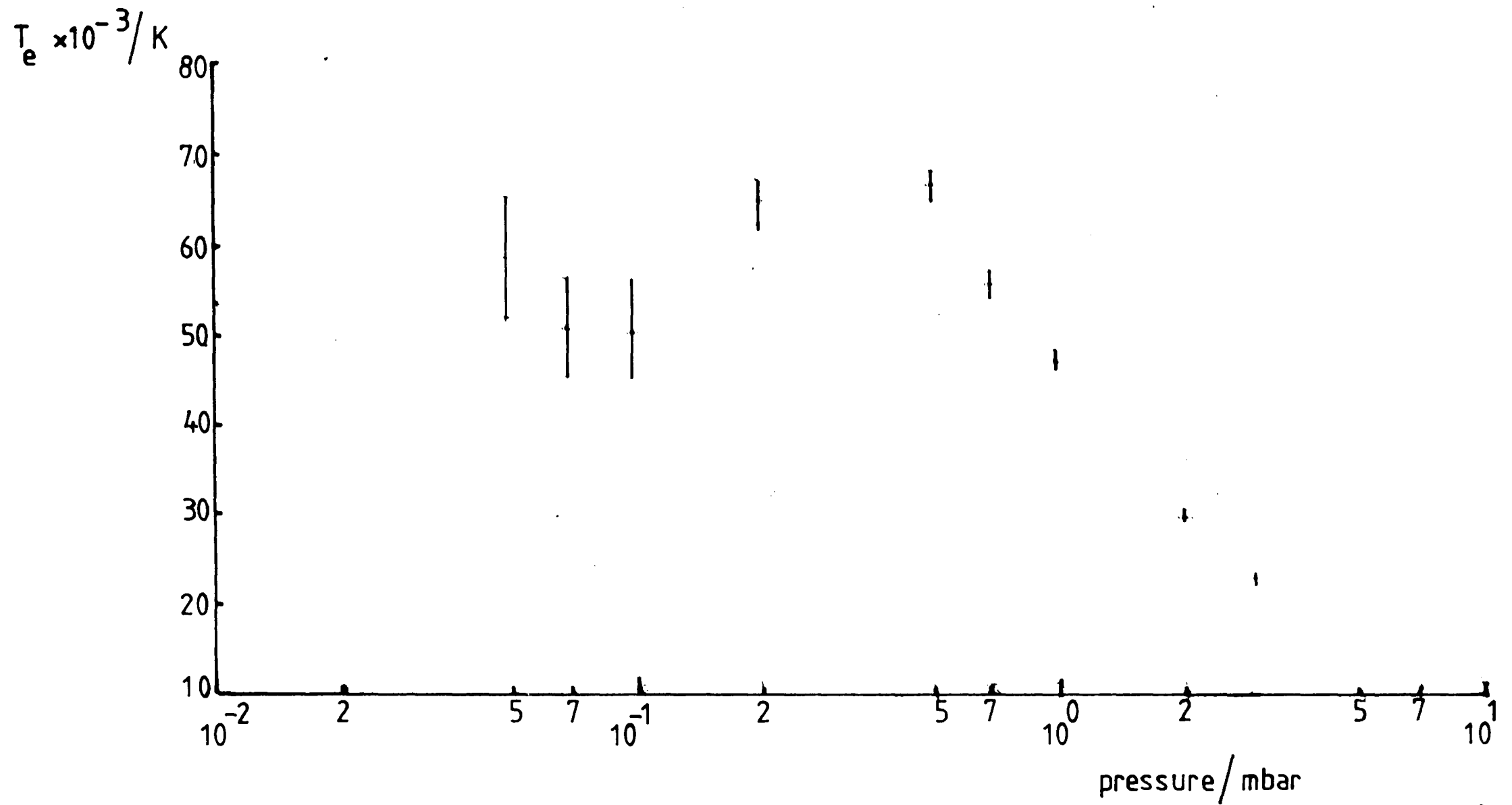


Figure 7.4b Variation of electron temperature with pressure. Magnetron current 50mA.

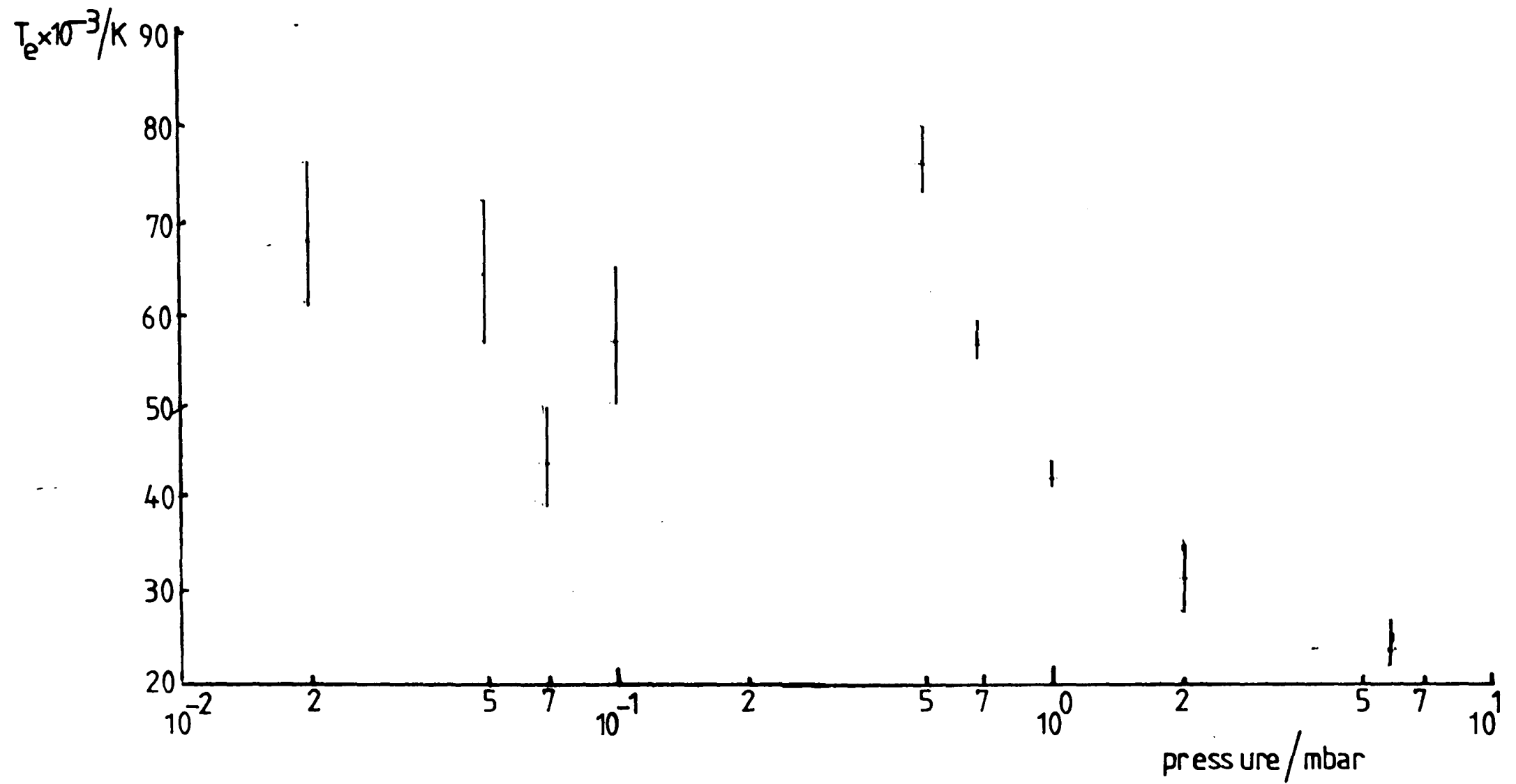


Figure 7.4c Variation of electron temperature with pressure. Magnetron current 100mA .

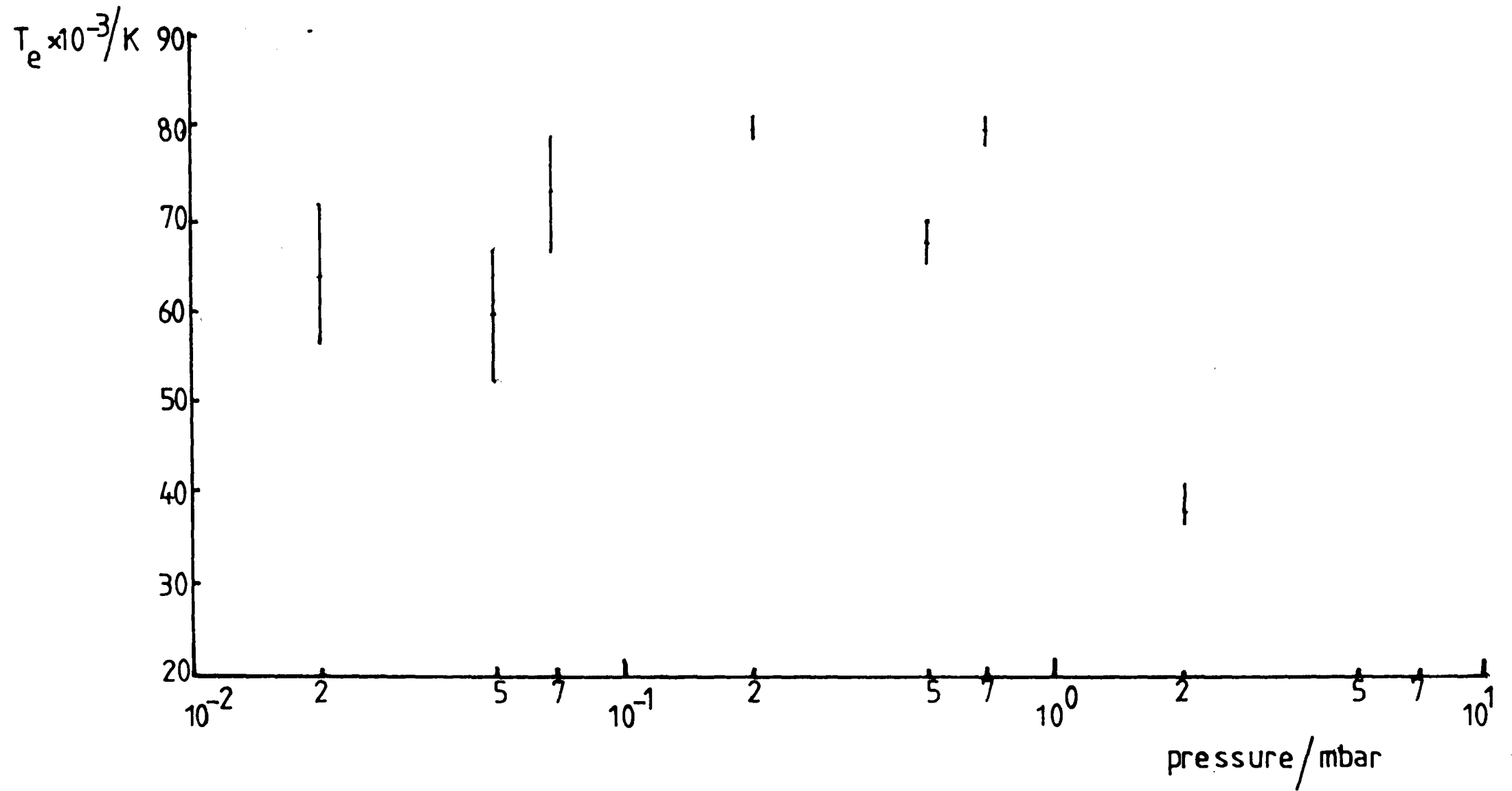


Figure 7.4d Variation of electron temperature with pressure. Magnetron current 150mA.

pressure range 0.1 mbar to 0.5 mbar, with a rapid drop in T_e towards the higher pressures and a gentle increase towards the lower pressures. The effect of an increase in magnetron current is to increase the value of T_e at all pressures.

7.2.2 Variation of T_e with power and pressure

The non-independence of pressure and net input power has already been mentioned in section 6.6. For this reason, the form of variation of electron temperature with net input power to the plasma also depends upon the gas pressure. Values of T_e plotted against net input power for pressures of 3.0 to 0.07 mbar are shown in fig. 7.5. The general form of the curves is similar for all but that at 0.5 mbar which possesses a maximum rather than minimum turning point, and at 0.2 mbar which possesses both. As the electron temperature derived from probe characteristics is a measure of the mean energy of the electron distribution, this may be indicative of a change in the process responsible for the production of free electrons, especially when consideration is given to the fact that 0.5 mbar was the highest pressure for which the argon ion levels were sufficiently excited to be detected spectroscopically.

By reading the values of T_e for different pressures at a given input power from fig. 7.5, a graph of T_e against pressure, for normalised input power, may be obtained. This is presented in fig. 7.6. It is now clear that the peak in electron temperature occurs at 0.2 mbar for input powers of 40 and 50W but at 0.5 mbar for input powers of 25 and 30W. It is also clear that the relative increase in electron

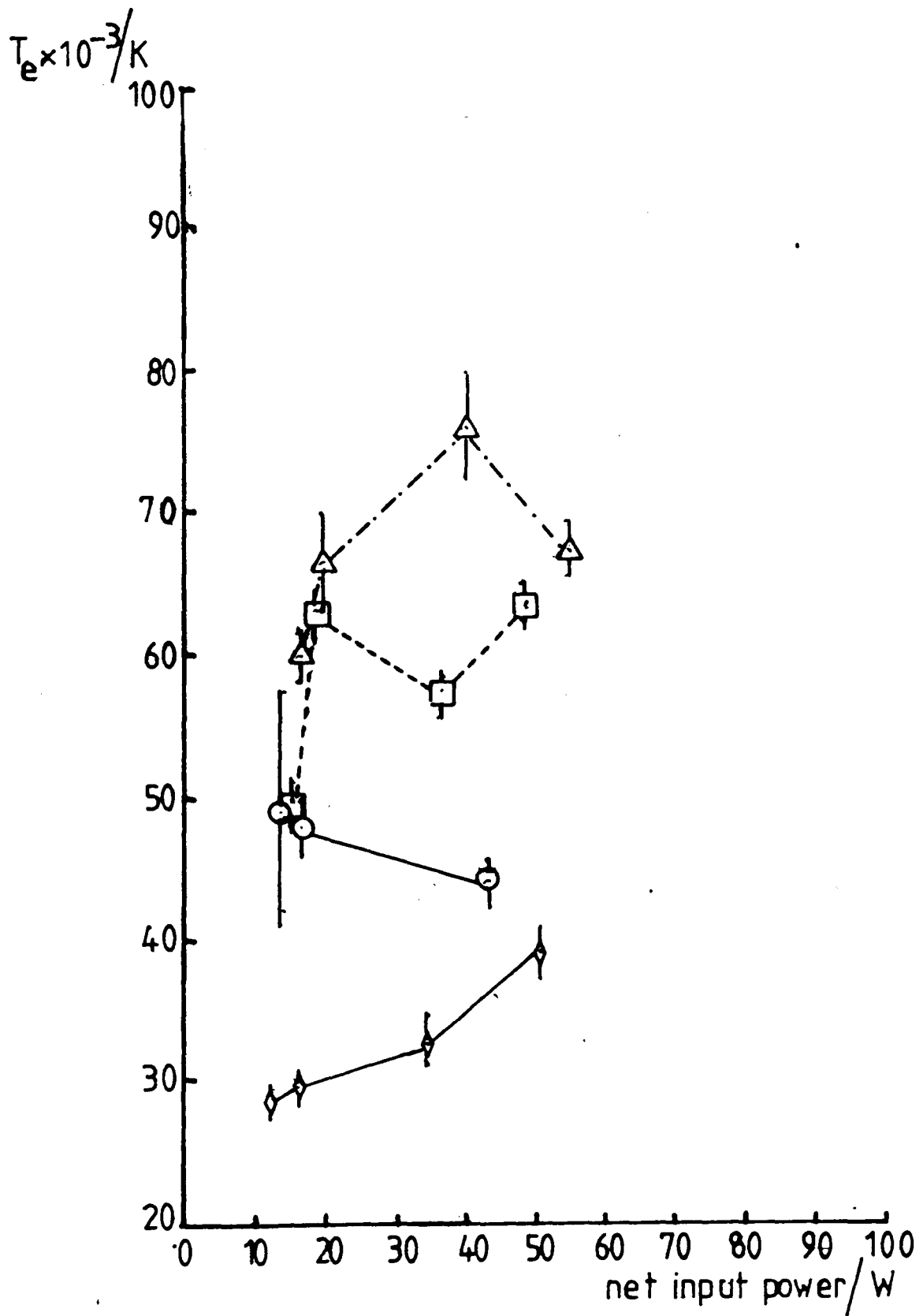


Figure 7.5a Electron temperature as a function of input power.

Pressures in mbar: \diamond 2.00, \circ 1.00, \square 0.70, \triangle 0.50.

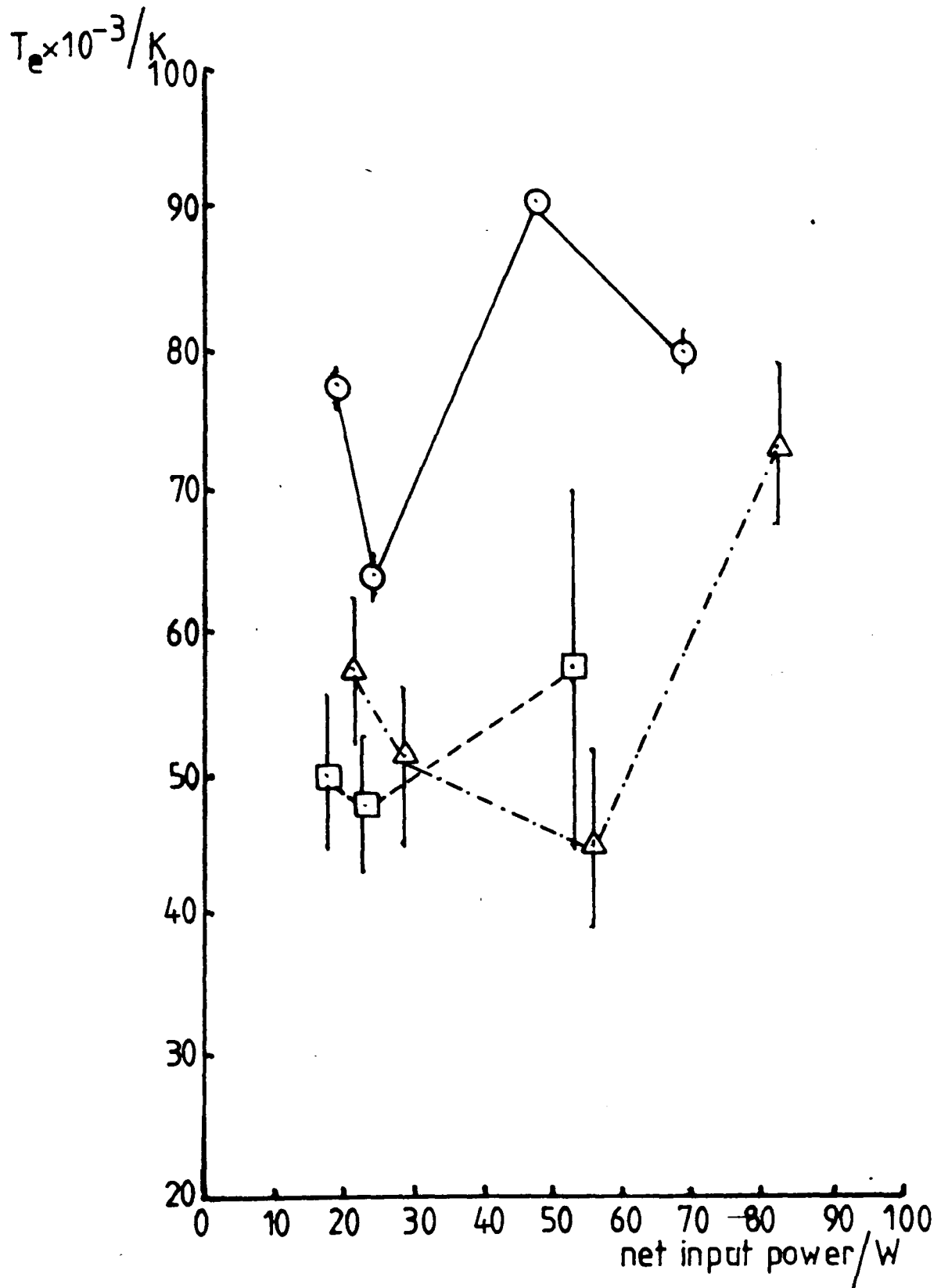


Figure 7.5b Electron temperature as a function of input power.

Pressures in mbar: \circ 0.20, \square 0.10, \triangle 0.07.

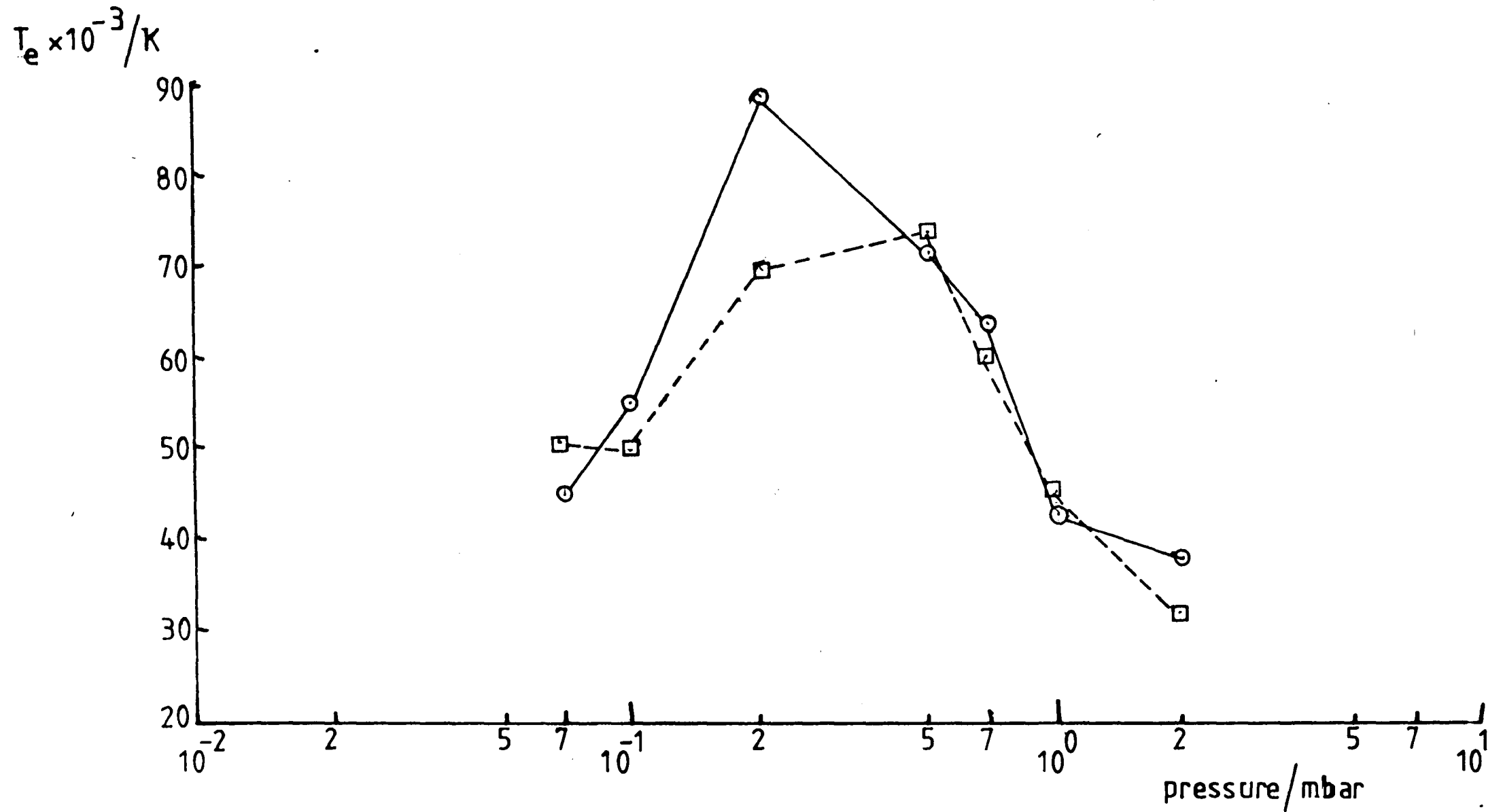


Figure 7.6a Variation of electron temperature with pressure. Normalised input powers: \circ 50W, \square 30W

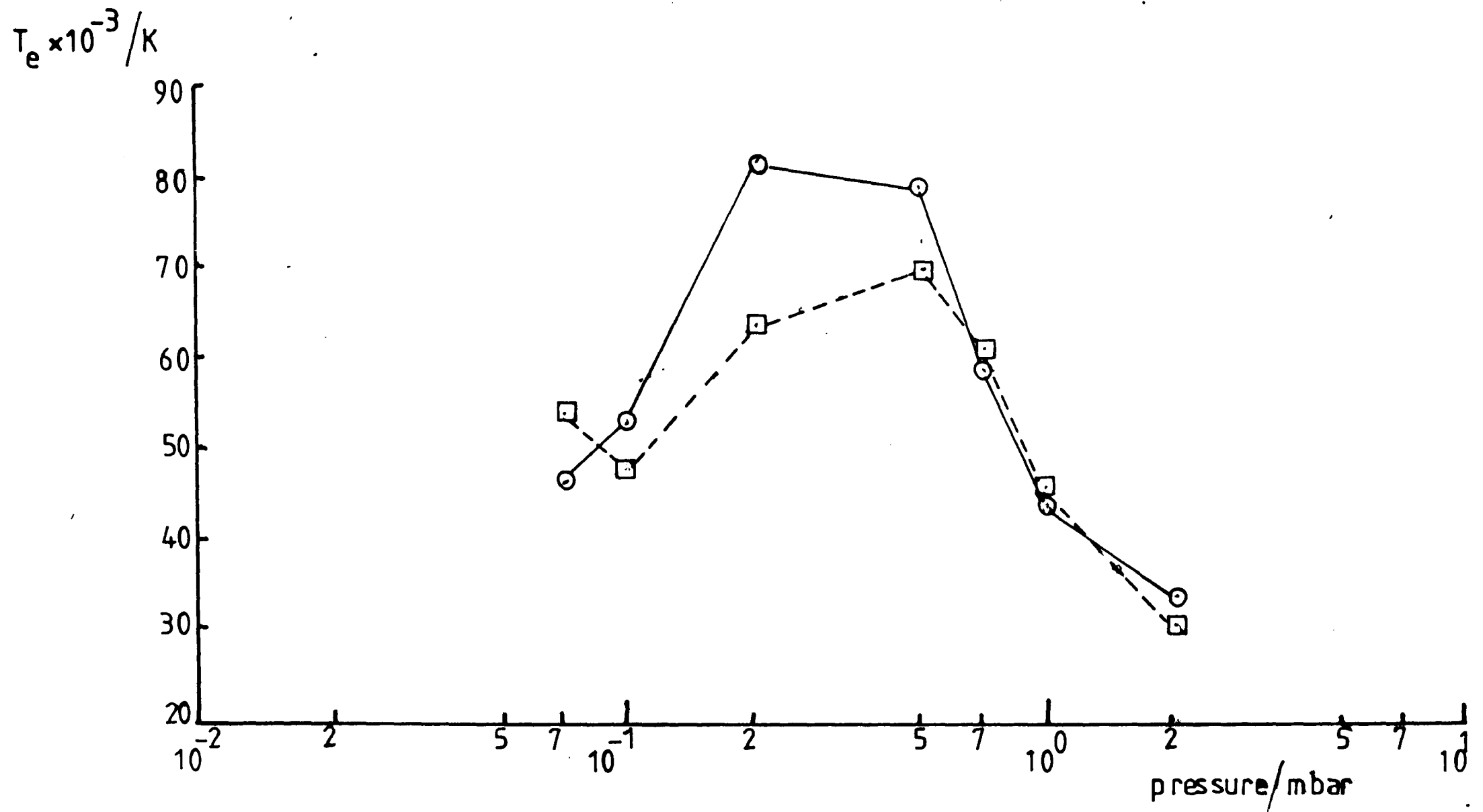


Figure 7.6b Variation of electron temperature with pressure. Normalised input powers: \circ 40W, \square 25W.

temperature with power is most marked at a pressure of 0.2 mbar.

7.2.3 Calculation of Carrier Density, n_+

The values of electron temperature tabulated in table 7.1 were substituted into equation 5.9. The ion current i_+ was taken as the average value of i_{+1} and i_{+2} . The use of equation 5.9 is, strictly speaking, only valid when the ion flux to the probe is "sheath limited" (Swift & Schwar 1970). The distinction between "sheath" and "orbital" limits is vague and arises from a consideration of the orbital motions of the ions around the probe. Calculation of the Debye length λ_D from the equation

$$\lambda_D = \left(\frac{\epsilon_0 k T_e}{n_e e^2} \right)^{\frac{1}{2}} \quad 7.1$$

(Mitchner & Kruger 1973) showed that the ratio r_p/λ_D (where r_p is the probe radius) varied from approximately 10 to 53 so that the approximation $A_s = A_p$ would not introduce any sizeable error. (The Debye length can be considered as representative of the positive ion sheath radius around the probe).

Furthermore since r_p/λ_D is never less than ten, the condition stipulated by Swift & Schwar for a "sheath limited" ion flux is fulfilled and hence the use of equation 5.9 is justified.

The carrier mean free path length ℓ was then calculated for both electrons and the argon ion. The ion mean free path length ℓ_+ was estimated from the hard sphere approximation

$$\ell_+ = \frac{1}{\sqrt{2} \pi n d^2} \quad 7.2$$

where n is the number of atoms and d is the atomic diameter of argon ($d \approx 3.82 \times 10^{-10}$ m Am. Inst Phys. Handbook). For electrons, it was first necessary to determine the electron temperature at which inelastic excitation of the argon atom by collision with electrons becomes important. The mean relative speed v of the electrons and argon atoms is given by

$$v = \left(\frac{8kT_e}{\pi M_e} \right)^{\frac{1}{2}} \quad 7.3$$

For excitation to the metastable level an energy in excess of 11.5 eV is required. However, the metastable levels of the argon atom derive much of their populations by de-excitation from higher levels and so a more reasonable estimation would be obtained by considering excitations from the metastable levels to the 4p levels. This transition requires energies in excess of 1.2 eV, equivalent to a temperature of 14 400K. Thus inelastic collisions could be expected to contribute to the cross-section. From existing data (Mitchner & Kruger 1973) the inelastic cross-section is typically some two orders of magnitude smaller than the total elastic cross-section. As the equations used to evaluate the electron mean free path length, ℓ_e , is itself an approximation, it was considered unnecessary to include inelastic collisions in the calculation.

The electron mean free path length was calculated from

$$\ell_e = \frac{1}{n Q(T_e)} \quad 7.4$$

where $Q(T_e)$ is the total elastic cross-section. The values of mean

free path lengths calculated indicated that $\ell_e > \lambda_D$ and $\ell_+ > \lambda_D$ and so it is reasonable to assume that no collisions between atoms and electrons or ions occur within the sheath region.

The values of carrier density calculated from equation 5.9 are tabulated in table 7.2. Figures 7.7(a) to (d) show the variation of (ion) carrier density with pressure for each magnetron current.

Although all the curves show the same general features of a steadily increasing value of ion density, n_+ , with pressure, there are two distinct forms of curve. For magnetron currents of 100 and 150 mA, the curves rise smoothly with pressure. For magnetron currents of 40 and 50 mA, the curves show a sudden increase between pressures of 0.1 and 0.2 mbar. Despite this variation in the form of the curve, the actual values of n_+ show little variation with magnetron current.

The values of n_+ for a given pressure vary only by a maximum factor of three (at a pressure of 2.0 mbar between magnetron currents of 50 and 100 mA). This almost constant value of carrier density was not unexpected as the discharge is unrestricted in length. Thus as more electron-ion pairs are generated, the discharge is free to expand in length keeping the ion density almost constant.

7.2.4 Variation of n_+ with power and pressure

As for the electron temperature, the interdependence of pressure and input power must be eliminated from the carrier density measurements before interpretation can be considered.

It should be stated here that equation 5.9 measures the ion density, n_+ , and only by assuming some relationship between n_+ and the electron

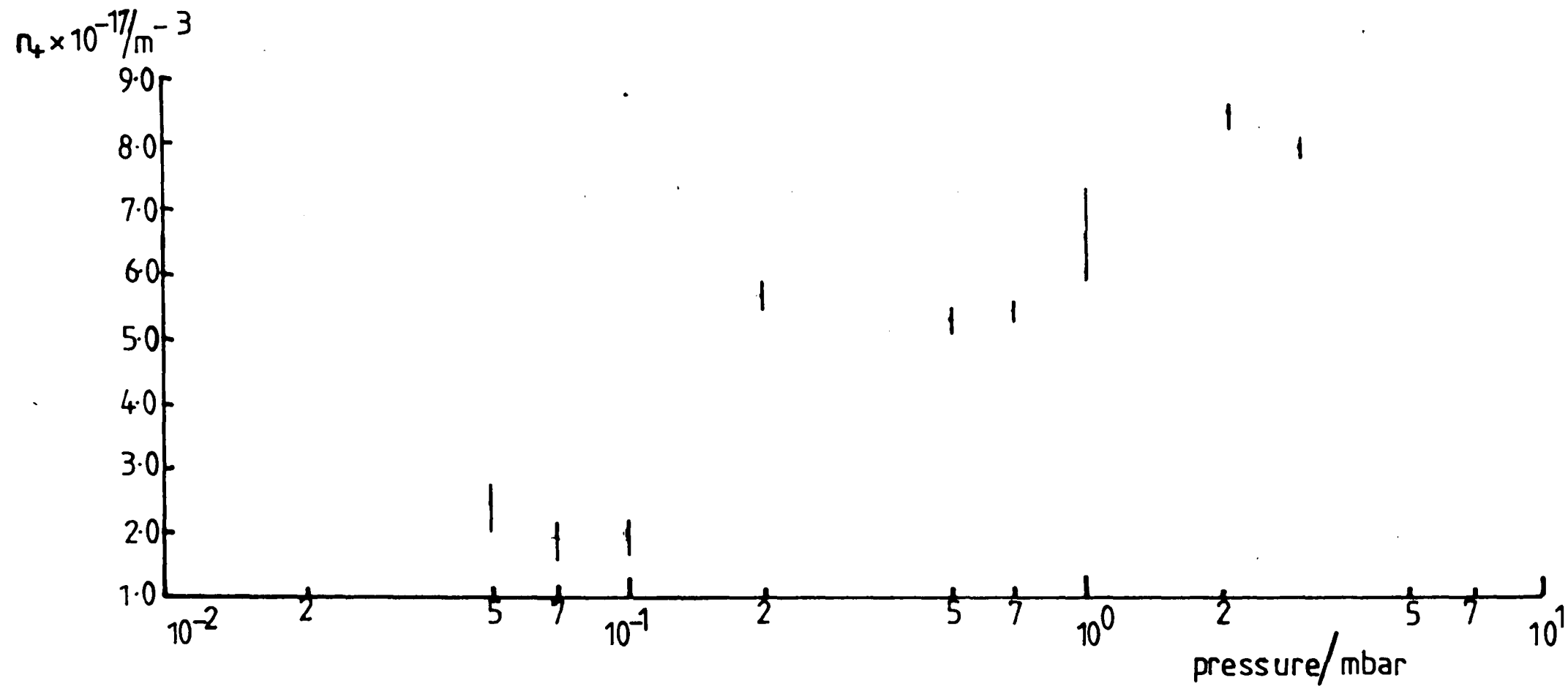


Figure 7.7a Ion density as a function of pressure. Magnetron current 40mA.

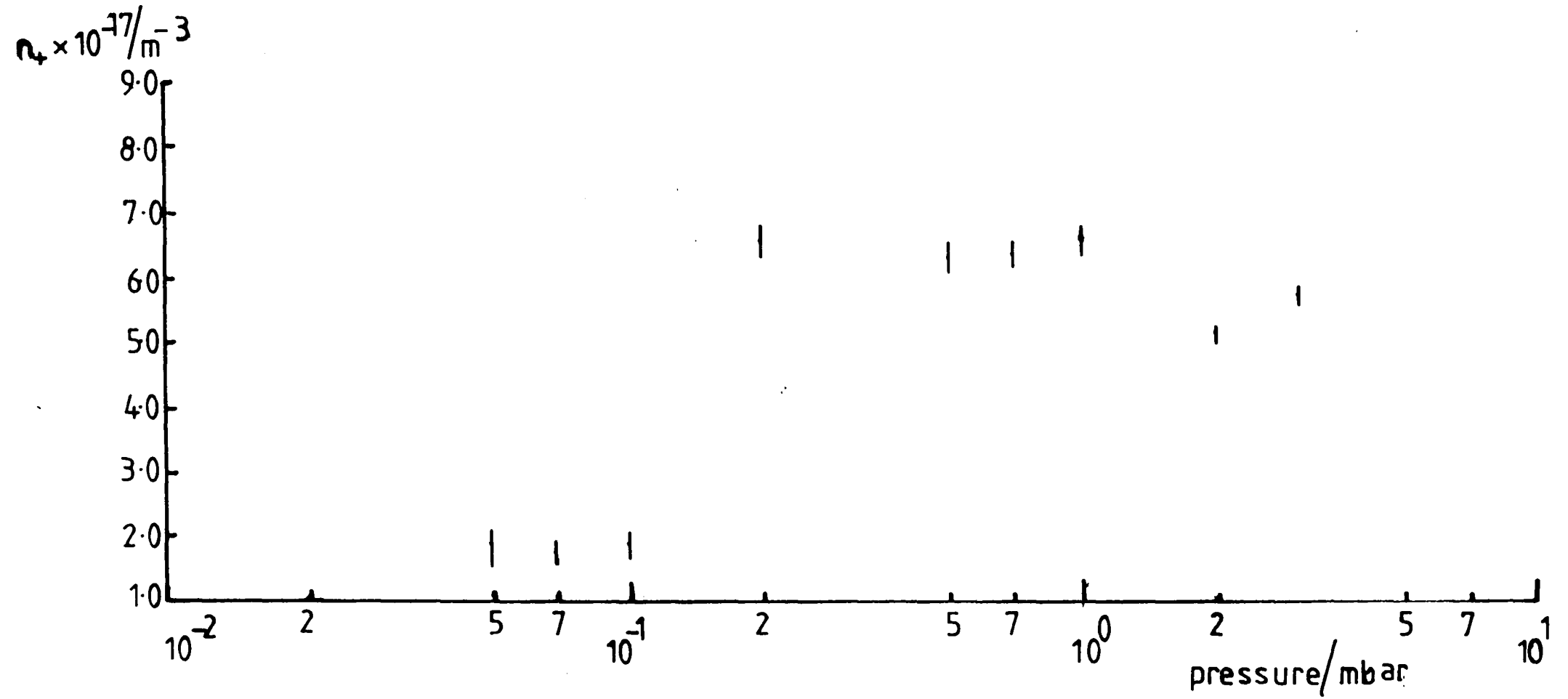


Figure 7.7b Ion density as a function of pressure. Magnetron current 50mA.

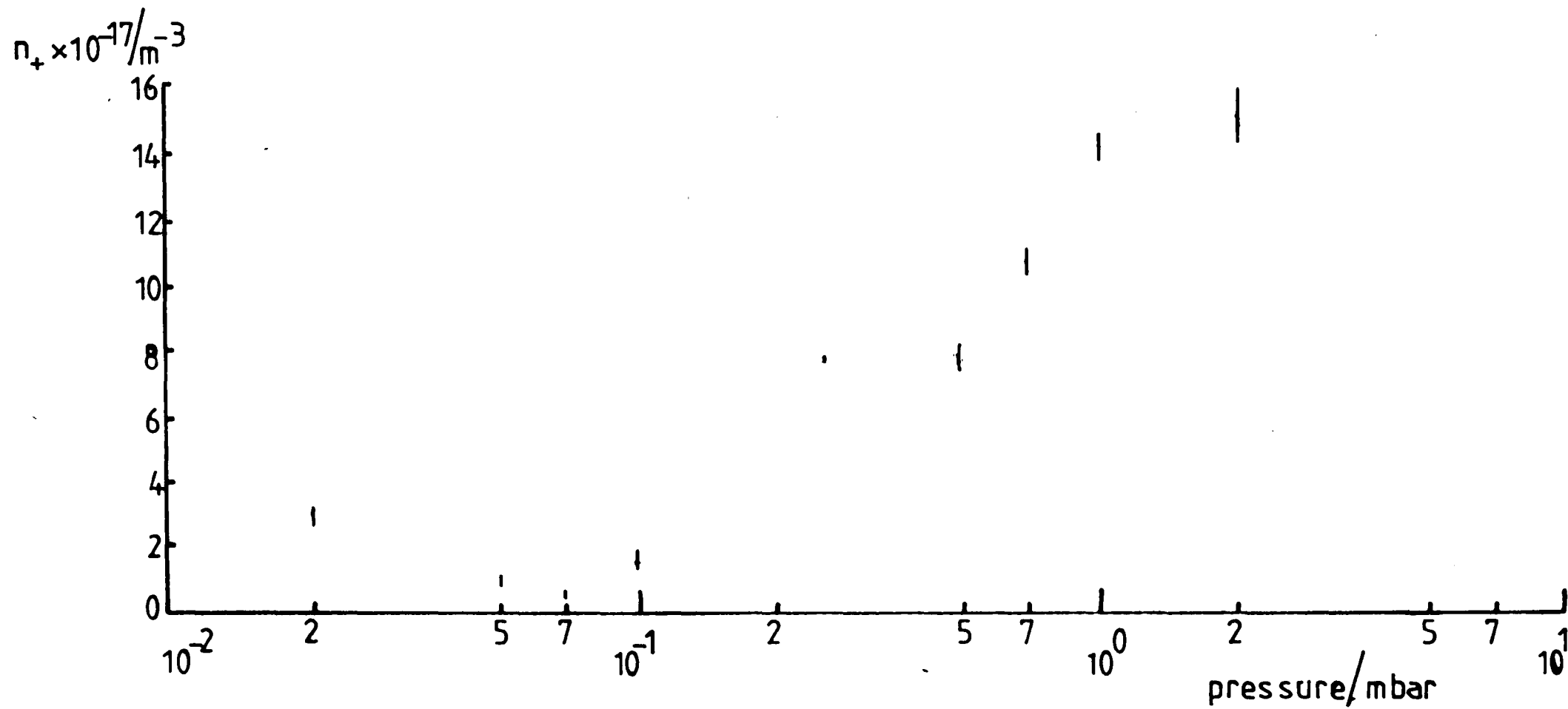


Figure 7.7c Ion density as a function of pressure. Magnetron current 100mA.

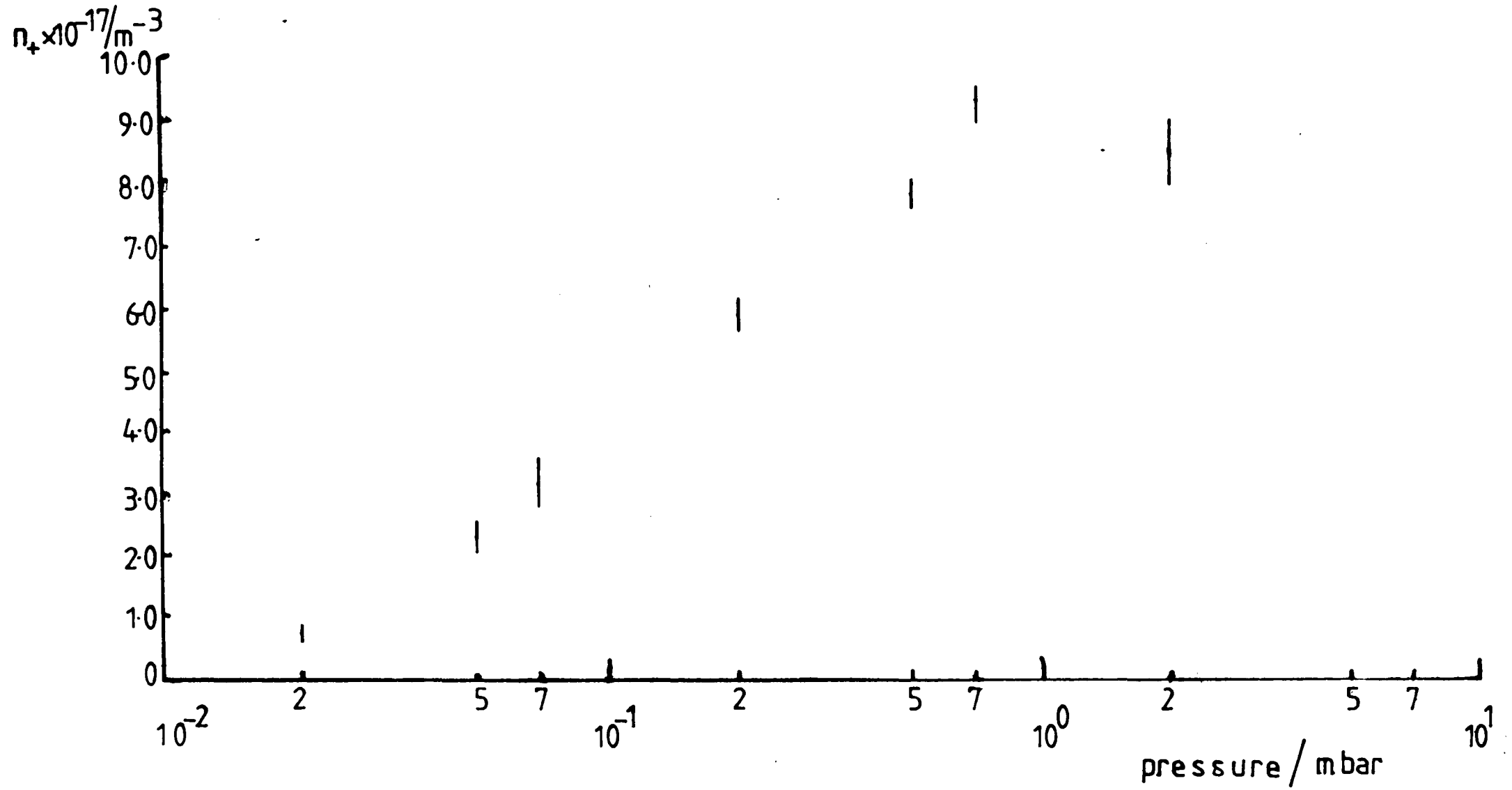


Figure 7.7d Ion density as a function of pressure. Magnetron current 150mA.

density, n_e , can these results be used to infer an electron density. It does not necessarily follow, particularly in a narrow bore tube, that electrical neutrality is maintained. Thus the assumption that

$$n_+ = n_e \qquad 7.5$$

is not necessarily valid.

The measured values of ion density, n_+ , are presented in fig. 7.8, as a function of net input power. The values of n_+ are those derived from the two pairs of probes closest to the cavity. It can be seen from fig. 7.8 that the form of the n_+ vs input power curve changes between pressures of 0.7 and 0.5 mbar, assuming that the 1.0 mbar curve follows the same form as the 2.0 and 0.7 mbar curves.

From fig. 7.8 the variation of ion density with pressure, normalised for a given input power, may be obtained. This is shown in fig. 7.9. Eliminating the power dependence reduces the maximum variation of the n_+ values to a factor of two. Perhaps unexpectedly, the value of n_+ is lowest for the greatest input power for most values of pressure. This may be due to diffusion or recombination effects and clearly, at the lowest pressures, where the mean free path is longest, the lower powers give the greatest n_+ values.

The two forms of curve observed in figs. 7.7(a) to (d) are represented in fig. 7.9 where, between the pressures of 0.2 and 0.5 mbar, a gradual transition between the two forms of curve can be observed.

It should be noted that the form of 7.9 does not conform readily with

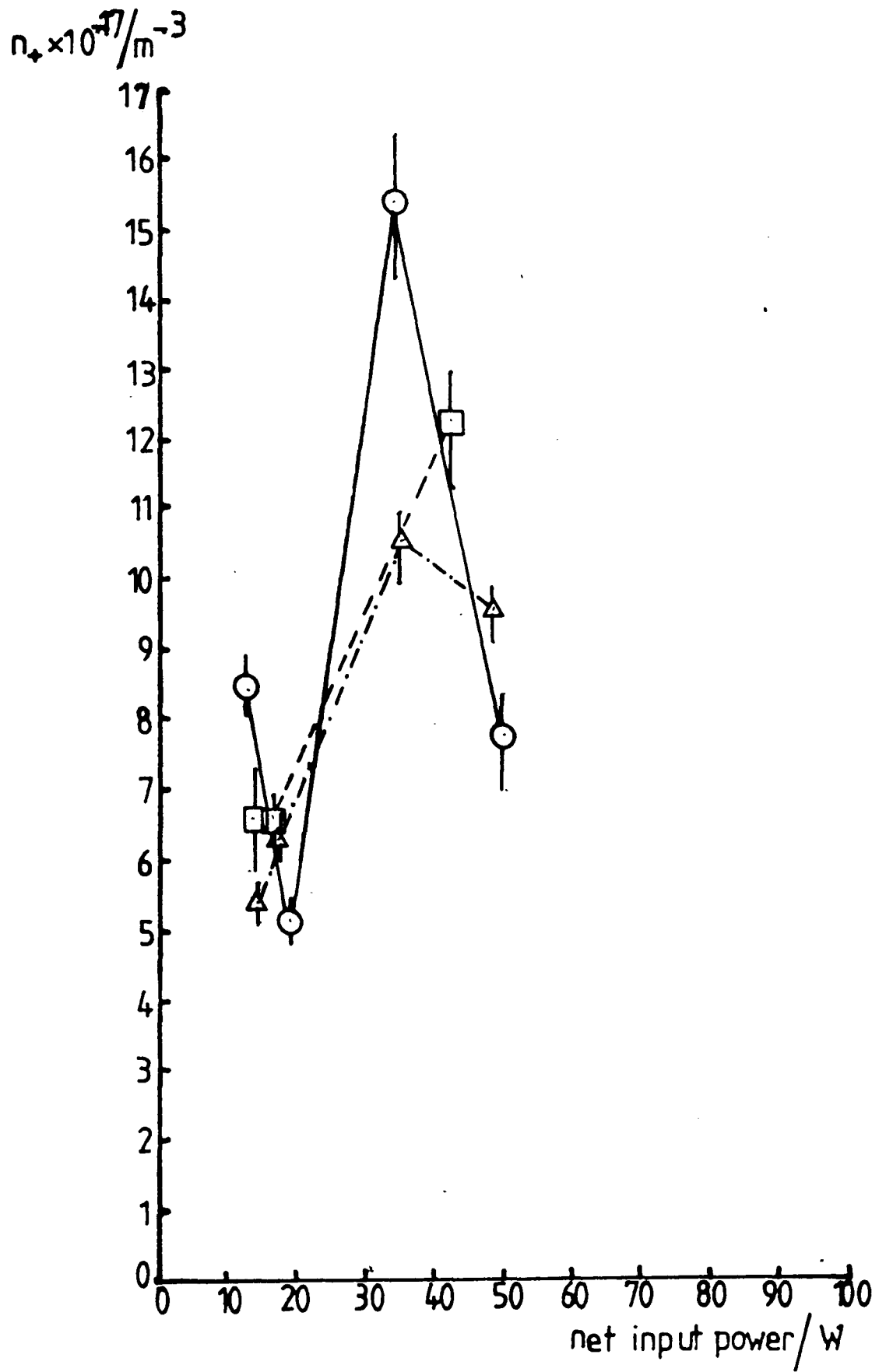


Figure 7.8a Variation of ion density with input power.
 Pressures in mbar: \circ 2.00, \square 1.00, \triangle 0.70.

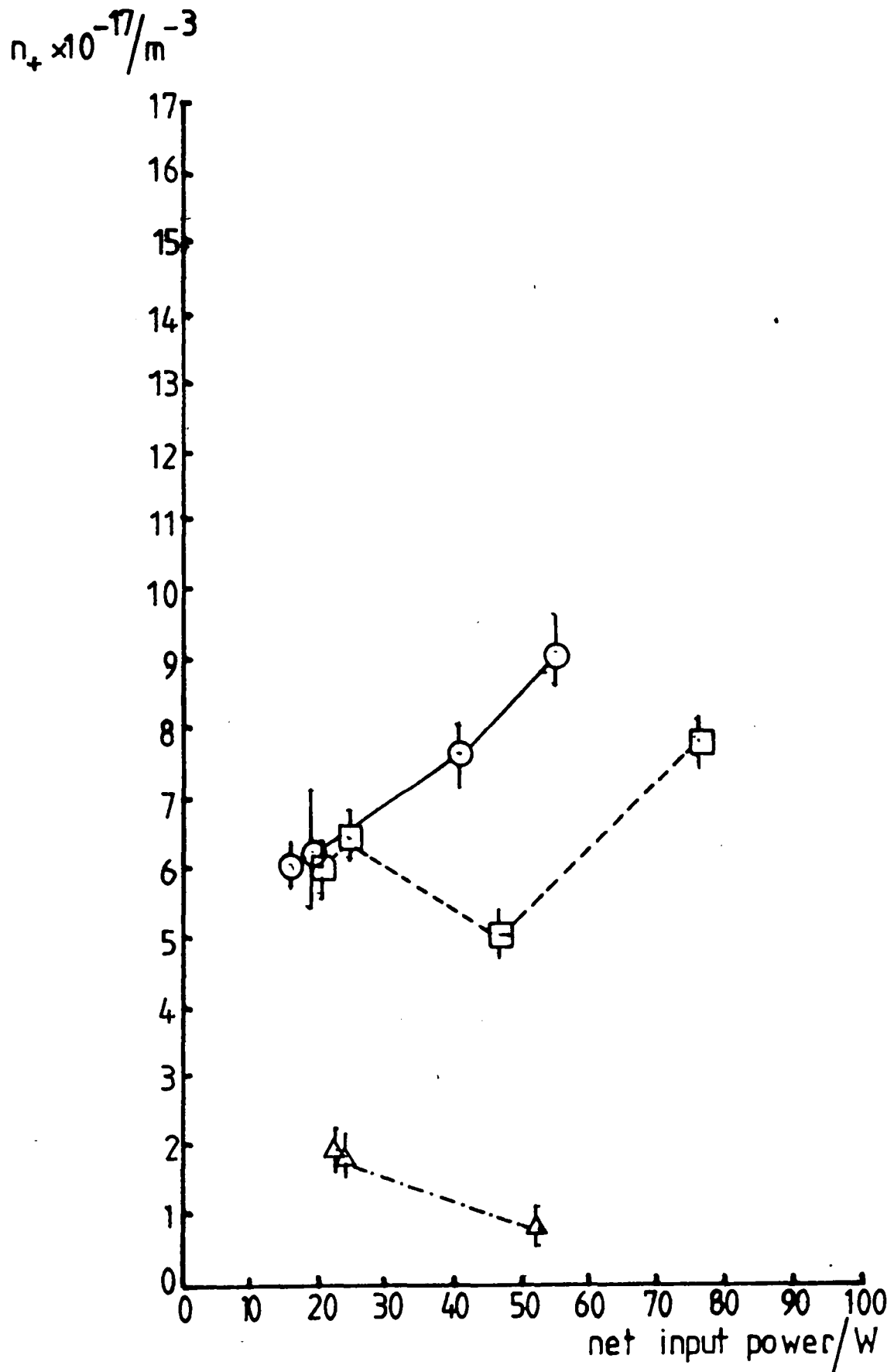


Figure 7.8b Variation of ion density with input power.
 Pressures in mbar: \circ 0.50, \square 0.20, \triangle 0.10.

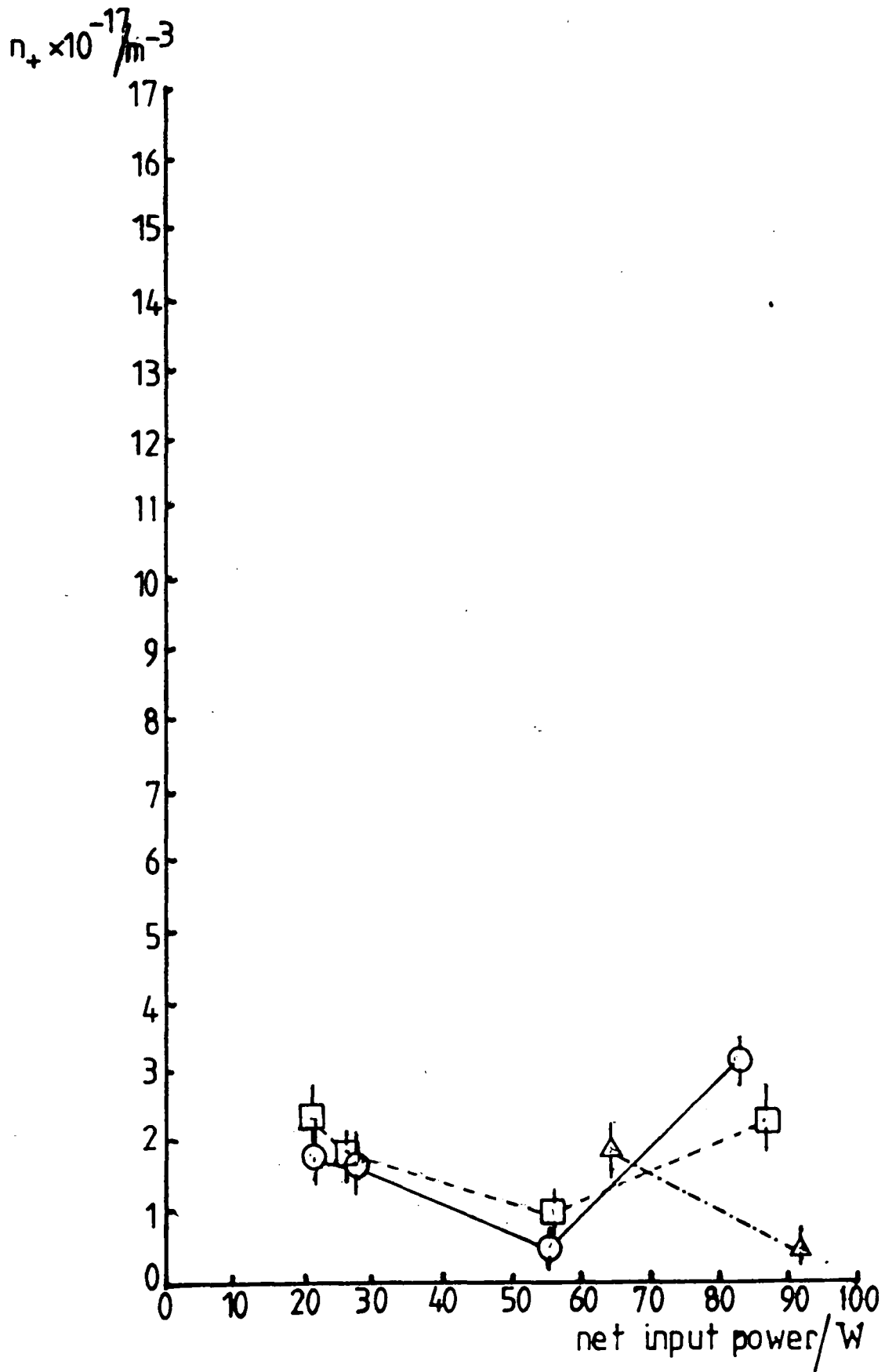


Figure 7.8c Variation of ion density with input power.
 Pressures in mbar: \circ 0.07, \square 0.05, \triangle 0.02.

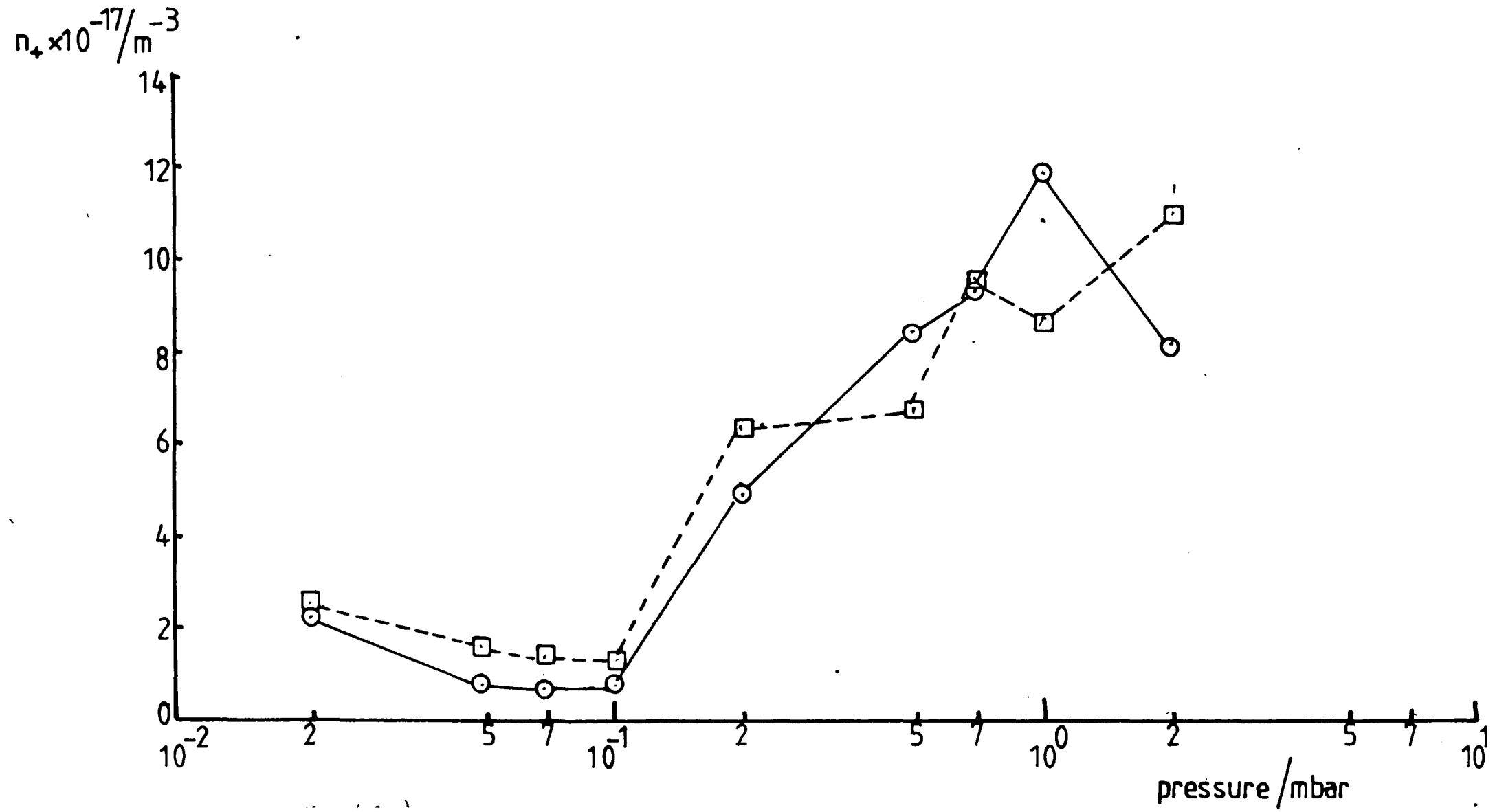


Figure 7.9a Ion density as a function of pressure. Normalised input powers: \circ 50W, \square 30W

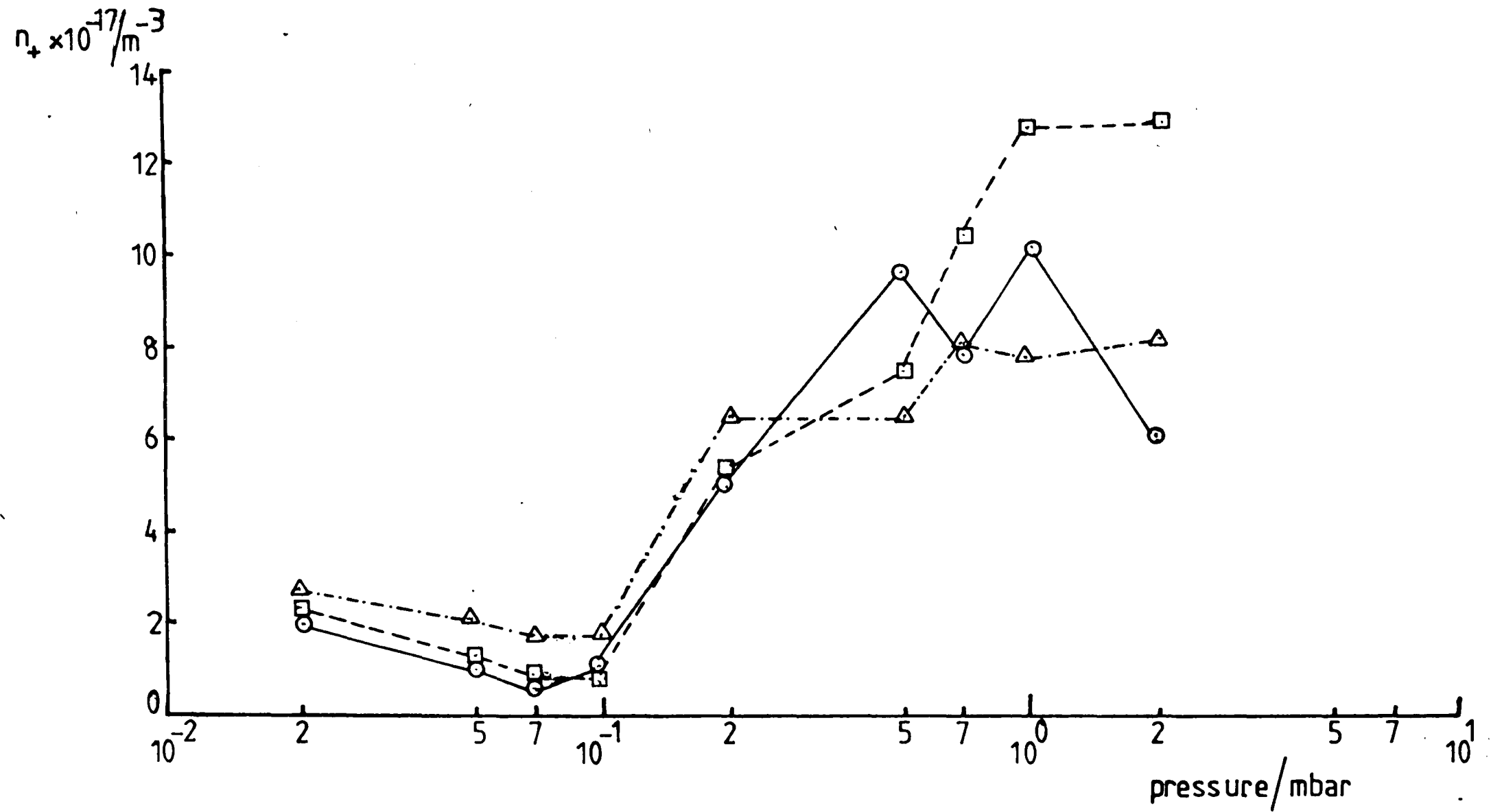


Figure 7.9b Ion density as a function of pressure. Normalised input powers: \circ 60W, \square 40W, \triangle 25W.

the results of the argon ion population densities of chapter 6. However, the results of section 6.8 imply that the assumption of a Maxwellian distribution function may not be valid. Since the form of the distribution function is an essential element in the derivation of the double floating probe equations, any variation of the ion and electron distributions from the Maxwellian would have serious consequences for the applicability of equations 5.2 to 5.9.

7.3 Variation of T_e and n_+ with Distance from the Cavity

As stated in section 7.1, the restriction in length of the discharge prevented comprehensive data from the more distant probes being obtained. It was possible, at certain pressures, to obtain characteristics from the probes situated at distances of 6 and 9 cm from the cavity centre. The results of these measurements are tabulated in table 7.3, together with the corresponding results from the probes 3 cm distant from the cavity centre.

As can be seen there appears to be little variation of T_e with distance until the lowest pressure of 0.5 mbar is reached. An interesting feature is the increase in T_e at a distance of 9 cm for the 2.00 mbar, 150 mA results. For the ion density, the results show that the ion density generally decreases with distance from the cavity.

Table 7.3 Variation of T_e and n_+ with Distance from Cavity Centre

Magnetron current = 100 mA		Electron Temperature (K)		
Distance/cm	3	6	9	
Pressure/mbar				
6.00	-	24511 ⁺ 2696	-	
3.00	-	33705 ⁺ 3708	-	
2.00	32137 ⁺ 2250	32496 ⁺ 1300	-	
1.00	43820 ⁺ 1753	42239 ⁺ 2112	-	
0.50	76307 ⁺ 3815	49798 ⁺ 1992	-	
Ion Density (10^{17} m^{-3})				
Distance/cm	3	6	9	
Pressure/mbar				
6.00	-	1.0 ⁺ 0.1	-	
3.00	-	0.8 ⁺ 0.2	-	
2.00	15.4 ⁺ 1.1	5.7 ⁺ 0.3	-	
1.00	12.3 ⁺ 0.5	5.9 ⁺ 0.3	-	
0.50	10.6 ⁺ 0.4	4.5 ⁺ 0.2	-	
Magnetron current = 150 mA		Electron Temperature (K)		
Distance/cm	3	6	9	
Pressure/mbar				
6.00	-	30497 ⁺ 3965	-	
3.00	-	31353 ⁺ 4389	-	
2.00	38886 ⁺ 1944	33665 ⁺ 673	50334 ⁺ 503	
0.70	63654 ⁺ 1273	63639 ⁺ 3182	-	
Ion Density (10^{17} m^{-3})				
Distance/cm	3	6	9	
Pressure/mbar				
6.00	-	1.8 ⁺ 0.3	-	
3.00	-	1.6 ⁺ 0.3	-	
2.00	7.8 ⁺ 0.6	7.4 ⁺ 0.2	5.43 ⁺ 0.05	
0.70	9.5 ⁺ 0.3	3.2 ⁺ 0.3	-	

CHAPTER 8
MICROWAVE RESULTS

8.1 Calculation of the Microwave Impedance

The microwave impedance, Z , of the plasma was calculated from equation 3.14 using the values of the voltage standing wave ratio calculated from equation 3.15. The impedance was evaluated by the computer programme MDATA3 given in appendix II. The impedance was expressed in terms of resistive and reactive components in addition to the modulus of this complex impedance. An impedance value was calculated for each voltage standing wave ratio minimum on the slotted line. Thus six values of Z were calculated for each combination of pressure and magnetron current. The values of impedance tabulated in table 8.1 are the averages of these six impedance measurements.

The variation of microwave impedance with pressure for four magnetron currents are shown in figures 8.1(a) to (d) for the results of the probe tube and in fig. 8.1(e) for the plain tube with a magnetron current of 100 mA. The figs 8.1(a) to (d) all show a slight decrease of impedance with decreasing pressure until a pressure between 0.1 and 0.07 mbar is reached. Between these points a sudden increase in impedance occurs.

It is notable that in all cases except for 150 mA magnetron current, the maximum impedance coincides with the minimum ion density calculated from the probe characteristics. The absence of probe data at 0.1 mbar pressure for the 150 mA magnetron current is due to the failure of the probe characteristics to saturate, implying that n_+ would be large. This correlates with the minimum value of $|Z|$

Table 8.1 Measured Impedance Values (Z/Ω)

Values are for probe tube

Magnetron Current/mA	40	50	100	150
Pressure/mbar				
6.00	98.8 \pm 0.2	151.91 \pm 0.02	149.75 \pm 0.02	185.82 \pm 0.0
3.00	149.15 \pm 0.03	154.88 \pm 0.01	155.198 \pm 0.01	161.46 \pm 0.0
2.00	145.11 \pm 0.02	152.54 \pm 0.03	190.770 \pm 0.003	191.80 \pm 0.0
1.00	131.92 \pm 0.04	132.06 \pm 0.07	180.472 \pm 0.007	180.36 \pm 0.0
0.70	128.65 \pm 0.08	122.77 \pm 0.08	167.66 \pm 0.02	175.60 \pm 0.0
0.50	113.68 \pm 0.08	119.55 \pm 0.08	163.00 \pm 0.03	172.72 \pm 0.0
0.20	116.3 \pm 0.9	93.1 \pm 0.4	128.0 \pm 0.1	140.88 \pm 0.0
0.10	315.5 \pm 1.1	133.56 \pm 0.04	116.0 \pm 2.0	101.7 \pm 0.5
0.07	224.5 \pm 0.1	286.2 \pm 0.4	591.0 \pm 5.0	252.8 \pm 0.2
0.05	-	195.5 \pm 0.2	398.0 \pm 1.0	453.0 \pm 4.0
0.02	-	-	332.8 \pm 0.4	371.0 \pm 1.0

Table 8.2 Calculated Values of Electron Density ($n_e \times 10^{-18}/m^{-3}$)

Values are for probe tube

Magnetron Current/mA	40	50	100	150
Pressure/mbar				
6.00	1.730 \pm 0.004	1.12 \pm 1 $\times 10^{-4}$	1.14 \pm 2 $\times 10^{-4}$	0.983 \pm 0.00
3.00	1.140 \pm 0.0003	1.110 \pm 8 $\times 10^{-5}$	1.10 \pm 6 $\times 10^{-5}$	1.026 \pm 0.00
2.00	1.19667 \pm 3 $\times 10^{-5}$	1.14 \pm 3 $\times 10^{-4}$	0.887 \pm 0.0001	0.891 \pm 0.00
1.00	1.3075 \pm 2 $\times 10^{-4}$	1.295 \pm 9 $\times 10^{-4}$	0.944 \pm 0.0003	0.948 \pm 0.00
0.70	1.325 \pm 0.001	1.390 \pm 1 $\times 10^{-3}$	1.01 \pm 1 $\times 10^{-4}$	0.975 \pm 0.00
0.50	1.52 \pm 0.002	1.440 \pm 1 $\times 10^{-3}$	1.06 \pm 2 $\times 10^{-3}$	0.986 \pm 0.00
0.20	1.46 \pm 0.01	1.53 \pm 0.01	1.34 \pm 1 $\times 10^{-3}$	1.22 \pm 0.01
0.10	0.542 \pm 0.002	1.27 \pm 4 $\times 10^{-4}$	1.48 \pm 0.03	1.68 \pm 0.02
0.07	0.7560 \pm 3 $\times 10^{-4}$	0.593 \pm 0.008	0.290 \pm 0.002	0.68 \pm 0.02
0.05	-	0.859 \pm 0.009	0.427 \pm 0.001	0.377 \pm 0.00
0.02	-	-	0.511 \pm 6 $\times 10^{-4}$	0.461 \pm 0.00

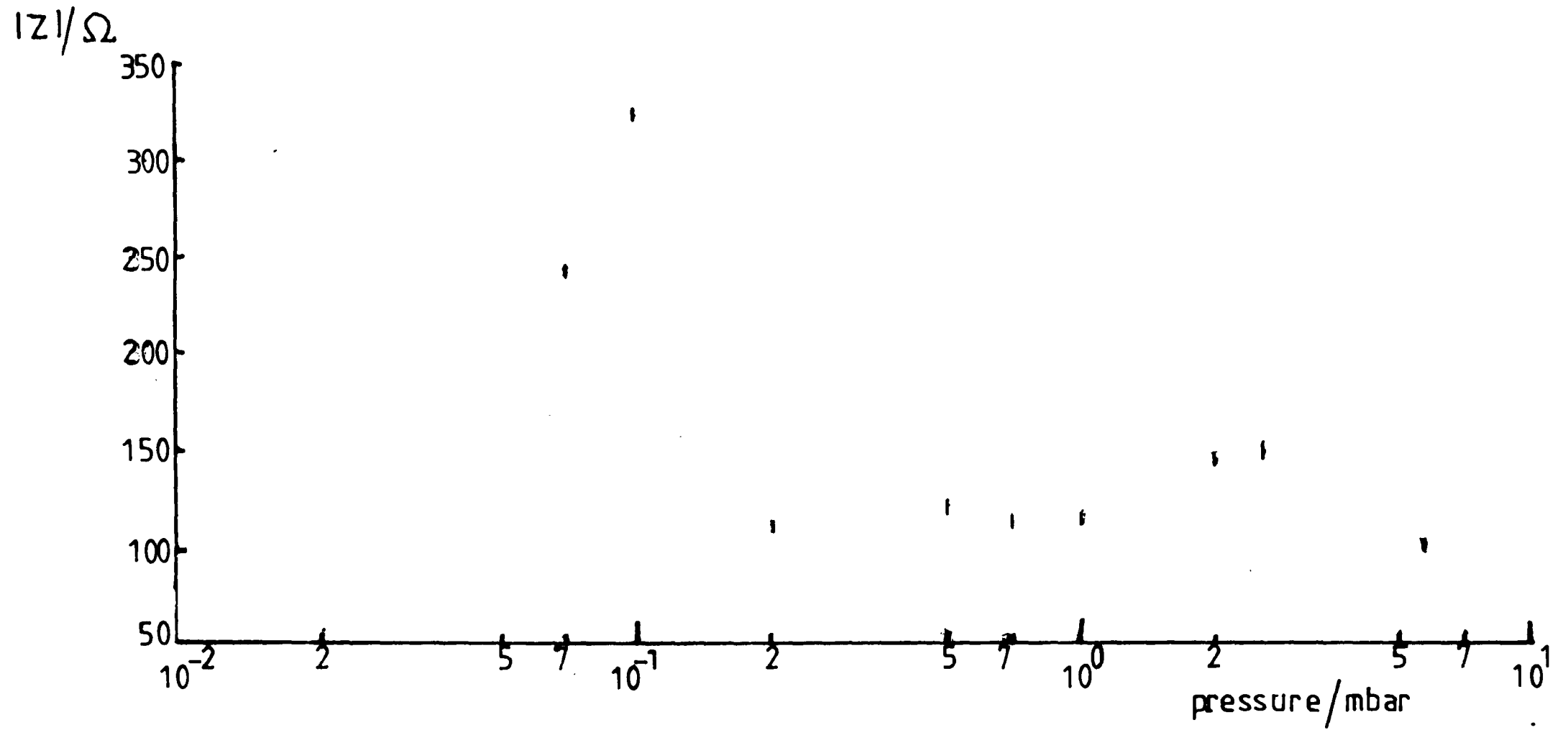


Figure 8.1a Variation of microwave impedance with pressure for probe discharge tube.
Magnetron current 40mA.

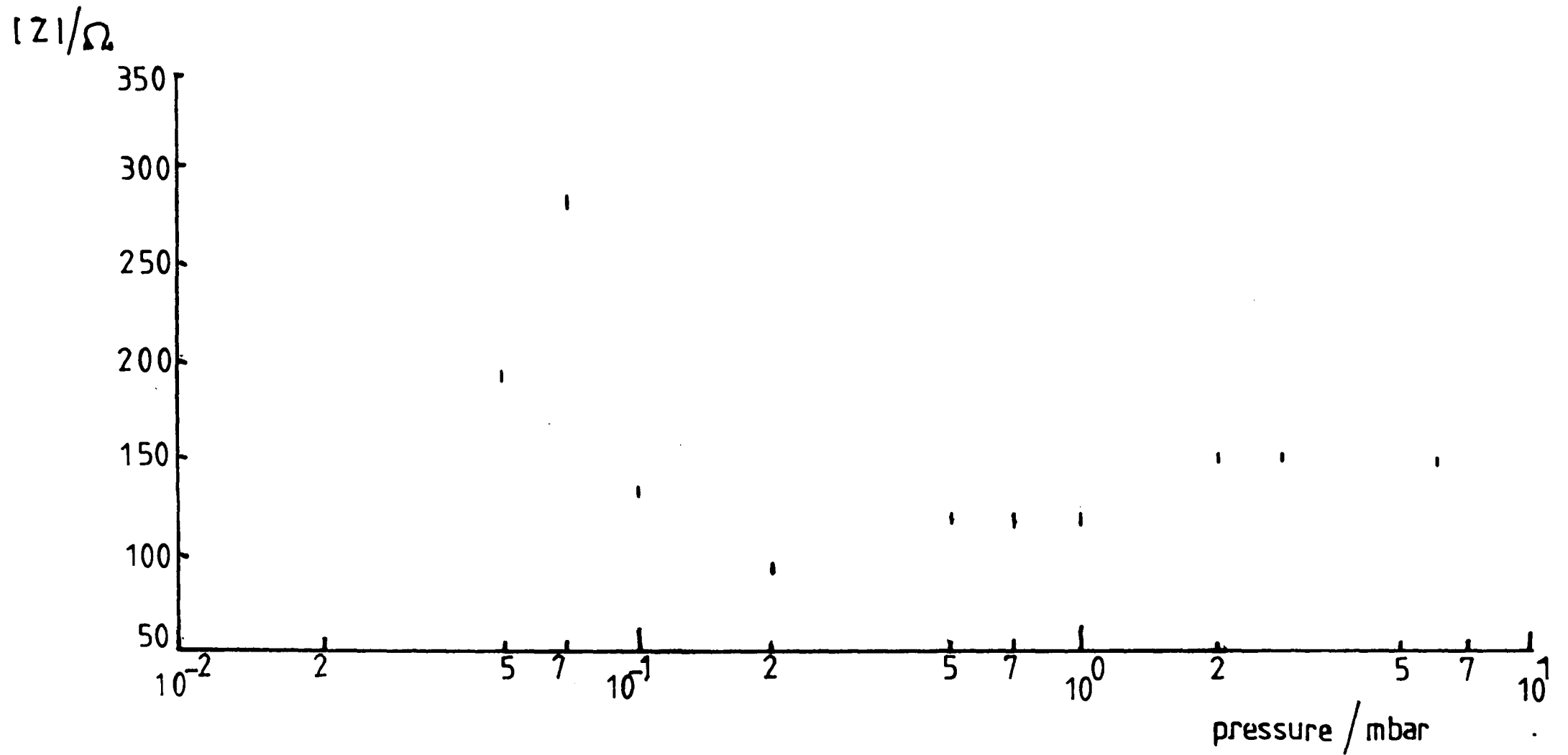


Figure 8.1b Variation of microwave impedance with pressure for probe discharge tube.
Magnetron current 50mA.

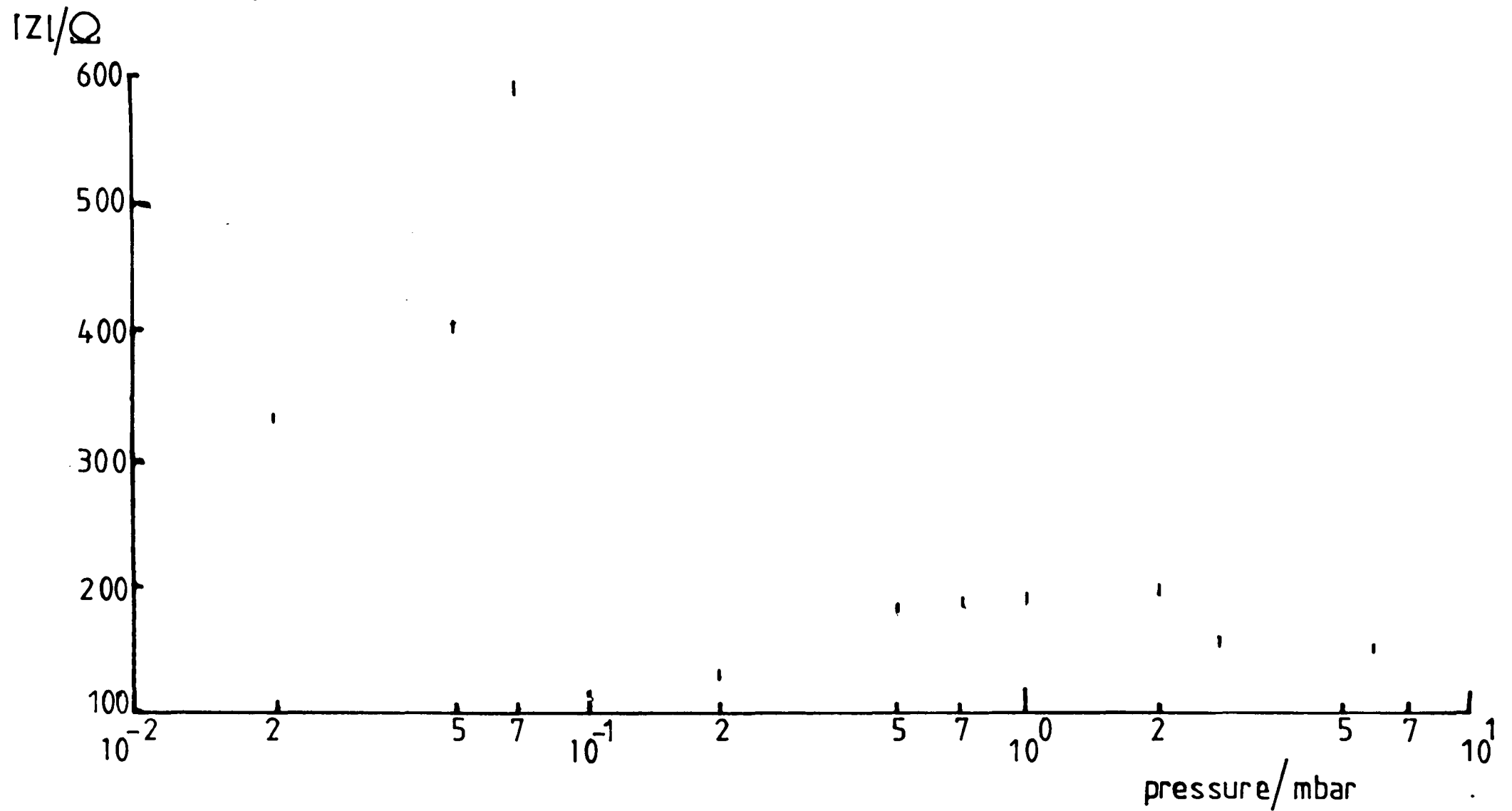


Figure 8.1c Variation of microwave impedance with pressure for probe discharge tube.
Magnetron current 100mA.

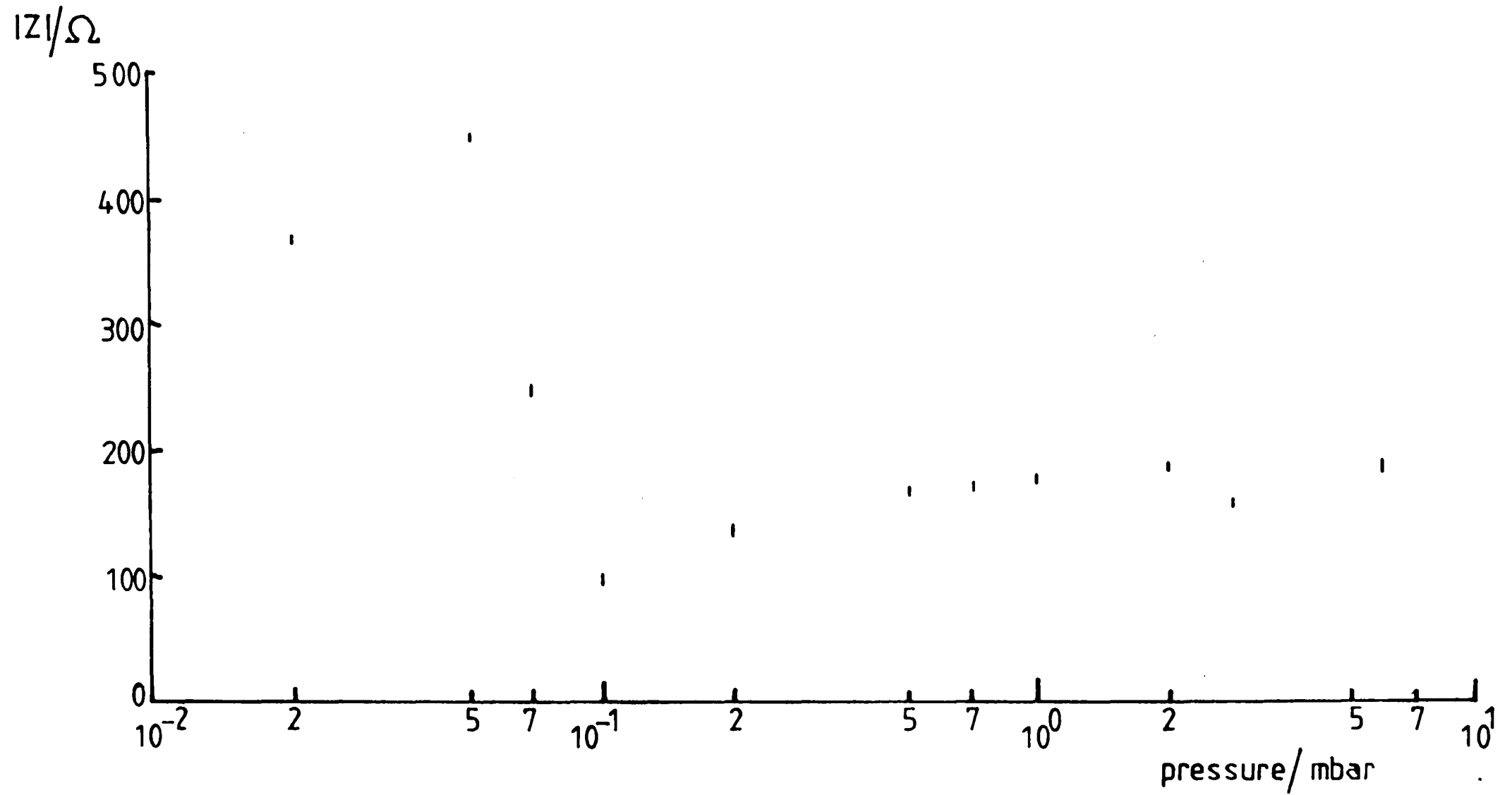


Figure 8.1d Variation of microwave impedance with pressure for probe discharge tube.
Magnetron current 150mA.

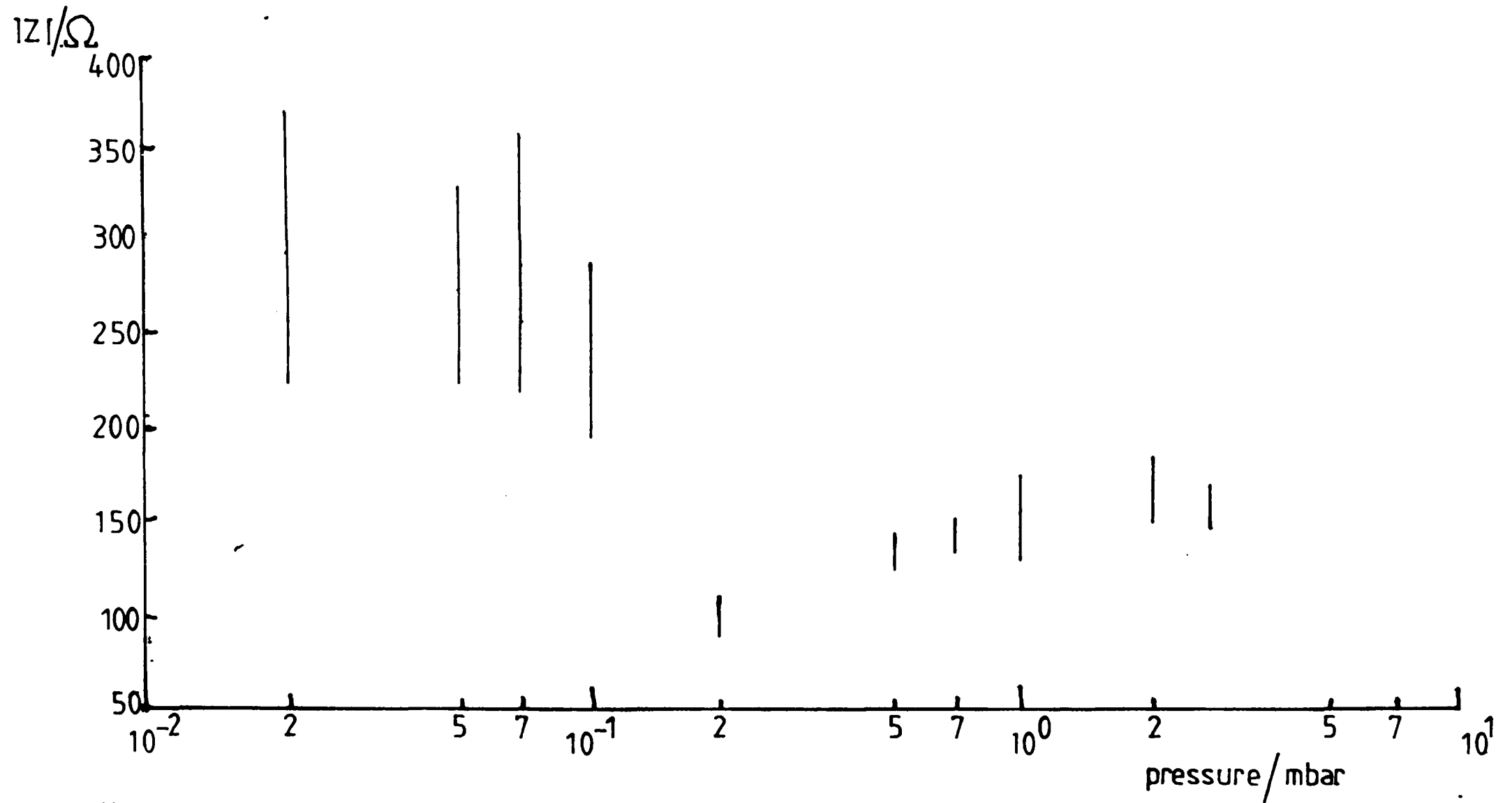


Figure 8.1e Variation of microwave impedance with pressure for plain discharge tube. Magnetron current 100mA.

occurring at 0.1 mbar for 150 mA.

The plain tube result is slightly different in that the sudden increase occurs between 0.2 and 0.1 mbar, although the general shape of the curve is similar.

The impedance values given in table 8.1 are a factor of ten lower than those measured by Hammond (1978) for argon, although the form of the variation of Z with pressure is the same. It is not clear whether the results from Hammond were conducted in the "loose" or "tight" coupling arrangement, the latter giving a higher effective impedance.

8.2 Variation of Impedance with Power

As with other plasma parameters, the inter-dependence of pressure and power affects the form of variation of impedance with either variable. The variation of $|Z|$ with input power is shown in fig. 8.2. The dependence of $|Z|$ with power is relatively weak for pressures greater than and including 0.2 mbar. For lower pressure, the impedance becomes strongly dependent upon input power.

8.3.1 Calculation of Electron Density

It was considered desirable to obtain a second set of values for the carrier density independent of those derived from the probe results and, as Stark broadening proved impractical (section 6.9), it was decided to use the microwave impedance measurements to obtain a value for the electron density. This is not a frequently adopted method although it offers the advantage of measuring directly the electron density, in contrast to the double floating probe technique.

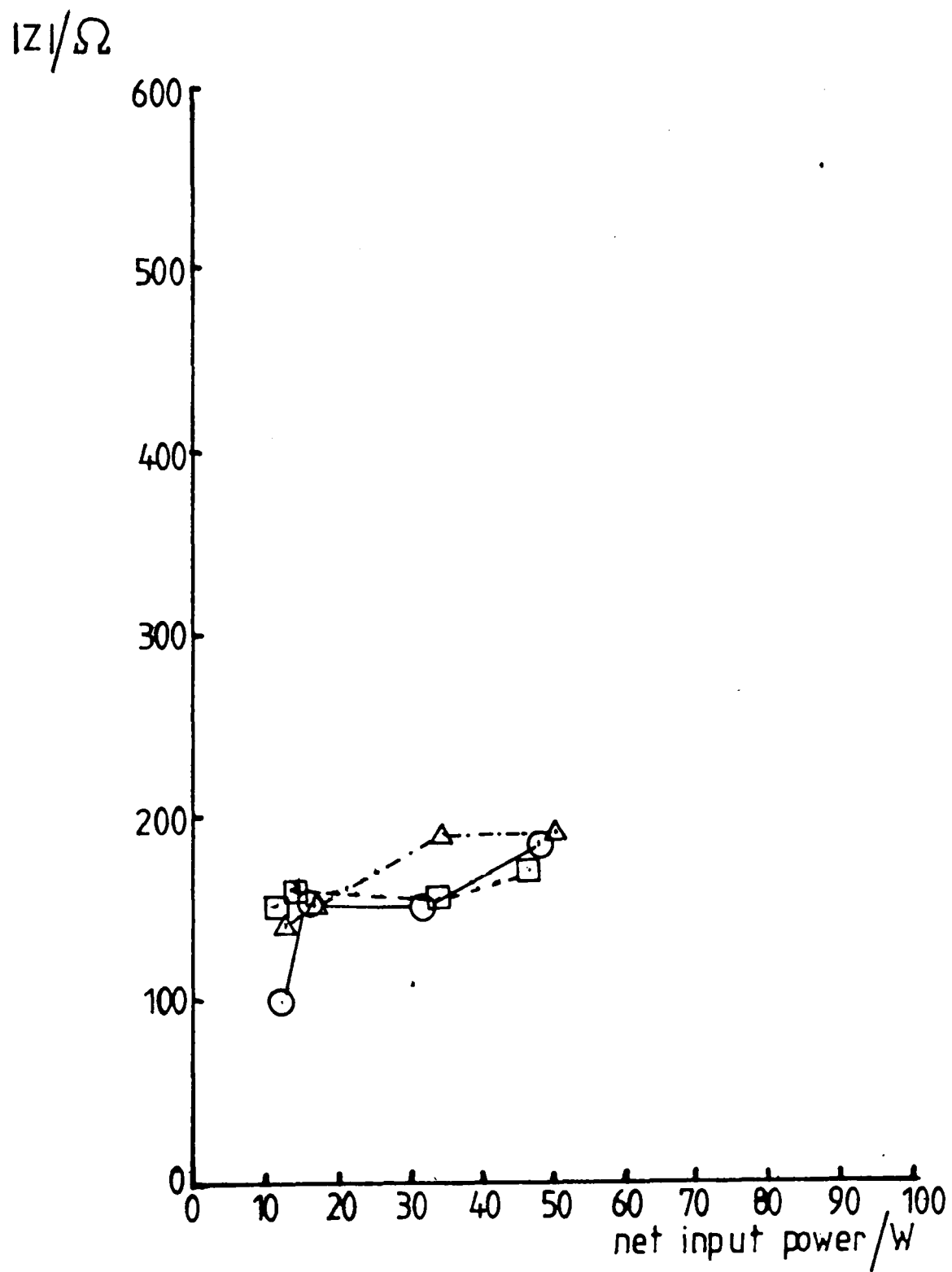


Figure 8.2a Microwave impedance as a function of input power.
 Pressures in mbar: ○ 6.00, □ 3.00, △ 2.00.

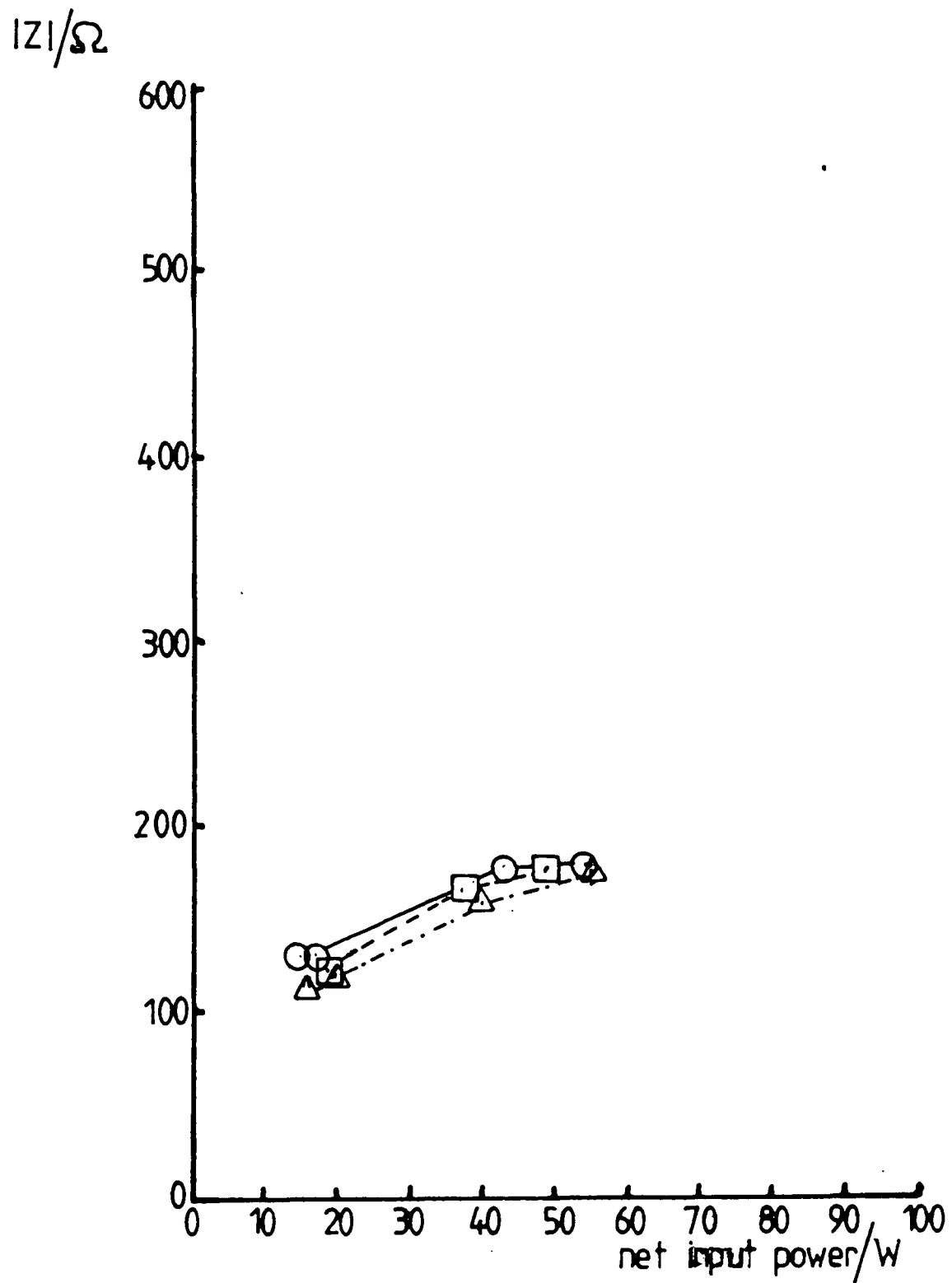


Figure 8.2b Microwave impedance as a function of input power.
 Pressures in mbar: \circ 1.00, \square 0.70, \triangle 0.50.

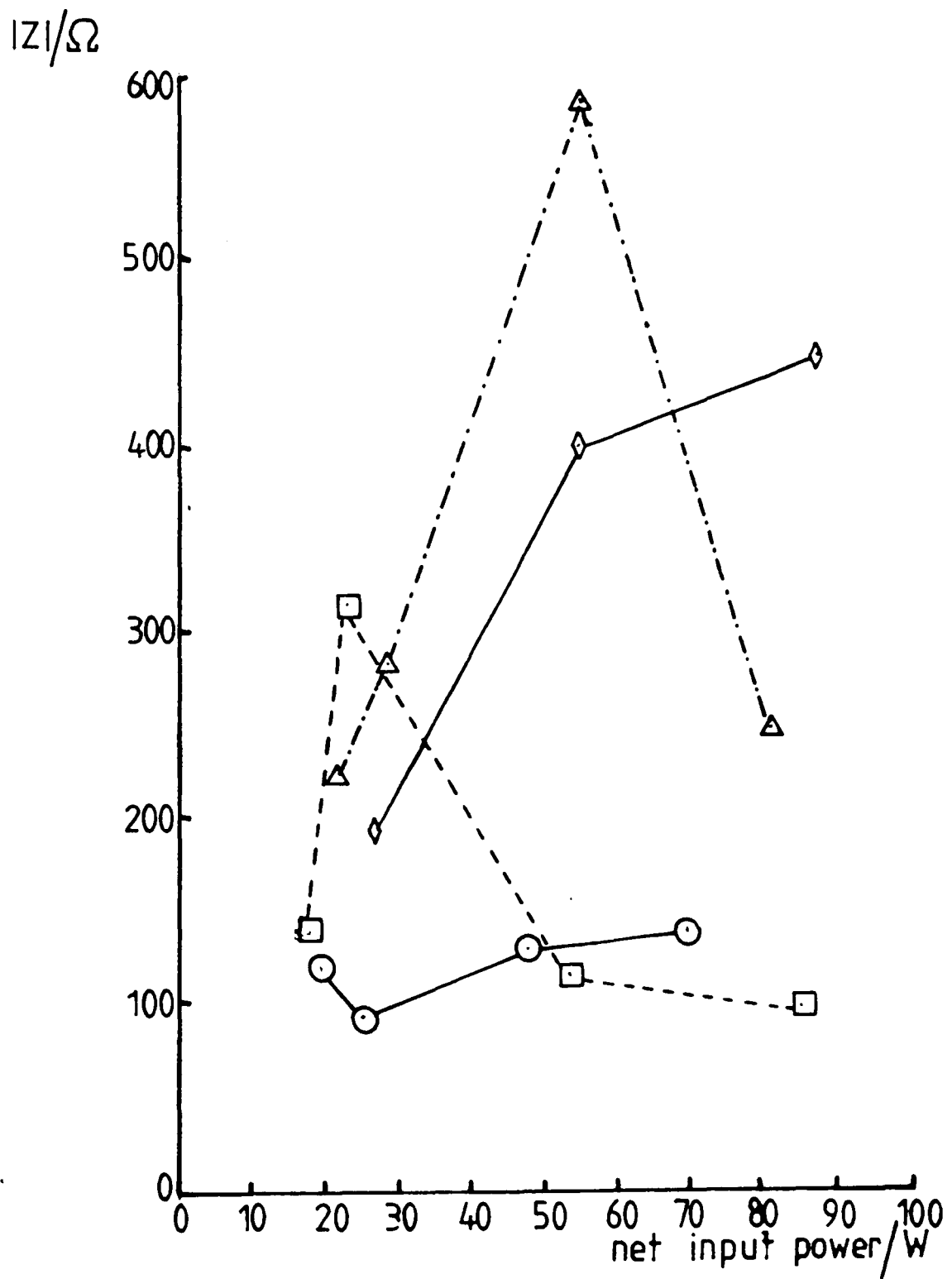


Figure 8.2c Microwave impedance as a function of input power.
 Pressures in mbar: ○ 0.20, □ 0.10, △ 0.07, ◇ 0.05.

The conductivity, σ , of a plasma containing n_e free electrons per cubic metre is given by Wharton (1965) as:

$$\sigma = \frac{n_e e^2}{m_e} \left(\frac{v - iw}{w^2 + v^2} \right) \quad 8.1$$

where

v is the collision frequency for momentum transfer

$w = 2\pi f$ where f is the frequency of the driving electromagnetic field

m_e is the electron mass

$$i = \sqrt{-1}$$

The imaginary term arises from consideration of collisions between the electrons and the field ^{of the} atoms of the parent gas; these collisions are treated as a damping effect in the equation of motion of the electrons. Thus taking the modulus of σ gives

$$|\sigma|^2 = \left(\frac{n_e e^2}{m_e} \right)^2 \left(\frac{v^2 + w^2}{(v^2 + w^2)^2} \right) = \left(\frac{n_e e^2}{m_e} \right)^2 \cdot \frac{1}{(v^2 + w^2)} \quad 8.2$$

Now the collision frequency v is related to the cross-section for momentum transfer Q by the equation

$$v = n_e Q V_e$$

where V_e is the electron speed. Typically, Q , is of the order of 10^{-20} m^2 and V_e is of the order of 10^6 ms^{-1} . Thus

$$\sigma Q V_e \ll \frac{e^2}{m_e}$$

and so using this inequality, the electron density may be written in

terms of the conductivity as

$$n_e = \frac{|\sigma| w}{e^2/m_e} \quad 8.3$$

The modulus of the conductivity $|\sigma|$ is related to the modulus of the impedance $|Z|$ by:

$$|\sigma| = \frac{1}{|Z| A}$$

Where

l is the length of the conducting body and A its cross-sectional area. The equation 8.1 is derived from considerations of the electron motion under the influence of a sinusoidal electric field. Thus, l was taken as the distance between the cavity plates and A the cross-sectional area of the discharge tube, these being the appropriate dimensions in the direction of the electric field. The values of electron density calculated from equation 8.3 are given in table 8.2 and the variation with pressure of n_e for the four magnetron currents are shown in fig. 8.3(a) to (d). Comparing tables 8.2 and 7.2 shows that, generally speaking, the values of n_e and n_+ are of a similar order of magnitude.

8.3.2 Variation of Electron Density with Pressure and Power

The variation of electron density with net input power is shown in fig. 8.4. As would be expected, this is effectively an "inversion" of fig. 8.2.

The variation of electron density with pressure for normalised powers is shown in fig. 8.5. For the lowest pressures (0.02 to 0.07 mbar),

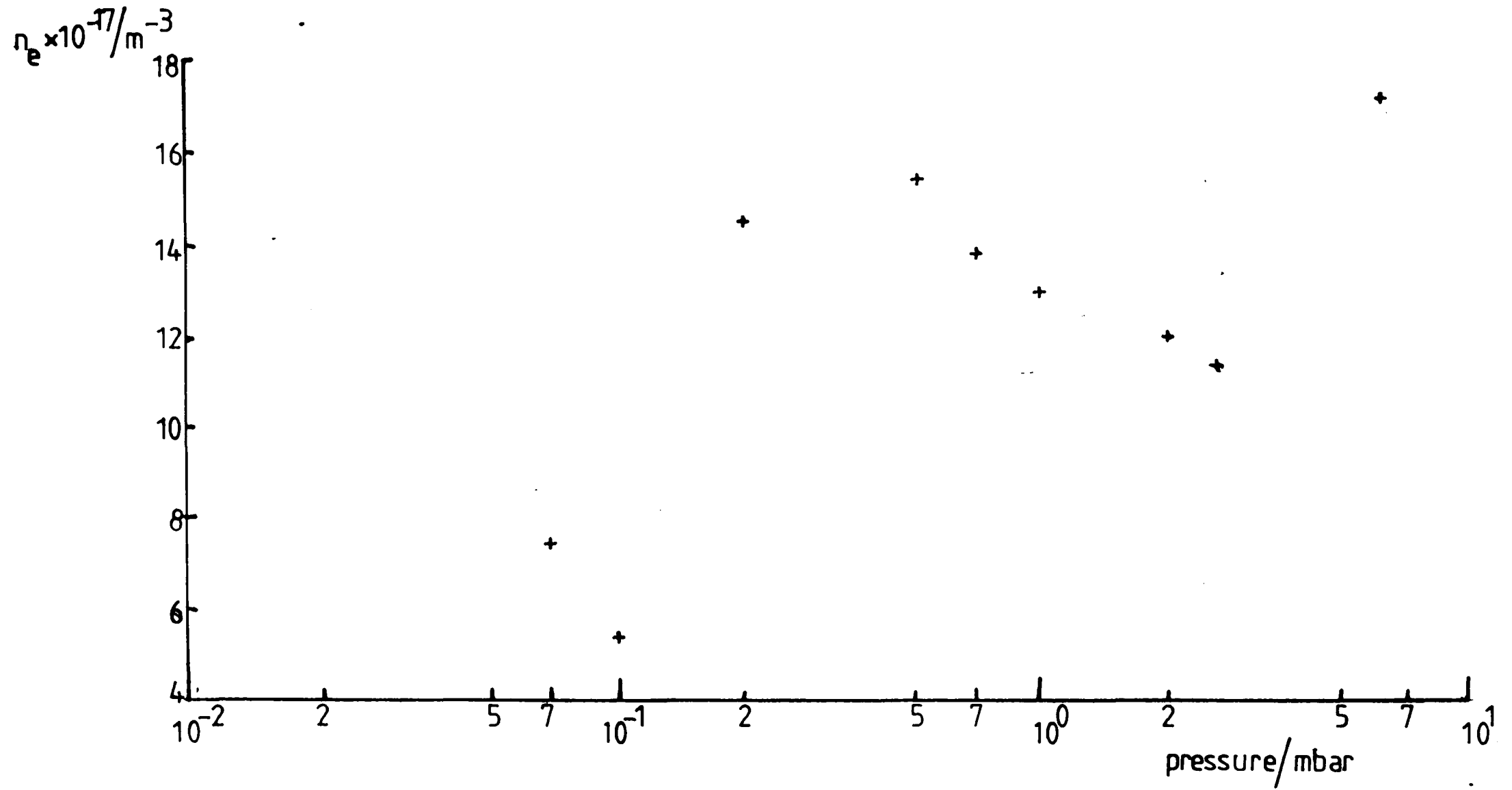


Figure 8.3a Variation of electron density with pressure, magnetron current 40mA.

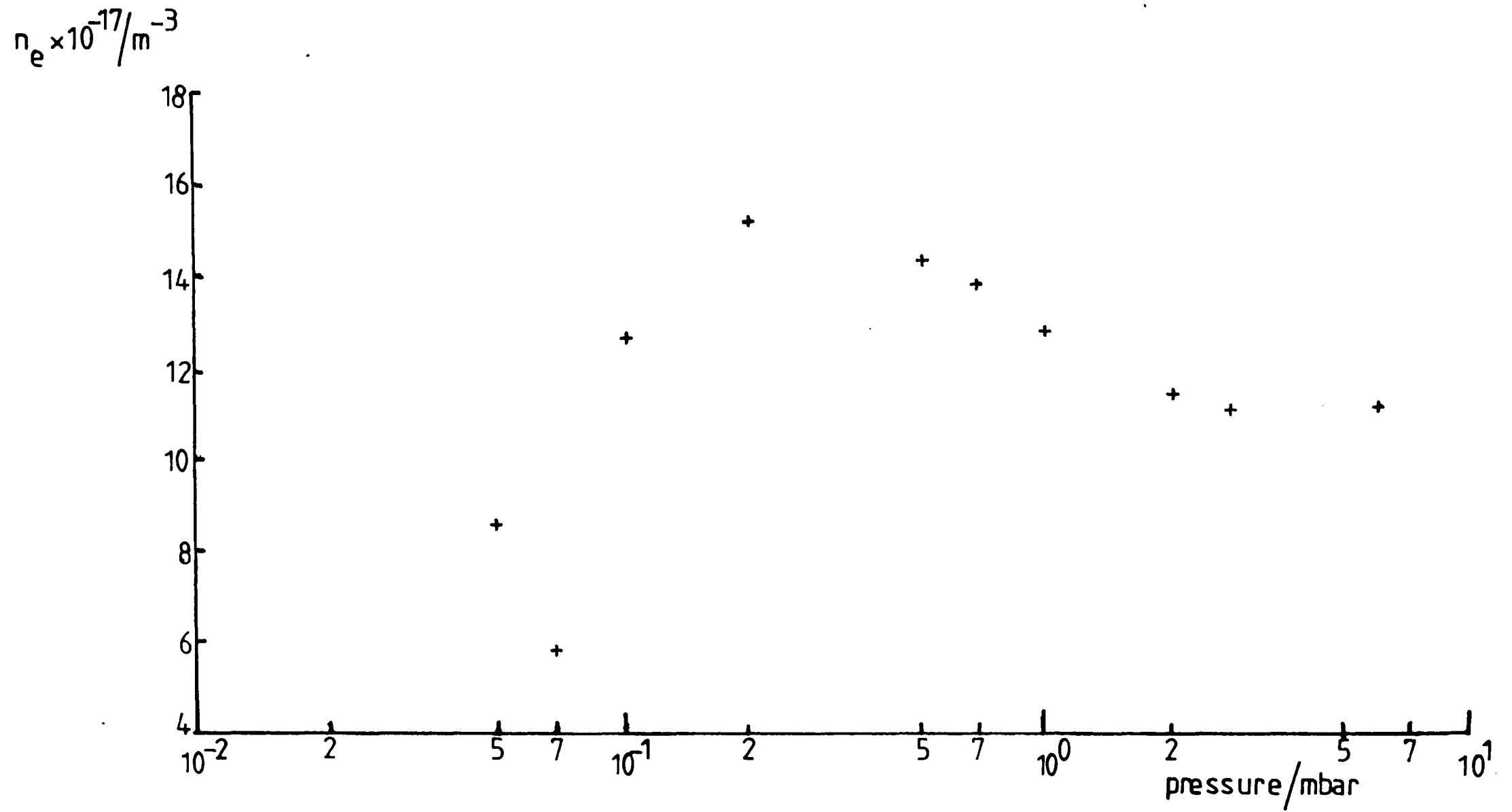


Figure 8.3b Variation of electron density with pressure, magnetron current 50mA.

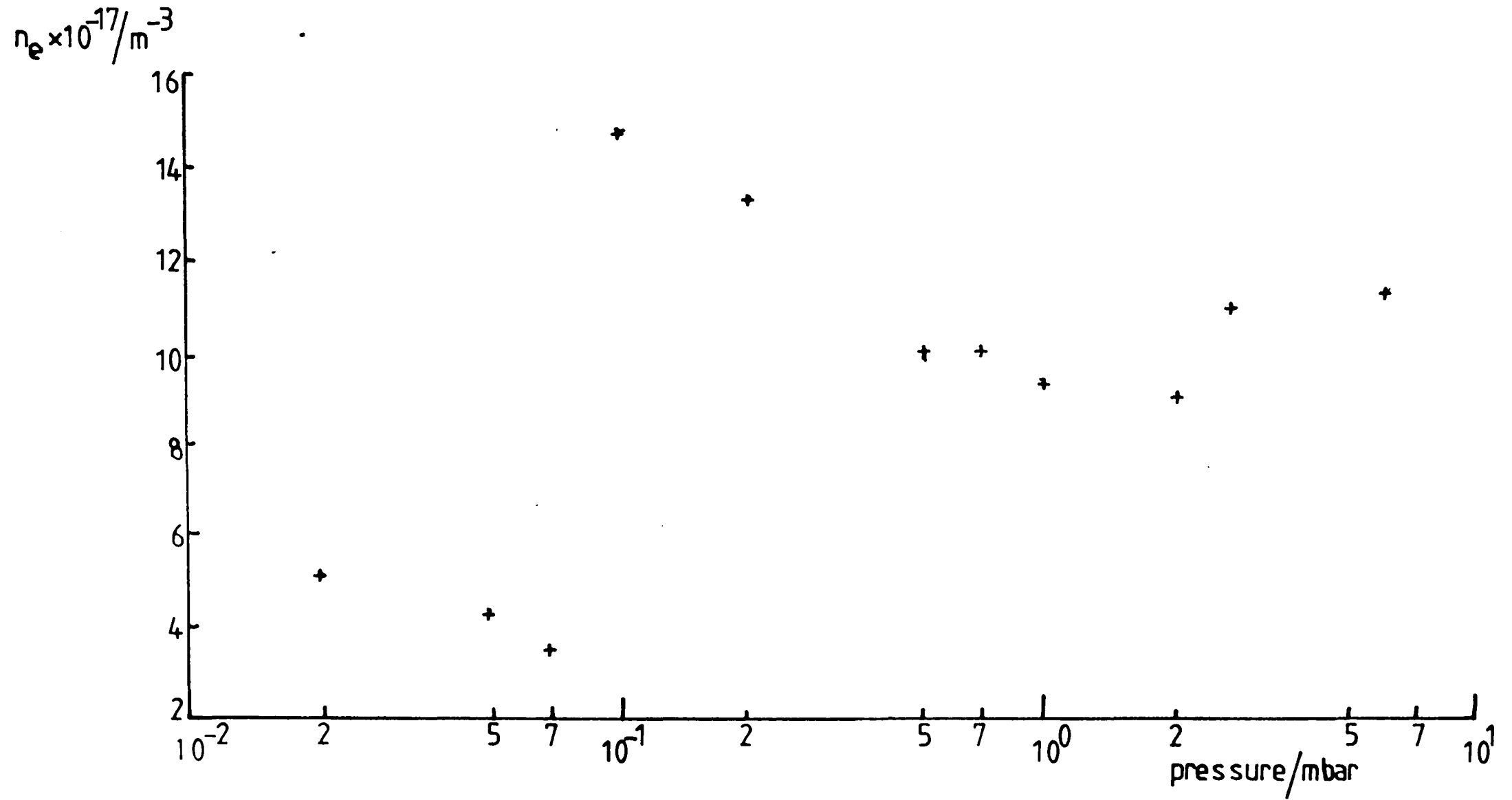


Figure 8.3c Variation of electron density with pressure, magnetron current 100mA.

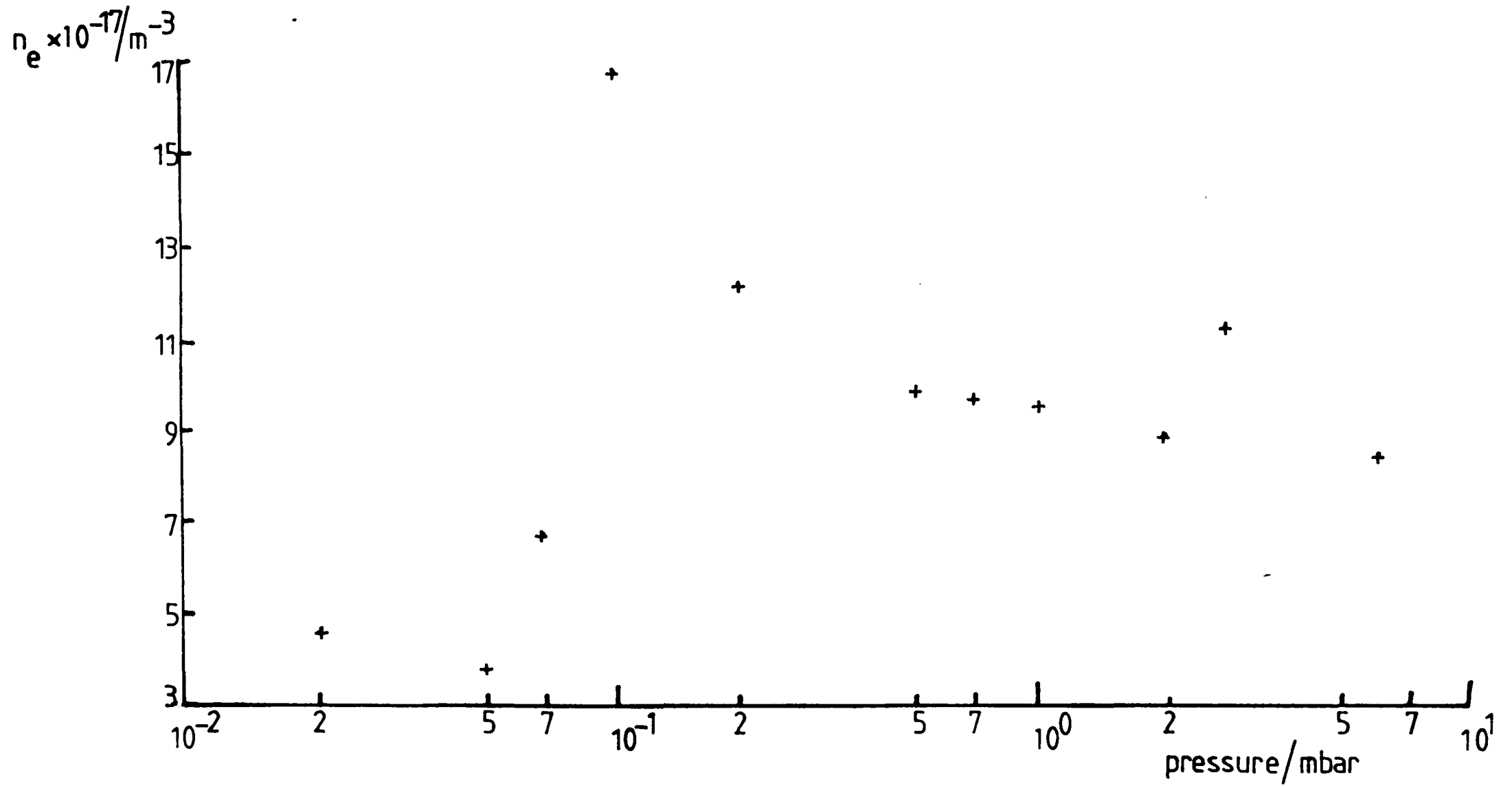


Figure 8.3d Variation of electron density with pressure, magnetron current 150mA.

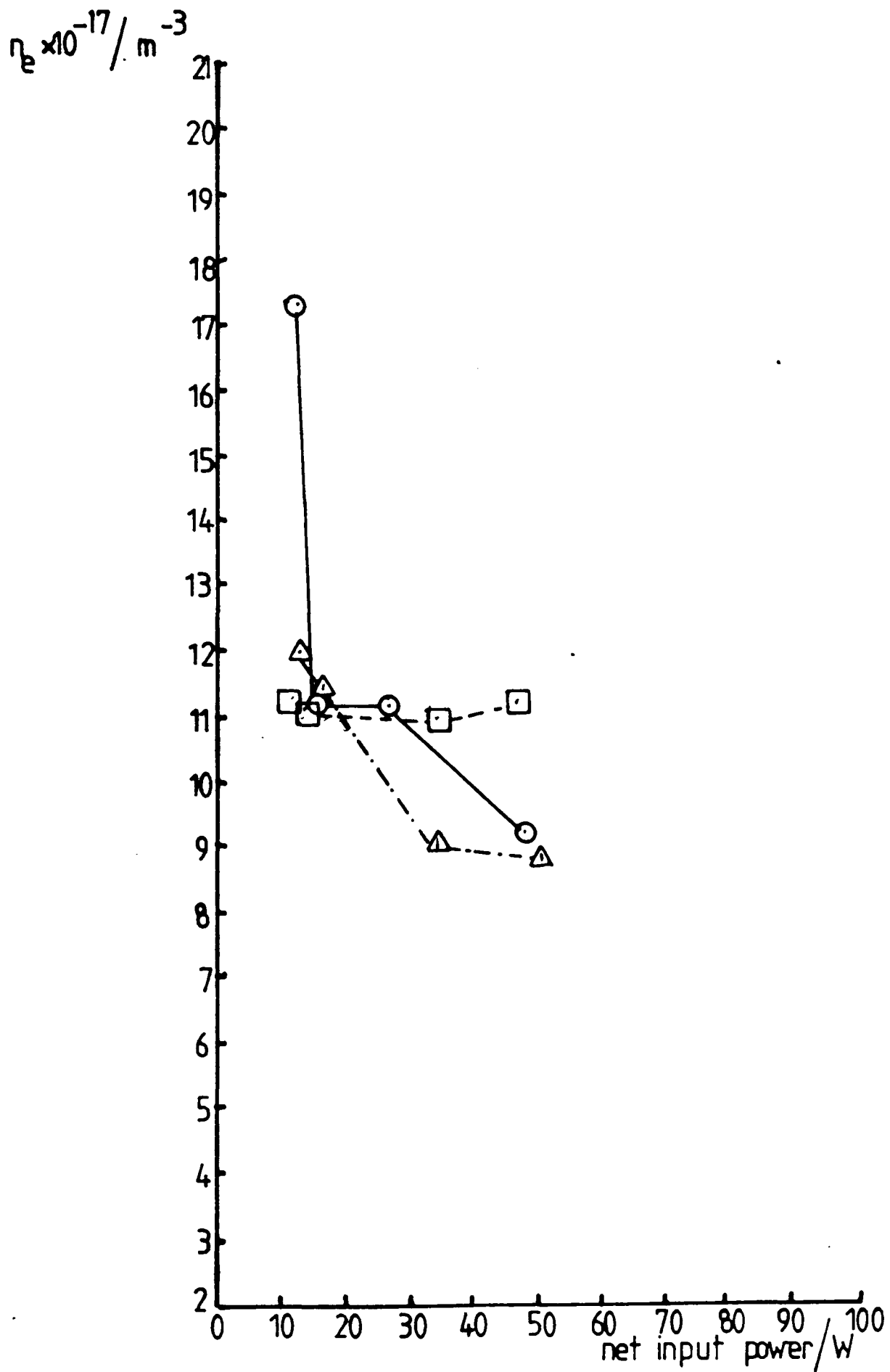


Figure 8.4a Electron density as a function of input power.
 Pressures in mbar: \circ 6.00, \square 3.00, \triangle 2.00.

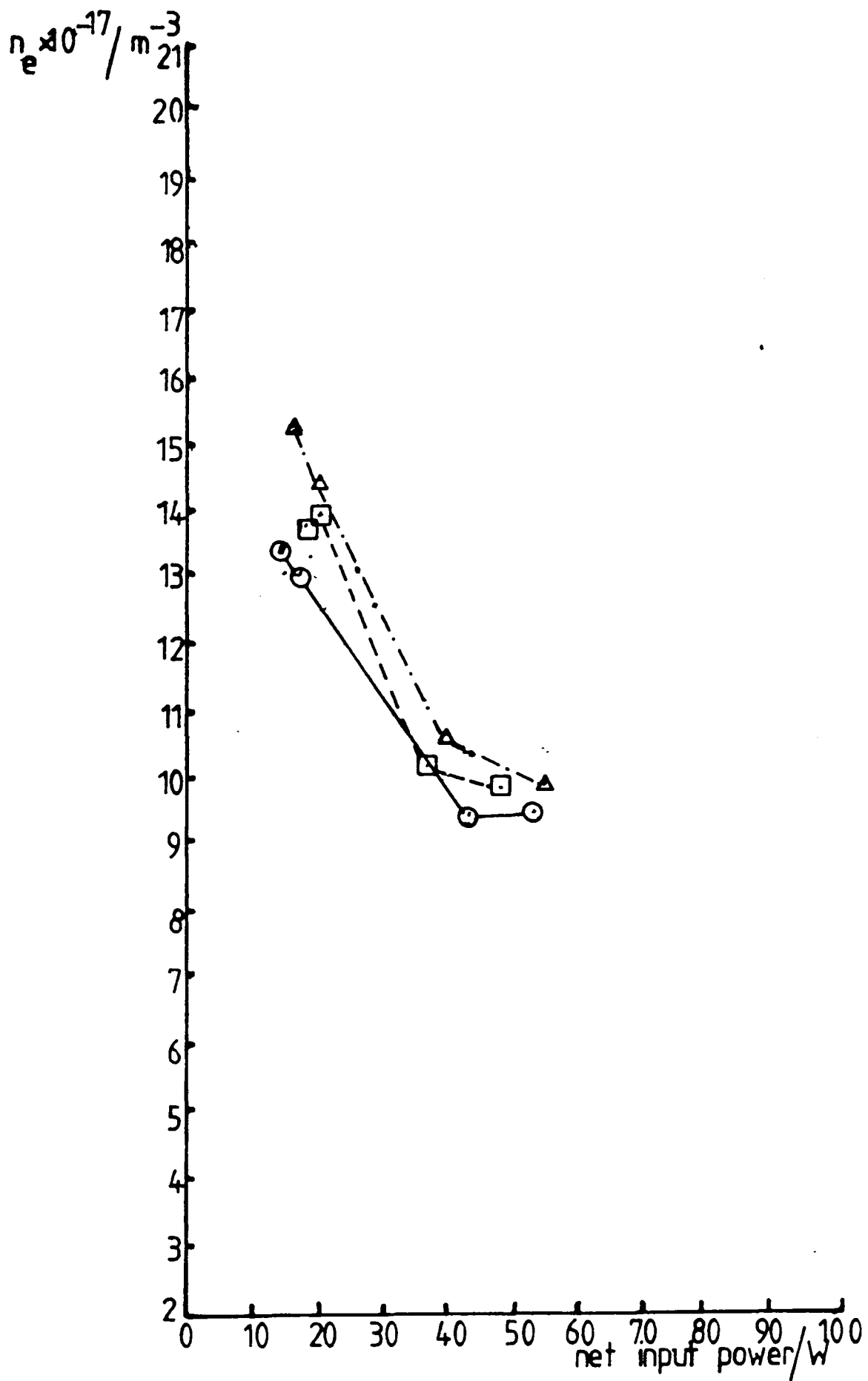


Figure 8.4b Electron density as a function of input power.
 Pressures in mbar: \ominus 1.00, \square 0.70, Δ 0.50.

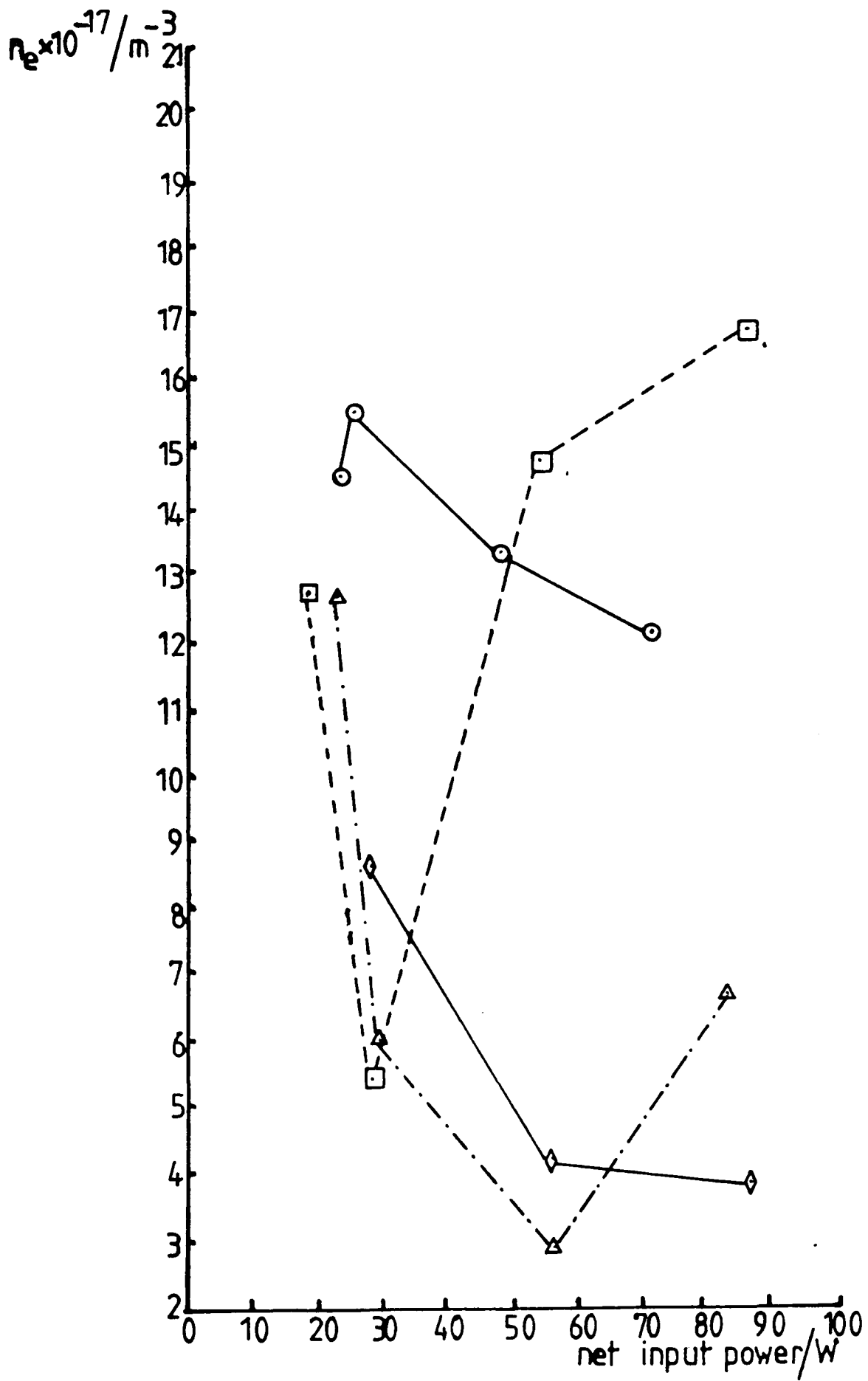


Figure 8.4c Electron density as a function of input power.

Pressures in mbar: ○ 0.20, □ 0.10, △ 0.07, ◇ 0.05.

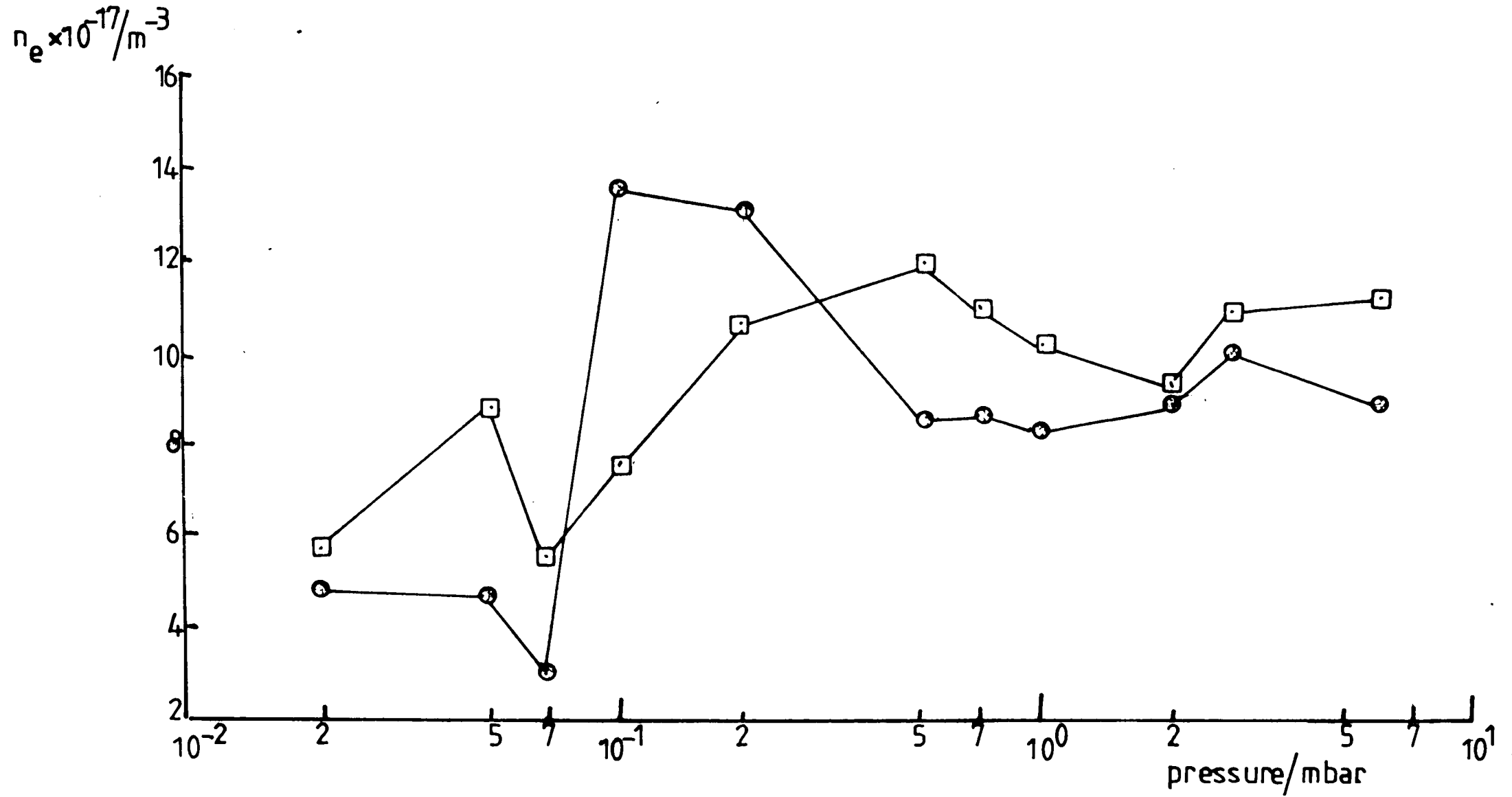


Figure 8.5a Variation of electron density with pressure. Normalised input powers: \odot 50W, \square 30W.

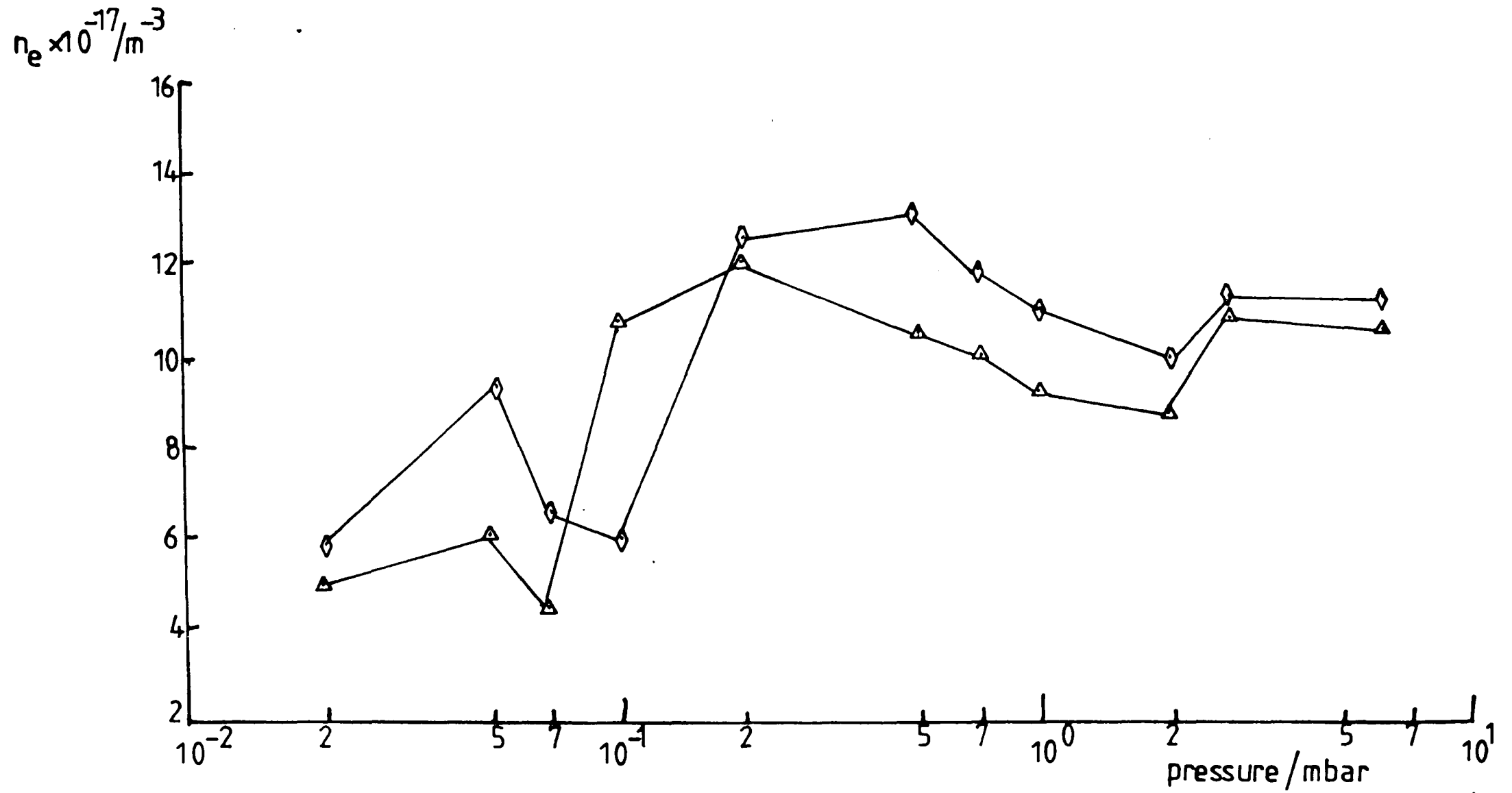


Figure 8.5b Variation of electron density with pressure. Normalised input powers: Δ 40W, \diamond 25W.

the lower input power yields the highest n_e values. At a pressure of 0.1 mbar, this relationship shows a sudden change when the n_e value rapidly increases for the higher input powers. However, as the pressure increases, the original relationship between n_e and input power is re-established.

8.4 Comparison of Real and Imaginary Components of Z

From equation 8,1, the real and imaginary components of the impedance are given by

$$\text{Re}Z = \frac{m_e l v}{n_e e^2 A} \qquad \text{Im}Z = \frac{m_e l w}{n_e e^2 A}$$

Thus the ratio of the imaginary and real components gives an indication of the magnitude of the collisional damping between the electrons and the gas atoms (the frequency of the electric field f is effectively constant). The ratio

$$\frac{\text{Im}(Z)}{\text{Re}(Z)} = \frac{w}{v}$$

is plotted as a function of input power in fig. 8.6 and this diagram was used to plot the ratio as a function of pressure for normalised input powers shown in fig. 8.7. It is clear that the collision frequency v is generally greater for the highest input power of 50W and increases for all powers at pressure below 1.00 mbar. Comparison with fig. 7.6 shows that the form of the $(1/v)$ curve does not completely follow the electron temperature vs pressure curve. Since the electron speed V_e is a function of the electron temperature, this difference implies a change in the total cross-section value at these

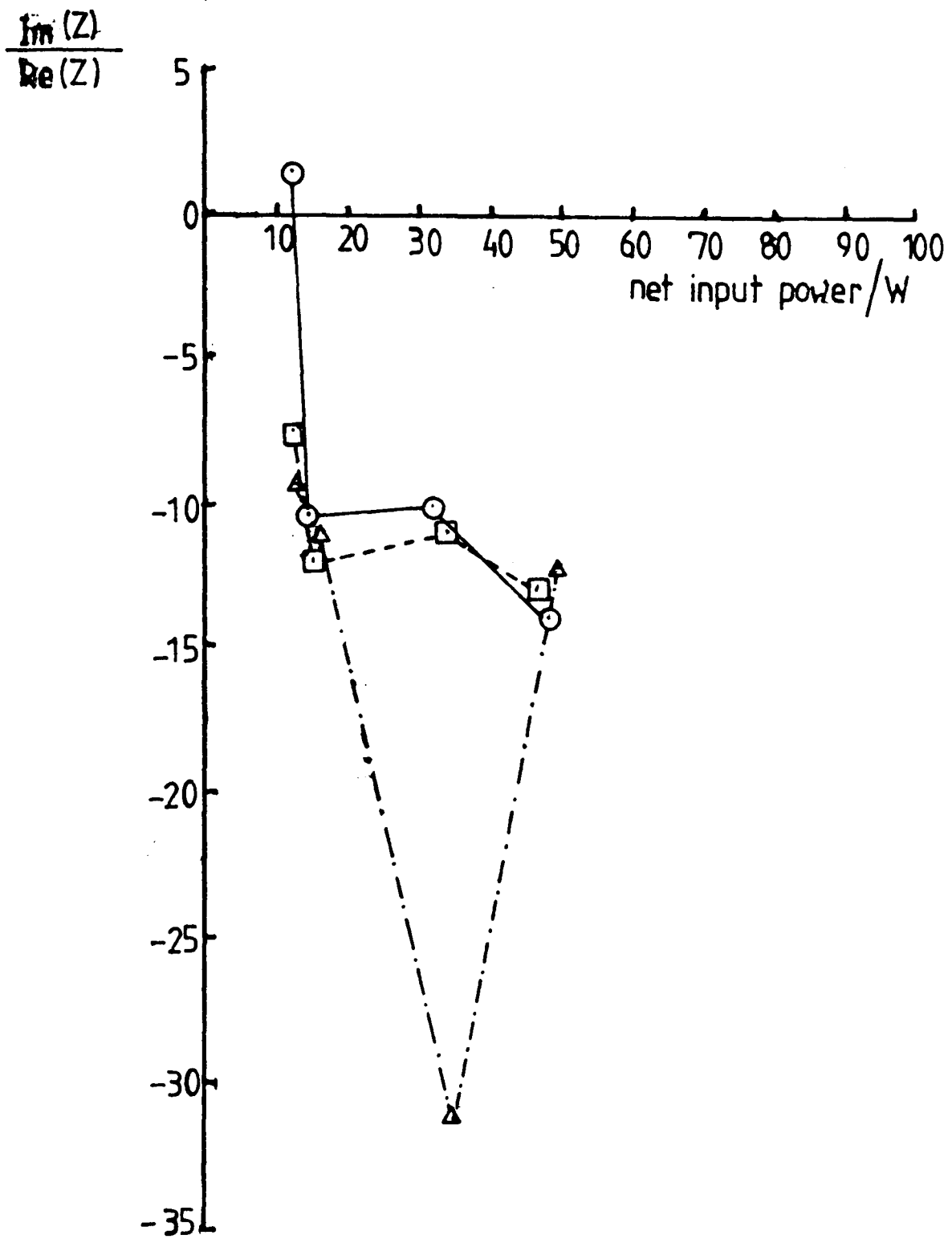


Figure 8.6a Ratio of imaginary to real parts of microwave impedance as a function of input power. Pressures in mbar: ○ 6.00, □ 3.00, △ 2.00.

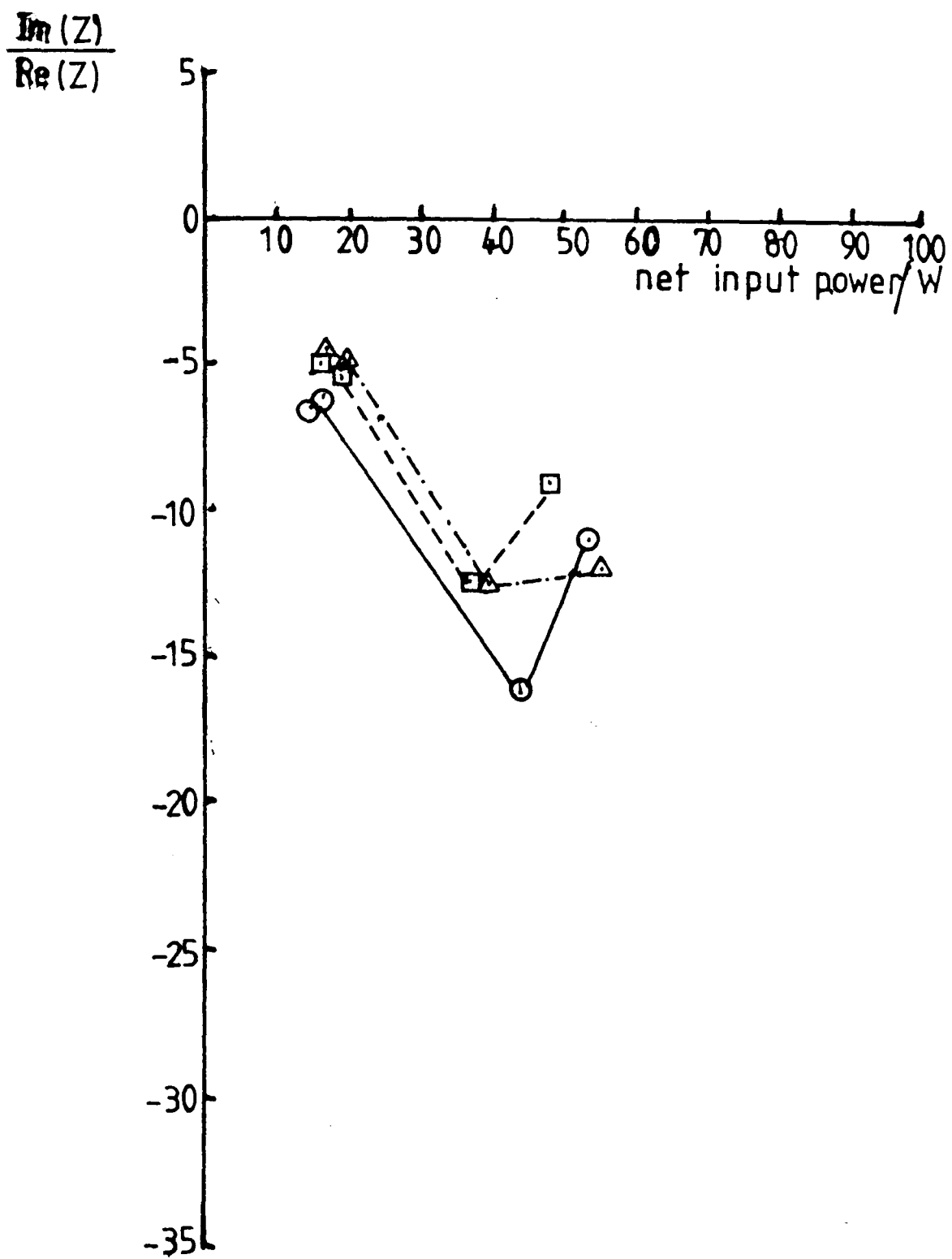


Figure 8.6b Ratio of imaginary to real parts of microwave impedance as a function of input power. Pressures in mbar: \circ 1.00, \square 0.70, \triangle 0.50.

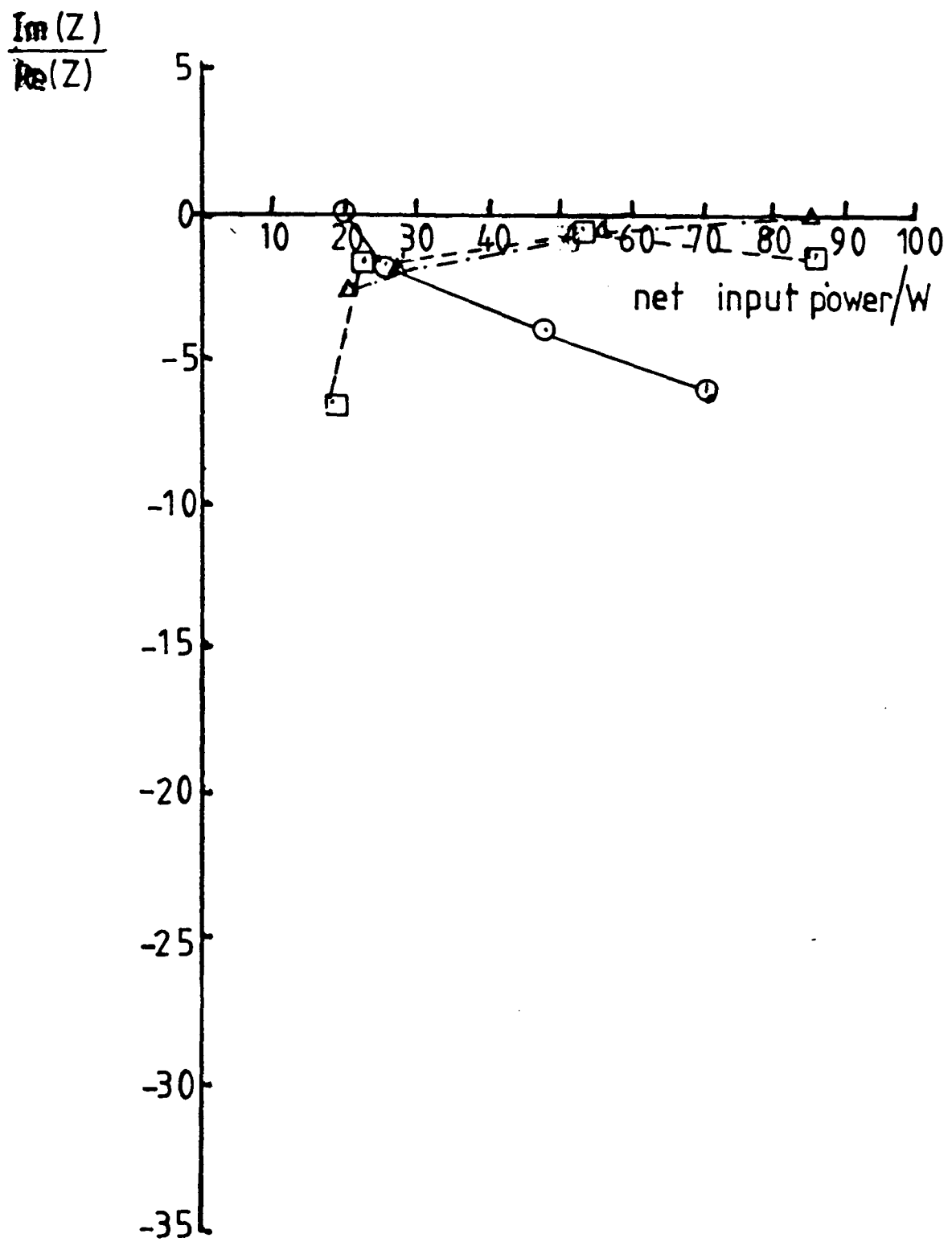


Figure 8.6c Ratio of imaginary to real parts of microwave impedance as a function of input power. Pressures in mbar: \circ 0.20, \square 0.10, \triangle 0.07.

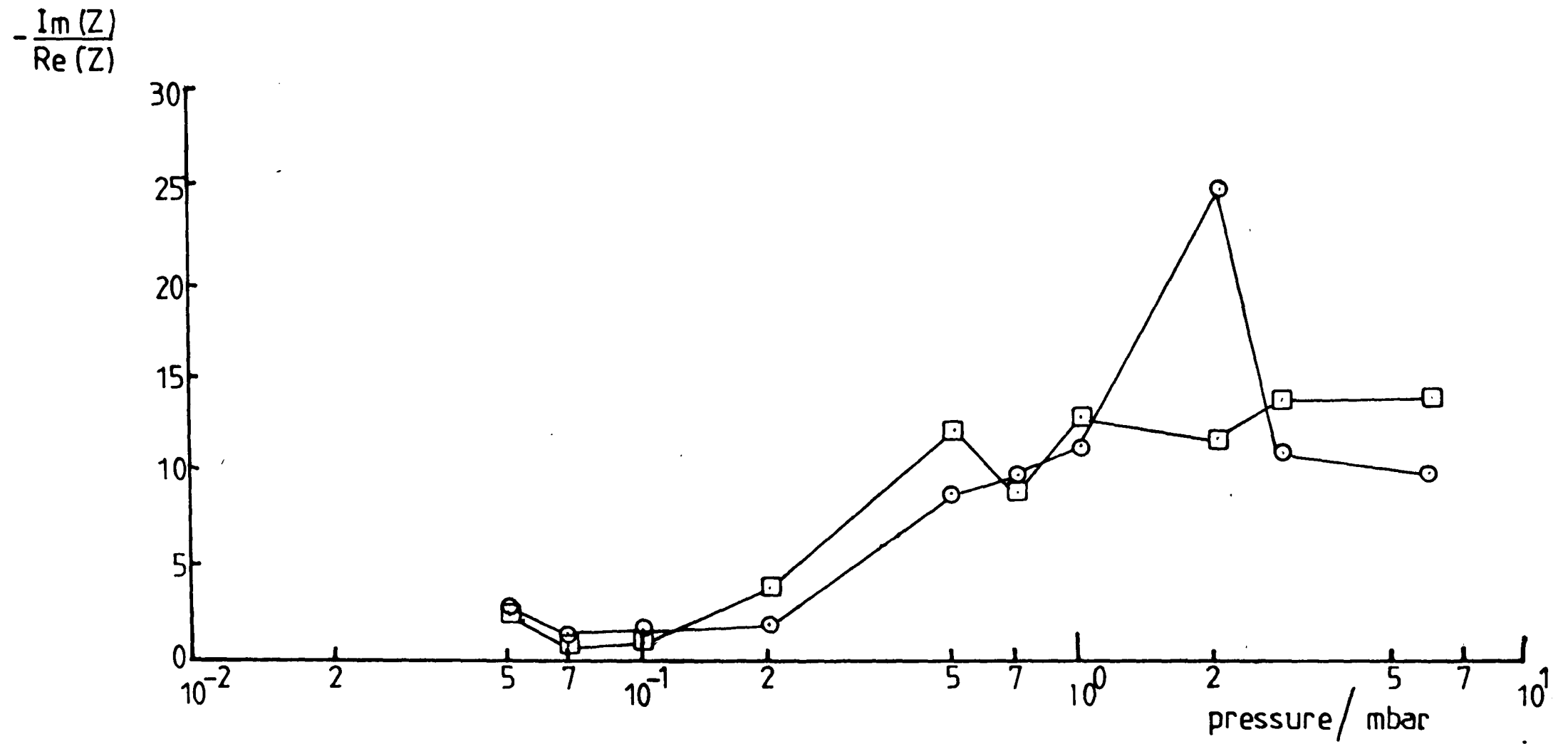


Figure 8.7a Ratio of imaginary to real parts of microwave impedance as a function of pressure.

Normalised input powers: \square 50W, \circ 30W

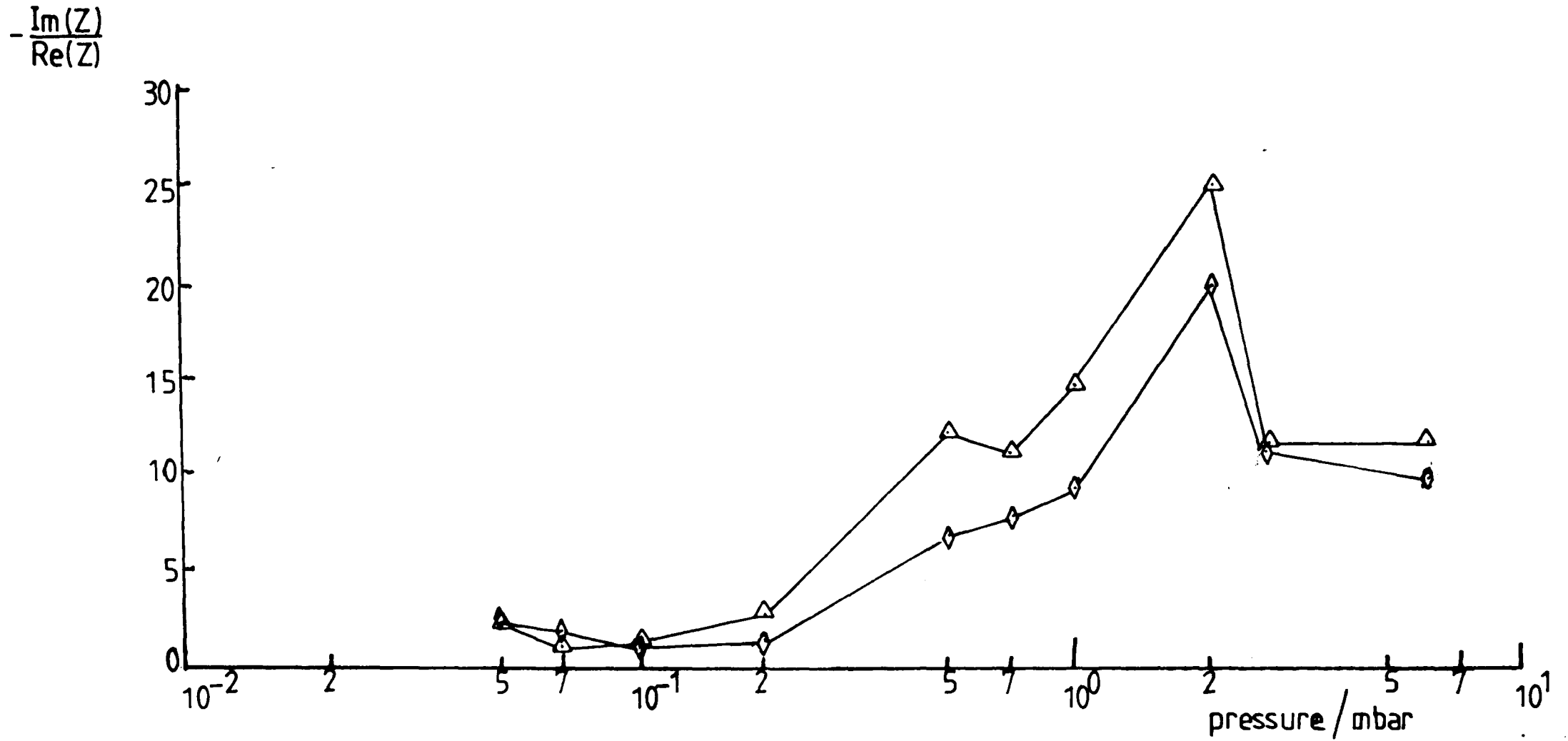


Figure 8.7b Ratio of imaginary to real parts of microwave impedance as a function of pressure.
Normalised input powers: Δ 40W, \diamond 25W.

pressures. Such a change would be due to a change in the number of electrons with energies such that the cross-section Q is significant. For 50W input power, the electrons seem to be mainly in this energy region, according to the low value of imaginary to real impedance ratio. The increase of the collision frequency below 0.5 mbar, with v taking relatively large values for pressures less than 0.2 mbar explains the features of the impedance curves of fig. 8.8 which shows an increase in impedance for pressures below 0.2 mbar.

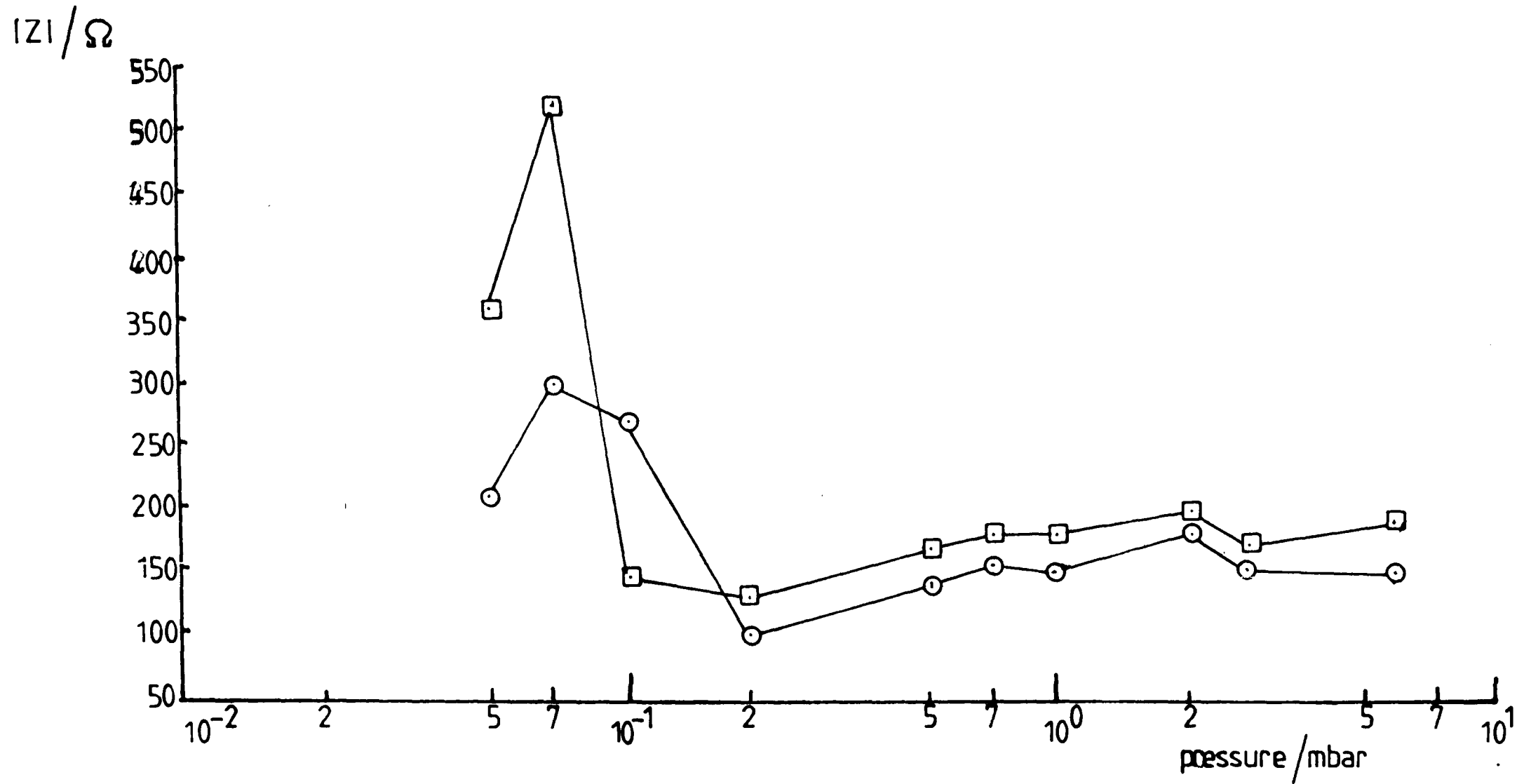


Figure 8.8a Variation of microwave impedance with pressure. Normalised input powers: \square 50W, \circ 30W.

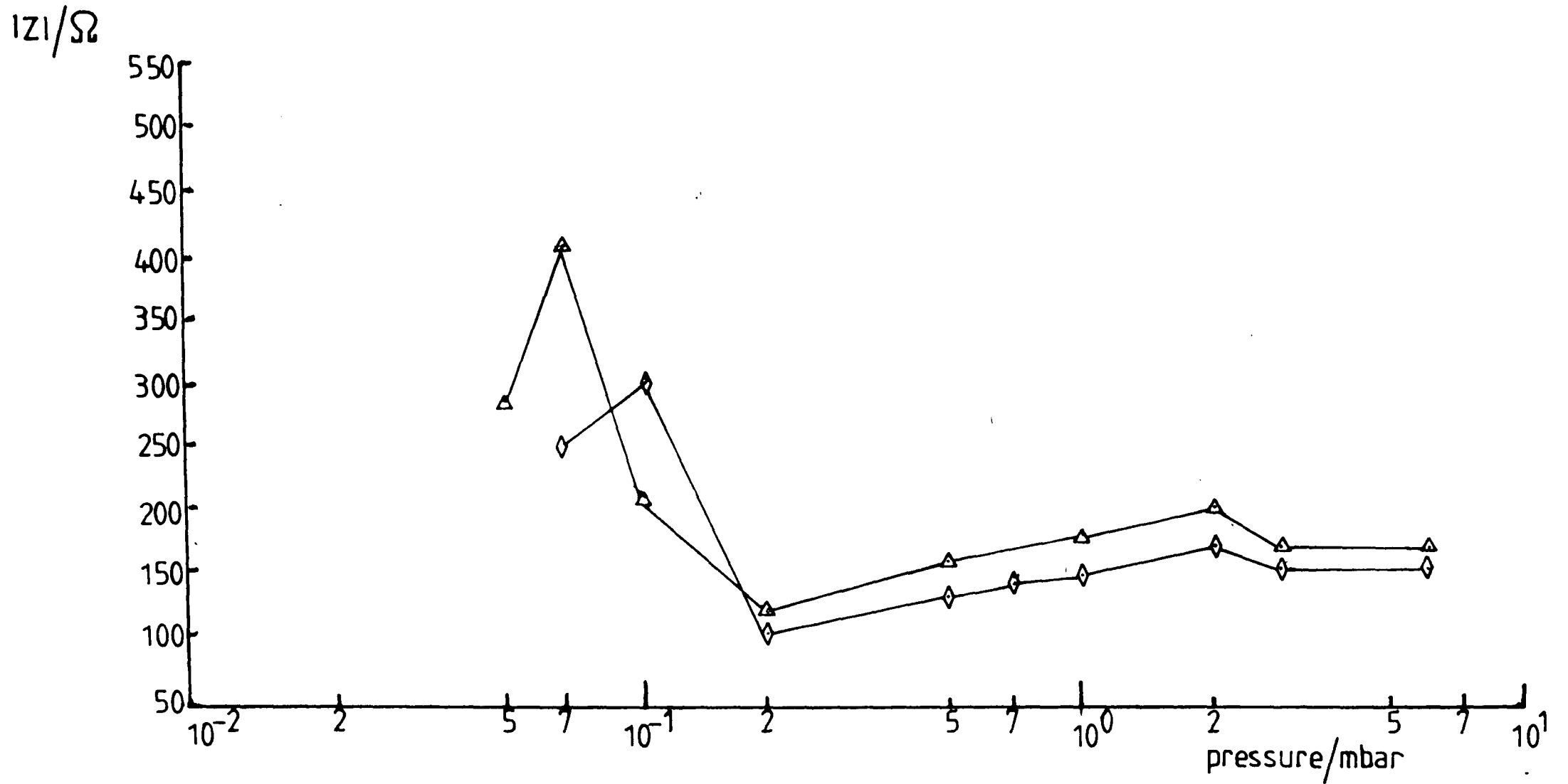


Figure 8.8b Variation of microwave impedance with pressure. Normalised input powers: Δ 40W, \diamond 25W.

CHAPTER 9
CHARACTERISTION OF THE PLASMA
& CONCLUSIONS

9.1 Preamble

In chapters 6, 7 and 8, the results of the three measurement techniques have been described individually. In this chapter it is intended to compare the electron and ion density measurements of chapters 8 and 7 respectively and by combining the results of the previous three chapters determine the character and phase of the plasma with reference to the collisional-radiative model of Fujimoto (1979).

9.2 Comparison of the Carrier Density Measurements

Two methods of obtaining a value for the carrier density have been described: from microwave impedance measurements where the electron density, n_e , is determined directly and from double floating probe characteristics where the ion density, n_+ , is determined and from this the electron density inferred. The relationship between n_e and n_+ which is used to obtain n_e in this case obviously has a direct bearing upon the value of n_e obtained and it would be useful to consider some of the relationships used by previous workers.

9.2.1 Relationship between the ion and electron density

As stated in section 7.2.3, the use of double floating probes to determine the electron density has one major disadvantage in that it does not provide a direct measurement of the electron density. The parameter which is directly obtained is the ion density and some assumption regarding the relationship between the two must be made in order to obtain n_e .

The most popular assumption is that of electrical neutrality, ie.

$$n_e = n_+$$

and this is indeed the relationship employed by the vast majority of authors (Brassem & Maessen 1974, Busch & Vickers 1973). However, the assumption of electrical neutrality may not always be justified. Avni & Winefordner (1975) argue that, in the case of low pressure electrodeless discharges, more collisions occur between the tube walls and electrons than occur in high pressure discharges and they adopt the following condition:

$$n_e (V_e)_{\text{drift}} \approx 2n_+ (V_+)_{\text{drift}}$$

where $(V_e)_{\text{drift}}$ and $(V_+)_{\text{drift}}$ are the respective drift velocities of the electrons and ions. Since $(V_e)_{\text{drift}}$ is greater than $2(V_+)_{\text{drift}}$, this would imply that the electron density is less than the ion density viz

$$n_e < n_+$$

An alternative view is taken by Tachibana & Fukuda (1973) who argue that "gas drive-out" of the ions and neutral atoms must be taken into consideration. These effects can be evaluated using either the free-fall diffusion model of Tonks & Langmuir (1929) or the ambipolar model of Schottky (1924). In cases where the mean free path length of the ion is greater than, or of similar magnitude to, the dimensions of the discharge tube, the free-fall model should be applied. The ambipolar case applies to cases where the mean free path length is sufficiently shorter than the discharge tube dimensions.

For the free-fall case, the current density flowing to the wall due

to the diffusion of ions is given by

$$j_w = 0.382 n_{eo} e \sqrt{\frac{kT_e}{m_+}} \quad 9.1$$

where

$n_{eo} = n_e / 0.7$ with n_{eo} the electron density at the tube axis and n_e the radially averaged density.

m_+ is the ion mass.

For the ambipolar case, the wall current density is given by

$$j_w = \frac{7.83}{2} n_{eo} e \frac{D_a}{R} \quad 9.2$$

where

$$n_{eo} = n_e / 0.432$$

R is the radius of the discharge tube

D_a is the ambipolar diffusion coefficient and is given by

$$D_a = \frac{b_o^+}{n/n_L} \cdot \frac{kT_e}{e} \quad 9.3$$

where

b_o^+ is the ion mobility in the parent gas

n_L the particle density at 1 mbar pressure and 300K temperature.

For the case of ionic diffusion to the wall, it would be expected that the electron density would be greater than the measured ion density, viz:

$$n_e > n_+$$

9.2.2 Comparison of the ion and electron densities

The ratio of the electron density (from microwave impedance measurements) to the ion density (from probe measurements) is shown in fig. 9.1 as a function of pressure for four values of normalised input power.

It can be clearly seen that at the higher pressures the values of n_e and n_+ are approximately equal but, as the pressure is decreased, the discrepancy becomes greater with the electron density n_e being greater. Indeed, at a pressure of 0.1 mbar with 50W input power, the electron density is approximately twenty times the ion density. In addition, the higher input powers create a greater difference between the two quantities.

It would appear that the concept of electrical neutrality does not apply to the microwave discharge at the pressures studied here.

Calculations of the ionic mean free path (section 7.2.3) show that for pressures below approximately 0.2 mbar, this quantity is more than one tenth of the discharge tube radius, indicating that for these pressures the free-fall theory might be expected to be applicable. For higher pressures, the ambipolar diffusion model should be considered when calculating the loss of ions to the wall.

Values of j_w were calculated from equation 9.2 for all pressures, using a value of $b_o^+ = 0.12m^2v^{-1}s^{-1}$ (Tachibana & Fukuda 1973) in equation 9.3. For pressures below 0.7 mbar, a value of j_w from the free-fall case was also calculated from equation 9.1. The values of

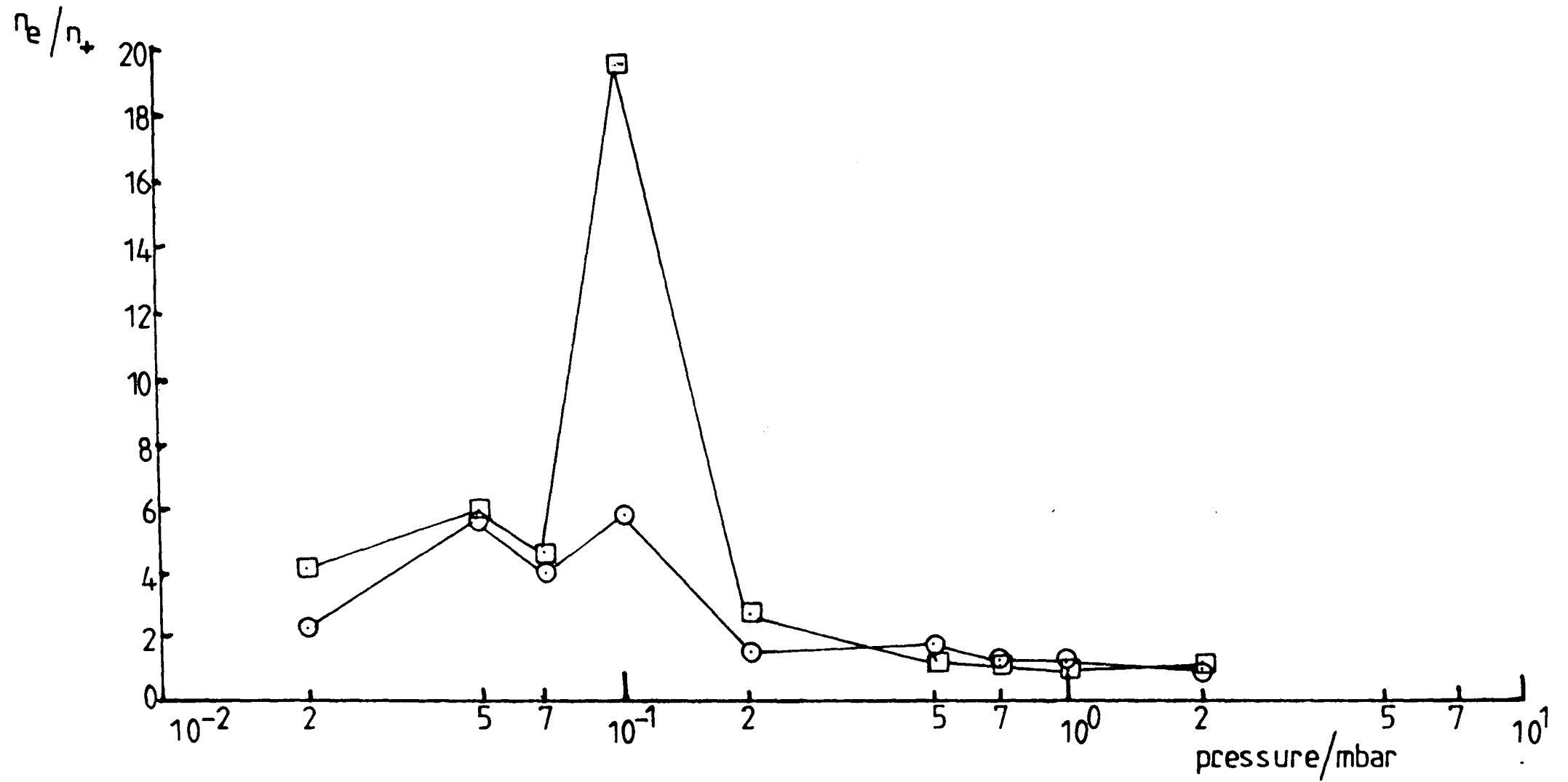


Figure 9.1a Ratio of electron to ion density as a function of pressure. Normalised input powers: \square 50W, \circ 30W.

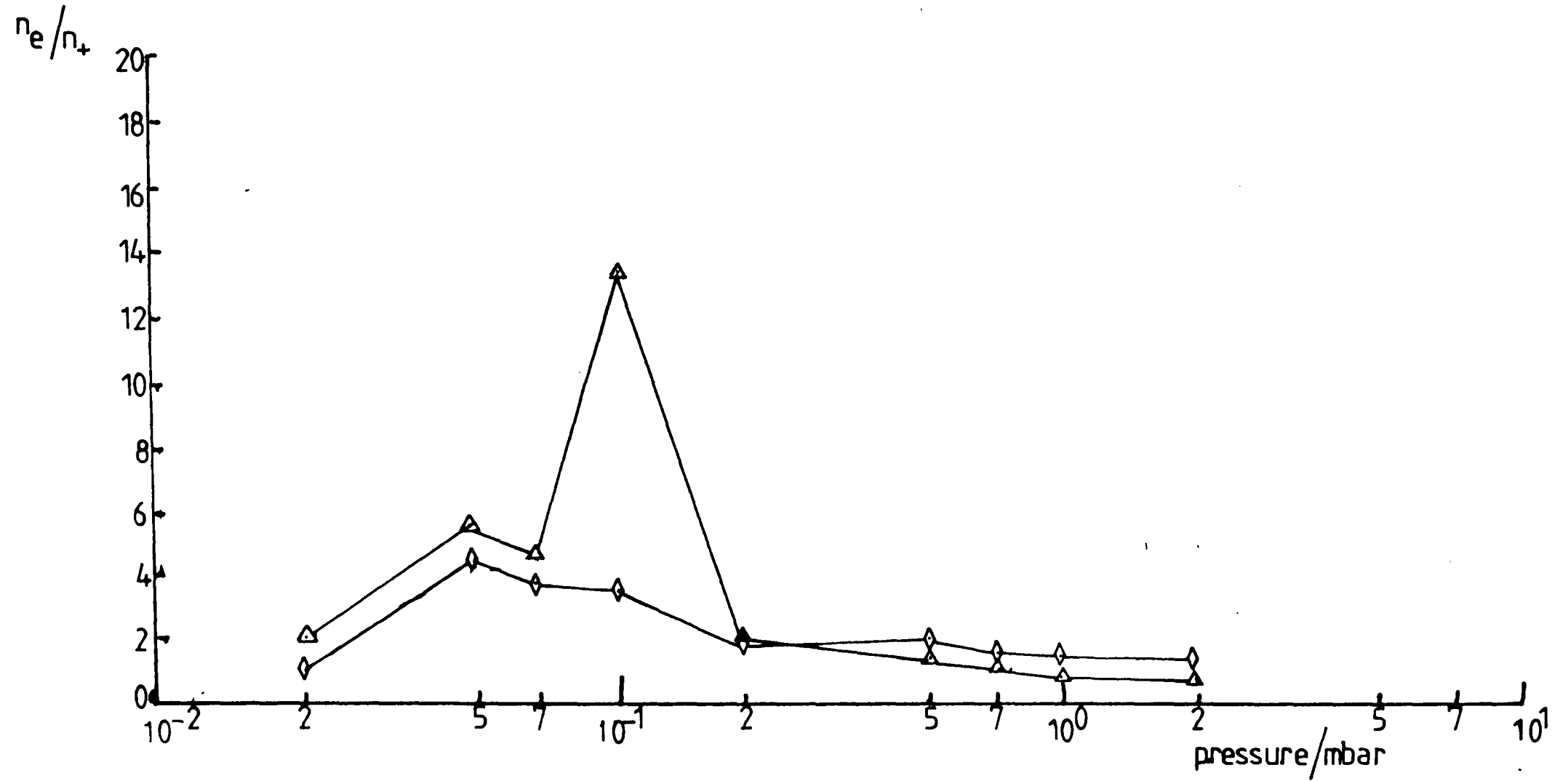


Figure-9.1b Ratio of electron to ion density as a function of pressure. Normalised input powers: \triangle 40W, \diamond 25W.

j_w are presented in table 9.1. (Strictly b_o^+ is a function of gas temperature but this was neglected in the present case). The values of current were then used to estimate the equivalent ion density being lost to the wall. The wall current density can be obtained from:

$$j_w = n_{+w} e (V_+)_{\text{drift}} \quad 9.4$$

where

n_{+w} is the ion density lost to the wall

$(V_+)_{\text{drift}}$ the ion drift velocity.

The ion drift velocity can be calculated from the following (Avni & Winefordner 1975):

$$(V_+)_{\text{drift}} \approx 0.4 \sqrt{\frac{2kT_e}{m_+}}$$

Hence from equation 9.4, the number density of ions lost to the wall can be estimated. Calculation of $(V_+)_{\text{drift}}$ showed it to be of the order of $2 \times 10^3 \text{ms}^{-1}$. The calculated values of n_{+w} for both the ambipolar and free-fall cases can then be compared with the lost ion density calculated from $(n_e - n_+)$, assuming electrical neutrality is the original condition. The electron density measured by the microwave impedance was taken to be the radially averaged electron density for the purposes of equations 9.1 and 9.2. The results are tabulated in table 9.1.

From table 9.1, the calculated ion loss to the walls is seen to exceed the measured value. However, it should be noted that for pressures below 0.5 mbar, the agreement between measured and calculated ion loss

Table 9.1 Comparison of Measured and Calculated Values of Ion loss to the Discharge Tube Walls

Normalised Input Power/W	Pressure/ mbar	Measured lost Ion Density ($n_e - n_+$)/ m^{-3}	Ion Current to Wall (ambipolar) j_w / Am^{-2}	Ion Density lost to wall n_{+WA} / m^{-3}	n $= \frac{n_{+WA}}{n_e - n_+}$	Ion Current to Wall (Free-fall) j_w / Am^{-2}	Ion Density lost to Wall n_{+WF} / m^{-3}	n $= \frac{n_{+WF}}{n_e - n_+}$
25	0.07	4.9×10^{17}	1541.4	5.12×10^{18}	10.4	194.6	6.46×10^{17}	1.3
	0.10	4.3×10^{17}	873.5	3.05×10^{18}	7.1	165.9	5.79×10^{17}	1.3
	0.20	5.7×10^{17}	1174.3	3.57×10^{18}	6.3	387.6	1.18×10^{18}	2.1
	0.50	6.7×10^{17}	560.8	1.62×10^{18}	2.4	440.1	1.27×10^{18}	1.9
	0.70	3.9×10^{17}	312.3	9.72×10^{17}	2.5	369.1	1.15×10^{18}	2.9
	1.00	2.5×10^{17}	153.4	5.47×10^{17}	2.2	-	-	-
	2.00	1.6×10^{17}	46.2	2.02×10^{17}	1.3	-	-	-
30	0.07	4.2×10^{17}	1216.2	4.16×10^{18}	9.9	158.0	5.40×10^{17}	1.3
	0.10	6.3×10^{17}	1140.6	3.92×10^{18}	6.2	213.4	7.33×10^{17}	1.2
	0.20	4.1×10^{17}	1105.3	3.21×10^{18}	7.8	348.9	1.01×10^{18}	2.5
	0.50	5.3×10^{17}	555.1	1.57×10^{18}	3.0	411.9	1.17×10^{18}	2.2
	0.70	1.8×10^{17}	283.9	8.94×10^{17}	5.0	340.0	1.07×10^{18}	5.9
	1.00	-0.4×10^{17}	139.3	5.02×10^{17}	-12.6	-	-	-
	2.00	-2.4×10^{17}	44.5	1.92×10^{17}	-0.8	-	-	-
40	0.07	3.3×10^{17}	754.1	2.84×10^{18}	8.6	107.8	4.05×10^{17}	1.2
	0.10	9.7×10^{17}	1702.3	5.68×10^{18}	5.6	309.3	1.03×10^{18}	1.1
	0.20	6.4×10^{17}	1286.8	3.46×10^{18}	5.4	433.8	1.17×10^{18}	1.8
	0.50	3.0×10^{17}	484.2	1.35×10^{18}	4.5	364.7	1.01×10^{18}	3.4
	0.70	-0.6×10^{17}	251.2	7.95×10^{17}	-13.3	302.0	9.55×10^{17}	15.9
	1.00	-3.5×10^{17}	122.2	4.49×10^{17}	-1.3	-	-	-
	2.00	-4.4×10^{17}	44.4	1.85×10^{17}	-0.4	-	-	-
50	0.07	2.6×10^{17}	619.3	2.24×10^{18}	3.2	85.2	3.09×10^{17}	1.2
	0.10	1.3×10^{18}	2323.4	7.52×10^{18}	13.7	325.7	1.32×10^{18}	1.0
	0.20	8.4×10^{17}	1790.0	4.60×10^{18}	13.3	499.7	1.28×10^{18}	1.5
	0.50	1.3×10^{17}	418.0	1.20×10^{18}	9.7	325.7	9.36×10^{17}	7.2
	0.70	0.3×10^{17}	267.0	8.11×10^{17}	9.7	308.2	9.36×10^{17}	-5.9
	1.00	-1.6×10^{17}	122.1	4.51×10^{17}	9.4	-	-	-
	2.00	7.5×10^{16}	56.1	2.01×10^{17}	8.9	-	-	-

densities is better for the free-fall diffusion model than for the ambipolar model. This is in accord with the calculated values of the ratio of discharge tube diameter to mean free path length. For cases where these two dimensions are of a similar order of magnitude numerical solutions to the diffusion model are required.

In addition, it should be remembered that the ion mobility b_o^+ was considered to be constant. In fact the mobility decreases with increasing gas temperature (Dalgano 1958). Thus at gas temperatures higher than 300K (which it seems reasonable to assume were achieved) the values of wall current calculated from the ambipolar model would be reduced.

The measured values of lost ion density are plotted in figures 9.2(a) and (b) as functions of the calculated values for each theoretical model. The difference between the results of the two models is now clear. It seems reasonable to conclude that, at lower pressures, i.e. below 0.5 mbar, where the free-fall diffusion model is valid, the discrepancy between the probe ion density measurement and the microwave electron density measurement can be accounted for in terms of diffusion to the walls of the argon ions.

For pressures of 0.5 mbar and above, the two diffusion theories are inadequate to describe the processes within plasma and the poor correlation between the calculated and measured ion deficiency is not surprising.

As a consequence of the results of this section, the use of double

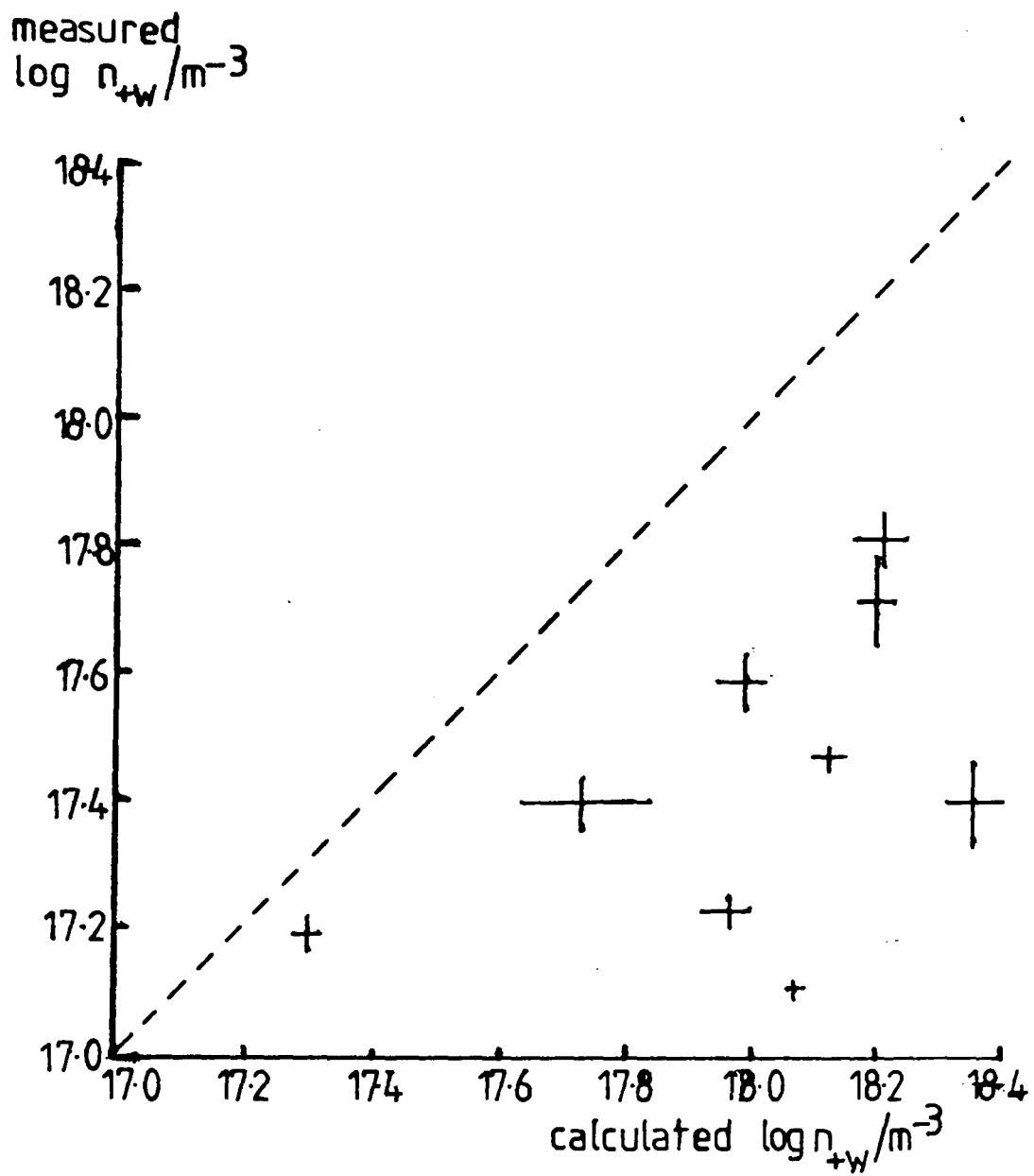


Figure 9.2a Comparison of measured ion loss to the tube walls and loss calculated from ambipolar diffusion theory.

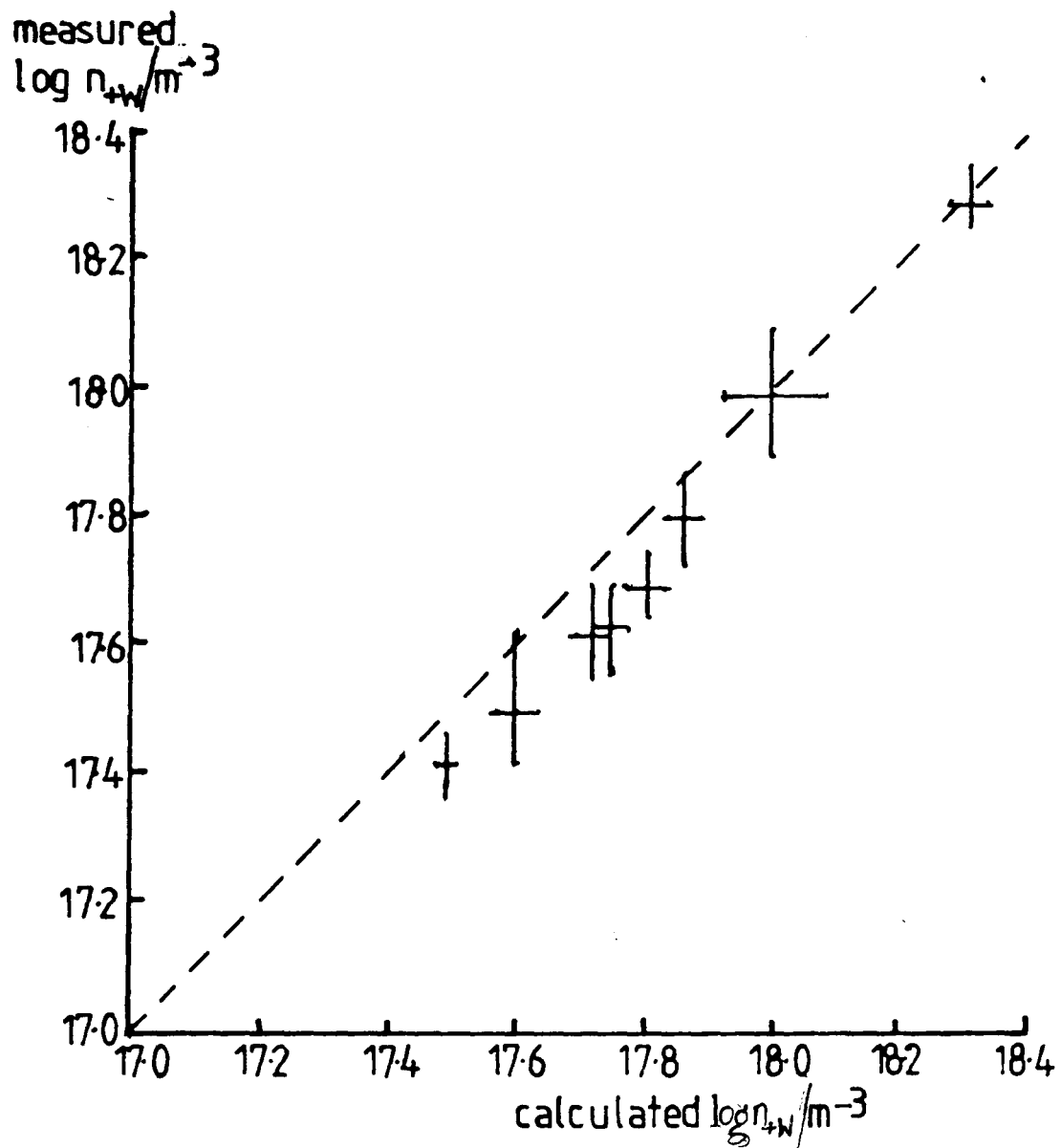


Figure 9.2b Comparison of measured ion loss to the tube walls and loss calculated from free-fall theory.

floating probes to measure the ion density and hence infer the electron density should be treated with caution. This is especially so if the probes are positioned close to the wall of the discharge tube. As probes are often positioned thus in order to avoid perturbation of the plasma by probe supports, the use of double floating probe measurements, without correction being made for ionic diffusion to the discharge tube walls, could lead to serious errors in the resulting values of electron density.

9.3 Determination of Plasma Phase

9.3.1 The Plasma Regimes

The collisional-radiative model of Schlüter as later developed by Fujimoto (1972) can be used to describe plasmas which are far from partial local thermodynamic equilibrium (p - LTE) as well as those in p - LTE.

The population density n_m of an atomic level m is given by the equation (Fujimoto 1979)

$$n_m = r_m^{(0)} n_m^S + r_m^{(1)} n_m^B \quad 9.5$$

where

n_m^S is the population density of level m calculated from the Saha-Boltzmann equation

n_m^B is the population density of level m calculated from the Boltzmann equation

$r_m^{(0)}$, $r_m^{(1)}$ are the "population coefficients" which are characteristic of the atomic system.

Thus equation 9.5 can be used to determine the value of n_m for any set of plasma conditions provided that $r_m^{(0)}$ and $r_m^{(1)}$ are known. The population coefficients are only weakly dependent upon electron temperature and $r_m^{(0)}$ is only weakly dependent upon electron density. However for $r_m^{(1)}$, Fujimoto has determined the variation with n_e for the hydrogen atom as being that shown in fig. 9.3.

Three plasma phases (or regimes) can be determined from the behaviour of $r_m^{(1)}$ and $r_m^{(0)}$. These are as follows:

- (i) the coronal phase: here the second term of the right hand side of equation 9.5 dominates and $r_m^{(1)}$ is proportional to n_e . This corresponds to the region AB in fig. 9.3 for a level $m = 5$. In the coronal phase collisional excitation is balanced by radiative de-excitation.
- (ii) the saturation phase: here, again, the second term of the right hand side of equation 9.5 dominates but now $r_m^{(1)}$ is independent of n_e . Thus n_m is also independent of n_e . This corresponds to the region CD in fig. 9.5. In the saturation phase collisional excitation is balanced by collisional de-excitation.
- (iii) partial LTE: here, the first term of the right hand side of equation 9.5 dominates and, as complete LTE is approached, $r_m^{(0)}$ tends to unity. Thus if $n_e = n_+$ it follows that n_m is proportional to n_e^2 . In the p - LTE phase, recombination becomes significant and the level m is in equilibrium with the continuum.

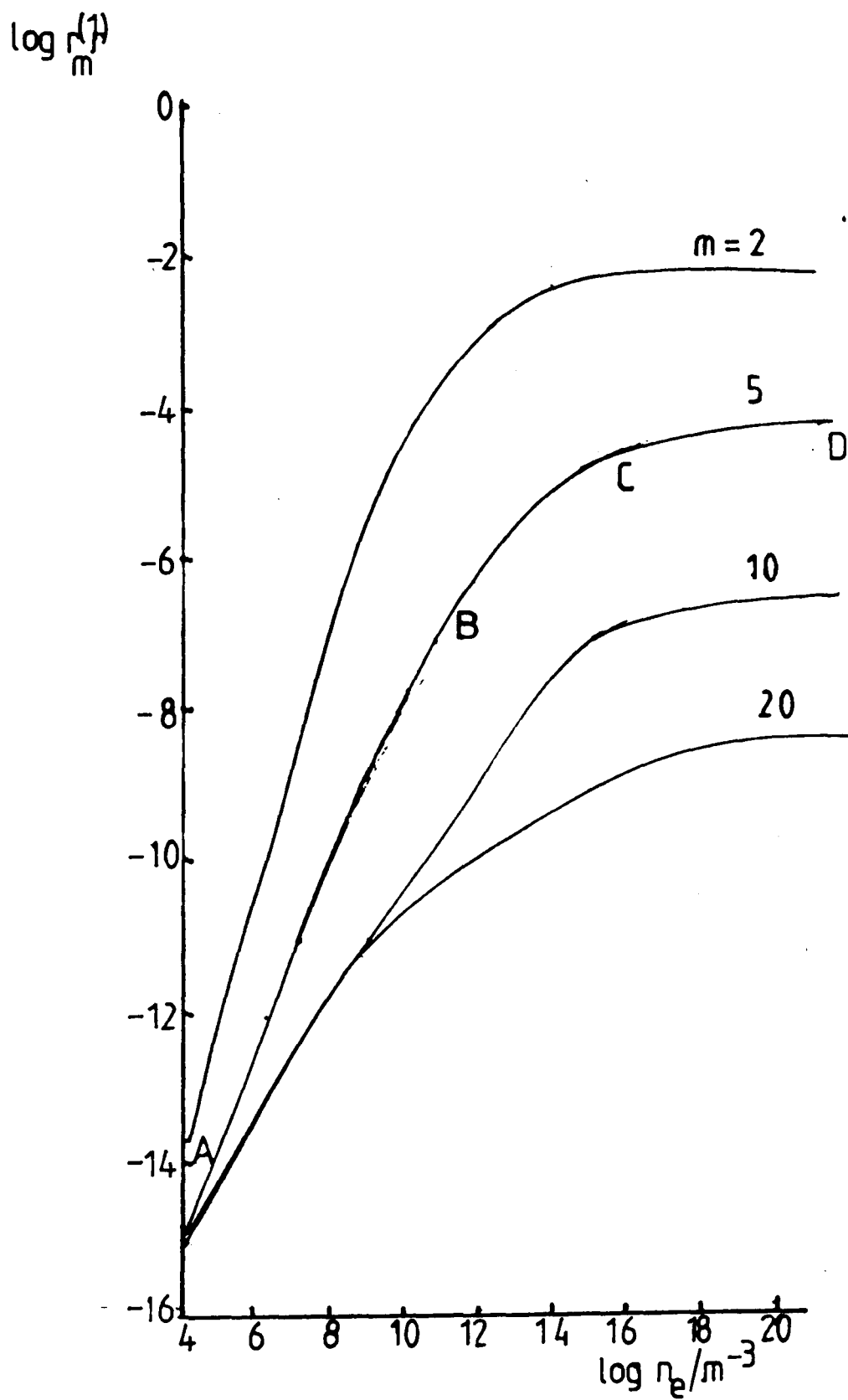


Figure 9.3 Variation of population coefficient $r_m^{(1)}$ with electron density calculated by Fujimoto.

The transition between phases (i) and (ii) above is relatively slow and is termed the quasi-saturation phase (section BC in fig. 9.3). In this region full collisional-radiative models must be used. Figure 9.3 also shows that the values of $r_m^{(1)}$ fall consecutively into quasi-saturation from the upper levels downwards with increasing electron density. Thus it would be expected that the higher lying levels of the atom would reach ^{quasi-}saturation at a lower electron density than for the lower levels.

By studying the population density of a given level as a function of the electron density, the plasma phase can be determined.

9.3.2 The Plasma Phase

In order to eliminate the power dependence of the values of electron density and population density of the argon levels, the values of these variables for different pressures, at a given input power were obtained from figure 8.4 and the equivalent plots of figures 6.6 for each atomic level respectively. Thus for a given input power values of n_e and $\log_{10} n_m$ for pressures between 6.00 and 0.07 mbar can be obtained. These are then plotted to produce a figure which shows the plasma phase.

The input powers selected were 25, 30, 40 and 50W as for most pressures these powers lay inside the extreme limits of the available data, thus avoiding extrapolation. The results are shown in figures 9.4(a) to (e). For clarity it was not possible to display all the atomic argon levels on a single diagram; a series of diagrams (figs. 9.4(a) to (d)) for the above normalised input powers are shown together with a pair of diagrams

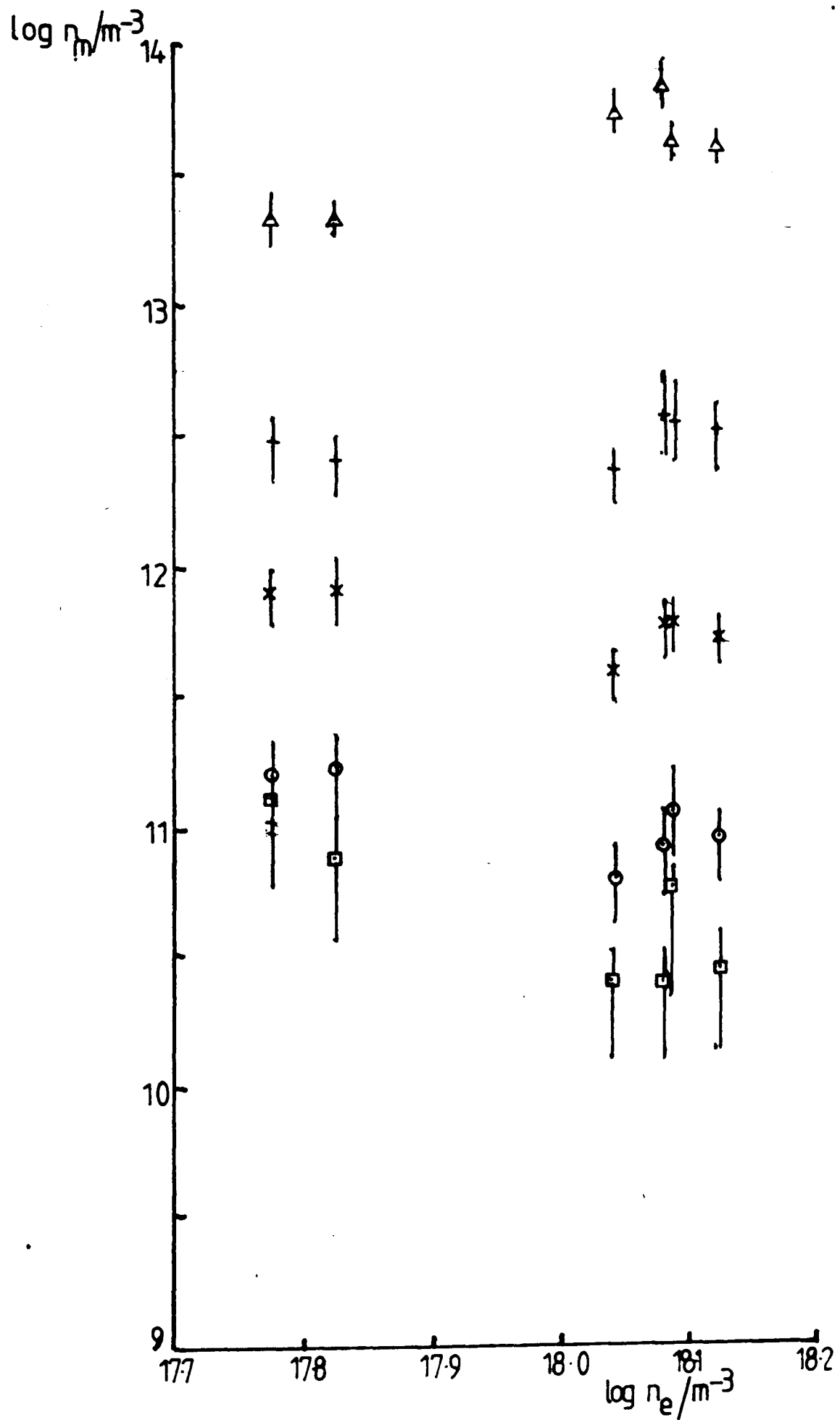


Figure 9.4a Variation of population density with electron density for normalised input powers of 25W.

Atomic levels: Δ 4p', * 5p, x 5d, \circ 8s, \square 9s.

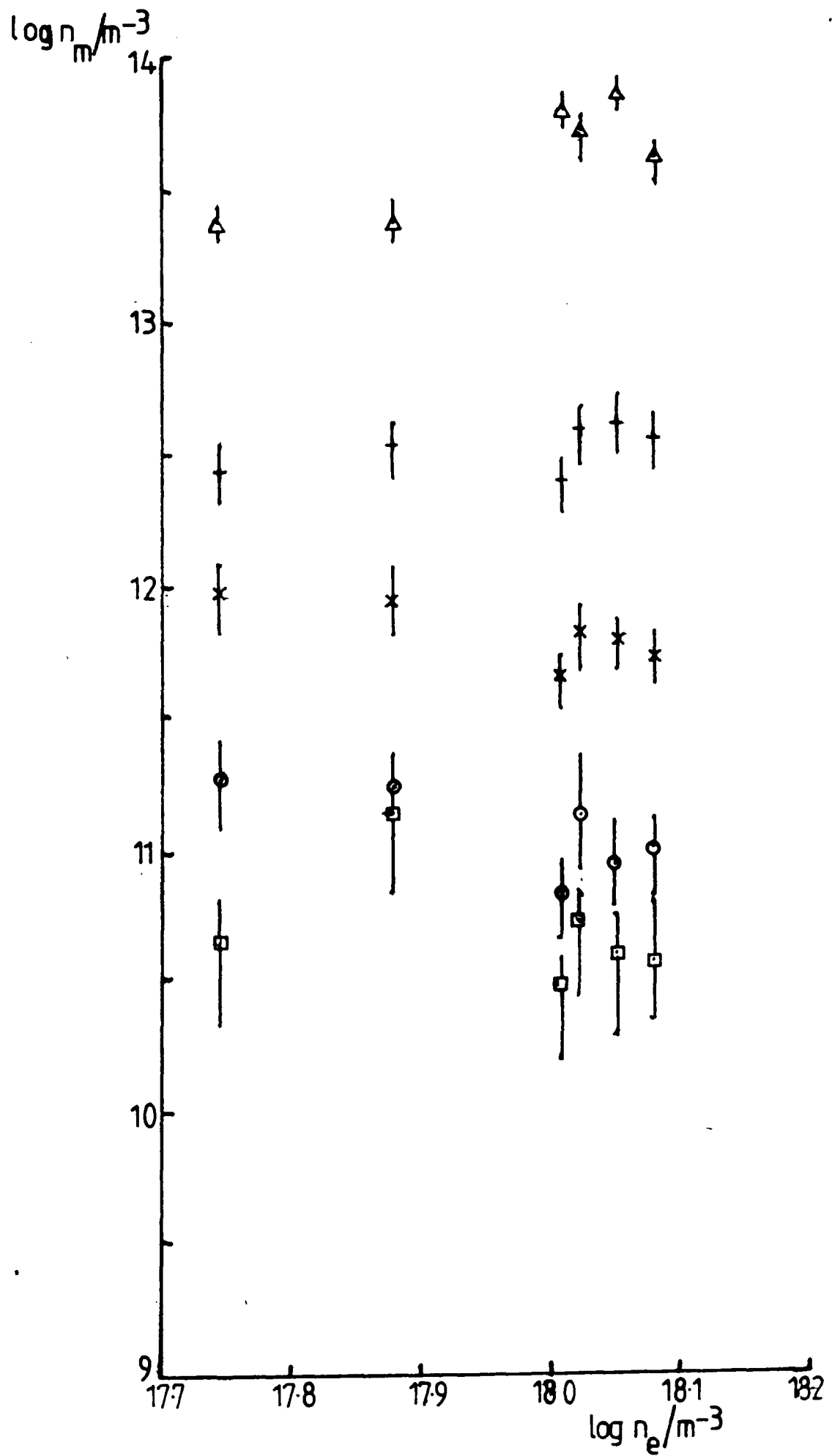


Figure 9.4b Variation of population density with electron density for normalised input powers of 30W.

Atomic levels: Δ 4p', + 5p, x 5d, o 8s, \square 9s.

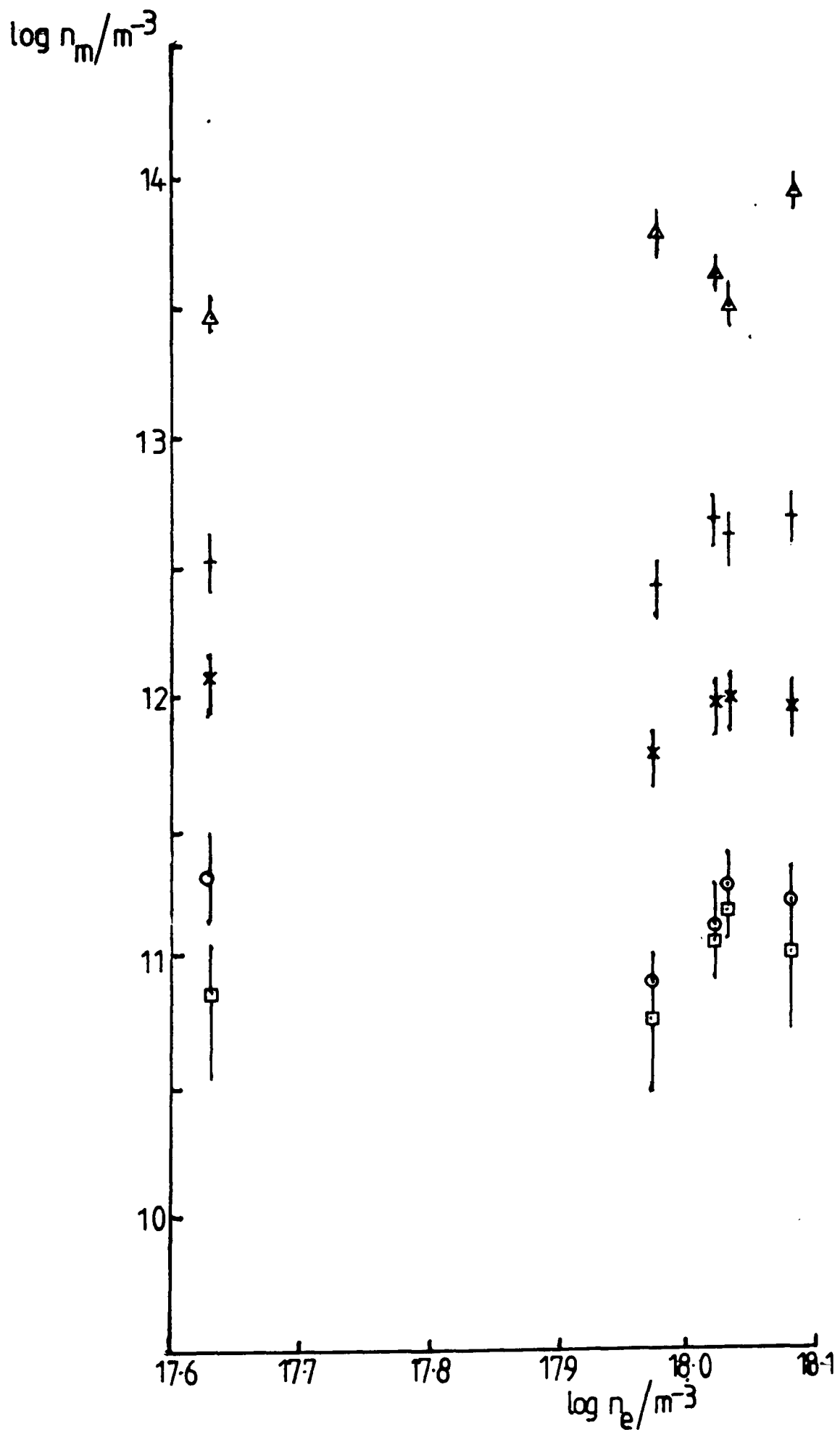


Figure 9.4c Variation of population density with electron density for normalised input powers of 40W.

Atomic levels: Δ 4p', + 5p, x 5d, o 8s, \square 9s.

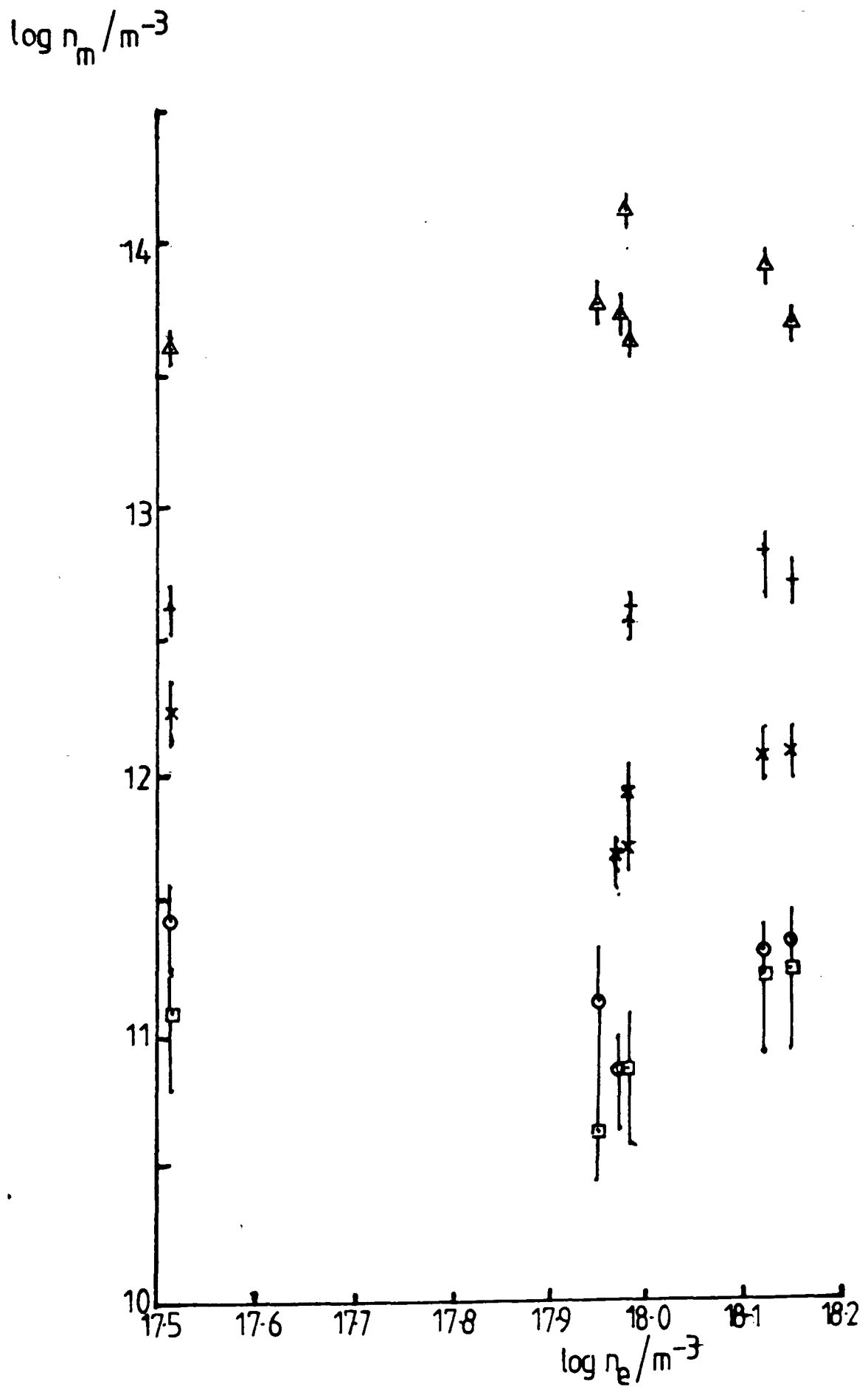


Figure 9.4d Variation of population density with electron density for normalised input powers of 50W.
 Atomic levels: Δ 4p', + 5p, x 5d, O 8s, \square 9s.

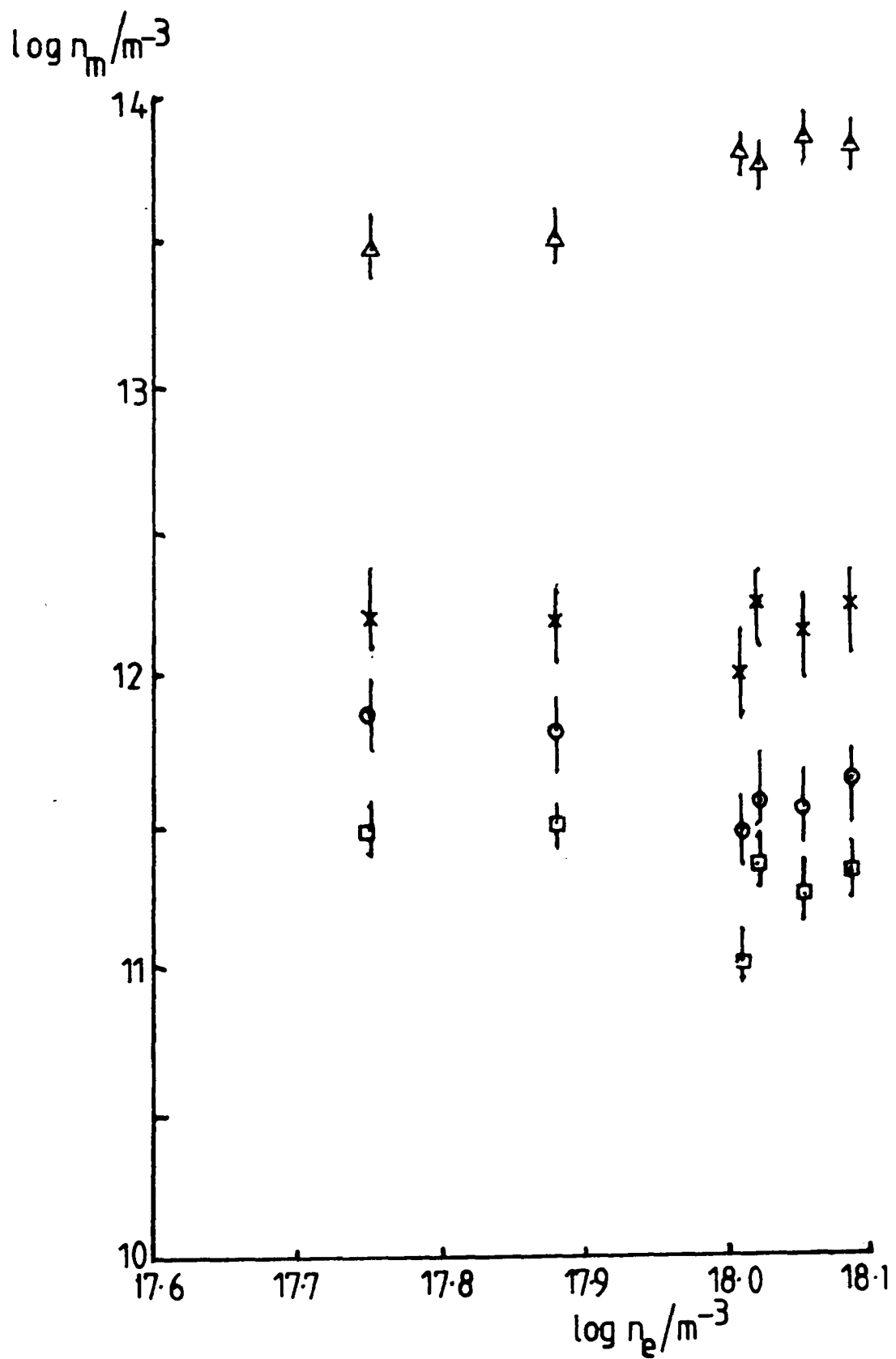


Figure 9.4e Variation of population density with electron density for normalised input powers of 50W.

Atomic levels: Δ 4p, \times 6s', \circ 7s, \square 6d.

(figs. 9.4(d) and (e)) showing results for all the atomic levels investigated at an input power of 50W.

It should be noted that figures 9.4(a) to (e) do not include any results for the pressures 2.00, 3.00 and 6.00 mbar. It was found that the values of population density calculated for these pressures were anomalously low, considering the electron densities at these pressures. These low values seem to indicate a decrease in the radiative de-excitation of all the atomic levels at these pressures; the corollary implication being an increase in collisional de-excitation.

In section 6.2, it was noted that, at pressures of 6.00 and 3.00 mbar, the Boltzmann plot "straightens" for the higher lying levels indicating an approach towards partial local thermodynamic equilibrium. Thus the apparent increase in collisional de-excitation, at the expense of radiative de-excitation, at these pressures is supported by the evidence of movement toward the approach to equilibrium.

An example of the anomalous population densities is provided in fig. 9.5. This is a reproduction of fig. 9.4(d) but includes the population densities measured at 2.00, 3.00 and 6.00 mbar, which are circled. As can be seen the values at these pressures are reduced by factors between ≈ 2.0 and ≈ 10.0 , depending upon the level concerned. It appears that the diminution increases as the energy of the level increases until an approximately constant value is achieved.

From figs. 9.4(a) to (e) it can be clearly seen that for all values of input power, the atomic levels above and including the 5d level are

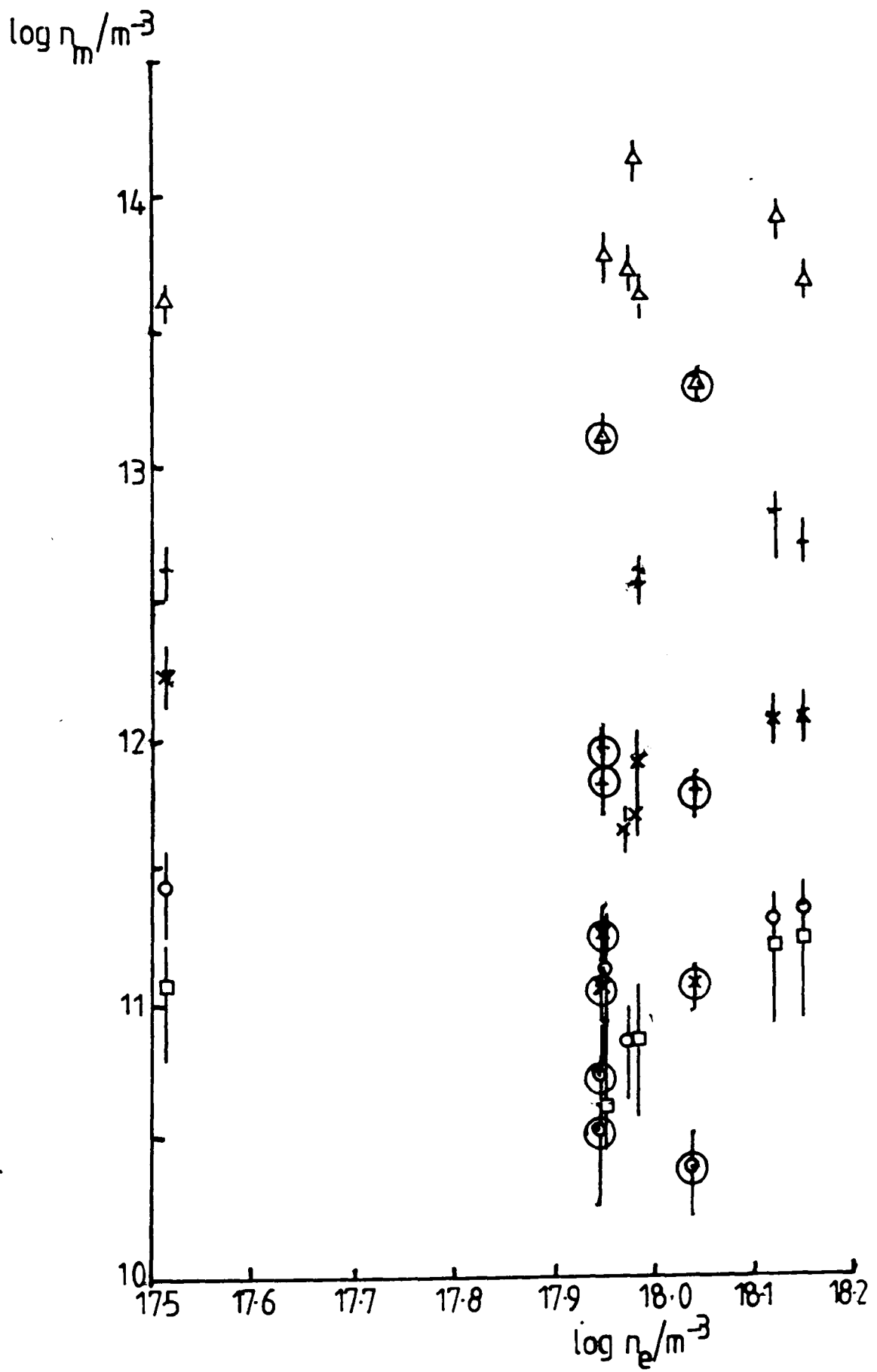


Figure 9.5 Population density vs n_e . Normalised input power 50W. Circled points pertain to pressures ≥ 2.00 mbar.

in the saturation phase. Only the three lowest levels considered, namely the 5p, 4p' and 4p groups of levels, are not in this phase. It would appear that these levels are approaching saturation and occupy the quasi-saturation phase.

9.4 Determination of the Population Coefficient $r_m^{(1)}$

Theoretical calculations of the population coefficients $r_m^{(0)}$ and $r_m^{(1)}$ exist for hydrogen (Fujimoto 1972), argon (Katonis 1976), helium and ionic helium (Drawin 1977). Experimentally derived values for the 4p, 4d, 5d and 6d levels have been tabulated by van der Mullen, et al (1980). The demonstration in section 9.3.2 of the existence of the saturation phase in the argon electrodeless microwave discharge provides an opportunity to extend the range of tabulated values for the coefficient $r_m^{(1)}$.

For the saturation phase, the expression for the population density n_m of a level m is dominated by the second term of the right hand side of equation 9.5. That is

$$n_m = r_m^{(1)} n_m^B = r_m^{(1)} \frac{n_1 g_m}{Z g_1} \exp\left(\frac{-E_m}{kT_e}\right) \quad 9.6$$

where the symbols have their previously assigned meanings. Thus, if the expected Boltzmann population density of the level can be calculated, $r_m^{(1)}$ may be derived.

For the levels 4p, 4p' and 5p, equation 9.6 is not valid and the $r_m^{(0)}$ values would be required in order to describe fully the population densities of these levels. Values of $r_m^{(1)}$ for the remaining levels were calculated from equation 9.6. The only sources of error in the

calculation were the measured population density n_m and the electron temperature T_e . It should be noted from fig. 7.6 and table 7.1 that the errors in T_e increase considerably for the lower pressures. To accommodate this, $r_m^{(1)}$ was calculated at each of six pressures between 1.00 and 0.07 mbar for a given input power. The weighted mean of the $r_m^{(1)}$ values thus generated was then evaluated and these values are presented in table 9.2.

The values of $r_m^{(1)}$ for each level are plotted as a function of the energy of the level in fig. 9.6. With the exception of the 5d level (which appears to have an anomalously low $r_m^{(1)}$ value), the population coefficient increases smoothly with decreasing energy above the ground state. Comparison with the values of van der Mullen et al for the 5d and 6d levels shows reasonable agreement for the latter. Inspection of fig. 9.6 shows that the curve would pass through a value of 5.2×10^{-6} for the 5d level, which would agree with the value of $r_m^{(1)}$ for this level given by van der Mullen et al. It would not be expected to find the 6s and 6s' levels in the saturation phase when the 5d level was in the quasi-saturation phase. It must therefore be concluded that the anomalous value of $r_m^{(1)}$ for the 5d level is due to error in the data.

9.5.1 Determination of Plasma Type

The determination of the plasma type, that is the predominant process (ionisation or recombination) within the plasma may be achieved by a consideration of the measured population densities of the atomic levels and the expected values calculated from the Boltzmann and Saha equations.

Table 9.2

Calculated Values of the Population Coefficient $r_m^{(1)}$

Atomic Level	$r_m^{(1)}$	v.d. Mullen et al
5d	$(3.9 \pm 0.4) \times 10^{-6}$	5×10^{-6}
6s	$(1.2 \pm 0.3) \times 10^{-5}$	-
6s'	$(9.4 \pm 0.8) \times 10^{-6}$	-
7s	$(3.9 \pm 1.3) \times 10^{-6}$	-
6d	$(1.4 \pm 0.1) \times 10^{-6}$	2×10^{-6}
8s	$(7.5 \pm 1.0) \times 10^{-7}$	-
9s	$(5.0 \pm 0.7) \times 10^{-7}$	-

TABLE 9.3 GRADIENTS OF $\log(n_m/g_m)$ vs $\log(E_m^{\text{ion}})$

Magnetron Current/mA	40	50	100	150
Pressure/mbar				
6.00	3.9 ± 1.4	4.1 ± 1.3	3.9 ± 1.2	2.9 ± 0.6
2.00	3.3 ± 0.6	3.9 ± 0.9	3.7 ± 1.1	3.3 ± 0.9
0.70	3.3 ± 0.4	3.5 ± 0.4	2.8 ± 0.9	3.1 ± 0.3
0.20	2.4 ± 0.9	3.4 ± 0.6	2.9 ± 0.3	3.0 ± 0.3
0.07	2.3 ± 1.0	2.7 ± 0.6	3.0 ± 0.9	2.7 ± 0.3

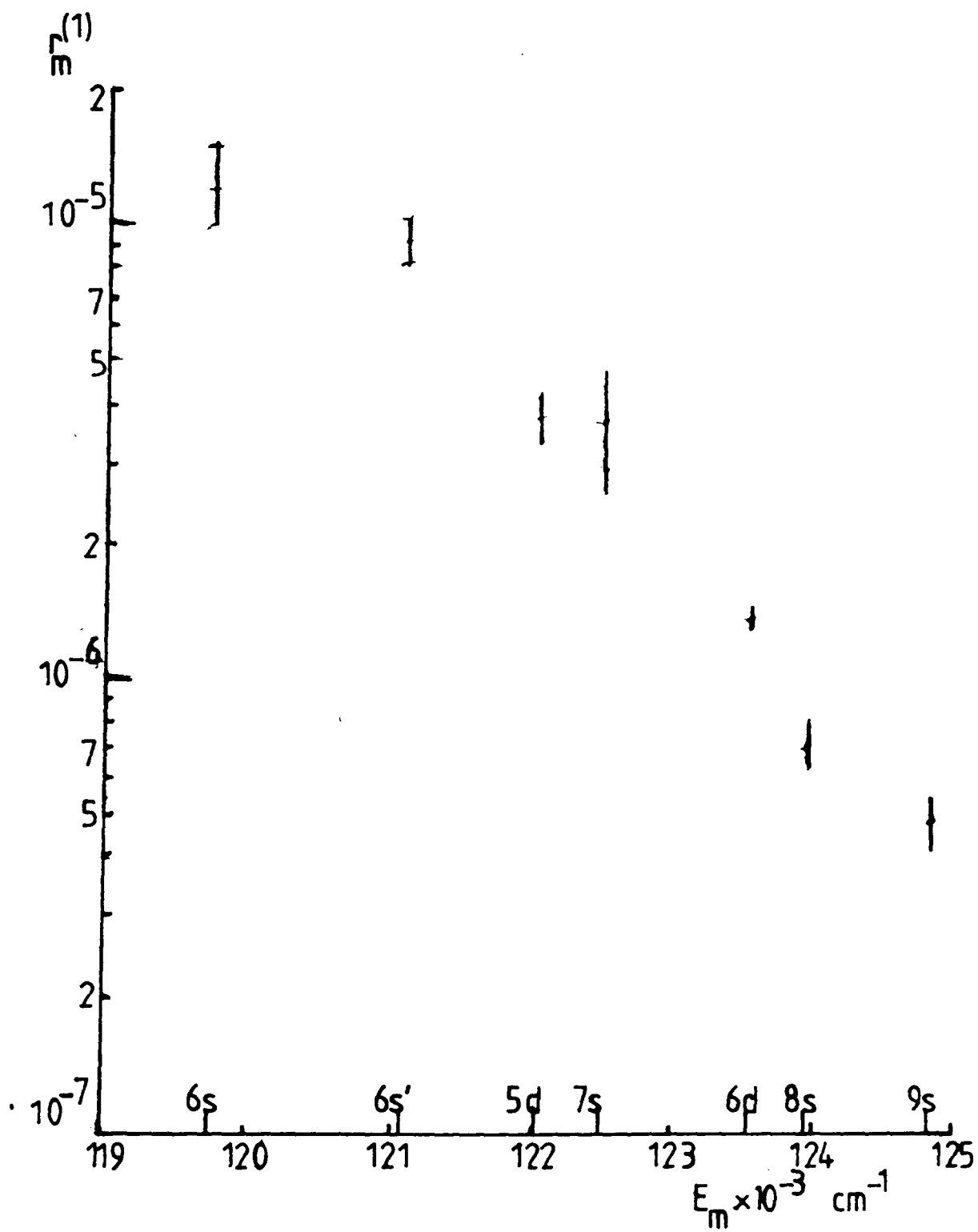


Figure 9.6 Variation of $r_m^{(1)}$ with E_m

Fujimoto (1979) and Raaijmakers et al (1983) have shown that for "ionising"¹ plasmas, the ground and lower levels are relatively over-populated with respect to the values calculated from the Saha equation. For a predominantly "recombining"¹ plasma, the opposite is true and the lowest atomic levels are relatively under-populated.

Comparison of the measured and calculated values is represented by fig. 9.7. The diagram is constructed in the following way: the ground state population density is calculated from the gas laws and the straight line B is drawn from the ground state value (at $E=0$), using the measured electron temperature T_e to give the gradient of $(kT_e)^{-1}$. The point n_{∞}/g_{∞} is calculated by assuming a fictitious level of energy equal to the ionisation energy E^+ . Substituting the value $E = E^+$ into the Saha equation:

$$S(T_e, E_i) = \frac{n_e n_+}{n_i} = \frac{2g_+}{g_i} \left(\frac{2\pi mkT_e}{h^2} \right)^{3/2} \exp \left(\frac{-E^+ - E_i}{kT_e} \right)$$

gives the value n_{∞}/g_{∞} :

$$\frac{n_{\infty}}{g_{\infty}} = \frac{n_e}{2} \cdot \frac{n_+}{g_+} \left(\frac{h^2}{2\pi mkT_e} \right)^{3/2}$$

where

g_+ is the effective statistical weight of the ion ground state ($g_+ = 6$ for argon).

The second line, S, may then be constructed, from the point n_{∞}/g_{∞} , parallel to B. The measured values of the population densities of the atomic levels can then be plotted in a Boltzmann plot.

¹ In this context "ionising" plasmas are those for which the dominant electron flow through the atomic levels is upwards by collisional excitation and "recombining" plasmas those for which the dominant electron flow is downwards.

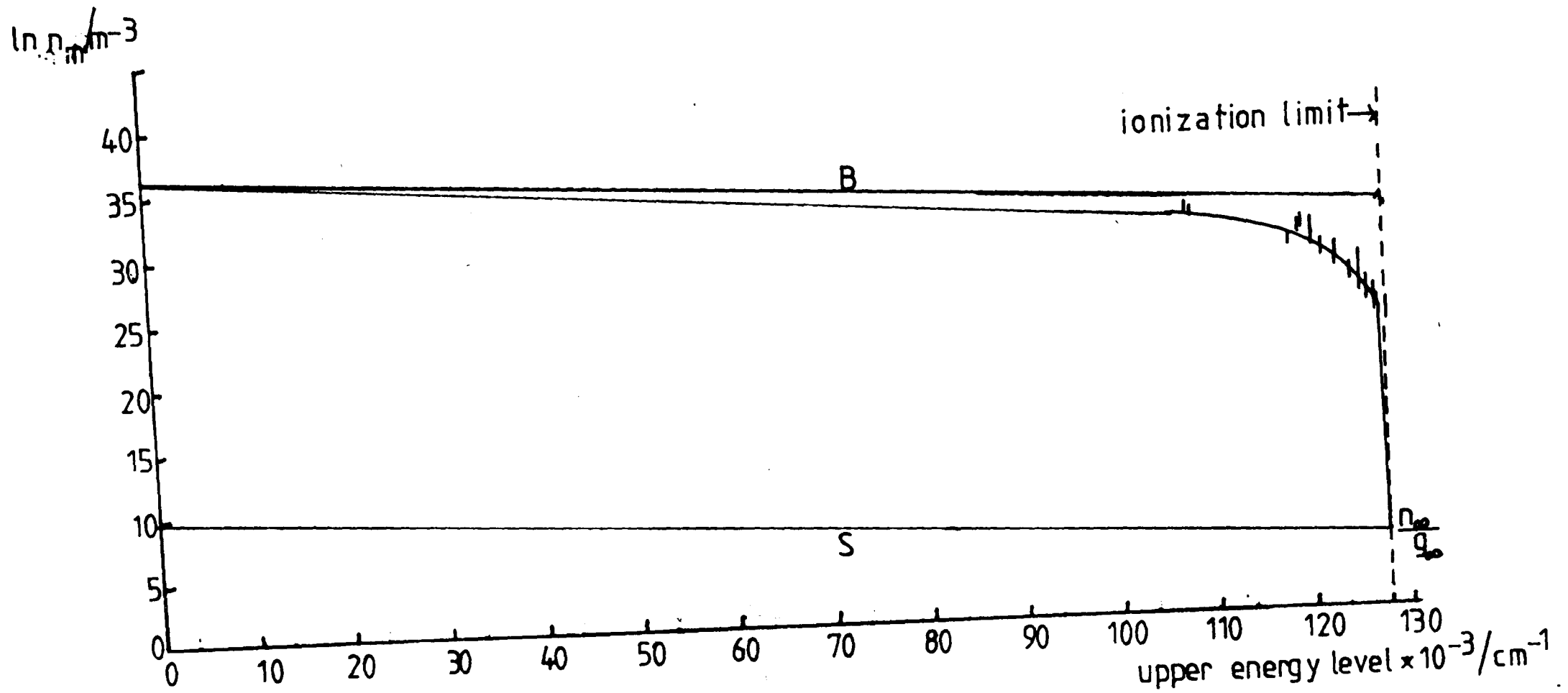


Figure 9.7 Comparison of Boltzmann & Saha equations with measured population density.
 Pressure 0.07mbar, magnetron current 100mA, $n_e = 2.9 \times 10^{17} \text{ m}^{-3}$, $T_e = 45065 \text{ K}$.

9.5.2 Results from the Cavity Centre

Construction of the diagrams described in section 9.5.1 for the results from the cavity centre, showed that for all pressures and magnetron currents the ground state and lower levels of the argon atom were overpopulated with respect to the Saha equation and so the plasma was predominantly ionising in this region of the discharge. It follows, therefore, that the collisional-radiative ionisation rate coefficient, S_{cr} , and the collisional-radiative recombination rate coefficient, α_{cr} , are related by

$$S_{cr} n_1 n_e \gg \alpha_{cr} n_+ n_e$$

Thus for the centre of the cavity, the upward (excitation) flow of electrons predominates over their downward (de-excitation flow).

9.5.3 Results from Outside the Cavity

Although few values of electron temperature were obtained, as described in section 7.3, for distances greater than 3 cm from the cavity centre, it was possible to construct diagrams as described in section 9.5.1 for certain pressures. At each of these pressures, the conclusion was the same as for the centre of the cavity: the plasma was predominantly ionising along the length of the discharge.

9.6 Relationship between Population Density and Energy of Level

It has been reported by previous workers (Fujimoto 1979, van der Mullen 1980) that for atomic levels in the saturation phase, the relationship between the population density, n_m , of a level m and the ionisation energy of that level can be expressed as

$$\frac{n_m}{g_m} \propto (E_m^{\text{ion}})^x \quad 9.7$$

where $x \approx 3$ and g_m is the statistical weight of the level m .

For the atomic levels considered here values of $\log_{10} (n_m/g_m)$ were plotted as functions of E_m^{ion} and the gradient of this curve found by a least squares fit method. Some results are tabulated in table 9.3. From the table it can be seen that, with few exceptions, a gradient of value three falls within the limits of error. The average value of gradient was found to be 3.2 with a standard deviation of 0.5. Values of correlation coefficient for the straight line fit varied from 0.93 to 0.99. The correlation coefficient could be improved by omitting data for the 4p, 4p' and 5p groups of levels, which, as shown in section 9.3.2, were not in the saturation phase.

Thus the value of x in equation 9.7 was found to be

$$x = 3.2 \pm 0.3$$

where the error in x has been approximated to two-thirds of the standard deviation. This is in agreement with the results in argon of previous workers.

9.7 Excitation Mechanism

The existence of the saturation phase is the result of the establishment of a "ladder-like" excitation mechanism. That is to say that the predominant populating mechanism of a level m is by excitation from a level $(m-1)$ due to electron collisions. Similarly, the predominant de-populating process of level m is collisional excitation

to the level (m+1). Thus electrons "climb" through the atomic system of levels until being liberated from the uppermost levels by ionisation.

The transition from the corona to the quasi-saturation phase occurs when the depopulating process in the former regime (spontaneous radiative de-excitation) is approximately equalled by depopulating processes in the latter (collisional excitation to the next highest level). Thus if $C(p,q)$ is the collisional rate coefficient from a level p to a higher level q , $A(p,q)$ the transition probability for radiative de-excitation from level p to a lower level q , the transition condition is

$$C(p,p+1)n_e \approx \sum_{q < p} A(p,q) \quad 9.8$$

For hydrogen, Fujimoto (1979) gives expressions for $C(p,q)$ and $A(p,q)$ which are:

$$C(p,q) = G \frac{R}{E_{p,q}} f_{p,q} \exp \frac{-E_{p,q}}{kT_e} \quad 9.9$$

with
$$G = \frac{8.69 \times 10^{-8}}{Z} \left(\frac{Z^2 R}{kT_e} \right)^{\frac{1}{2}} \text{cm}^3 \text{s}^{-1}$$

where Z is the effective nuclear charge

R is the Rydberg energy (13.6eV)

$f_{p,q}$ is the absorption oscillator strength

$E_{p,q}$ is the energy between levels p and q

and

$$\sum A(p,q) \approx H p^{-4.5} \quad 9.10$$

with
$$H = 1.65 \times 10^{10} Z^4 \text{s}^{-1}$$

From equations 9.9 and 9.10 with appropriate approximations, the electron density n_e^c at which the transition to the quasi-saturation phase occurs can be approximated from equation 9.8 by:

$$n_e^c \approx 2^3 \left(\frac{H}{G} \right)^p \text{cm}^{-3} \quad 9.11$$

Although equation 9.11 is strictly applicable to hydrogen it may be useful to calculate n_e^c values. For levels $p = 5$ to 9 , values of n_e^c were calculated to range from 7.59×10^{17} to $5.13 \times 10^{15} \text{m}^{-3}$ for an electron temperature of $T_e = 3 \times 10^4 \text{k}$.

Van der Mullen, et al (1980) record a lower bound of $1 \times 10^{19} \text{m}^{-3}$ for the transition electron density. In the work presented here, the saturation phase has been observed at an even lower electron density of $n_e = 3 \times 10^{17} \text{m}^{-3}$. It should be emphasised however that equation 9.11 is an approximation only. It may be that the appearance of the saturation phase at a slightly lower electron density than predicted is due to the optical thickness of the argon resonance lines which effectively reduces the spontaneous radiative decay probability $A(p,q)$ and hence reduces the $A(p,q)$ term in equation 9.8.

9.8 Evaluation of Spectral Excitation Temperature

Although the plasma has been shown not to be in partial-local thermodynamic equilibrium, and hence the temperature T in equations 6.1 and 6.2 is not equal to the electron temperature, a spectral excitation temperature may still be evaluated from the equation 6.1, that is

$$kT_{s,m} \equiv \left(\frac{1}{n_m} \frac{dn_m}{dE_m} \right)^{-1} \quad 9.12$$

Obviously, the value $T_{s,m}$ is not equal for all levels of the atomic system and can only apply to each individual level m .

Values of $T_{s,m}$ calculated from equation 9.11 varied from, typically 14000K for the lowest (4p) level to 1075K for the 9d level. The values of $T_{s,m}$ appear to be relatively insensitive to pressure and power, but are always at least one order of magnitude less than the electron temperature except for the lowest levels. For the pressures at which the upper atomic levels tend toward equilibrium (ie. 6.00, 3.00 and 2.00 mbar) the excitation temperatures associated with these upper levels is of the same order of magnitude as that associated with the lower 4p and 4p' level. Thus, at these pressures the highest and lowest levels of the atom have very similar excitation temperatures whilst the intermediate levels have temperatures at least one order of magnitude lower. It is probable that the large value of excitation temperature for the highest levels at these pressures is due to an increase in recombination. Recall that in the "ladder-like" excitation mechanism of the saturation phase, the dominant populating mechanism of a level m is collisional excitation from a level $(m-1)$. If ion-recombination is now increased (as the particle density increases), population of the upper atomic levels due to recombination would also increase. Thus the populating mechanism of the higher levels is no longer only the "ladder-like" excitation. It should be noted that in the context of a non-equilibrium plasma, the term "temperature" is somewhat meaningless. The spectral excitation temperature of a level, $T_{s,m}$, effectively becomes a measure of the deviation of that level from the expected equilibrium value. In this context the high values

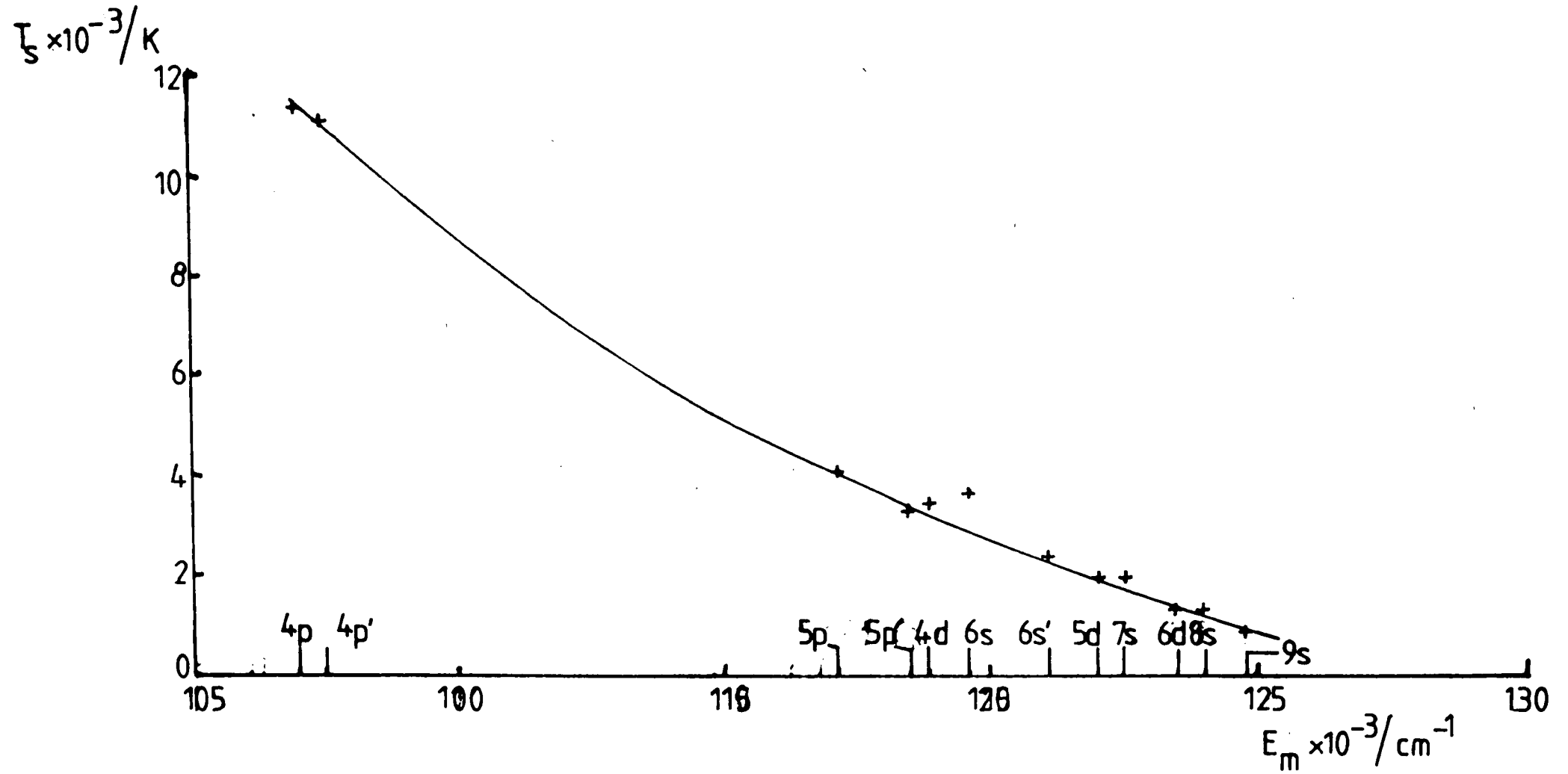


Figure 9.8 Variation of spectral excitation temperature with energy of atomic level

of $T_{s,m}$ for the highest upper levels merely indicate a relative increase in the population densities of those levels compared with the expected values if the ladder-like excitation mechanism were the sole source of population.

At pressures below 2.00 mbar, the excitation temperatures vary smoothly with the energy of the level. This variation is shown in fig. 9.8 for a pressure of 0.5 mbar and a magnetron current of 150mA.

9.9 Probe Characteristics of the Third Type

it was reported in section 7.1 that a form of double floating probe characteristic was observed which is not covered by existing theory. The form of this characteristic is illustrated in fig. 7.2. It is intended here to demonstrate that the form of this characteristic may be explained by considering the formal probe equations in the presence of two Maxwellian electron distributions.

The concept of a double Maxwellian electron distribution is not new. The existence of two such electron groups, one with a large number density but low mean energy and the second of small number density but much higher mean energy, has been postulated by Schlüter (1963) in the radiative-ionisation-recombination model and has been reported by many authors (eg. Thomas 1965).

9.9.1 Double Floating Probe Equations for a Double Maxwellian Electron Distribution

Consider a double-floating probe system such as that described in section 5.1 and assume that the free electrons consist of two Maxwellian

distributions: the first of number density n_e with energy characterised by a temperature T_e , the second of number density n'_e with energy characterised by a temperature T'_e . Let the first group be of high number density but low energy and the second of low number density but high energy, such that:

$$n_e > n'_e \quad \text{and} \quad T_e < T'_e$$

If the areas of the two probes are equal, then the electron current $I_{e1,2}$ to each probe is given by:

$$I_{e1} = i_{e1} \exp\left(\frac{V_1}{V}\right) + i'_{e1} \exp\left(\frac{V_1}{V'}\right) \quad V_1 < 0$$

$$I_{e2} = i_{e2} \exp\left(\frac{V_2}{V}\right) + i'_{e2} \exp\left(\frac{V_2}{V'}\right) \quad V_2 < 0$$

where i_{e1}, i_{e2} are the random electron currents of the group (n_e, T_e)
 i'_{e1}, i'_{e2} are the random electron currents of group (n'_e, T'_e)
 V_1, V_2 are the probe to plasma voltages of probes 1 and 2
and

$$V = \frac{kT_e}{e} \quad \text{and} \quad V' = \frac{kT'_e}{e}$$

The floating condition that ^{the} sum of the ion and electron currents to each probe should be equal gives

$$I_{+1} + I_{+2} = -(I_{e1} + I_{e2}) = I_d$$

where

$I_{+1,2}$ are the ion currents to probes 1 and 2

I_d is the current in the measuring circuit.

Assuming that the ion currents are equal we have

$$\begin{aligned} \sum I_+ &= - \left[i_{e1} \exp\left(\frac{V_1}{V}\right) + i'_{e1} \exp\left(\frac{V_1}{V'}\right) + i_{e2} \exp\left(\frac{V_2}{V}\right) + i'_{e2} \exp\left(\frac{V_2}{V'}\right) \right] \\ &= -I_{e1} \left[\frac{1 + \frac{i_{e2} \exp(V_2/V) + i'_{e2} \exp(V_2/V')}{i_{e1} \exp(V_1/V) + i'_{e1} \exp(V_1/V')}}{1} \right] \end{aligned}$$

$$\text{Hence } I_{e1} = \frac{-2I_+}{\frac{1 + i_{e2} \exp(V_2/V) + i'_{e2} \exp(V_2/V')}{i_{e1} \exp(V_1/V) + i'_{e1} \exp(V_1/V')}}}$$

where $I_{+1} = I_{+2} = I_+$

Hence, the circuit current is given by

$$I_d = I_+ \left[\frac{i \exp(V_2/V) + i' \exp(V_2/V')}{i \exp(V_1/V) + i' \exp(V_1/V')} \right] / \left[\frac{i \exp(V_2/V) + i' \exp(V_2/V') + 1}{i \exp(V_1/V) + i' \exp(V_1/V')} \right]$$

9.13

where $i = i_{e1} = i_{e2}$ and $i' = i'_{e1} = i'_{e2}$

Unfortunately equation 9.13 is insoluble algebraically. In order to solve the equation for I_d it is necessary to obtain the probe to plasma voltages in terms of the applied voltage V_d . Referring to fig. 5.1, it can be seen that

$$V_1 + V_d = V_2 + V_s$$

when V_2 is the more negative probe.

Multiplying equation 9.13 by the expression

$$\frac{i \exp(-V_1/V) + i' \exp(-V_1/V')}{i \exp(-V_1/V) + i' \exp(-V_1/V')}$$

gives

$$\frac{I_d}{I_+} = \frac{(e^{(V_d - V_s)/V} - 1) + (i'/i)^2 (e^{(V_d - V_s)/V'} - 1)}{(e^{(V_d - V_s)/V} + 1) + (i'/i)^2 (e^{(V_d - V_s)/V'} + 1) + 2i'/i (e^{0.85V_d y} + e^{-0.85V_d y})}$$

9.14

where $y = \left(\frac{1}{V'} - \frac{1}{V} \right)$ and Schwar's approximation relating the plasma to probe potential V_p to the applied voltage V_d ie.

$$\frac{V_p}{V_d} \simeq 0.85$$

has been employed.

Similarly, multiplying equation 9.13 by the expression

$$\frac{i \exp(-V_2/V) + i' \exp(-V_2/V')}{i \exp(-V_2/V) + i' \exp(-V_2/V')}$$

gives as second expression for I_d/I_+ :

$$\frac{I_d}{I_+} = \frac{(1 - e^{(V_s - V_d)/V}) + (i'/i)^2 (1 - e^{(V_s - V_d)/V'})}{(1 + e^{(V_s - V_d)/V}) + (i'/i)^2 (1 + e^{(V_s - V_d)/V'}) + 2i'/i (e^{0.85V_d y} + e^{-0.85V_d y})}$$

9.15

Summing both equations (9.14 and 9.15) and substituting suitable values of i'/i , T_e , T'_e and V_s gives a curve of the form of fig. 9.9. Here the following values have been taken.

$$T_e = 5 \times 10^4 K \quad T'_e/T_e = 10 \quad i'/i = 0.1 \quad V_s = 2.0$$

Figure 9.9 should be compared with fig. 9.10, which shows one of the

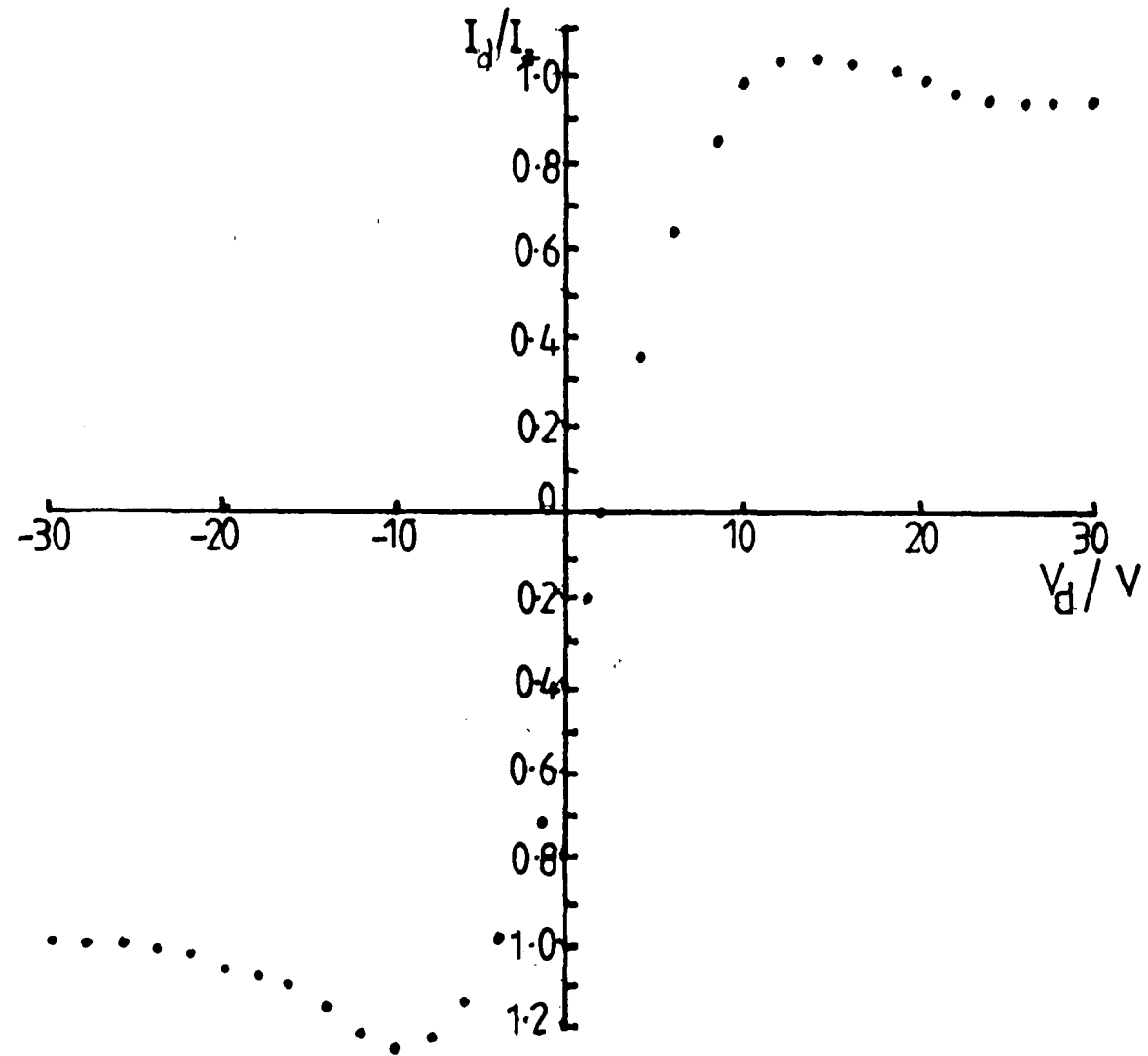


Figure 9.9 Result of plotting the sum of equations 9.14 and 9.15

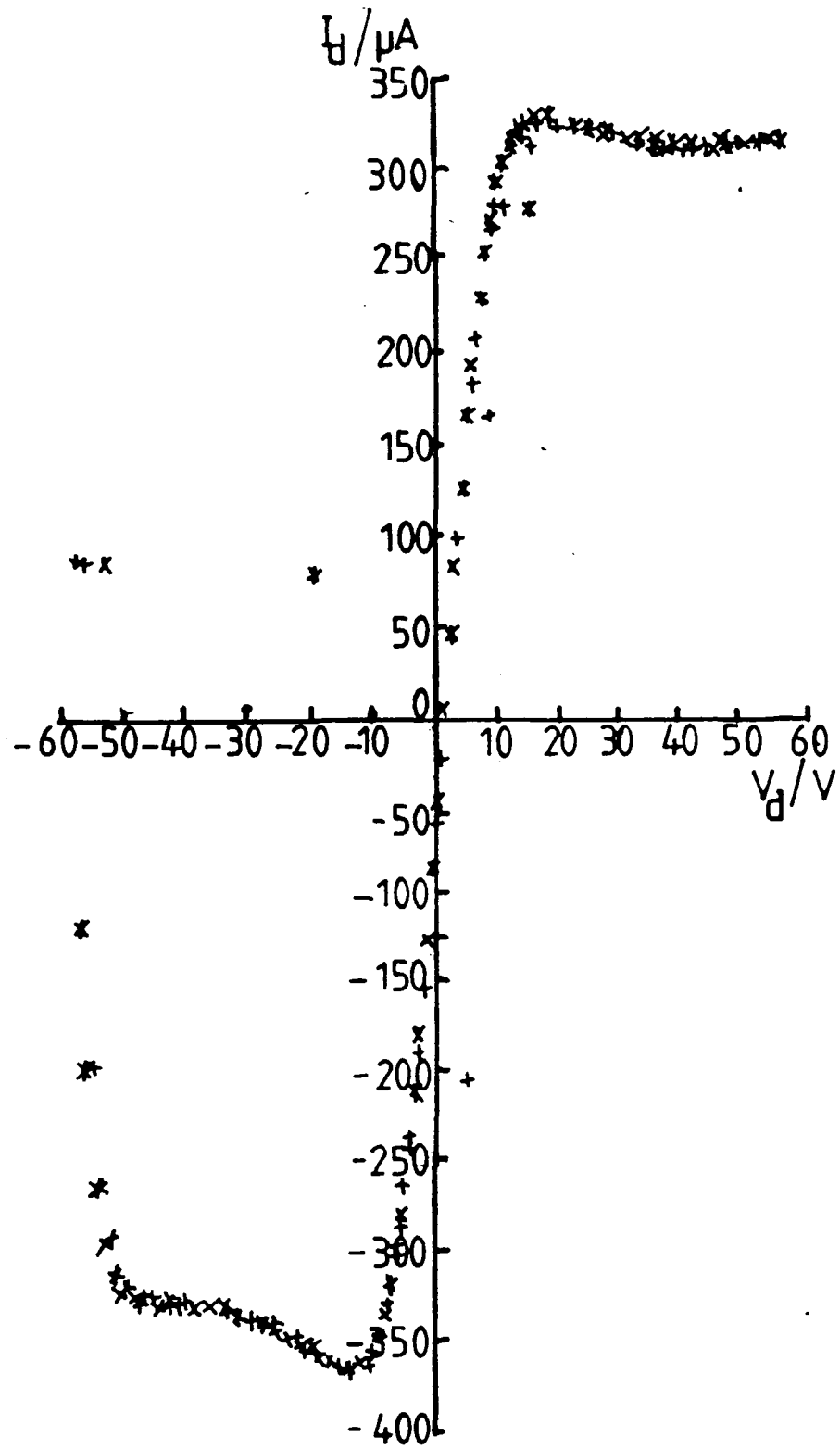


Figure 9.10 Example of a type III characteristic.
 Pressure 1.00mbar, magnetron current 100mA

type III characteristics. It should be noted that fig. 9.9 plots the ratio (I_d/I_+) along the ordinate axis whereas fig. 9.10 plots I_d in μA .

It will be seen that the forms of figs. 9.9 and 9.10 are surprisingly similar, given the arbitrary values of T_e , T'_e , i'/i and V_s chosen for the former. It should also be noted that the results of equation 9.14 and 9.15 also account for the slight asymmetry of the characteristic about the V_d axis.

9.9.2 Behaviour of the Equations

To ascertain the behaviour of the equations 9.14 and 9.15 when the three parameters T_e , T'_e/T_e and i'/i are varied, values of these parameters were substituted into the computer program PRFIT1 and PRFIT2 given in appendix III.

The effect of varying the "temperature", T of the low energy group, is shown in figs. 9.11(a), (b) and (c). Values of $2 \times 10^4\text{K}$, $5 \times 10^4\text{K}$ and $8 \times 10^4\text{K}$ were used, these corresponding to measured electron temperatures, whilst the other parameters are held constant. Of interest is fig. 9.11(a) where $T_e = 2 \times 10^4\text{K}$. At this value, the arm of the characteristic corresponding to a positive V_d does not exhibit a turning point. Characteristics of this form were observed for pressures of 3.00 and 2.00 mbar for all magnetron currents for which results were available (see Table 7.3). The results of figs. 9.11(a)

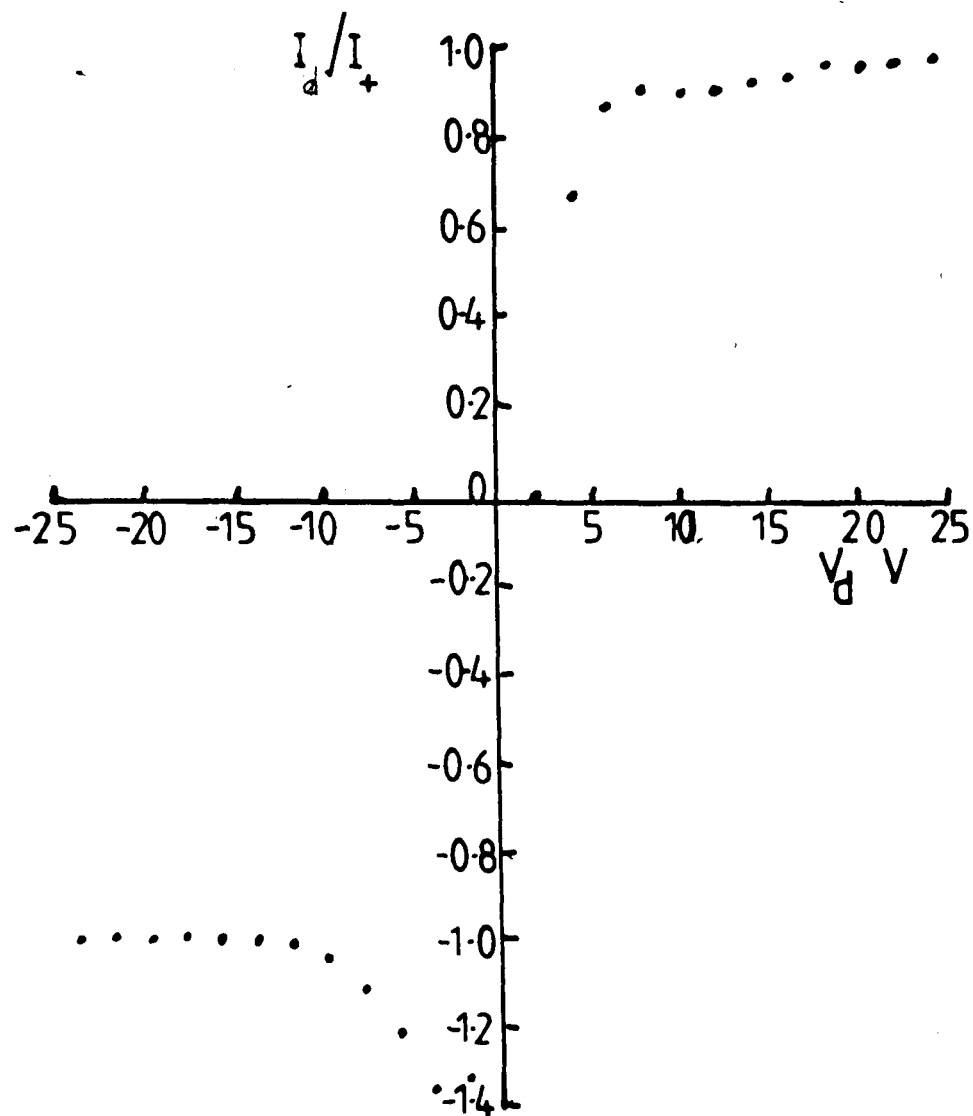


Figure 9.11a Variation of type III characteristic with T_e $T_e=2 \times 10^4 K$, $T_e'/T_e=10$, $i'/i=0.1$, $V_S=2.0V$

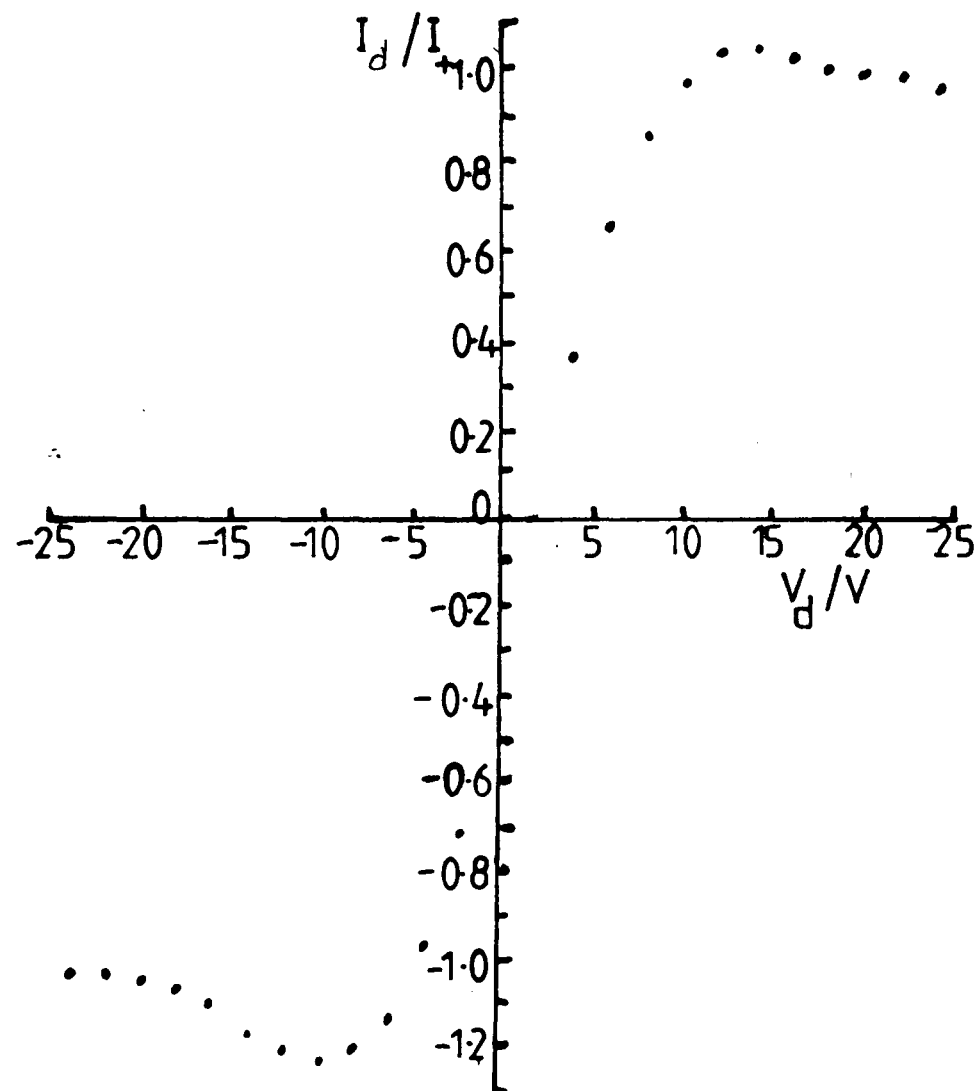


Figure 9.11b Variation of type III characteristic with T_e $T_e=5 \times 10^4 K$, $T_e'/T_e=10$, $i'/i=0.1$, $V_S=2.0V$

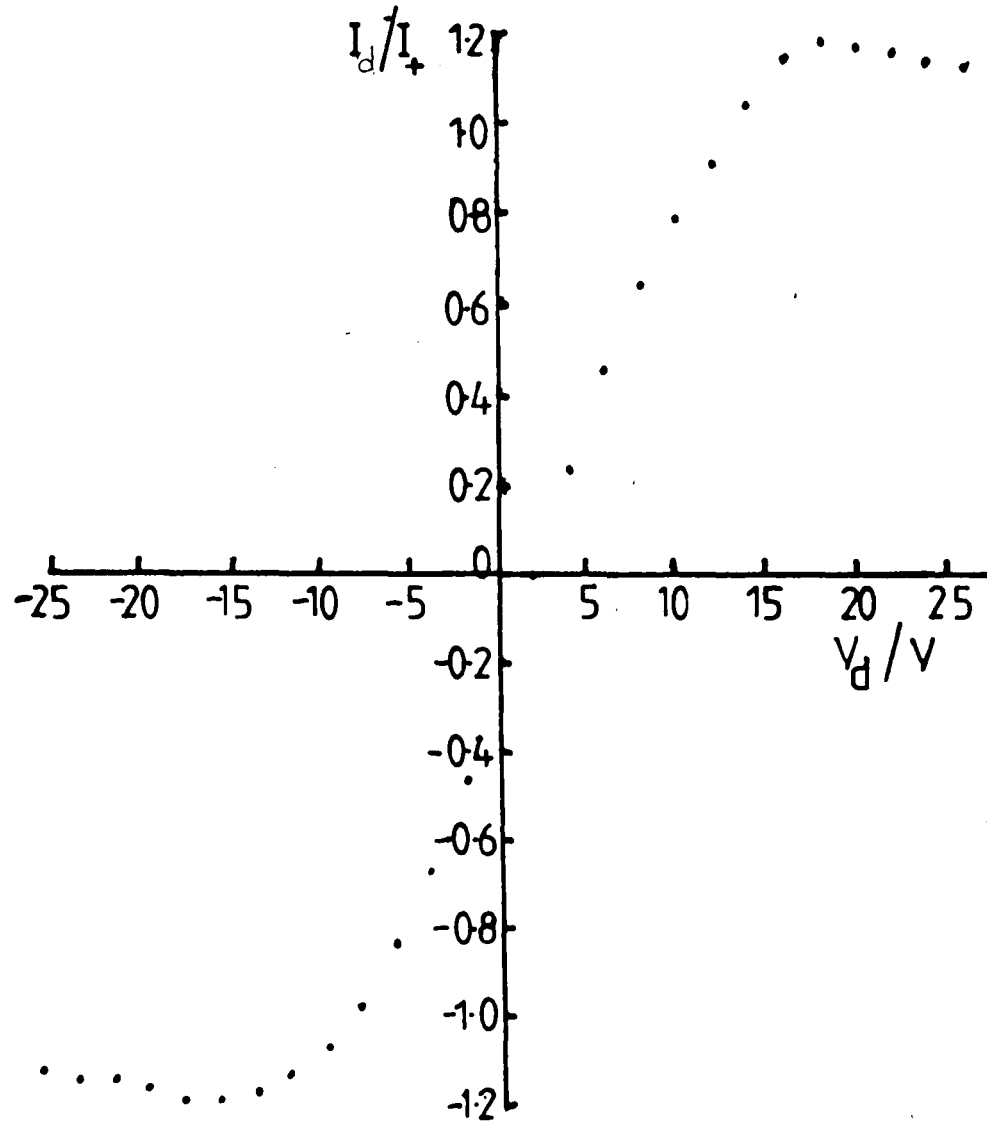


Figure 9.11c Variation of type III characteristic with T_e $T_e=8 \times 10^4 K$, $T_e'/T_e=10$, $i'/i=0.1$, $V_S=2.0V$

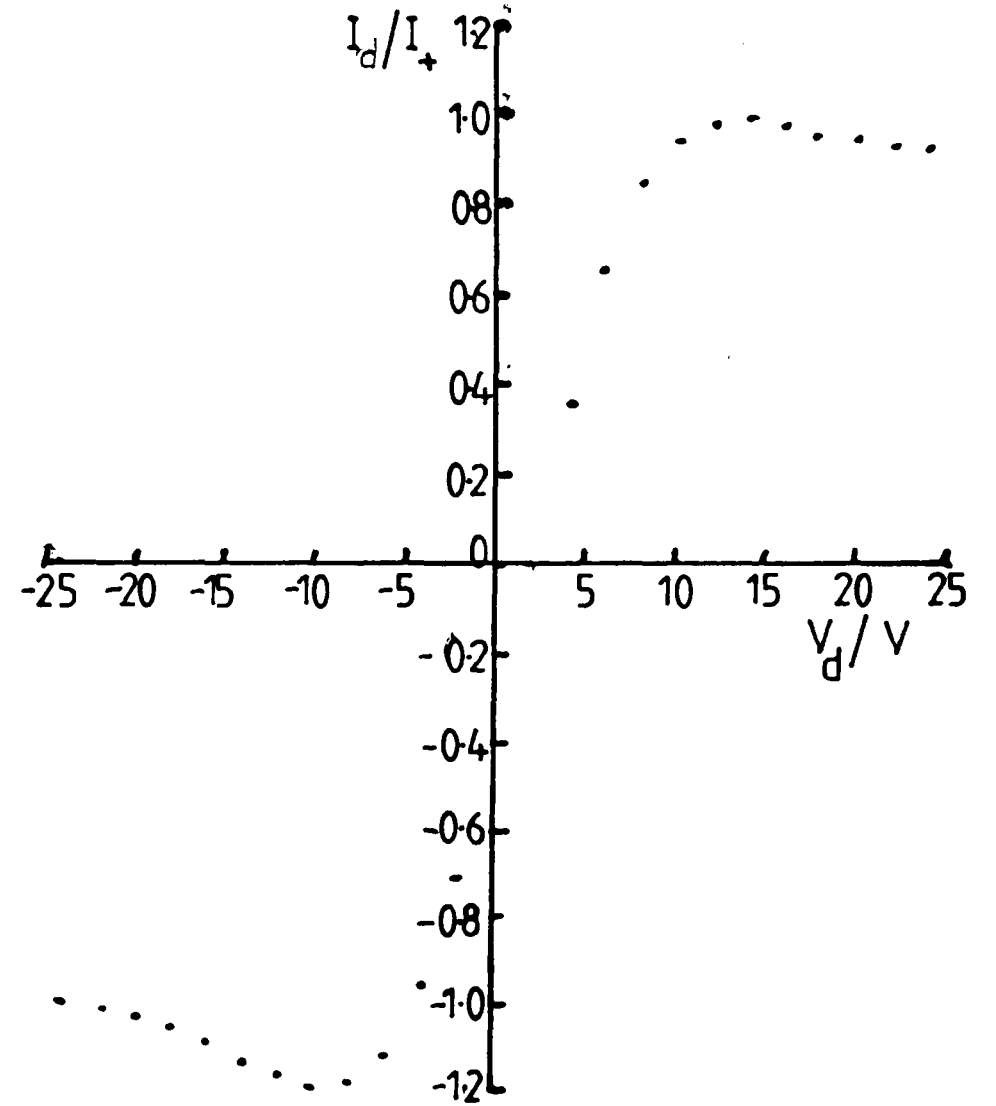


Figure 9.12a Variation of type III characteristic with T_e'/T_e $T_e=5 \times 10^4 K$, $T_e'/T_e=50$, $i'/i=0.1$, $V_S=2.0V$

and (b) imply that for $T_e < 5 \times 10^4 \text{K}$ this is a consequence of a double Maxwellian electron distribution. This is borne out by the temperature measurements for these pressures which are all below $5 \times 10^4 \text{K}$.

Figures 9.12(a), (b) and (c) show the effect of changing the ratio T'_e/T_e . This ratio does not appear to have any effect upon the shape of the curve but for smaller values of T'_e/T_e , the circuit current exceeds the positive ion current by greater amounts. That is to say that the ratio I_d/I_+ exceeds unity.

Finally, figures 9.13(a) to (d) show the effect of the ratio of random electron currents i'/i . For values of i'/i less than 0.5 the form of the curve is the type III characteristic. However, for a value i'/i between 0.1 and 0.5 the characteristic changes to that shown in fig. 9.13(c). This is similar to the type II characteristic, with a linear gradient in the 'saturated' portion. Clearly this similarity of form between fig. 9.13(c) and the type II characteristic could have serious consequences for the interpretation of probe characteristics. If a characteristic of this form, which is due to a double electron distribution, is interpreted in the manner of a type II characteristic (Chapter 5), the ion current will be seriously underestimated. For example, in fig. 9.13(c), at the point where the "saturated" arm deviates from the main body of the characteristic, $I_d/I_+ \approx 0.5$. Thus the value of I_+ would have been underestimated by a factor of two. Hence the ion density, as calculated from equation 5.9 would also be underestimated.

The suppression of the ion current increases with increasing value of i'/i . Unfortunately the random electron current is a function of both

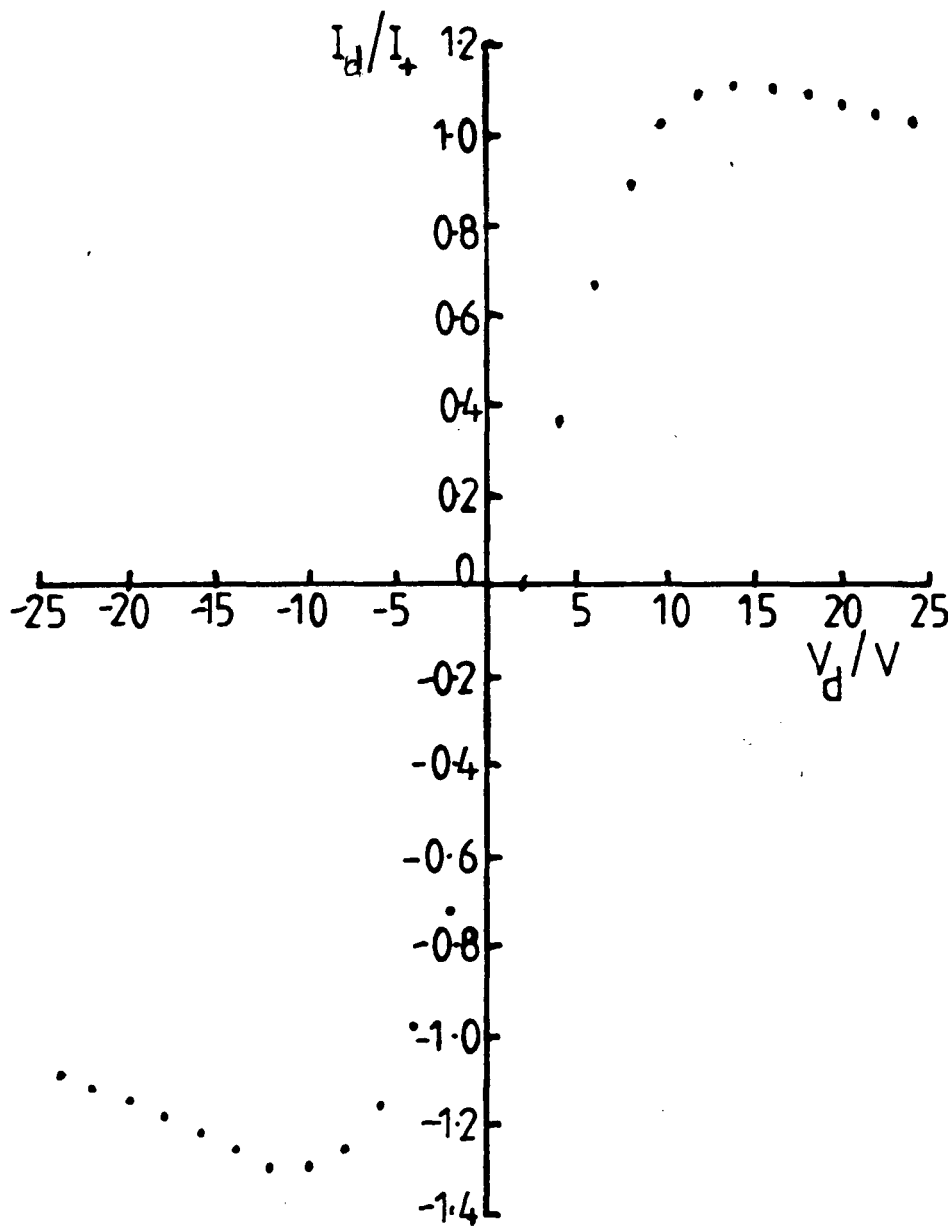


Figure 9.12b Variation of type III characteristic with T_e'/T_e
 $T_e=5 \times 10^4 K$, $T_e'/T_e=5$, $i'/i=0.1$, $V_s=2.0V$

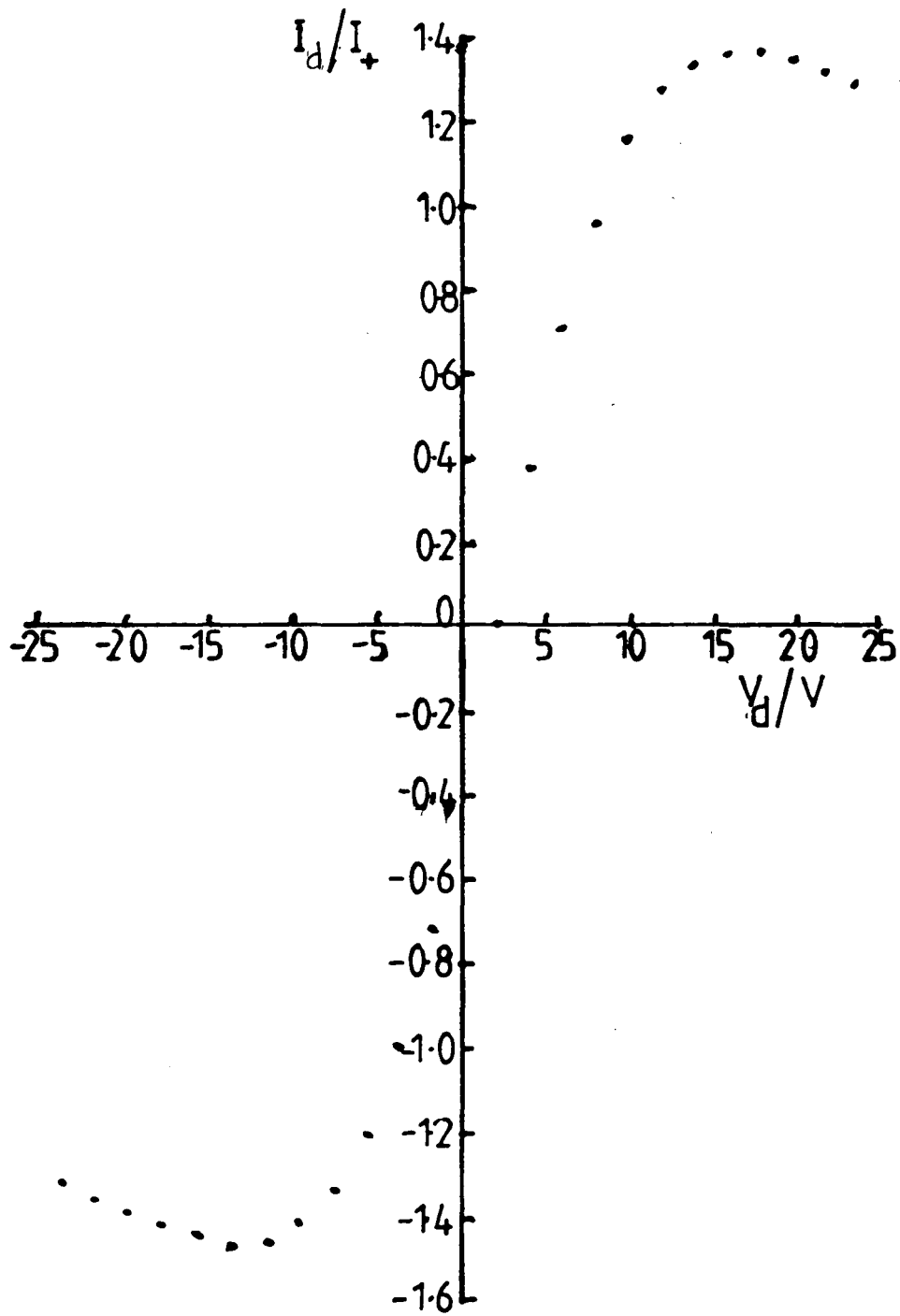
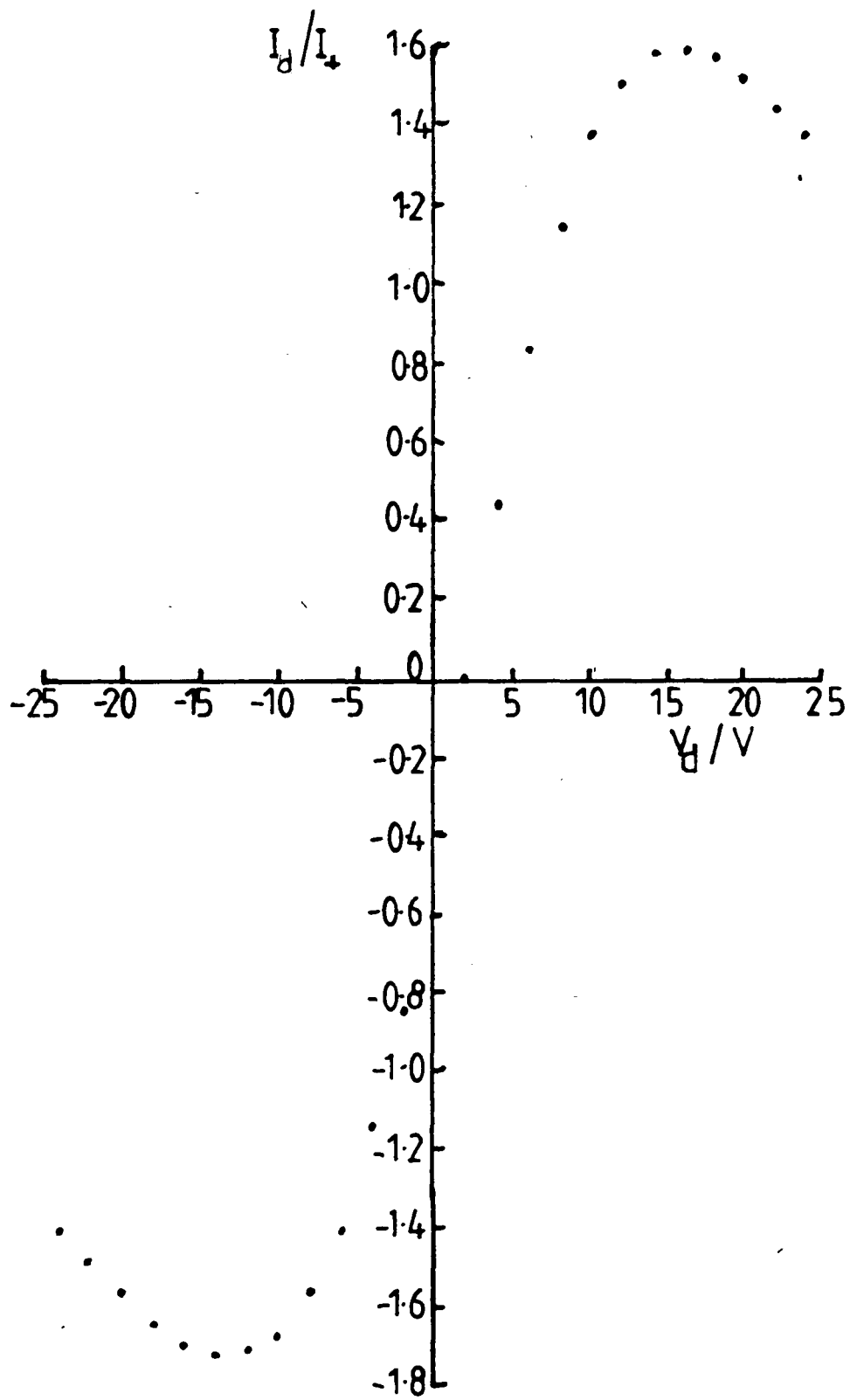


Figure 9.12c Variation of type III characteristic with T_e'/T_e
 $T_e=5 \times 10^4 K$, $T_e'/T_e=2$, $i'/i=0.1$, $V_s=2.0V$



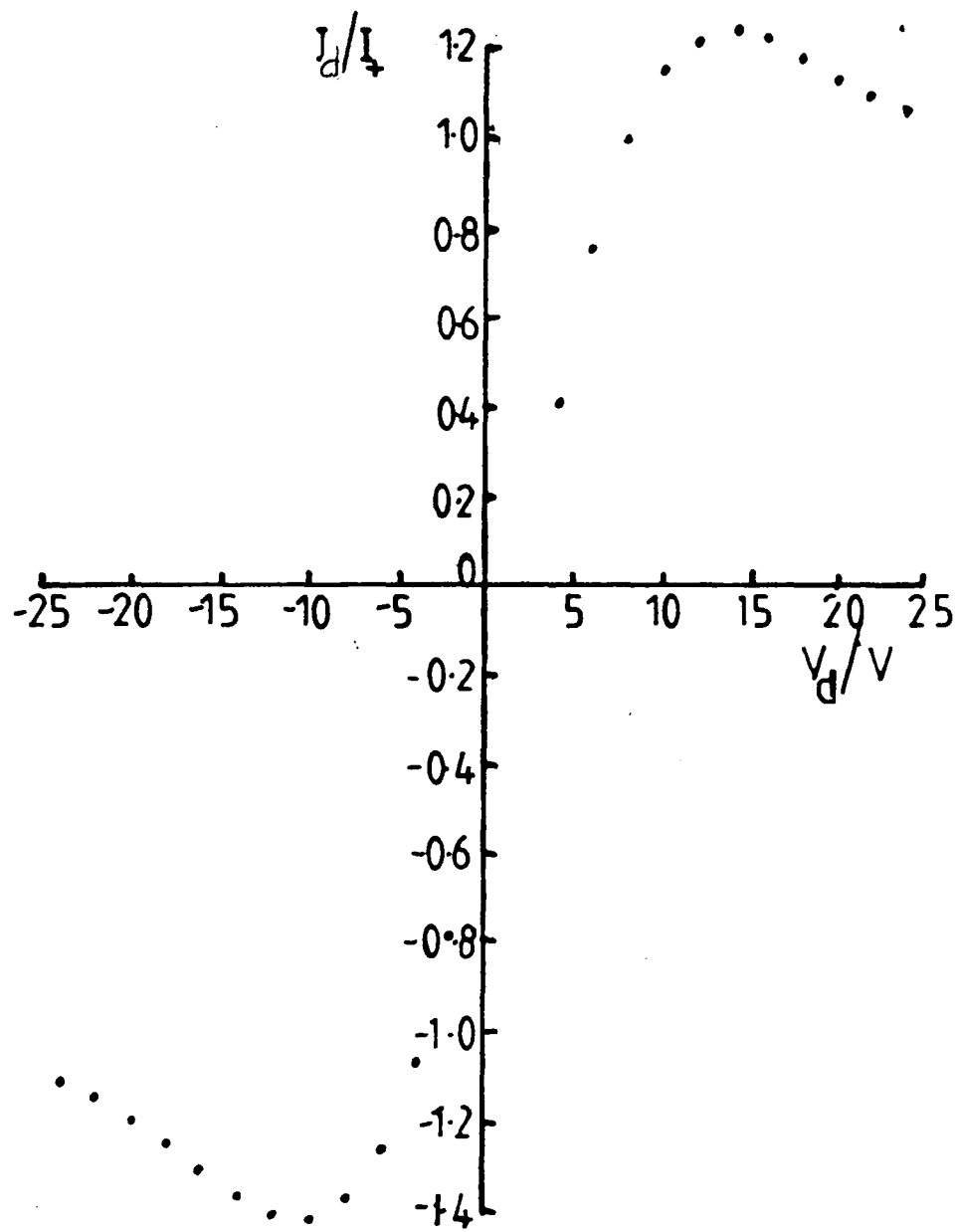


Figure 9.13b Variation of type III characteristic with i'/i
 $T_e=5 \times 10^4 K$, $T'/T=10$, $i'/i=0.05$, $V_s=2.0V$

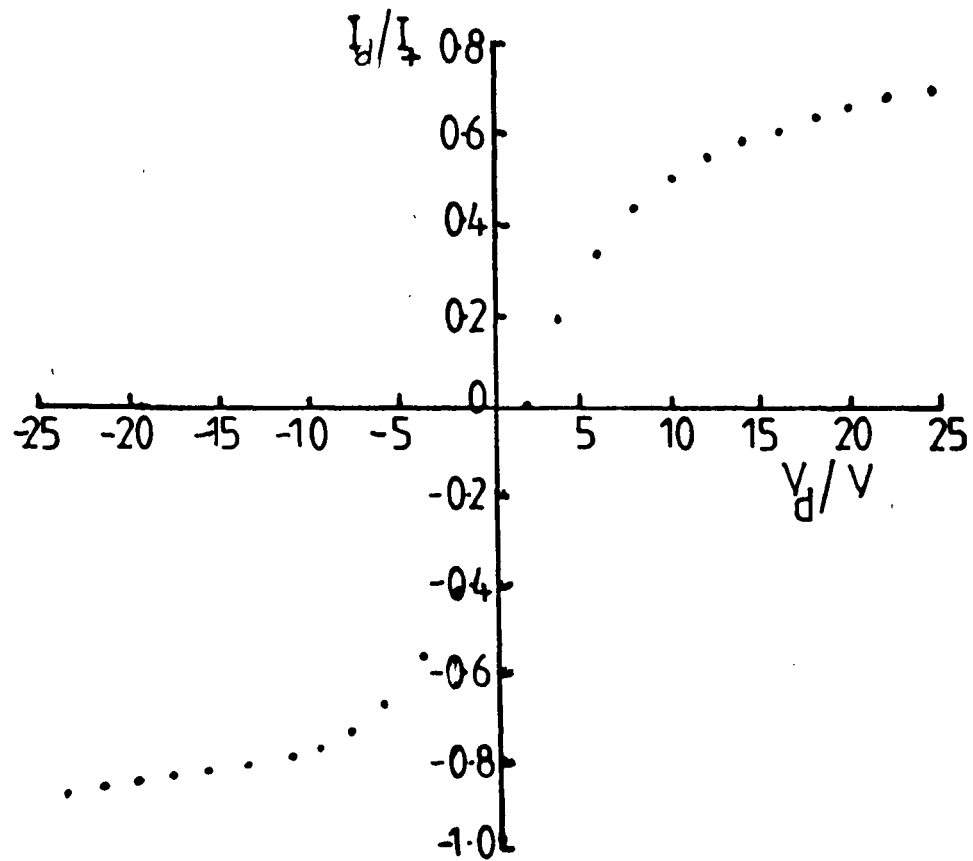


Figure 9.13c Variation of type III characteristic with i'/i $T_e=5 \times 10^4 K$, $T'/T=10$, $i'/i=0.5$, $V_S=2.0V$

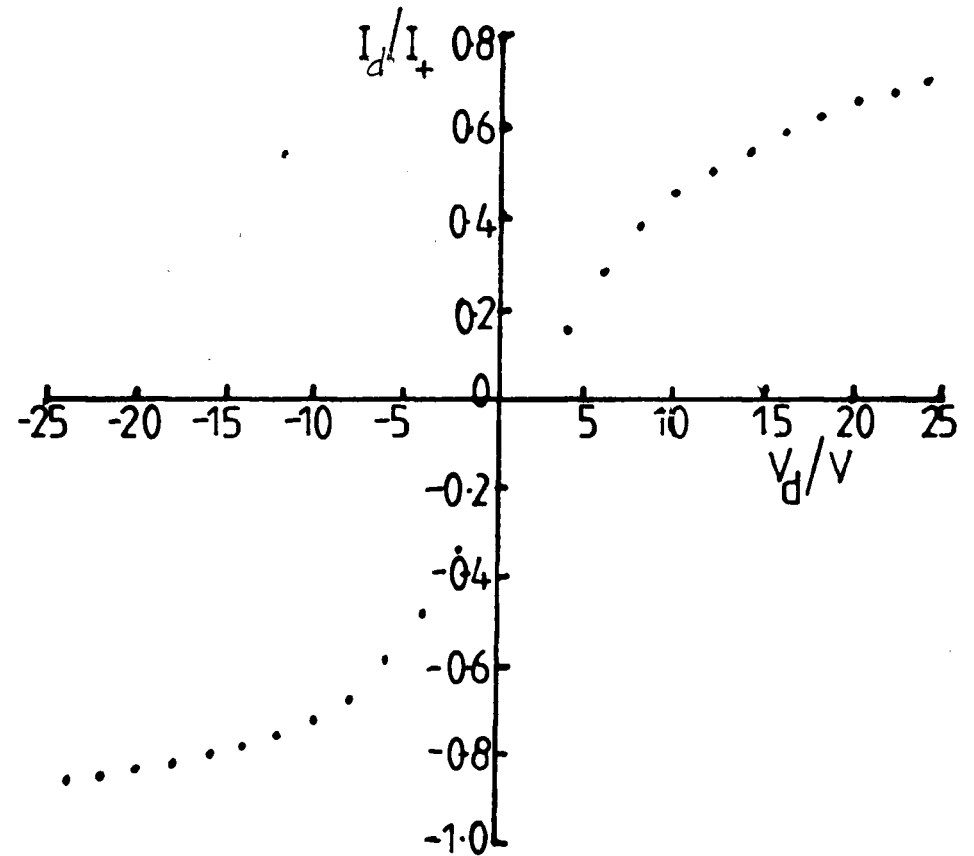


Figure 9.13d Variation of type III characteristic with i'/i $T_e=5 \times 10^4 K$, $T'/T=10$, $i'/i=1.0$, $V_S=2.0V$

the number density of the distribution and its characteristic temperature, being given by

$$i = An_e e \bar{c}$$

where A is the probe or sheath area

\bar{c} is the mean speed of the electrons

For a Maxwellian distribution

$$\bar{c} = \left(\frac{8kT_e}{\pi m_e} \right)^{\frac{1}{2}}$$

Thus, the parameters T'_e/T_e and i'/i are not independent and as the equations 9.14 and 9.15 are not solvable algebraically, this leaves curve fitting as the only method of solving these equations for T'/T and i'/i .

9.9.3 Electron Temperature and Ion Density Results

Having shown in sections 9.9.1 and 9.9.2 that the presence of two Maxwellian distributions of electrons has serious consequences for the interpretation of double-floating probe measurements, it would therefore be desirable to obtain some indication as to which distribution the measured values of T_e and n_+ apply.

9.9.3 (i) Ion density measurements

It has been shown in section 9.9.2 that for certain values of the ratio T'_e/T_e , the circuit current can exceed the positive ion current. This effect may account for some of the results in table 9.1 where the measured ion density exceeds the measured electron density for the highest pressures. Indeed, the plotted probe characteristics at these

pressures are of the form of fig. 9.11(a) and the ion current was taken from the maximum turning point in the original calculation. From fig. 9.9, however, it can be seen that the ion current should be measured from the 'arms' following the turning point.

In section 9.2 it was suggested that the difference between the measured ion and electron densities may be due to diffusion of the ions into the wall of the discharge tube. In the preceding section, the effect of a double electron distribution with $i'/i = 0.5$ was shown to produce an effective, but unreal, diminution of ion current. It is not possible from the measurements presented here, to distinguish between the two effects and triple probe systems, which determine directly the electron distribution, are necessary to establish which case is applicable.

9.9.3 (ii) Electron temperature measurements

The problem of interpreting probe measurements in the presence of two electron groups has been approached before. Busch & Vickers (1973) argue that because both probes are negative with respect to the plasma, only electrons from the higher energy group will reach the probes. Whether an electron reaches a probe, or not, depends upon its energy. Furthermore, the electron current depends on both the energy and the number of electrons with that energy (or greater). It does not necessarily follow, therefore, that only the high energy group will reach the probe. The 'type' of electron contributing to the current depends upon the relative temperatures and number densities of the two distributions and the magnitude of the negative probe to plasma potential.

In order to test the argument of Busch & Vickers, values of $T'/T = 0.5$ with $T = 5 \times 10^4 \text{K}$ and $i'/i = 10$ were substituted into equations 9.14 and 9.15 and the results summed. In this case the higher energy group has parameters T and i , whilst the low energy group has parameters T' and i' . It was found that under these conditions the circuit current tended to zero with increasing applied voltage. Similarly, substituting values of $T'/T = 10$ with $T = 5 \times 10^3 \text{K}$ and $i'/i = 0.1$ or 0.5 , the characteristics resembled those of the type I.

It would appear that, at least for type III characteristics, the value of electron temperature, T_e , measured from the characteristic by the logarithmic plot method is that of the low energy group. This is not too surprising since, for small negative applied voltages, the electron current to the probe will be dominated by the more numerous low energy group. Thus, provided that data for the T_e calculation is taken from the centre portion of the characteristic, the T_e value should be that of (or closer to) the low energy group.

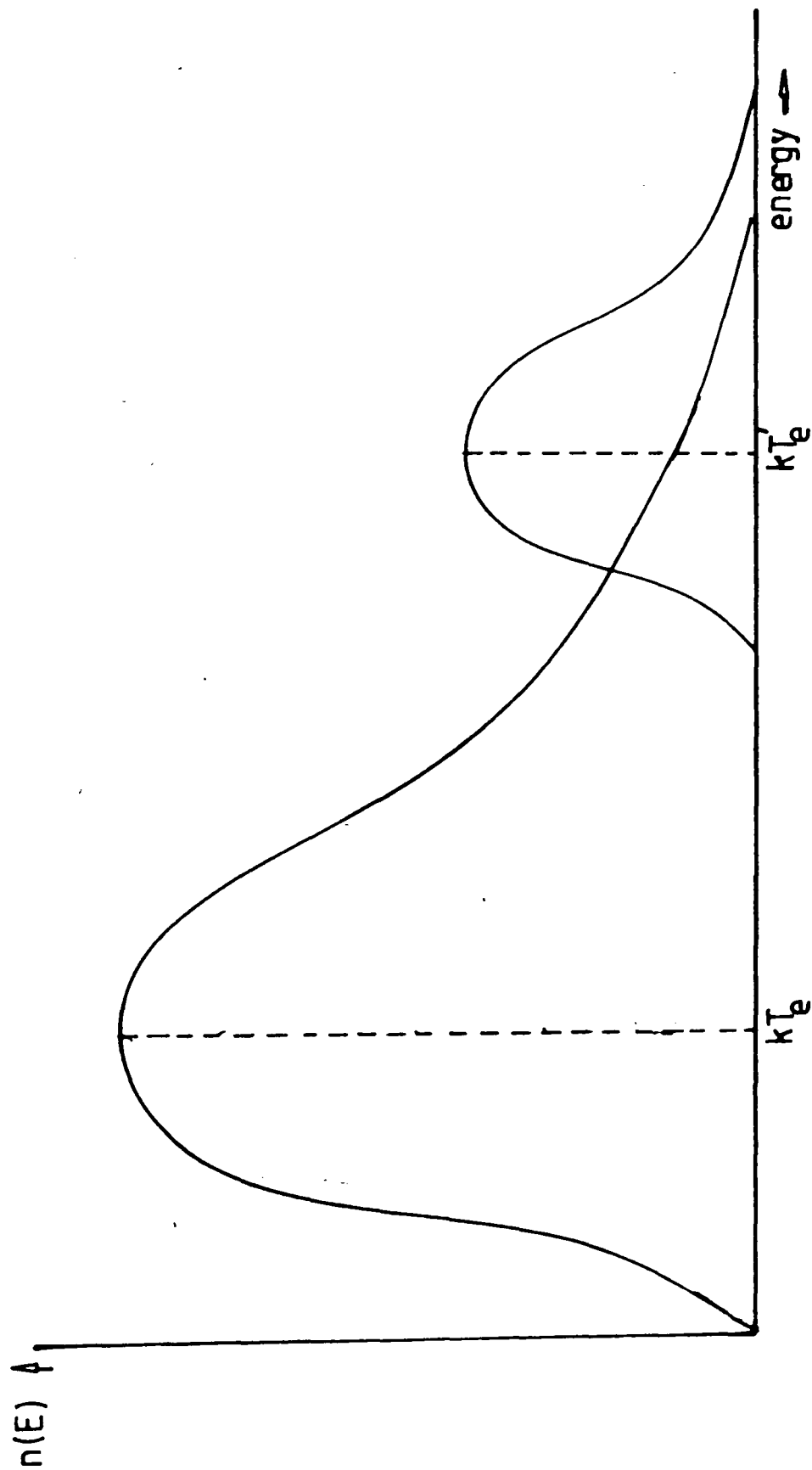


Figure 9.14 Example of a double distribution function.

9.10 Conclusions

9.10.1 Spectroscopic Features

The spectroscopic features of the electrodeless microwave excited argon discharge have been investigated between the pressures of 6.00 and 0.02 mbar for different magnetron currents.

The plasma has been demonstrated to conform to the saturation phase for pressures below 2.0 mbar in similarity to the positive column and hollow cathode discharges. The saturation phase occurs at lower electron densities than are predicted and this is attributed to the optical thickness of the resonance lines of argon. For the electron densities encountered ($10^{17} - 10^{18} \text{ m}^{-3}$) a set of values for the population coefficients of levels from 6s to 9s have been determined. These have been shown to be in approximate agreement with published values.

The plasma has been shown to be predominantly ionising and the predicted relationship between the population density of a given atomic level n_m and the ionisation energy of that level E_m^{ion} has been confirmed ie.

$$n_m \propto (E_m^{\text{ion}})^3$$

Thus the saturation phase and the relationship between n_m and E_m^{ion} above seem to be a general feature of low pressure argon plasmas.

The suppression of the population densities of all the atomic levels, as measured by spectroscopic techniques, above pressures of 1.00 mbar is attributed to collisional de-excitation. At these pressures, the

highest atomic levels approach equilibrium and are overpopulated with respect to calculated values from the saturation phase. This overpopulation has been attributed to population by ionic recombination of the upper levels whilst the lower levels are populated by the ladder-like excitation of the saturation phase.

9.10.2 Measurement of Electron Density

The electron density has been measured directly from the microwave impedance of the plasma. This method has provided an independent method to compare with that of double floating probe measurements. The features of the variation of impedance with pressure has been explained in terms of an increase in collisions between electrons and atoms which acts as a "viscous" drag force on the electron.

The electron density has been shown to remain almost constant with changing pressure and power. This is due to the discharge being free to expand as the number of electrons liberated increases, thus keeping the electron density constant.

9.10.3 Power Dependence of Plasma Parameters

The fundamental plasma parameters electron temperature, electron density and the population densities of the atomic and ionic levels have been shown to be strongly dependant upon input power and pressure. It has been shown that an increase in incident microwave power does not necessarily correspond to a commensurate increase in power input to the plasma. Thus for comparison of parameters at different pressures, for example, the input power must be monitored.

The variation of plasma parameters with input power has been shown to change with pressure, implying that pressure and input power are

dependant variables

9.10.4 Probe Measurements

Double-floating probes were used to measure the electron temperature and ion density of the plasma. The presence of the probes was shown not to cause detectable perturbation to the spectroscopic measurements.

9.10.4 (i) Ion Density

The ion density measurements were shown to vary considerably from the electron density measurements of section 10.2. The excess of ion density was explained in terms of the effect of a double Maxwellian distribution of electrons. The low ion density values could be explained in terms of diffusion of ions to the discharge tube walls. Although estimates of ion loss due to the free-fall diffusion model generally over-estimate the diminution of ion density, the exact value is dependant upon the unknown gas temperature. Supporting evidence for the diffusion of ions and atoms to the discharge tube walls is provided by the observation of "gas drive-out" at pressures of 0.1 mbar and below. It was observed that the pressure registered on the pirani gauge steadily decreased after the discharge had been operating for a period of time.

9.10.4 (ii) Effect of electron distribution function

A set of double-floating probe equations was derived for the condition of a double Maxwellian electron distribution function. The effect of this form of distribution upon the observed probe characteristic was demonstrated from the equations.

The equations accounted for a type of probe characteristic which was observed but for which no previous explanation was available. For other values of the two parameters T'/T and i'/i appearing in the double distribution equations, it was shown that the probe characteristics resemble those explained in terms of an increasing sheath potential. It was not possible to distinguish between the two cases and the provision of triple probe systems to provide the distribution function was shown to be desirable.

Contrary to the assumptions of previous workers, it has been shown that, for certain values of T'/T and i'/i , the probe characteristics provide the electron temperature of the low energy electron group.

The form of the probe characteristics indicated the existence of two electron distributions at pressures of 2.00 mbar and above, thus increasing the probability of collisional de-excitation of the atomic levels. It is probable that the collisional de-excitation^t of atomic levels contributes to the creation of the higher energy group through the transfer of the energy of de-excitation. The existence of the two groups of electrons would then increase the probability of ion recombination, thus contributing to the 'excess' population densities of the higher atomic levels observed at these pressures (section 10.1).

REFERENCES

- Avni R & Winefordner J D 1975 Spectrochim Acta 30B 281-303
- Brassem P & Maessen F J M J 1974 Spectrochim Acta 29B 203-210
- Brassem P & Maessen F J M J 1975 Spectrochim Acta 30B 547-556
- Brassem P, Maessen F J M J & de Galan L 1976 Spectrochim Acta 31B
537-545
- Brassem P, Maessen F J M J & de Galan L 1978 Spectrochim Acta 33B
753-764
- Burke P E private communication
- Burrows K M 1962 Aust. J Phys 15 162-168
- Busch K W & Vickers T J 1973 Spectrochim Acta 28B 85-104
- Dalgarno A 1958 Phil. Trans Roy Soc 250 426-439
- Drawin H W & Emard F 1977 Physica 85C 333-356
- Fujimoto T, Ogata Y, Sugiyama I, et al 1972 Jap J. App Phys 11 718-725
- Fujimoto T 1979 J. Phys Soc Japan 47 265-272 and 273-281
- Griem H R 1964 "Plasma Spectroscopy" McGraw-Hill 259
- Hall L S & Fries R P 1965 Proc. 7th International Conference on
Phenomena in Ionized Cases (Beograd) 5.1.1.(1).
- Hammond C B 1978 PhD Thesis University of London
- Johnson E O & Malter L 1949 Phys Rev 76 1411-1412
- Johnson E O & Malter L 1950 Phys Rev 80 58-68
- Kagan & Perel 1964 Soviet Phys-Usp 6 767-772
- Katsonis K 1976 Doctoral Thesis Univ Paris Sud
- Keyston J E 1933 Phil Mag 16 625-639
- Kojevic N & Roberts J R 1976 Phys Chem Ref Data 5 209-257
- Lincke R 1968 "Plasma Diagnostics" North Holland Publishing Co.
347-419
- Llewellyn Jones F 1936 Proc Phys Soc 48 513-526
- Mitchner M & Kruger C H 1973 "Partially Ionised Gases" John Wiley
& Sons

- Van der Mullen J J A M, van der Sijde B & Schram D C 1980
Phys Lett 79A 51-54
- Outred M & Hammond C B 1976 Phys Scripta 14 81-84
- Outred M 1980 Spectochim Acta 35B 447-450
- Outred M & Hammond C B 1980 J Phys D 13 1069-78
- Polman J 1966 Thesis Univ Groningen, Netherlands
- Raaijmakers I J M M, Boumans P W J M, van der Sijde B & Schram D C
1983 Spectrochim Acta 38B 697-706
- Schlüter H 1963 Z Naturforsch 18a 439-446
- Schottkey W 1924 Phys Z 25 635-640
- Schwar M J R 1966 MSc Thesis University of London
- Swift J D & Schwar M J R 1970 "Electrical Probes for Plasma
Diagnostics" Iliffe Books
- Tachibana K & Fukuda K 1973 Jap. J. App Phys 12 895-902
- Thomas D 1965 PhD Thesis University of London
- Tonks L & Langmuir I 1929 Phys Rev 34 876-922
- Waldron R A 1970 "Theory of Guided Electromagnetic Waves" Van Nostrand
- Wharton 1965 "Plasma Diagnostic Techniques" Academic Press 477-515
- Wiese W L, Smith M W & Miles B M 1969 NSRDS-NBS22 National Bureau of
Standards

APPENDIX I

SDATA 3

```

C   CALCULATION OF NUMBER DENSITIES FROM ARGON I SPECTRAL
C   INTENSITIES
REAL LAMBDA
DIMENSION LAMBDA(21),CAL(21),SPECH(21),SPSENS(21),
1  FUNC(21),REL(21),ER1(21),ER2(21)
COMMON LAMBDA,CAL,SPECH,SPSENS,
1  KDATE1,KDATE2,KGAS,PRESS,KUR,NLINES
CALL FIL
READ(1,5)KD
5  FORMAT(I2)
KAN=0
OPEN (UNIT=2,NAME='DX1:ARI.DAT',TYPE='OLD')
OPEN(UNIT=3,NAME='DX1:TUNG.DAT',TYPE='OLD')
30  CALL SINP
WRITE(6,100)KDATE1,KDATE2
100 FORMAT(1H ,//' INTENSITY CALCULATION',20X,2I4///)
WRITE(6,110)KGAS,PRESS
110 FORMAT(1H , 'Pressure of ',A2,' gas was ',E10.3,'mbar')
WRITE(6,120)KUR
120 FORMAT(1H , 'Microtron current= ',I3,'mA')
DO 130 I=1,NLINES
KK=0
136 READ(3,125)WAVEI,TRQ,TRG
125 FORMAT(F7.2,5X,2F4.2)
IF(LAMBDA(I).EQ.WAVEI) KK=1
IF(KK.EQ.0) GO TO 136
SPECH(I)=SPECH(I)/((TRQ**3.0)*TRG)
130 CONTINUE
C   CALCULATION OF NUMBER DENSITIES FOR GAS
WRITE(6,210)
DO 150 I=1,NLINES
KK=0
176 READ(2,160)WAVE,ENU,ENK,KGU,KGL,
1  PROB,GF,KAC
160 FORMAT(F7.2,2F8.0,2I2,F7.5,F6.3,I3,24X)
IF(LAMBDA(I).NE.WAVE) GO TO 170
ARG(I)=SPECH(I)*SPSENS(I)
ARG1(I)=ARG(I)*CAL(I)
FUNC(I)=ALOG(ARG1(I)*LAMBDA(I)*1.0E-18/
1  (KGU*PROB*6.626E-34))
REL(I)=FUNC(I)/FUNC(1)
IF(KAC.LE.50) GO TO 250
KAC=75
250 KAC=IABS(KAC)
ERR(I)=KAC*ARG1(I)/100.0
ER1(I)=ALOG((ARG1(I)+ERR(I)*LAMBDA(I)*1.0E-18/
1  (KGU*PROB*6.626E-34))

```

```

ER2(I)=ALOG((ARG1(I)-ERR(I))*LAMBDA(I)*1.0E-18/
1 (KGU*PROB*6.626E-34))
210 FORMAT(1H , 'Lambda',3X, 'Ln no. dens',3X, 'Upper level',3X,
1 'Rel',6X, 'ErrU',11X, 'ErrL')
255 WRITE(6,215)LAMBDA(I),FUNC(I),ENU,REL(I),ER1(I),ER2(I)
215 FORMAT(1H ,F7.2,3X,E9.3,5X,F8.0,3X,F6.3,3X,E9.3,3X,E9.3)
KK=1
170 IF(KK.EQ.0) GO TO 176
150 CONTINUE
KAN=KAN+1
REWIND 2
REWIND 3
IF(KAN.LT.KD) GO TO 30
CLOSE(UNIT=3,DISPOSE='KEEP')
CLOSE(UNIT=2,DISPOSE='KEEP')
STOP
END

```

CAL

```

C CALIBRATION OF RESPONSE OF OPTICAL SYSTEM
REAL LAMBDA
DIMENSION LAMBDA(21),CAL(21),CALH(21),CSENS(21)
COMMON KON
OPEN(UNIT=1,NAME='DX1:TUNG.DAT',TYPE='OLD')
17 TYPE 10
10 FORMAT(1H , 'Enter number of lines,(I2) ', $)
ACCEPT 15,NLINES
15 FORMAT(I2)
TYPE 20,NLINES
20 FORMAT(1H , 'Number of lines= ',I2)
CALL REPLY
IF(KON.EQ. 'Y')GO TO 25
GO TO 17
25 DO 30 I=1,NLINES
50 TYPE 35
35 FORMAT(1H, 'Enter wavelength,(F7.2)', $)
ACCEPT 40,LAMBDA(I)
40 FORMAT(F7.2)
TYPE 45,LAMBDA(I)
45 FORMAT(1H , 'Wavelength= ',F7.2)
CALL REPLY
IF(KON.EQ. 'Y')GO TO 55
GO TO 50
55 TYPE 60
60 FORMAT(1H , 'Enter calibration intensity,(F6.2)', $)
ACCEPT 65,CALH(I)
65 FORMAT(F6.2)
TYPE 70,CALH(I)
70 FORMAT(1H , 'Calibration intensity= ',F6.2)
CALL REPLY
IF(KON.EQ. 'Y')GO TO 75
GO TO 55

```

```

75 TYPE 80
80 FORMAT(1H , 'Enter calibration sensitivity,(E10.3)', $)
ACCEPT 85, CSENS(I)
85 FORMAT(E10.3)
TYPE 90, CSENS(I)
90 FORMAT(1H , 'Calibration sensitivity= ', E10.3)
CALL REPLY
IF(KON.EQ. 'Y') GO TO 30
GO TO 75
30 CONTINUE
DO 105 I=1, NLINES
KK=0
100 READ(1, 95) WAVE, EMM, TRQ, TRG
95 FORMAT(F7.2, F5.3, 2F4.2, 52X)
IF(LAMBDA(I).EQ.WAVE) KK=1
IF(KK.EQ.0) GO TO 100
TEMP=1.0/(0.4361E-03-(0.62614E-08*LAMBDA(I)))
B1=1.191E-16/((LAMBDA(I)*1.0E-10)**5.0)
B2=(EXP(0.01439E10/(LAMBDA(I)*TEMP)))-1
BB=B1/B2
COR=BB*EMM*(TRQ**3.0)*TRG
CAL(I)=COR/(CALH(I)*CSENS(I))
105 CONTINUE
WRITE(6, 115)
115 FORMAT(1H , 'Lambda', 5X, 'Calibration')
DO 110 I=1, NLINES
WRITE(6, 120) LAMBDA(I), CAL(I)
120 FORMAT(1H , F7.2, 5X, E9.3)
110 CONTINUE
CLOSE(UNIT=1, DISPOSE='KEEP')
STOP
END

SUBROUTINE FIL
LOGICAL*1 CN(14)
DATA CN/'D', 'X', '1', ':', 'M', 'Y', 'P', 'R', 'O', 'G', '.',
1 'D', 'A', 'T' /
TYPE 10
10 FORMAT(1H , 'Enter name of data file to be used,(6A1) ', )
ACCEPT 20, (CN(I), I=5, 10)
20 FORMAT(6A1)
OPEN(UNIT=1, NAME=CN, READONLY, TYPE='OLD')
RETURN
END

SUBROUTINE SINP
REAL LAMBDA
COMMON LAMBDA(21), CAL(21), SPECH(21), SPSENS(21),
1 KDATE1, KDATE2, KGAS, PRESS, KUR
READ(1, 30) KDATE1, KDATE2, KGAS, PRESS, KUR
30 FORMAT(2I4, A2, E10.3, I3)
READ(1, 40) NLINES
40 FORMAT(I2)
DO 60 I=1, NLINES
READ(1, 50) LAMBDA(I), CAL(I), SPECH(I), SPSENS(I)
50 FORMAT(F7.2, E10.3, F6.2, E10.3)
60 CONTINUE
RETURN
END

```

```
    SUBROUTINE REPLY
    COMMON KON
    TYPE 10
10  FORMAT(1H , 'Correct'?)
60  TYPE 20
20  FORMAT(1H , 'Type Y or N and press RETURN ' , )
    ACCEPT 30, KON
30  FORMAT(A1)
    IF(KON.EQ.'Y'.OR.KON.EQ.'N') GO TO 40
    TYPE 50, KON
50  FORMAT(1H , 'Reply', A1, ' not understood- RETYPE!')
40  GO TO 60
    RETURN
    END
```

APPENDIX II

M DATA 3

```

REAL LAMBDA,GAIN,LSL2,LCO2
DIMENSION X(9,2),VSWR(8),SWRS(8)
COMPLEX S11,S12,S22,S21,T11,T12,T22,T21,CRHO,RHOL,ZIN,ZLO,V
COMMON KDATE1,KDATE2,KGAS,PRESS,KUR,POWIN,POWRE,SL1,
1 SL2,LSL2,CO1,CO2,LCO2,X,VSWR,SCPOS,RMSDW,LAMBDA,THETA,
2 RMSDT,NMIN,NVSWR,RMSDV,S,ZINR,ZINI,ZLOR,ZLOI,POWABS
DATA PI,SIGMA,ZO/3.141592,1.OE6,50.0/
CALL FIL
READ(1,5) KD
5 FORMAT(T2)
KAN=0
30 CALL INP
CALL MINI
C CONVERSION OF POWER READINGS
DBI=19.7
DBR=19.5
DBI=10.0**(DBI/10)
DBR=10.0**(DBR/10)
POWIN=POWIN*DBI
POWRE=POWRE*DBR
POWABS=POWIN-POWRE
WRITE(6,100)KDATE1,KDATE2
100 FORMAT(1H//'IMPEDANCE CALCULATION',20X,2I4///)
WRITE(6,110)KGAS,PRESS
110 FORMAT(1H,'Pressure of ',A2,' gas was ',E10.3,'mbar'//)
WRITE(6,120)KUR,POWIN,POWRE,POWABS
120 FORMAT(1H,'MICROWAVE CONDITIONS'//' Microtron current = ',I3,
1 ' mA'/' Incident power = ',F5.1,' W'/' Reflected power = ',
2 F5.1,' W'/' Net input power = ',F5.1,' W')
WRITE(6,130) LAMBDA,RMSDW
130 FORMAT(1H,'Wavelength = ',F6.3,' cms',5X,'RMSD on',
1 ' wavelength = ',F5.3)
WRITE(6,140) THETA,RMSDT
140 FORMAT(1H,'Phase angle = ',F6.2,' radians',5X,'RMSD on',
1 ' phase angle = ',F5.2///)
C CALCULATION OF CAVITY PARAMETERS
C ATTENUATION
FREQ=29.9777/LAMBDA
SL1A=SL1*4/PI
ALPHA=9.95*(10.0**(-6))/0.434294
ALPHAC=ALPHA*(1.0/CO1+1.0/CO2)/ALOG(CO1/CO2)
ALPHAS=ALPHA*(1.0/SL1A+1.0/SL2)/ALOG(CO1/CO2)
FRE=SQRT(FREQ*(10.0**9)/SIGMA)
ALPHAC=ALPHAC*FRE/20
ALPHAS=ALPHAS*FRE/20
C CALCULATION OF U VALUES
ZC=59.933*ALOG(CO1/CO2)
ZS=59.933*ALOG(SL1A/SL2)
U1=(ZO+ZC)/(2.0*ZO)

```

```

U2=(ZO-ZC)/(2.0*ZO)
C  CALCULATION OF S PARAMETERS
S11=CMPLX((ZC+ZS)/(2.0*ZC),0.0)
S12=CMPLX((ZC-ZS)/(2.0*ZC),0.0)
S22=S11
S21=S12
C  CALCULATION OF T PARAMETERS
BETA=2*PI/LAMBDA
B1=BETA*(LSL2+LCO2)
B2=BETA*(LSL2-LCO2)
A1=ALPHAS*LSL2+ALPHAC*LCO2
A2=ALPHAS*LSL2-ALPHAC*LCO2
T11=U1*S11*(EXP(A1))*CMPLX(COS(B1),SIN(B1))+
1  U2*S12*(EXP(A2))*CMPLX(COS(B2),SIN(B2))
T12=U2*S11*(EXP(A1))*CMPLX(COS(B1),SIN(B1))+
1  U1*S12*(EXP(A2))*CMPLX(COS(B2),SIN(B2))
T22=U2*S21*(EXP(-A2))*CMPLX(COS(-B2),SIN(-B2))+
1  U1*S22*(EXP(-A1))*CMPLX(COS(-B1),SIN(-B1))
T21=U1*S21*(EXP(-A2))*CMPLX(COS(-B2),SIN(-B2))+
1  U2*S22*(EXP(-A1))*CMPLX(COS(-B1),SIN(-B1))
C  CALCULATION OF VSWR
DO 10 I=1,NVSWR
VS=VSWR(I)/20
SWRS(I)=10.0**VS
S=SWRS(I)
C  CALCULATION OF INPUT REFLECTION COEFFICIENT
RHOIN=(S-1)/(S+1)
CRHO=RHOIN*CMPLX(COS(THETA),SIN(THETA))
C  CALCULATION OF LOAD REFLECTION COEFFICIENT
RHOL=(CRHO*T11+T12)/(T22+CRHO*T21)
C  CALCULATION OF CAVITY INPUT AND LOAD IMPEDANCE
ZIN=50.0*(1.0+CRHO)/(1.0-CRHO)
ZLO=ZS*(1.0+RHOL)/(1.0-RHOL)
C  VOLTAGE ACROSS END OF CAVITY INNER
V=(T22*T11-T12*T21)*(1+RHOL)/(T11-T21*RHOL)
C  OUTPUT VALUES
GAIN=CABS(V)
RHO=CABS(RHOL)
ANG=57.29578*ATAN2(AIMAG(RHOL),REAL(RHOL))
ZINR=REAL(ZIN)
ZINI=AIMAG(ZIN)
ZLOR=REAL(ZLO)
ZLOI=AIMAG(ZLO)
Z=CABS(ZLO)
AG=57.295778*ATAN(ZLOI/ZLOR)
IF (I.GT.1) GO TO 240
WRITE(6,170)
170  FORMAT(1H /'  VSWR',7X,'Input impedance',6X,'Load impedance',7X,
1  '/Z/',8X,'Phase'/17X,'(ohms)',15X,'(ohms)',11X,'(ohms)',
2  4X,'(degrees)')
240  WRITE(6,180) S,ZINR,ZINI,ZLOR,ZLOI,Z,AG
180  FORMAT(1H ,F6.2,5X,F7.2,2X,F7.2,'j',4X,F7.2,2X,F7.2,'j',4X,F7.2,
1  5X,F7.2)
10  CONTINUE
KAN=KAN+1
IF (KAN.LT.KD) GO TO 30
STOP
END

```

```

SUBROUTINE MINP
  REAL LAMBDA,LS2,LCO2
  COMMON KDATE1,KDATE2,KGAS,PRESS,KUR,POWIN,POWRE,SL1,
1  SL2,LSL2,CO1,CO2,LCO2,X(9,2),VSWR(8),SCPOS,RMSDW,LAMBDA,THETA,
2  RMSDT,NMIN,NVSWR,RMSDV,S,ZINR,ZINI,ZLOR,ZLOI,POWABS
  READ(1,30) KDATE1,KDATE2,KGAS,PRESS,KUR,POWIN,POWRE
30  FORMAT(2I4,A2,E10.3,I3,2F5.3)
  READ(1,40) SL1,SL2,LSL2,CO1,CO2,LCO2
40  FORMAT(2F5.3,F6.4,2F5.3,F6.4)
  READ(1,50) NMIN
50  FORMAT(I1)
  DO 60 I=NMIN,1,-1
  READ(1,70) X(I,1),X(I,2)
70  FORMAT(2F6.3)
60  CONTINUE
  READ(1,50) NVSWR
  DO 90 I=1,NVSWR
  READ(1,80) VSWR
80  FORMAT(F4.1)
90  CONTINUE
  READ(1,100) SCPOS
100 FORMAT(F6.3)
  RETURN
  END

```

```

SUBROUTINE MINI
C  CALCULATION OF MINIMA POSITION,LAMBDA & PHASE SHIFT
  REAL LAMBDA,LSL2,LCO2
  DIMENSION XM(8),XK(8),THET(8)
  COMMON KDATE1,KDATE2,KGAS,PRESS,KUR,POWIN,POWRE,SL1,
1  SL2,LSL2,CO1,CO2,LCO2,X(9,2),VSWR(8),SCPOS,RMSDW,LAMBDA,THETA,
2  RMSDT,NMIN,NVSWR,RMSDV,S,ZINR,ZINI,ZLOR,ZLOI,POWABS
C  CALCULATION OF MINIMA POSITION
  XMZ=0.0
  DO 10 I=1,NMIN
  XM(I)=(X(I,1)+X(I,2))/2
10  CONTINUE
  KK=NMIN-1
  DO 20 I=1,KK
  XK(I)=XM(I+1)-XM(I)
  XMZ=XK(I)+XMZ
20  CONTINUE
C  CALCULATION OF LAMBDA
  XMZ=XMZ/(NMIN-1)
  SD=0.0
  DO 30 I=1,(NMIN-1)
  SD=(XK(I)-XMZ)**2+SD
30  CONTINUE
  RMSDW=2*SQRT(SD/(NMIN-2))
  LAMBDA=2*XMZ
C  CALCULATION OF THETA
  DO 40 I=1,NMIN

```

```
      THET(I)=12.566368*(XM(I)+SCPOS+LAMBDA/4-(3+I)*LAMBDA/2)/LAMBDA
40  CONTINUE
      THETA=0.0
      DO 50 I=1,NMIN
      THETA=THET(I)+THETA
50  CONTINUE
      THETA=THET/NMIN
      SD=0.0
      DO 60 I=1,NMIN
60  CONTINUE
      RMSDT=SQRT(SD/(NMIN-1))
      RETURN
      END
```

APPENDIX III

PROBE

```

DIMENSION A(45,5,2),V(45),W(45)
BYTE X(16),Y(16)
LOGICAL*1 CN(14),D(3),B(3),C(3)
COMMON KON
DATA CN/'D','X','1',':','M','Y','P','R','O','G','.',',',
1  'D','A','T'/
C  PROBE DATA FILE
   TYPE 2
   2  FORMAT(1H ,'Enter file name,(6A1) ',,$)
      ACCEPT 4,(CN(I),I=5,10)
   4  FORMAT(6A1)
      OPEN(UNIT=1,NAME=CN,TYPE='NEW')
      TYPE 10
  10  FORMAT(1H0,'Enter date & control(e.g. 11128301),(2I4) ',,$)
  60  ACCEPT 20,KDATE1,KDATE2
  20  FORMAT(2I4)
      TYPE 30,KDATE1,KDATE2
  30  FORMAT(1H ,'Date entered is ',2I4)
      CALL REPLY
      IF (KON.EQ.'Y') GO TO 130
      TYPE 50
  50  FORMAT(1H ,'Enter correct date !',,$)
      GO TO 60
 130  TYPE 80
   80  FORMAT(1H0,'Enter gas used (e.g. AR),(A2) ',,$)
      ACCEPT 90,KGAS
   90  FORMAT(A2)
      TYPE 100,KGAS
 100  FORMAT(1H ,'Gas used was ',A2)
      CALL REPLY
      IF (KON.EQ.'Y') GO TO 145
      TYPE 120
 120  FORMAT(1H ,'Retype value(s) !')
      GO TO 130
 145  TYPE 150
 150  FORMAT(1H0,'Enter gas pressure,(E10.3) ',,$)
      ACCEPT 160,PRESS
 160  FORMAT(E10.3)
      TYPE 170,PRESS
 170  FORMAT(1H ,'Pressure = ',E10.3)
      CALL REPLY
      IF (KON.EQ.'Y') GO TO 195
      TYPE 120
      GO TO 145
 195  TYPE 200
 200  FORMAT(1H0,'Enter microtron current,(I3) ',,$)
      ACCEPT 210,KUR
 210  FORMAT(I3)
      TYPE 220

```

```

220 FORMAT(1H , 'Incident power reading,(F5.3) = ', $)
    ACCEPT 230, POWI
230 FORMAT(F5.3)
    TYPE 240
240 FORMAT(1H , 'Reflected power reading,(F5.3) = ', $)
    ACCEPT 230, POWR
    TYPE 250, KUR, POWI, POWR
250 FORMAT(1H , 'Microtron current = ', I3/' Incident power = ',
1 F5.3/' Reflected power = ', F5.3)
    CALL REPLY
    IF (KON.EQ.'Y') GO TO 260
    TYPE 120
    GO TO 195
260 WRITE(1,270) KDATE1,KDATE2,KGAS,PRESS,KUR,POWI,POWR
270 FORMAT(2I4,A2,E10.3,I3,2F5.3)
    TYPE 275
275 FORMAT(1H , 'Enter number of probes to be used,(I,())', $)
    ACCEPT 281, NP1, NP2
281 FORMAT(I,I)
    TYPE 285
285 FORMAT(1H , 'Enter resistor switch no.(I2)', $)
    ACCEPT 290, IR
290 FORMAT(I2)
    WRITE(1,290) IR
C   Clear dpm's
    J=IBUP(2,2)
    J=IBUP(2,3)
280 FORMAT(I)
C   Read 200V dpm
300 J=IBUP(3,2)
    TI=SECNDS(0.)
320 DELTA=SECNDS(TI)
    IF(DELTA.LT.(0.5)) GO TO 320
    J=IBUP(1,2,X,7)
    DECODE(J-1,340,X)Z
340 FORMAT(F7.2) .OR
    IF(Z.LT.(0.00) .OR Z.GE.5.00) GO TO 300
    D(1)=49
    D(2)=(IR-10)+48
    D(3)=10
    J=IBUP(0,4,D,3)
    KON=NP1
    TYPE 901, KON
901 FORMAT(1H , 'KON= ', I)
900 B(1)=43
    B(2)=48+KON
    B(3)=10
    WRITE(1,280) KON
    J=IBUP(0,4,B,3)
C   Read both dpms for 5 cycles
    DO 850 K=1,5

```

```

DO 400 I=1,45
J=IBUP(3,2)
J=IBUP(3,3)
TI=SECNDS(0.)
380 DELTA=SECNDS(TI)
IF(DELTA.LT.0.5) GO TO 380
J=IBUP(1,2,X,7)
J=IBUP(1,3,Y,7)
DECODE(J-1,340,X)V(I)
DECODE(J-1,340,Y)W(I)
400 CONTINUE
DO 600 I=1,45
A(I,K,1)=V(I)
A(I,K,2)=W(I)
WRITE(1,70)A(I,K,1),A(I,K,2)
70 FORMAT(2F7.2)
600 CONTINUE
850 CONTINUE
C Check voltage on dpm
800 J=IBUP(3,2)
TI=SECNDS(0.)
700 DELTA=SECNDS(TI)
IF(DELTA.LT.0.5) GO TO 700
J=IBUP(1,2,X,7)
DECODE(J-1,340,X)Z
IF(Z.LT.0.0.OR.Z.GE.5.0) GO TO 800
C(1)=45
C(2)=48+KON
C(3)=10
J=IBUP(0,4,C,3)
C Switch to next probe
KON=KON+1
IF(KON.LE.NP2) GO TO 900
CLOSE(UNIT=1,DISPOSE='KEEP')
STOP
END

```

PRFIT 1

```

C THIS PROGRAMME CALCULATES THE RATIO OF CIRCUIT TO ION
CURRENTS FOR EQUATION 9.14
9 TYPE 1
1 FORMAT(1H , 'ENTER T' / T ' )
ACCEPT 2,RATT
TYPE 15
15 FORMAT(1H , 'ENTER T' )
ACCEPT 16,T
16 FORMAT(F7.1)
WRITE(6,110)RATT,T
110 FORMAT(1H ,F4.1,3X,F7.1)
2 FORMAT(F4.1)
TYPE 3
3 FORMAT(1H , 'ENTER I' / I & VB' )

```

```

ACCEPT 4,RATI,VB
4  FORMAT(F7.3,F4.0)
WRITE(6,150)RATI,VB
150 FORMAT(1H ,F7.3,3X,F4.0)
V1=(1.38E-23*T)/1.6E-19
V2=V1*RATT
TYPE 100,V1,V2
100 FORMAT(1H ,2F7.3)
R=1.0
6  V=R
F1=EXP((VB-V)/V1)
F2=EXP((VB-V)/V2)
F3=EXP(0.85*V*((1/V2)-(1/V1)))
F4=EXP(0.85*V*((1/V1)-(1/V2)))
CUR1=(1-F1)+((RATI**2)*(1-F2))
CUR2=(1+F1)+((RATI**2)*(1+F2))+(2*RATI*(F3+F4))
CUR=CUR1/CUR2
VX=-R
FX1=EXP((VX-VB)/V1)
FX2=EXP((VX-VB)/V2)
FX3=EXP(0.85*VX*((1/V2)-(1/V1)))
FX4=EXP(0.85*VX*((1/V1)-(1/V2)))
CURX1=(FX1-1)+((RATI**2)*(FX2-1))
CURX2=(FX1+1)+((RATI**2)*(FX2+1))+(2*RATI*(FX3+FX4))
CURX=CURX1/CURX2
WRITE(6,5) CUR,CURX
5  FORMAT(1H ,F8.3,3X,F8.3)
R=R+1.0
IF(R.EQ.50.0) GO TO 10
GO TO 6
10 TYPE 7
7  FORMAT(1H ,'ANOTHER RUN ? Y/N')
ACCEPT 11,X
11 FORMAT(A)
IF(X.EQ.Y) GO TO 9
STOP
END

```

PRFIT 2

```

C  THIS PROGRAMME CALCULATES THE RATIO OF CIRCUIT TO ION
CURRENTS FOR EQUATION 9.15
9  TYPE 1
1  FORMAT(1H ,'ENTER T'/T ')
ACCEPT 2,RATT
TYPE 15
15 FORMAT(1H ,'ENTER T')
ACCEPT 16,T
16 FORMAT(F7.1)
WRITE(6,110)RATT,T
110 FORMAT(1H ,F4.1,3X,F7.1)
2  FORMAT(F4.1)
TYPE 3

```

```

3  FORMAT(1H , 'ENTER I' / I ' VB' )
   ACCEPT 4, RATI, VB
4  FORMAT(F7.3, F4.0)
   WRITE(6, 150) RATI, VB
150 FORMAT(1H , F7.3, 3X, F4.0)
    V1=(1.38E-23*T)/1.6E-19
    V2=V1*RATI
    TYPE 100, V1, V2
100 FORMAT(1H , 2F7.3)
    R=1.0
    6  V=-R
       F1=EXP((VB-V)/V1)
       F2=EXP((VB-V)/V2)
       F3=EXP(0.85*V*((1/V2)-(1/V1)))
       F4=EXP(0.85*V*((1/V1)-(1/V2)))
       CUR1=(1-F1)+((RATI**2)*(1-F2))
       CUR2=(1+F1)+((RATI**2)*(1+F2))+ (2*RATI*(F3+F4))
       CUR=CUR1/CUR2
       VX=R
       FX1=EXP((VX-VB)/V1)
       FX2=EXP((VX-VB)/V2)
       FX3=EXP(0.85*VX*((1/V2)-(1/V1)))
       FX4=EXP(0.85*VX*((1/V1)-(1/V2)))
       CURX1=(FX1-1)+((RATI**2)*(FX2-1))
       CURX2=(FX1+1)+((RATI**2)*(FX2+1))+ (2*RATI*(FX3+FX4))
       CURX=CURX1/CURX2
       WRITE(6, 5) CUR, CURX
    5  FORMAT(1H , F8.3, 3X, F8.3)
       R=R+1.0
       IF(R.EQ.50.0) GO TO 10
       GO TO 6
10  TYPE 7
    7  FORMAT(1H , 'ANOTHER RUN ? Y/N' )
       ACCEPT 11, X
11  FORMAT(A)
       IF(X.EQ.Y) GO TO 9
       STOP
       END

```